
Magnetic fields in Sun-like stars and their effects on circumstellar environments

Julián David Alvarado-Gómez



München 2016

Magnetic fields in Sun-like stars and their effects on circumstellar environments

Julián David Alvarado-Gómez

Dissertation
an der Fakultät für Physik
der Ludwig-Maximilians-Universität
München

vorgelegt von
Julián David Alvarado-Gómez
aus Bogotá, Kolumbien

München, den 22. Juli 2016

Erstgutachter: Prof. Dr. Thomas Preibisch

Zweitgutachter: Prof. Dr. Artie Hatzes

Tag der mündlichen Prüfung: 29. September 2016

Is the force of the Sun that drives me.

Contents

Table of Contents	vii
List of Figures	xi
List of Tables	xv
Zusammenfassung	xvii
Abstract	xix
Motivation	xxi
1 Introduction	1
1.1 State of the art	1
1.1.1 Magnetism in cool main sequence stars	1
1.1.2 Stellar magnetism as noise	5
1.1.3 Magnetic fields and stellar winds	6
1.1.4 Magnetised environment in planet-hosting stars: 3D MHD modelling	11
1.2 Open issues	18
1.3 About this Thesis	19
2 Activity and magnetic field structure of the Sun-like planet-hosting star HD 1237	23
2.1 Chapter organization	23
2.2 HD 1237 stellar properties	24
2.3 Observational data	25
2.4 Magnetic activity and variability	25
2.4.1 Index calibration	26
2.4.2 Activity indicators	28
2.5 Magnetic field signatures	30
2.5.1 Longitudinal magnetic field	32
2.6 Surface magnetic field mapping	33
2.6.1 Optimal line profile and stellar parameters	33
2.6.2 Optimal fit quality: Entropy content in ZDI maps	35
2.6.3 ZDI maps and synthetic Stokes V profiles	37
2.7 Summary and discussion	39

2.8	Chapter conclusions	42
3	A spectropolarimetric study of the planet-hosting G dwarf HD 147513	43
3.1	Chapter organization	43
3.2	HD 147513	44
3.3	Spectropolarimetric observations	45
3.4	Chromospheric activity	46
3.5	Photospheric line profiles & stellar magnetic field	47
3.5.1	LSD profiles	48
3.5.2	Longitudinal magnetic field	49
3.5.3	Radial velocity and activity	49
3.6	Large-scale magnetic field maps of HD 147513	50
3.7	Discussion and chapter conclusions	52
4	Simulating the environment – I. Coronal structure	55
4.1	Chapter organization	55
4.2	Large-scale magnetic field maps	56
4.3	3D MHD numerical simulation	61
4.4	Results	62
4.4.1	Evaluation of the solar case	62
4.4.2	HD 1237 (GJ 3021)	66
4.4.3	HD 22049 (ϵ Eridani)	68
4.4.4	HD 147513 (HR 6094)	70
4.5	Analysis and discussion	71
4.5.1	Thermodynamic coronal properties	71
4.5.2	High-Energy emission and magnetic flux	73
4.5.3	Coronal features and rotational modulation	76
4.6	Summary and chapter conclusions	78
5	Simulating the environment – II. Stellar winds and inner astrospheres	81
5.1	Chapter organization	82
5.2	3D MHD simulation	82
5.3	Numerical results	83
5.3.1	Alfvén surface, mass and angular momentum loss rates	83
5.3.2	Stellar winds and astrospheric current sheet	89
5.3.3	Environment of the HD 1237 system	93
5.4	Analysis and discussion	99
5.4.1	Magnetism and mass / angular momentum loss rates	99
5.4.2	Stellar winds and habitable zones	103
5.5	Summary and chapter conclusions	106
	Outlook	111

A ZDI maps from the December 2012 dataset of HD 1237	113
Bibliography	115
Acknowledgements	129

List of Figures

1.1	General properties of the large-scale magnetic fields of cool main sequence stars.	2
1.2	Examples of large-scale magnetic field topologies in Sun-like stars.	3
1.3	Examples of large-scale magnetic field topologies in M-dwarf stars.	4
1.4	Solar RV variations observed with HARPS compared with various activity proxies.	5
1.5	Schematic diagram of the heliosphere components.	7
1.6	Mass loss rates vs. coronal X-ray activity in main sequence cool stars.	8
1.7	Mass loss rates vs. coronal X-ray activity for stars with magnetic topologies recovered with ZDI.	9
1.8	Example of 2D MHD simulations of thermally-driven solar/stellar winds using realistic magnetic field topologies.	10
1.9	Mapped evolution of the large-scale magnetic field topology of τ Boo with ZDI (2007–2008).	12
1.10	Mapped evolution of the large-scale magnetic field topology of τ Boo with ZDI (2011–2015).	13
1.11	ZDI-driven 3D MHD simulations of the stellar wind around τ Boo.	14
1.12	ZDI-driven 3D MHD simulation of the stellar wind around EV Lac.	16
1.13	Simulated magnetospheric response for planets inside and outside the Alfvén surface of EV Lac.	17
2.1	Calibration to the S_{MW} scale of the HARPS fluxes $\left(\frac{H+K}{R+V}\right)_{\text{H}}$	27
2.2	Core regions of the Ca II K and H lines of HD 1237.	28
2.3	HARPS fluxes $(H + K)/(R + V)$ for the available observations of HD 1237.	29
2.4	Line mask comparison on the derived LSD profiles of HD 1237.	31
2.5	Observed evolution of the longitudinal magnetic field (B_{ℓ}) of HD 1237.	32
2.6	Determination of the rotation period (P_{rot}) of HD 1237.	34
2.7	Proposed selection criteria for the optimal fit quality in ZDI reconstructions.	36
2.8	Reconstructed ZDI maps of HD 1237.	38
3.1	Chromospheric activity in HD 147513.	46
3.2	LSD Profiles of HD 147513.	48
3.3	B_{ℓ} measurements of HD 147513.	49

3.4	Extracted RV variability of HD 147513 from HARPSpol observations.	50
3.5	Results of the ZDI analysis for HD 147513.	51
4.1	Radial magnetic field maps of HD 1237 used to drive the MHD model.	57
4.2	Radial magnetic field maps of HD 22049 used to drive the MHD model.	58
4.3	Radial magnetic field maps of HD 147513 used to drive the MHD model.	59
4.4	SOHO /MDI solar magnetograms covering activity minimum and maximum.	60
4.5	Simulated coronal structure during solar minimum (CR 1922).	63
4.6	Simulated coronal structure during solar maximum (CR 1962).	63
4.7	Simulated coronal structure of HD 1237 driven by the ZDI map.	67
4.8	Simulated coronal structure of HD 1237 driven by the SH-ZDI map.	67
4.9	Simulated coronal structure of HD 22049 driven by the ZDI map.	69
4.10	Simulated coronal structure of HD 22049 driven by the SH-ZDI map.	69
4.11	Simulated coronal structure of HD 147513 driven by the SH-ZDI map.	71
4.12	Emission measure distributions calculated from the 3D MHD steady-state solutions.	72
4.13	Simulated high-energy coronal emission vs. unsigned radial magnetic flux $\langle \Phi_{Br} \rangle_s$	74
4.14	Spatial distribution of the surface radial magnetic flux $\langle \Phi_{Br} \rangle_s$	76
4.15	Rotational modulation of the simulated high-energy coronal emission of HD 1237.	77
5.1	Solar wind simulations inside the Solar /Stellar Corona (SC) domain.	84
5.2	Simulated stellar wind structure of HD 22049 inside the SC domain.	85
5.3	Simulated stellar wind structure of HD 1237 inside the SC domain.	86
5.4	Simulated stellar wind structure of HD 147513 inside the SC domain.	87
5.5	Solar wind simulations inside the Inner Heliosphere (IH) domain.	90
5.6	Simulated stellar wind structure for HD 22049 inside the IH domain.	92
5.7	Simulated stellar wind structure for HD 147513 inside the IH domain.	93
5.8	Simulated environment of the HD 1237 system driven by the ZDI magnetic field map.	94
5.9	Simulated environment of the HD 1237 system driven by the SH-ZDI magnetic field map.	95
5.10	Simulated pole-on view on the equatorial distribution of the kinetic power K_{sw}^{pow} from wind-magnetospheric interaction in the HD 1237 system.	98
5.11	Simulated mass loss rate (\dot{M}) and angular momentum loss rate (\dot{J}) as a function of the surface-averaged unsigned radial magnetic flux $\langle \Phi_{Br} \rangle_s$	100
5.12	Stellar wind characterisation at the inner edges of the Habitable Zone (HZ) of HD 22049.	105
5.13	Initial exploration for potential systems to be characterized with ZDI with current spectropolarimetric instrumentation.	112
A.1	Optimal fit quality criterion for the Dec. 2012 dataset of HD 1237.	113

A.2 Results of the ZDI analysis for the Dec. 2012 dataset of HD 1237. 114

List of Tables

2.1	HD 1237 basic properties.	24
2.2	Journal of HARPSpol observations of HD 1237.	26
2.3	Stars included in the α calibration.	27
2.4	Average activity indicators for HD 1237.	30
3.1	HD 147513 basic properties.	44
3.2	Journal of HARPSpol observations of HD 147513.	45
4.1	Planet-hosting systems and their observational properties.	56
4.2	Evaluation of the solar simulations in the EUV range.	65
4.3	Average physical properties of the inner corona region.	68
5.1	Stellar wind properties extracted at the Alfvénic surface (AS).	88
5.2	Parameters of the incident stellar wind and resulting properties inside the Global Magnetosphere (GM) in the HD 1237 system.	96
5.3	Stellar wind characterisation at the inner edge of the HZs of the considered systems.	104

Zusammenfassung

Diese Dissertation untersucht, wie verschiedene Eigenschaften der Oberflächenmagnetfelder in sonnenähnlichen Sternen, wie z.B. die Feldstärke, Topologie und Komplexität, die zirkumstellare Umgebung dieser Systeme beeinflussen. Diese Umgebung, die bis zum Rand der Astrosphäre reicht, versteht man als physikalische Bedingungen, die die Struktur des Koronal- und Sternwindes definieren. Während die Verbindung zwischen Sternmagnetismus und der erweiterten Umgebung für alle sonnenähnliche Sterne (G bis M-Typ) wichtig ist, werden in dieser Doktorarbeit solche Systeme untersucht, welche Planeten haben. Im Rahmen der Arbeit werden einige der modernsten Beobachtungstechniken in Sternmagnetismus mit den neuesten numerischen Simulationen kombiniert.

Der Beobachtungsaspekt umfasst bodengestützte, hochauflösende spektropolarimetrische Daten, aufgenommen mit dem High Accuracy Radial velocity Planet Searcher (HARPS), das am ESO La Silla 3.6m Teleskop angebracht ist. Hier wird eine vollständige spektropolarimetrische Analyse von zwei sonnenähnlichen Planeten-Muttersternen, HD 1237 (G8V) und HD 147513 (G5V), vorgestellt. Dies umfasst geeichte Aktivitätsmessungen der Chromosphäre und die erste Erfassung des Längs-Oberflächenmagnetfeldes. Darüber hinaus, werden in diesen Sternen, durch phasenaufgelöste spektropolarimetrische Zeitreihen und mit Hilfe der "Zeeman-Doppler-Imaging" (ZDI) tomographischen Technik, die fotosphärischen Magnetfelder auf großen Skalen rekonstruiert (ZDI Karten).

Verschiedene Elemente werden in Verbindung mit dem ZDI Verfahren erforscht, mit dem Ziel, die Qualität und Zuverlässigkeit der Feldrekonstruktion zu verbessern. Ein wichtiges Ergebnis dieser Analyse ist die Einbeziehung eines Abbruchkriteriums für den Grad des Fits an die Datenpunkte, basierend auf dem Informationsgehalt (image entropy) der ZDI Lösungsmenge. Dieses Kriterium hilft, den optimalen Grad der Anpassung des Modells an die Daten zu finden und verhindert das Auftreten von Artefakten in dem endgültig rekonstruierten Bild, die aufgrund vom Rauschen während der Anpassung auftreten können. Außerdem, da die gewonnenen Feldstärken in ZDI vom Grad der Anpassung abhängig sind, trägt diese Methode wesentlich zum systematischen Vergleich von magnetischen Karten von mehreren Epochen eines bestimmten Objekts bei und/oder zwischen anderen Sternen. Alle ZDI Rekonstruktionen in dieser Arbeit wurden mit Hilfe vom diesem Anpassungs-Abbruchkriterium erstellt.

Die numerische Komponente beinhaltet detaillierte datengestützte Modellierung der Corona, Sternwinden, inneren Astrosphären und der exoplanetaren Bedingungen um dieser Systeme. Die Simulationen werden mit einem leistungsstarken 3D-Magnetohydrodynamik

(MHD) Code durchgeführt, der am Center for Space Environment Modelling (CSEM) an der Universität in Michigan entwickelt wurde, und derzeit für Weltraumwetterstudien und Prognosen im Sonnensystem verwendet wird. Zwei Sonnensimulationen (für das Minimum und Maximum des Aktivitätszyklus) werden für ein qualitatives und quantitatives Bewertungsverfahren der Modelle im Vergleich zu Satellitendaten verwendet. Für jedes Sternsystem werden die ZDI Magnetfeldkarten in das Modell integriert, welche zu einer selbstkonsistenten Lösung führen. Auf diese Weise wird die Umgebung jedes Systems detailliert charakterisiert. Die wichtigsten Ergebnissen sind unter anderem die Massenverlusten die mit dem Sternwind verbunden sind, die hochenergetische Koronale Emission der Muttersterne und die Eigenschaften des Sternwindes an den inneren Rändern ihrer Habitablen Zonen (HZ). Diese Eigenschaften zeigen deutliche Abhängigkeit von der großskaligen magnetischen Feldstärke (genauer gesagt, mit dem absoluten Oberflächenmagnetfluss), welche parametrisiert und mit früheren Beobachtungen und numerischen Arbeiten verglichen werden. Insbesondere wurden die beobachteten Skalierungsbeziehungen zwischen dem Oberflächenmagnetfluss und der Röntgenleuchtkraft von unseren Beobachtungsdatengetriebenen Modellen reproduziert. Schließlich werden zusätzliche Simulationen durchgeführt um die Wind-Exoplaneten Wechselwirkungen an verschiedenen Orbitalpositionen im HD 1237 System zu bewerten. Dies zeigt, dass im Allgemeinen der Prozess der Teilchenzuführung in die Planetenatmosphären empfindlicher auf die Teilchendichte als das Geschwindigkeitsprofil des Sternwindes ist.

Da sich die Menge an spektropolarimetrischen Daten und ZDI Studien vergrößert, kann die Methodik die in dieser Arbeit untersucht wurde, auf sehr unterschiedliche weitere Systeme angewendet werden. Dies würde einen klaren Weg definieren, um die hier vorgestellten Ergebnisse zu erweitern und gleichzeitig wichtige Informationen für die wachsenden Forschungsgebiete der Exoplanetencharakterisierung und Astrobiologie liefern.

Abstract

This dissertation investigates how different properties of the surface magnetic field in Sun-like stars, such as the field strength, topology, and complexity, influence the circumstellar environment around these systems. This environment is understood as the physical conditions imposed by the coronal and stellar wind structure, extending up to the edge of the astrosphere. While the connection between stellar magnetism and the extended environment is important for all Sun-like stars (G to M type), planet-hosting systems are investigated in this thesis. The adopted framework combines some of the latest observational techniques in stellar magnetism with state-of-the-art numerical simulations.

The observational aspect comprises ground-based, high-resolution spectropolarimetric data from the High Accuracy Radial velocity Planet Searcher (HARPS) attached at the ESO La Silla 3.6m telescope. A complete spectropolarimetric analysis of two planet-hosting Sun-like stars, namely HD 1237 (G8V) and HD 147513 (G5V), is presented. This includes calibrated chromospheric activity measurements and the first detection of their surface longitudinal magnetic field. In addition, by using phase-resolved spectropolarimetric time-series and with the aid of the tomographic technique of Zeeman-Doppler Imaging (ZDI), the large-scale photospheric magnetic field in these stars is reconstructed (ZDI maps).

Various elements connected with the ZDI procedure are explored, with the aim of improving the quality and reliability of the large-scale field reconstructions. An important result of this analysis is the inclusion of a stopping criterion for the degree of fit to the data, based on the information content (image entropy) of the set of ZDI solutions. This criterion helps to identify the optimal model-to-observations degree of fit, preventing the appearance of artefacts in the final reconstructed image due to fitting noise. Furthermore, as the recovered field strengths in ZDI depend on the fit level, this methodology contributes substantially to the systematic comparison of multi-epoch magnetic maps of a given object and/or between different stars. All the ZDI reconstructions presented in this thesis have been obtained using this fit-stopping criterion.

The numerical component involves detailed data-driven modelling of the coroneae, stellar winds, inner astrospheres, and the exoplanetary conditions around these systems. Simulations are carried out using a high-performance 3D magnetohydrodynamics (MHD) code, developed at the Center for Space Environment Modelling (CSEM) of the University of Michigan, and currently used for solar system space weather studies and forecast. Two solar simulations (covering activity cycle minimum and maximum) are employed for a qualitative and quantitative evaluation procedure of the models against satellite data. For each

stellar system, the ZDI magnetic field maps are incorporated in the model to drive a self-consistent solution. In this way a detailed characterization of the environment of each system is obtained. The main results include the mass loss rates associated with the stellar wind, the high-energy coronal emission of the host-star, and the stellar wind properties at the inner edges of their Habitable Zones (HZ). These properties show clear dependencies on the large-scale magnetic field strength (more specifically with the unsigned surface magnetic flux), which are parametrised and compared with previous observational and numerical works. In particular, scaling relationships between the surface magnetic flux and the X-ray luminosity are properly recovered from these observationally-driven models. Finally, additional simulations are performed to assess wind-exoplanet interactions at different orbital locations in the HD 1237 system. This reveals that in general, the process of particle injection into the planetary atmosphere is more sensitive to the particle density rather than the velocity profile of the stellar wind.

As the amount of spectropolarimetric data and ZDI studies increase, the methodology investigated in this thesis can be applied to a wide variety of additional systems. This would represent a clear path to expand on the results presented here providing, at the same time, critical information for the growing fields of exoplanet characterization and astrobiology.

Motivation

We are at the gates of a historical transformation for the perception of Human kind in the cosmos, giving closure to the everlasting question: Are we alone in the Universe? Such achievement can only be compared with the Copernican revolution of the 16th century. In our rational brains the answer is almost certain, but our scientific roots push us to get conclusive evidence. In this Herculean endeavour, we have pointed our sharpest eyes towards the night sky and found thousands of other worlds orbiting another Suns. Nature has once more surprised us with a fascinating diversity of stellar systems, unanticipated even for the most visionary intellect. From gaseous giants nearly touching their parent stars, to double and even triple colourful sunsets for some systems; these unexpected discoveries have led us to expand our search beyond the parameters of our own solar system, and to include the most common stars in the Universe (M-dwarfs). Keeping a terrestrial connection, we look for planets at the right distance to their host stars, to be able to sustain liquid water on their surfaces; a cosmic mirror to reflect our beautiful "pale blue dot"...

Cutting-edge technology is bringing us closer to this goal, shedding a dim light into even harder questions on the origin and evolution of life. The brightest minds have engaged in this formidable quest, using our own Solar system as a beacon in the vastness of space. We are well aware of the tight tie between Earth's fate and the Sun's will. This royal bond extends to all members of this planetary brotherhood, from their very birth to an inexorable future end. In its extraordinary long reign, the Sun has slowly evolved into its current stage, starting and sustaining the spark of life somewhere along the road. During its evolution, the most striking change is perhaps the one regarding its magnetic nature. Just like any emperor, the Sun was active and aggressive in its youth, gradually becoming calm and peaceful while getting older. The majority of the planetary kingdoms of the galaxy are ruled by (M) dwarfs, who are known for being harsher and maintain longer hostile reigns than the Sun. This can dramatically affect the conditions of their subordinates throughout their lives, as they need to remain closer to their leaders to avoid the everlasting freeze of space. Furthermore, a battle between good and evil persists in these astrophysical realms, in the form of protection against invading cosmic rays, but sometimes also in attacks of flaring rage. Both factors could be essential either for the appearance, development or the eventual extinction of life in these systems. For these reasons, studying the impact of this magnetic dichotomy on the evolution of exoplanetary systems, is a fundamental step on our path to understand life in the Universe.

Chapter 1

Introduction

1.1 State of the art

1.1.1 Magnetism in cool main sequence stars

Analogous to the 11-year solar activity cycle, a large fraction of late-type stars ($\sim 60\%$) show chromospheric activity cycles, with periods ranging from 2.5 to 25 years (Baliunas et al. 1995). For a very limited number of these systems, including binaries, the coronal X-ray counterparts of these activity cycles have also been identified (e.g., Favata et al. 2008; Robrade et al. 2012). These periodic signatures appear as a result of the magnetic cycle of the star. In the case of the Sun, this is completed every 22 years, during which the polarity of the large-scale magnetic field is reversed twice (Hathaway 2010). These elements, the cyclic properties of the activity and magnetic field, constitute a major benchmark for any dynamo mechanism proposed for the magnetic field generation (Charbonneau 2014).

During the past two decades, the observational studies of magnetism in late-type stars have evolved dramatically; from these classical chromospheric activity diagnostics (e.g., Mount Wilson H-K project, Baliunas et al. 1995) to spectropolarimetric snapshot surveys (e.g. the BCool project, Marsden et al. 2014) and detailed long-term magnetic monitoring (e.g. Morgenthaler et al. 2012; Jeffers et al. 2014b; Boro Saikia et al. 2016). This has been enabled by the advent of improved instrumentation (e.g., HARPSpol@ESO3.6m, Mayor et al. 2003; Piskunov et al. 2011), together with advanced data analysis techniques for detection (e.g., least squares deconvolution, Donati et al. 1997; Kochukhov et al. 2010) and mapping of magnetic fields (e.g., Zeeman Doppler imaging - ZDI, Semel 1989; Brown et al. 1991; Donati & Brown 1997; Piskunov & Kochukhov 2002; Hussain et al. 2009; Kochukhov & Wade 2010). These recent studies have opened new possibilities for different areas of astrophysical research, such as dynamo processes and the origin of stellar magnetic fields across the HR diagram (Donati & Landstreet 2009).

Figure 1.1, taken from Donati (2011), contains the general observational properties obtained with ZDI of the large-scale magnetic fields in cool main sequence stars. These are presented as a function of stellar mass and rotation period. The symbol sizes indicate the relative strength of the large-scale magnetic field, covering 3 orders of magnitude (from

3 G to 1.5 kG). The colour scale synthesises the main geometry of the surface field, with red and blue representing purely poloidal and toroidal fields, respectively. The remaining colours indicate a mixture of these two fundamental topologies. Additionally, the symbol shapes denote the level of symmetry of the large-scale field, with decagons for purely axisymmetric configurations, and star-shaped symbols for purely non-axisymmetric fields.

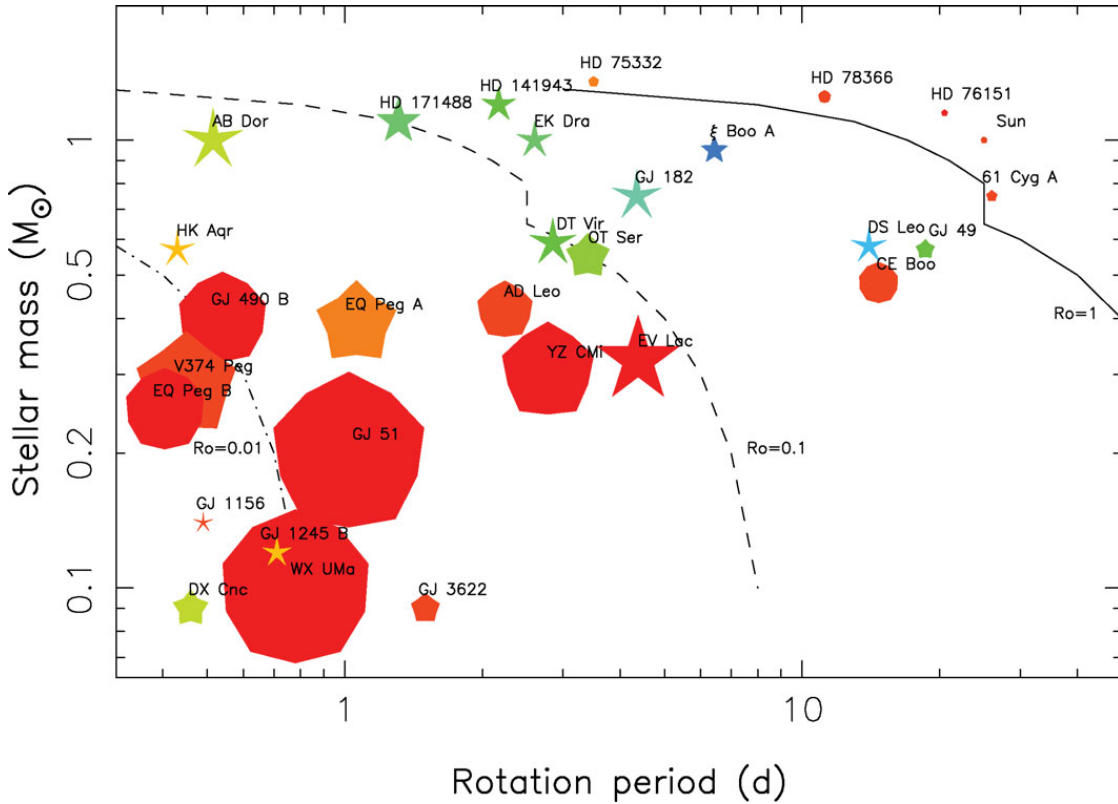


Figure 1.1: General properties of the large-scale magnetic fields of cool main sequence stars. The symbol size is indicative of the large-scale magnetic field strength (ranging from 3 G to 1.5 kG). The colours indicate the dominant topology of the field, with *blue* representing purely toroidal/azimuthal fields and *red* for purely poloidal magnetic configurations. The symbol shape represents the level of symmetry of the large-scale field (with decagon and star-shapes for purely axisymmetric and purely non-axisymmetric fields, respectively). **Taken from:** Donati (2011).

In the case of solar-type stars (with $M_* \simeq 1 M_\odot$), complex and relatively weak ($\ll 1$ kG) large-scale surface field topologies have been reported. The slowest rotators ($P_{\text{rot}} > 15$ d) possess the simplest and weakest large-scale fields. Fields strengthen and increase in complexity in more rapidly rotating stars (star-shapes in Fig. 1.1). Many of the maps for the most rapidly rotating stars also feature strong surface toroidal (or azimuthal) fields (see Fig. 1.2); a feature that has no clear counterpart on the Sun and very likely indicates a change in the underlying stellar dynamo (Petit et al. 2008; Petit et al. 2009; Fares et al. 2009; Morgenthaler et al. 2011, 2012; Boro Saikia et al. 2015). The BCool collaboration[†]

[†]BCool is part of the MagIcS initiative - See <http://www.ast.obs-mip.fr/users/donati/magics/v1/>.

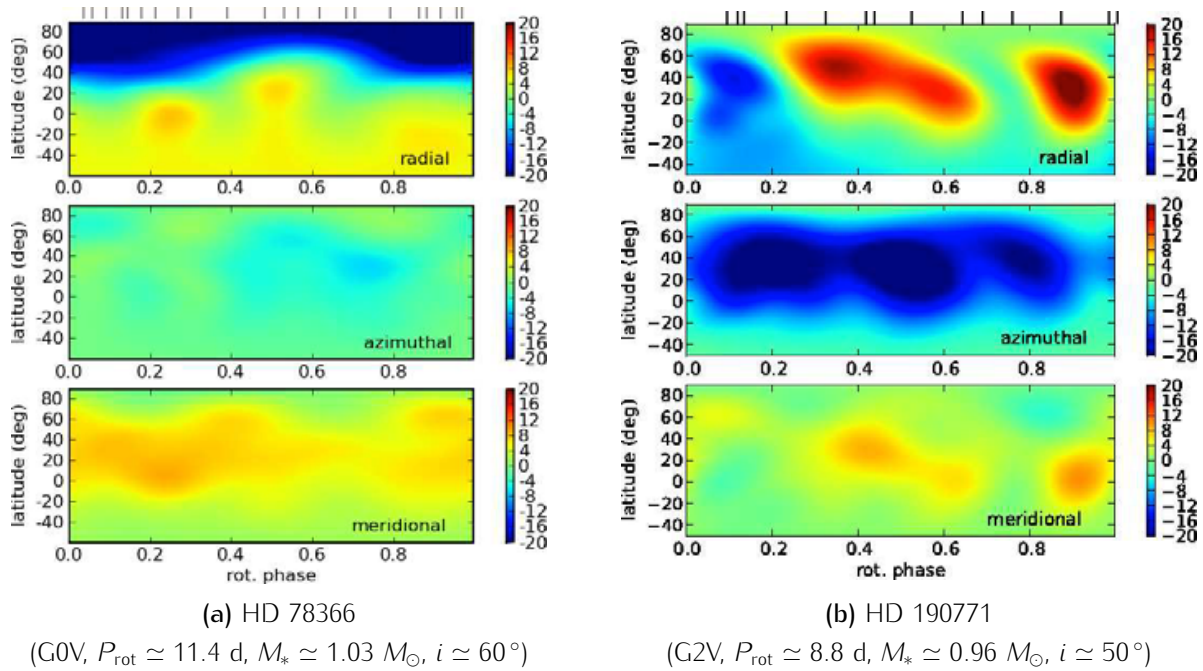
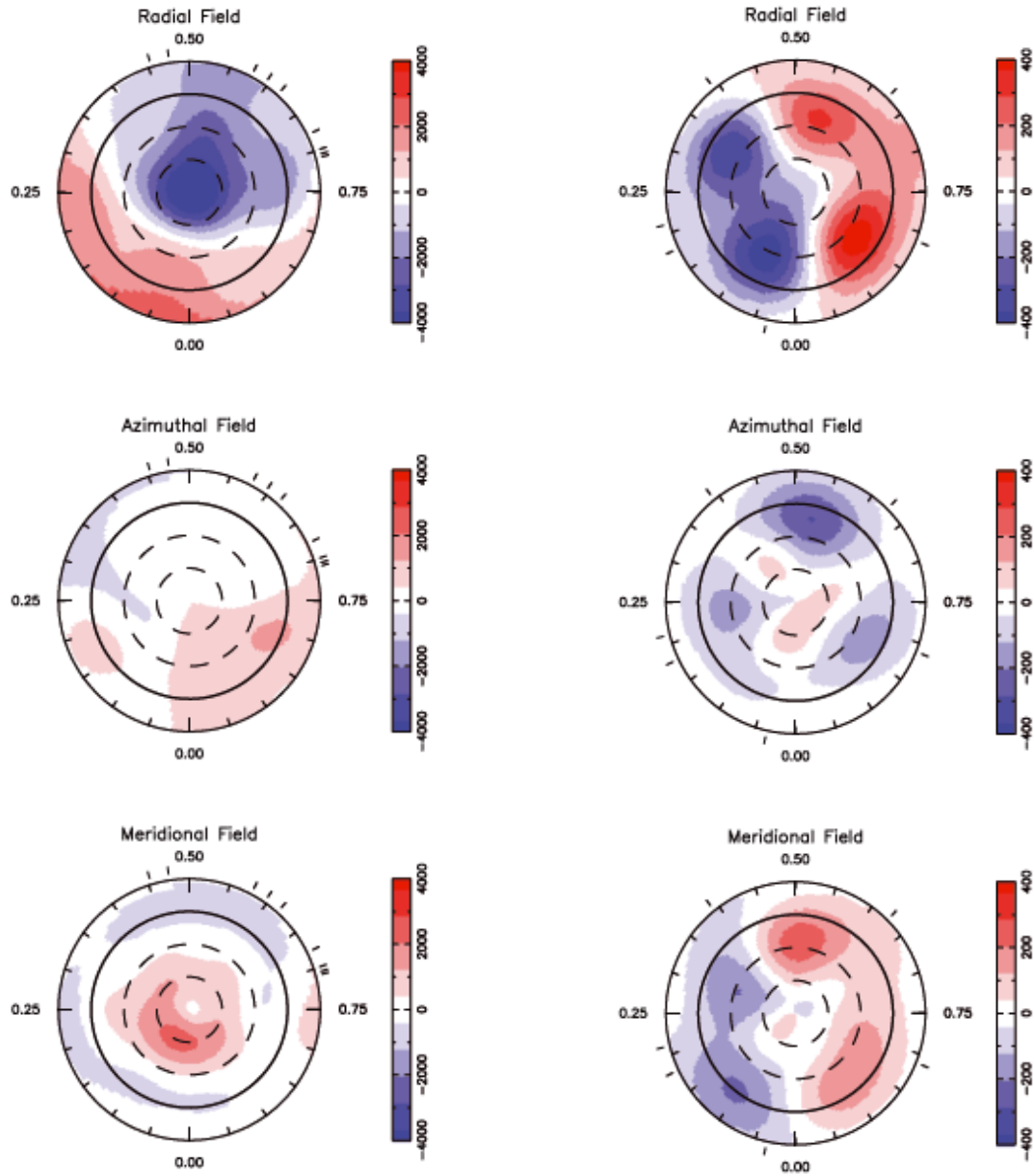


Figure 1.2: Examples of two large-scale magnetic field topologies in Sun-like stars recovered with ZDI. The colour scale denotes the polarity and surface field strength in Gauss (G). The field is decomposed into the radial (*top*), azimuthal (*middle*), and meridional (*bottom*) components. The phase coverage of each map is indicated by the black-tick marks in the top panels. The maps are presented in a latitude–phase Mercator projection. **Taken from:** [Morgenthaler et al. \(2011\)](#).

has collected and analysed spectropolarimetric data of over 170 solar-type stars. [Marsden et al. \(2014\)](#) report magnetic field detections on 67 of these stars and present these detections in the context of their activity, rotation and age. A recent analysis, performed by [Folsom et al. \(2016\)](#), has corroborated these global trends with rotation period, field strength and complexity, by reconstructing ZDI maps of 15 young solar-type stars with ages between 20–250 Myr.

As can be seen from Fig. 1.1, the stronger magnetic fields in these kind of stars have been detected in the low-mass end (e.g., $M_* \leq 0.5 M_{\odot}$), populated mostly by fully (or nearly fully) convective M-dwarfs. [Morin et al. \(2010\)](#) shows that as the rotation period decreases, very low-mass objects with similar stellar parameters seem to have two different classes of magnetic topologies; one with a tendency towards strong and simple magnetic geometries (i.e., mostly poloidal and axisymmetric configurations), and a second one with much weaker fields with a significant presence of non-axisymmetric configurations, including toroidal components (see Fig. 1.3). These properties are common in early ([Donati et al. 2008b](#)), mid ([Morin et al. 2008](#)), late M-dwarfs ([Morin et al. 2010](#)), and also have been recently observed in less active stars of this spectral type ([Hébrard et al. 2016](#)). These peculiar properties in the large-scale magnetic field have been interpreted as a signature of dynamo bistability occurring in these low-mass objects ([Morin et al. 2011](#); [Gastine et al. 2013](#)).



(a) GJ 51

(M5V, $P_{\text{rot}} \simeq 1.02$ d, $M_* \simeq 0.22 M_{\odot}$, $i \simeq 60^{\circ}$)

(b) GJ 1245B

(M5.5V, $P_{\text{rot}} \simeq 0.71$ d, $M_* \simeq 0.12 M_{\odot}$, $i \simeq 40^{\circ}$)

Figure 1.3: Examples of two large-scale magnetic field topologies in M-dwarfs stars recovered with ZDI. The colour scale denotes the polarity and surface field strength in G. Note the difference in the colour scale between both cases. The field is decomposed into the radial (*top*), azimuthal (*middle*), and meridional (*bottom*) components. The maps are presented in a flattened polar projection down to latitudes of -30° . The stellar equator is denoted by the internal black straight circle and the phase coverage of each map is indicated by the radial tick marks. **Taken from:** [Morin et al. \(2010\)](#).

1.1.2 Stellar magnetism as noise

As efforts to find planets around other stars intensify, there is a need to better characterise stellar magnetic activity on a range of timescales in moderate to very active stars. Such activity-related signatures in late-type stars are known to affect the detection techniques in the form of radial-velocity (RV) “jitter” and photometric “flicker” (Bastien et al. 2014). By simulating the effects induced by active regions and spots in Sun-like stars, recent tools have been developed to estimate and remove their contribution from the observations (e.g., Reiners et al. 2010; Boisse et al. 2012; Hébrard et al. 2014; Dumusque et al. 2014).

Other studies are performing Sun-as-a-star experiments, by measuring the solar RV variability with the same high-precision spectrographs used in current exoplanet searches (e.g., HARPS, HARPS-N), and taking advantage of the extensive satellite and ground-based record of solar activity (Dumusque et al. 2015; Haywood et al. 2016). One important result of such solar activity characterisations is the reliability of using different activity proxies to try to correct for the magnetically-induced effects in the RV data. Figure 1.4, taken from Haywood et al. (2016), shows the HARPS RV variability of the Sun as a star, in combination with the temporal evolution of several magnetic/activity proxies. The results of Haywood et al. (2016) indicate that the disc-averaged longitudinal magnetic flux, $|B_\ell|$ (panel b), and its filling factor, show a better correlation with the RV signal in comparison with other activity proxies such as the chromospheric index $\log(R'_{\text{HK}})$, plotted in panel f. As B_ℓ can be re-

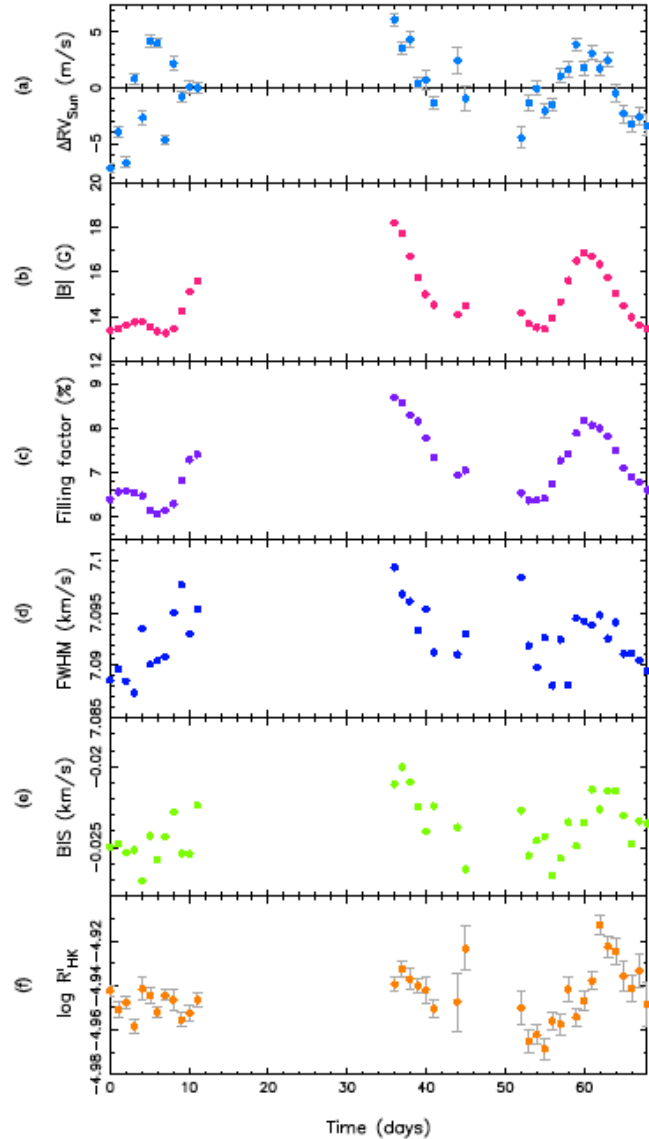


Figure 1.4: Solar RV variations observed with HARPS (panel a) compared with various activity proxies inferred from satellite and ground-based observations. The disk-averaged longitudinal magnetic flux, $|B_\ell|$ (panel b), and filling factor (panel c), show a better correlation with the RV signal in comparison with other activity proxies such as the chromospheric index $\log(R'_{\text{HK}})$, plotted in panel f.

Taken from: Haywood et al. (2016).

tried (to some extent) using spectropolarimetric observations, this could represent an important advantage for upcoming instrumentation with such capabilities (e.g., SPIRou, CRIRES+) in the area of exoplanet detection and characterisation (Pepe et al. 2014).

There are several examples in the literature concerning the activity-exoplanet detection interplay. A recent one is connected to the α Cen B system. By performing an initial harmonic-filtering of the activity signals of the star, Dumusque et al. (2012) showed evidence supporting an Earth-mass companion ($M_p = 1.13 \pm 0.09 M_\oplus$) with an orbital period of $P_{\text{orb}} \simeq 3.236$ d. However, this detection was shortly after challenged by Hatzes (2013b) who, applying different filtering methods to the RV data, demonstrated that the observed signal was most likely due to stellar activity alone. A similar situation occurred with the GL 581 system (M3V, $M_* \simeq 0.31 M_\odot$), where the existence of two out of the six exoplanetary companions, reported by Bonfils et al. (2005), Udry et al. (2007), Mayor et al. (2009), and Vogt et al. (2010), have been debated by Hatzes et al. (2013a), (2016), as the result of activity-induced signals in the RV variability.

Likewise, studies have considered the detectability of planets around active cool stars by modelling the stellar activity from starspot and magnetic field maps recovered from Doppler or Zeeman-Doppler imaging (Jeffers et al. 2014a; Donati et al. 2014; Hébrard et al. 2016). Connected to this, Petit et al. (2015) has explored the possibility of using a tomographic approach (based on maximum entropy), to assess the presence of exoplanets around very active stars where the standard RV detection method is not reliable (due to the large distortions of the line profiles). This methodology was successfully applied, yielding the detection of a hot-Jupiter planet ($M_p \simeq 0.77 M_{J_p}$, $a \simeq 0.057$ AU) orbiting around a very young (2 Myr), magnetically-active T Tauri star (V830 Tau, Donati et al. 2015, 2016). This constitutes the youngest exoplanet detected to date, providing strong support to the hot-Jupiter formation channel involving planet-disk interactions (Baruteau et al. 2014).

These examples and many others in the literature clearly show that knowing the characteristics of the stellar magnetic field and activity patterns is crucial for addressing the presence of exoplanets in a given system.

1.1.3 Magnetic fields and stellar winds

As well as driving stellar activity, magnetic fields strongly influence different aspects of the stellar structure and evolution. It is known that they play a major role in the coronal heating processes in the Sun and other late type stars (De Moortel & Browning 2015; Testa et al. 2015), as well as in the generation of persistent stellar winds and astrospheres (Wood 2004). These stellar winds are crucial to understand the evolution of rotation and magnetic activity in cool stars on the early main sequence. G to K type stars tend to rotate rapidly on the Zero Age Main Sequence (ZAMS); braking torques exerted by winds cause them to spin down, losing most of their angular momentum within the first 500 Myr (Barnes & Kim 2010; Amard et al. 2016). Strong winds from the young Sun have been used to explain both the stripping of the Martian atmosphere (Terada et al. 2009; Lammer 2013), and address the “faint young Sun paradox”. This paradox is that terrestrial geological records indicate that water existed in liquid form very early in the history of

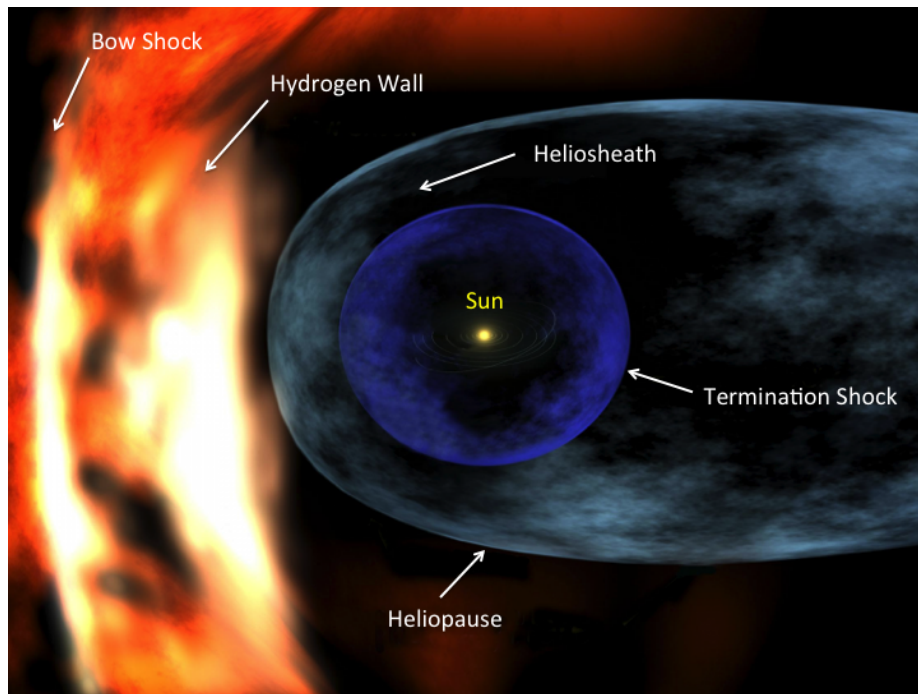


Figure 1.5: Schematic diagram of the heliosphere components. Hot and neutral H builds up, forming a hydrogen wall in the region between the heliopause and the bow shock through charge exchange between stellar wind ions and neutral local interstellar medium particles. For other Sun-like stars this region is detected as extra HI Lyman- α absorption in the UV spectra, allowing a rough mass loss rate estimation. **Adapted from:** [NASA](#).

Earth and Mars, despite the young Sun having only 70% of its current luminosity. [Shaviv \(2003\)](#) suggested that this discrepancy could be explained by a significantly stronger solar wind. Moreover, solar wind sputtering is a leading candidate to explain the loss of Mars' once-thick atmosphere, because Mars is not protected by a strong magnetosphere, unlike Earth ([Lundin et al. 2007](#)). However, recent work presented by [Wood et al. \(2014\)](#) argues that while the young Sun was more magnetically active, it does not necessarily follow that it would have hosted stronger winds (see Fig. 1.6).

This last result comes from the close relation between the winds in Sun-like stars and their surrounding astrospheres. In the case of the Sun, the solar wind creates a comet-like bubble (the heliosphere) that extends far past the orbits of the planets, and interacts with the local interstellar medium (LISM)[†]. The heliosphere is populated by hot hydrogen atoms created through charge exchange between the ionized gas in the solar wind and the cold LISM hydrogen. Hot hydrogen builds up particularly in the region between the termination shock and the heliopause (Fig. 1.5). This is the region which the *Voyager* mission may recently have crossed ([Gurnett et al. 2013](#)), although this is still a matter of

[†]This classical shape of the heliosphere has been recently revisited in various observational and numerical works, pointing towards a far more complex description including magnetized jets ([McComas et al. 2013](#); [Opher et al. 2015](#); [Drake et al. 2015](#)).

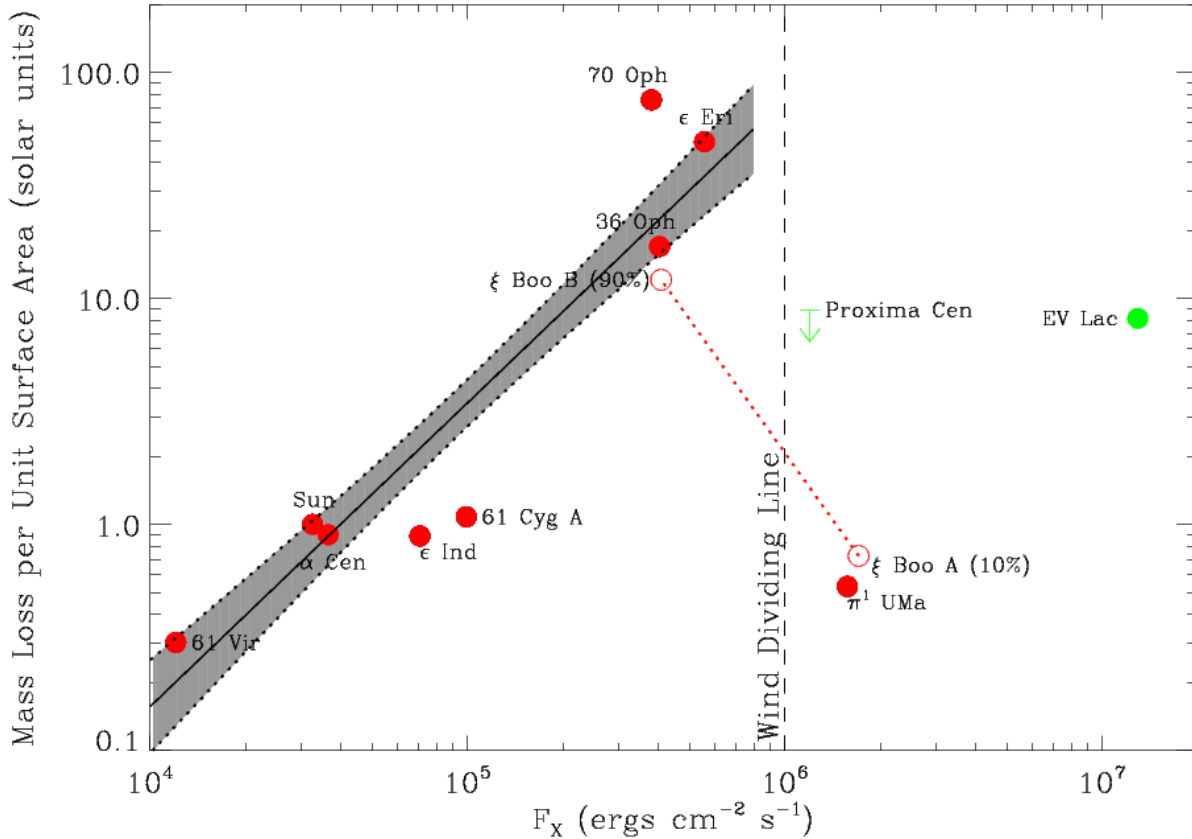


Figure 1.6: Mass loss rates (per unit surface area) vs. X-ray surface flux (F_X) in main sequence cool stars. This figure includes all the available observations to date. The red points correspond to Sun-like stars (spectral types G and K), while the two green points are M-dwarfs (Proxima Cen and EV Lac). In the case of the ξ Boo binary, a differential contribution to the system wind has been assumed, with a 90% fraction associated to ξ Boo B (K4V) and a 10% by ξ Boo A (G8V). The low and moderately active stars seem to follow the power-law relation, $\dot{M}_* \propto F_X^{1.34 \pm 0.18}$. This relation does not hold for the more active stars in the sample (i.e., to the right of the “wind dividing line”). **Taken from:** Wood et al. (2014).

debate (see Fisk & Gloeckler 2014; Gloeckler & Fisk 2015). This hydrogen wall is detected as extra H I Lyman- α absorption in the UV spectra of cool stars. Stronger winds result in a larger astrosphere and increased absorption (Linsky & Wood 2014). By measuring the column densities and velocities of this extra absorption it is possible to derive the only observational estimates available of mass loss rates in cool stars (Fig. 1.5, Wood et al. 2015). It is good to note here that these estimates strongly depend on the assumed characteristics and topology of the LISM (Linsky & Wood 2014), for which there is still no complete agreement in the literature (e.g., Koutroumpa et al. 2009; Gry & Jenkins 2014; Redfield & Linsky 2015).

Figure 1.6 contains the mass loss rate estimates in main sequence cool stars, obtained by Wood et al. (2005a), (2014) from astrospheric detections. These have been plotted as a function of the coronal activity of the star, given by the X-ray surface flux F_X . This plot

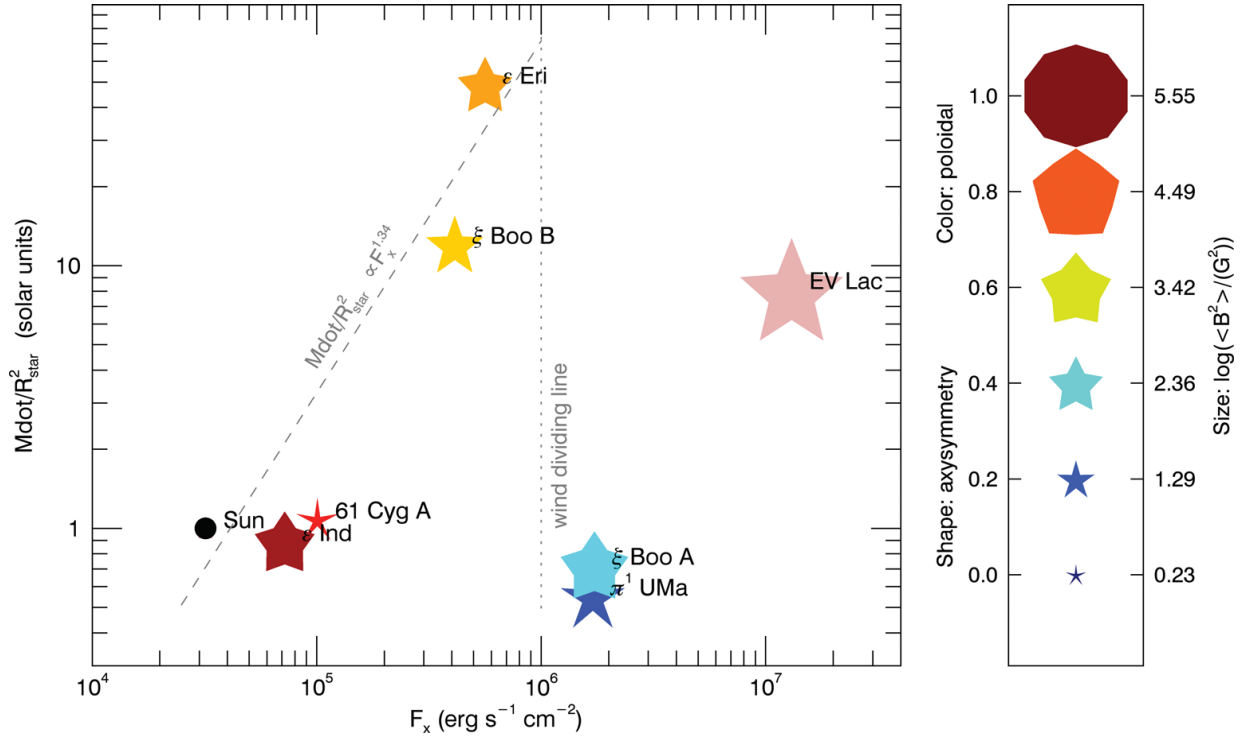


Figure 1.7: Mass loss rates (per unit surface area) vs. X-ray surface flux (see Fig. 1.6), including only the stars with magnetic topologies recovered with ZDI. The large-scale magnetic field properties are presented in a similar manner as in Fig. 1.1. The symbol shapes and colours are indicative of the field axisymmetry and dominant topology (*red*: poloidal | *blue*: toroidal), while the size is proportional to $\log(\langle B^2 \rangle / G^2)$. The $\dot{M}-F_X$ relation and the “wind dividing line” from Fig. 1.6, are shown for reference (segmented and dotted lines, respectively). **Taken from:** Vidotto et al. (2016).

includes all of the available estimates to date. The mass loss rates, \dot{M}_* , are expressed per unit surface area and have been normalised to solar units (where $\dot{M}_\odot \simeq 1.27 \times 10^{12} \text{ g s}^{-1} \simeq 2.0 \times 10^{-14} M_\odot \text{ yr}^{-1}$). In the low to moderate activity regime a stellar wind / corona relation, following the power law $\dot{M}_* \propto F_X^{1.34 \pm 0.18}$, has been proposed. This relation seems to break after the “wind dividing line” (i.e., $F_X > 10^6 \text{ ergs cm}^{-2} \text{ s}^{-1}$), where the most active stars of the sample are located. Given the fact that mass loss and X-ray activity are both magnetically driven phenomena in Sun-like stars, this behaviour should be connected with the underlying magnetic field in the stellar surface. However, recently Vidotto et al. (2016) presented the initial results of various ZDI mapping campaigns of some of the stars included in Fig. 1.6. They did not find strong evidence of an abrupt change in the field topology that could explain the break in the mass loss–activity relation (see Fig. 1.7).

On the theoretical and modelling side, recent studies have provided different frameworks for the stellar wind origin, behaviour, and influence in the angular momentum evolution of late-type stars. Among the 1D and 2D models, a non-comprehensive list includes semi-empirical approaches for thermally-driven winds, within a hydro- (e.g., Johnstone et al. 2015b, 2015a) or magneto-hydrodynamic (MHD) regime (e.g., Matt et al. 2008, 2012;

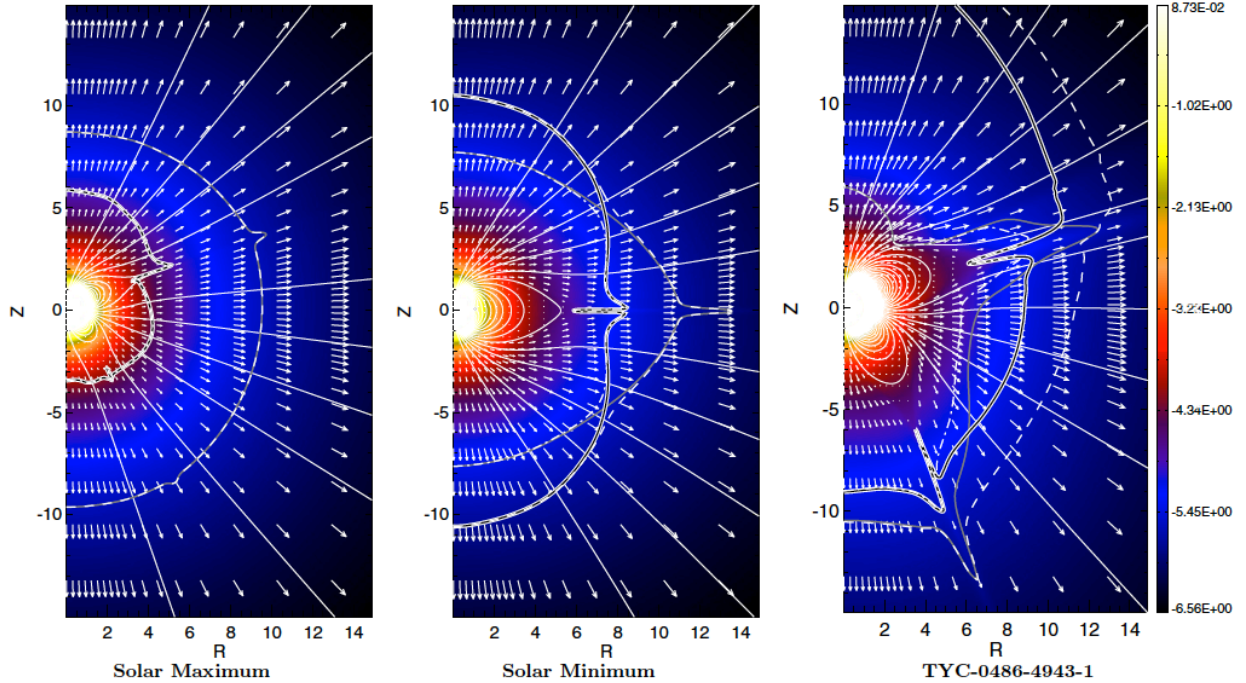


Figure 1.8: 2D MHD simulations of thermally-driven solar/stellar winds using realistic magnetic field topologies. These simulations use as boundary condition a low-order spherical harmonic expansion of the surface magnetic field. For the solar cases (*left*: maximum | *middle*: minimum), data from the Wilcox Solar Observatory is used (DeRosa et al. 2012). The stellar simulation (*right*), considers the ZDI map of the young K-dwarf TYC 0486-4943-1 (Age: 120 Myr, $P_{\text{rot}} \simeq 3.75$ d, $M_* \simeq 0.75 M_{\odot}$; Folsom et al. 2016). The colour scale corresponds the logarithm of the density, and the velocity field is indicated by the white arrows. **Taken from:** Réville et al. (2015a).

Réville et al. 2015a, 2015b), physically-motivated descriptions involving scaling relations for the stellar magnetic fields, rotation periods, convective properties, and X-ray fluxes (e.g., Reiners & Mohanty 2012; Blackman & Owen 2016), and semi-analytic and numerical formulations based on Alfvén wave MHD turbulence (e.g., Cranmer & Saar 2011; Suzuki et al. 2013). While providing reasonable agreement in the rotational evolution of late-type stars at different stages (e.g., Gallet & Bouvier 2013, Matt et al. 2015), such approaches are generic and cannot capture the specifics of the stellar wind of a given system, particularly when considering the complex interplay between the magnetic field topology, coronal structure, and the stellar wind. Furthermore, none of these approaches is able to explain (or model) the observed behaviour of the mass loss rates with coronal activity in cool main sequence stars (Fig. 1.6). In the particular case of planet-hosting stars, these elements are fundamental for a better understanding of the environment around these systems, including the relative influence of the wind and the high-energy emission on the exoplanetary conditions and habitability (Lammer et al. 2003; Lammer 2013; Shaikhislamov et al. 2014; Forget & Leconte 2014; Lammer & Khodachenko 2015). Such detailed descriptions are crucial for the current and future perspectives in the area of exoplanetary characterisation from the ground and space (Pepe et al. 2014; Hatzes 2014).

1.1.4 Magnetised environment in planet-hosting stars: 3D MHD modelling

The stellar magnetic field also dominates the circumstellar environment around late-type stars. This includes transient events, such as flares and coronal mass ejections (Shibata & Magara 2011; Chen 2011), and the development of persistent solar-like winds and astrospheres (see Sect. 1.1.3). These phenomena are known to have a profound impact on the structure of exoplanet atmospheres, a critical factor in the habitability of these systems (Cohen et al. 2011b, 2014; Vidotto et al. 2013). They can erode atmospheres through thermal evaporation or non-thermal processes, such as sputtering and ion pick-up. Significant mass loss has been detected on exoplanets which is driven by the stellar wind (Vidal-Madjar et al. 2003; Linsky et al. 2010; Jensen et al. 2012). Models of this interaction require accurate knowledge of the wind properties (Ekenbäck et al. 2010; Sanz-Forcada et al. 2011) and, therefore, of the host-star surface magnetic field. However, given the observational limitations, robust surface field distributions from ZDI are known for a limited number of late-type planet-hosting stars (e.g., Fares et al. 2013; Fares 2014). Still, this sample is currently growing within the framework of various international projects, such as Magnetic Protostars and Planets (MaPP), the Bcool project, and Star-Planet Interactions (SPI). Dedicated instrumentation, aimed to exploit the exoplanet-magnetism synergies via high-precision and high-resolution spectropolarimetry, will greatly expand this research field in the near future (e.g., SPiRou@CFHT, Neo-Narval@TBL, CRIRES+@VLT, PEPSI@LBT).

Up to now, most ZDI-based studies on the magnetised environment around planet-hosting stars have tended to focus on close-in exoplanetary systems. This has been performed by applying detailed global three-dimensional magnetohydrodynamic (MHD) models that were originally developed for the solar system (BATS-R-US code, Powell et al. 1999). These numerical simulations include all the relevant physics for calculating a stellar corona and wind model, using the ZDI surface magnetic field maps as the driver of a steady-state solution for each system.

Within the 3D MHD regime, two different approaches (concerning the treatment of the coronal structure and the origin of the stellar wind) have been commonly used in the literature. The first one considers an *ad hoc* thermally-driven polytropic stellar wind, i.e., $P \propto \rho^\gamma$, with γ as the polytropic index (e.g., Cohen et al. 2011b; Vidotto et al. 2012, 2015). This means that a hot corona (typically few MK) is imposed as the base condition of the simulation, from which the stellar wind develops as a result of the thermal expansion of the plasma. The second approach, implemented in the Space Weather Modelling Framework (SWMF, Tóth et al. 2005, 2012), considers Alfvén wave turbulence dissipation as a self-consistent driver of the coronal heating and the stellar wind acceleration in the model (Sokolov et al. 2013; van der Holst et al. 2014; Cohen et al. 2014, 2015). This last scheme is based on the strong observational evidence that Alfvén waves that are of sufficient strength to drive the solar wind permeate the solar chromosphere (De Pontieu et al. 2007; McIntosh et al. 2011). The following sections contain a summary of recent works based on these two ZDI-driven modelling schemes.

The magnetic field and wind environment of the τ Boo system

One well studied example, where the first modelling approach has been applied, is the τ Boo system (F7V, $P_{\text{rot}} \simeq 3.1$ d, $M_* \simeq 1.34 M_{\odot}$, [Catala et al. 2007](#); [Takeda et al. 2007](#)). This star is known to host a hot-Jupiter planet ($M_p \sin(i) = 4.13 \pm 0.34 M_{\text{J}}$), located at 0.048 AU in a 3.31 d orbit ([Butler et al. 1997](#); [Brogi et al. 2012](#); [Rodler et al. 2012](#)). The first detection of the magnetic field of τ Boo, and a preliminary phase-limited ZDI map of its large-scale field, was presented by [Catala et al. \(2007\)](#) using spectropolarimetric data from ESPaDOnS@CFHT ([Donati 2003](#)). With the aid of additional ESPaDOnS and NARVAL@TBL ([Aurière 2003](#)) observations, [Donati et al. \(2008c\)](#) confirmed this detection and presented a robust ZDI map of this star. This revealed a relatively complex topology on the surface, reaching up to 10 G in magnitude, and dominated by the radial field with minor contributions from the azimuthal component (Fig. 1.9, *left*).

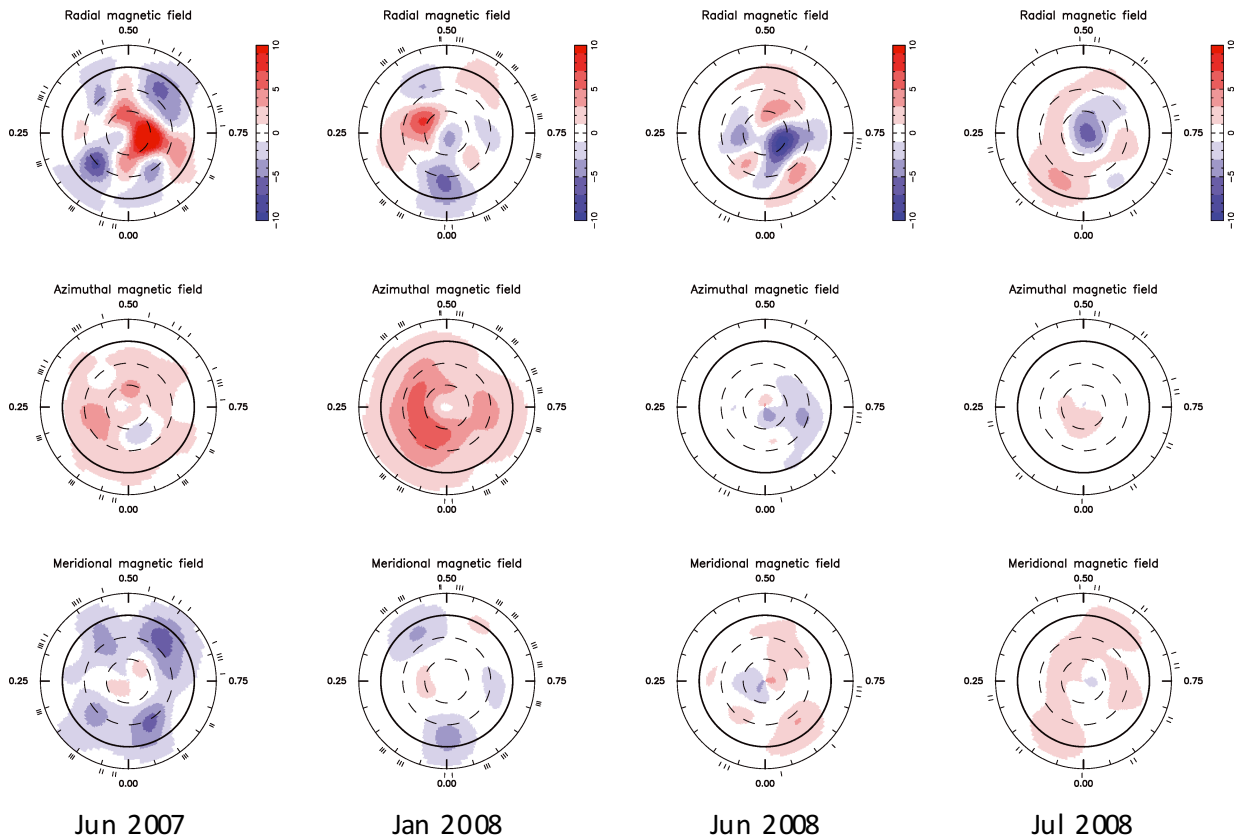


Figure 1.9: Mapped evolution of the large-scale magnetic field topology of τ Boo with ZDI (2007–2008). Each column contains the field reconstructions from independent observing epochs (at the indicated dates). The maps are displayed in a flattened polar projection (similar to Fig. 1.3), with the field decomposed in the radial (*top row*), azimuthal (*middle row*), and meridional (*bottom row*) components. Colours denote the field polarity in each case (positive: *red* | negative: *blue*), and the field strength range is identical in all cases (± 10 G). The ZDI map from the Jun 2007 dataset (*left*) was first published by [Donati et al. \(2008c\)](#). **Adapted from:** [Fares et al. \(2009\)](#).

Donati et al. (2008c) compared this field configuration with the preliminary ZDI map from Catala et al. (2007), and found an overall polarity switch of the large-scale magnetic field on a time-scale of one year. This constituted the first observation of a global polarity change in the magnetic field in a star different from the Sun. This behaviour was shortly after confirmed by Fares et al. (2009), with the detection of a second polarity reversal on roughly the same time-scale (Fig. 1.9, *center-right*), suggesting that this star is undergoing a magnetic cycle similar to the Sun, but on a much shorter time-scale. This motivated a ZDI monitoring campaign (performed by the Bcool collaboration), which observed more magnetic polarity reversals in τ Boo (Fares et al. 2013; Mengel et al. 2016, see Fig. 1.10). An important result from this program was the identification of two possible cycle periods in this star (i.e., 240 d and 720 d, Fares et al. 2013).

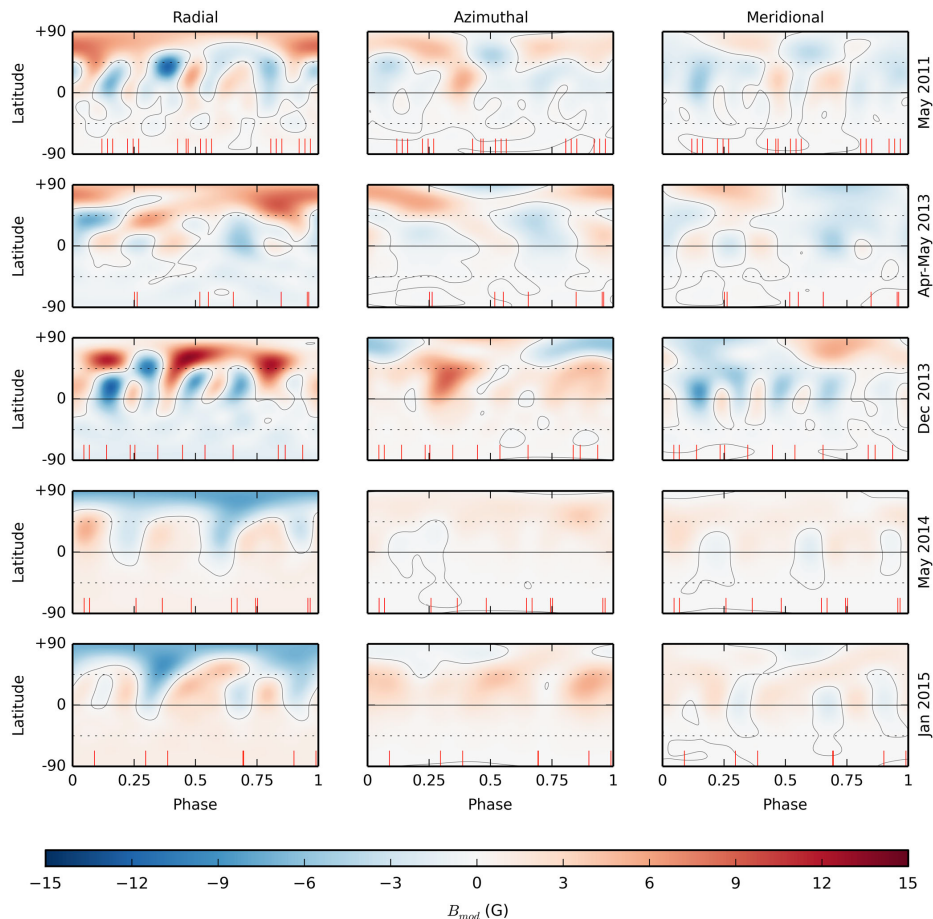


Figure 1.10: Mapped evolution of the large-scale magnetic field topology of τ Boo with ZDI (2011–2015). The maps are displayed in a latitude–phase Mercator projection (similar to Fig. 1.2), with the field decomposed in the radial (*left*), azimuthal (*middle*), and meridional (*right*) components. Each row contains the large-scale field reconstructions from independent observing epochs (at the indicated dates). The field polarity (positive: *red* | negative: *blue*) is reversed between the maps of Dec 2013 and May 2014. The field strength range is identical in all cases (± 15 G). The phase coverage is indicated by the red thick marks in each map. **Taken from:** Mengel et al. (2016).

Using the different radial ZDI large-scale magnetic field maps (from 2006 to 2008, Fig. 1.9), and following the thermally-driven approach discussed in Sect. 1.1.4, Vidotto et al. (2012) performed a series of MHD simulations of the stellar wind of τ Boo (Fig. 1.11). This work was recently expanded by Nicholson et al. (2016), generating models from additional ZDI reconstructions obtained during 2009 to 2015 (see Fig. 1.10, Mengel et al. 2016), and increasing the resolution of the simulation.

Both numerical studies obtained similar results concerning the stellar wind properties in this system; a relatively high mass loss rate ($\dot{M}_* \sim 2.3\text{--}2.7 \times 10^{-12} M_\odot \text{ yr}^{-1} = 115\text{--}135 \dot{M}_\odot$) with a minimal variation ($\sim 3\text{--}4\%$) against global changes in the large-scale field topology (i.e., field strength, polarity reversals, relative complexity). Related to the latter, they also found minor changes in the physical conditions experienced by the exoplanet of this system (e.g., stellar wind density, velocity, temperature).

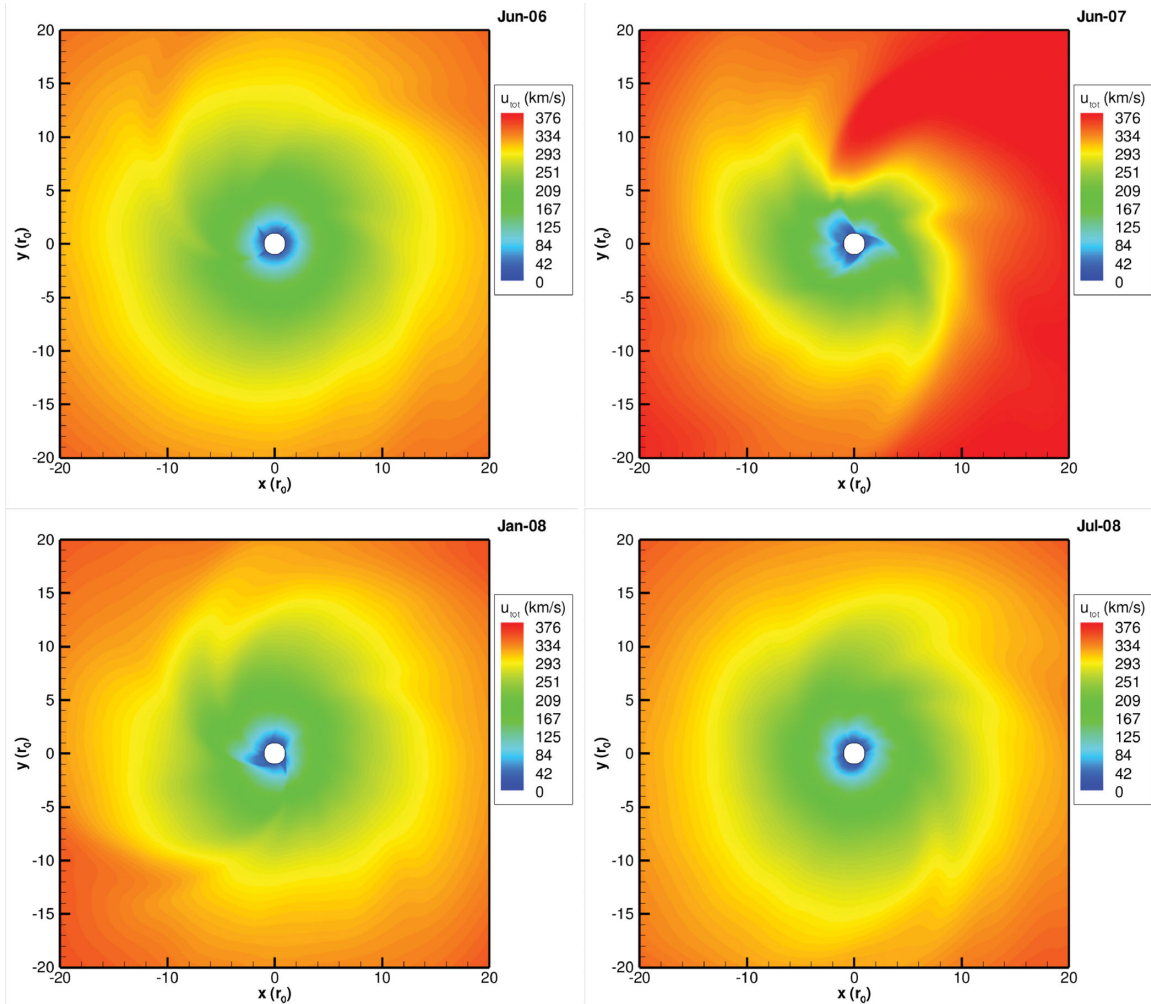


Figure 1.11: 3D MHD simulations of the stellar wind around τ Boo. The dates listed in each panel indicate the corresponding ZDI epoch used as a boundary condition (see Fig. 1.9). The colour scale represents stellar wind velocity (in km s^{-1}) displayed on the equatorial plane. The units of the x - and y - axes are stellar radii (R_*). Taken from: Vidotto et al. (2012).

While there are no observational estimates on the \dot{M}_* value of τ Boo, these values are consistent with other empirical and theoretical predictions for this system (Stevens 2005; Reiners & Christensen 2010; Cranmer & Saar 2011). However, the reasons behind such minimal variation of \dot{M}_* , with respect to large changes in the stellar magnetic field are unclear. Particularly given that in the solar case, the mass loss rate is known to vary by a factor of 2 over the course of the magnetic activity cycle (Cohen 2011).

Finally, by assuming a Jovian magnetosphere around the exoplanet of this system (with planetary dipolar field of 14 G), Vidotto et al. (2012) predicted the expected ranges of exoplanetary radio emission of this system (0.5–1.0 mJy at 34 MHz), and discussed the possibilities for detecting such emission from the ground with current instrumentation. A recent review about this topic can be found in Zarka et al. (2015).

The extreme environment around active M-dwarfs

Recently, Cohen et al. 2014 used the second ZDI-driven modelling scheme (i.e., the SWMF) to investigate the conditions experienced by Earth-like exoplanets around active M-dwarf stars. They considered three different *Kepler* exoplanet candidates, namely KOI[†] 2626.01 (planet A), KOI 1422.02 (planet B), and KOI 854.01 (planet C). These had been previously identified by Dressing & Charbonneau (2013) to be located inside the Habitable Zone (HZ)[‡] of M-dwarf stars (with effective temperatures, T_{eff} , between 3400–3600 K). Planet A has a radius of $R_p \simeq 1.37 R_{\oplus}$ and a mean orbital separation of $a \simeq 0.053$ AU. Planet B is slightly smaller, with $R_p \simeq 0.9 R_{\oplus}$ and $a \simeq 0.058$ AU. Planet C is the largest (and farthest) of the sample, with $R_p \simeq 1.69 R_{\oplus}$ and $a \simeq 0.167$ AU.

Unlike τ Boo (Sect. 1.1.4), there are no ZDI maps available for any of the considered KOI systems. This led Cohen et al. (2014) to follow a more generic approach, by using the ZDI map of a representative M-dwarf star with similar stellar parameters as of the systems of interest. The selected star was EV Lac ($M_* \simeq 0.32 M_{\odot}$, $R_* \simeq 0.3 R_{\odot}$, $P_{\text{rot}} \simeq 4.3$ d), an M3.5V star whose large-scale magnetic field map was previously reconstructed by Morin et al. (2008). This ZDI analysis showed that the large-scale field of this star is dominated by a strong radial component (roughly 1.5–2.0 kG in magnitude), with a relatively simple geometry (i.e., inclined dipole).

Figure 1.12 (left panel) shows the ZDI radial field map of EV Lac, incorporated as the boundary condition of the 3D MHD stellar wind simulation. Following the methodology developed by Tóth et al. (2011), the code uses this boundary condition to generate a potential field extrapolation, which initialises the magnetic field in the simulation domain. As described by Cohen et al. (2014), this model considers the thermodynamic boundary conditions at the base of the chromosphere, not at the corona like in the stellar wind models of τ Boo (Sect. 1.1.4) and other late-type stars (e.g., Vidotto et al. 2013, 2015; do Nascimento et al. 2016). In this case, the coronal heating and stellar wind acceleration

[†]KOI: *Kepler* Object of Interest.

[‡]Defined as the range of distances to the host star at which the planet could sustain liquid water on its surface (Kasting et al. 1993; Kopparapu et al. 2013; Kopparapu et al. 2014).

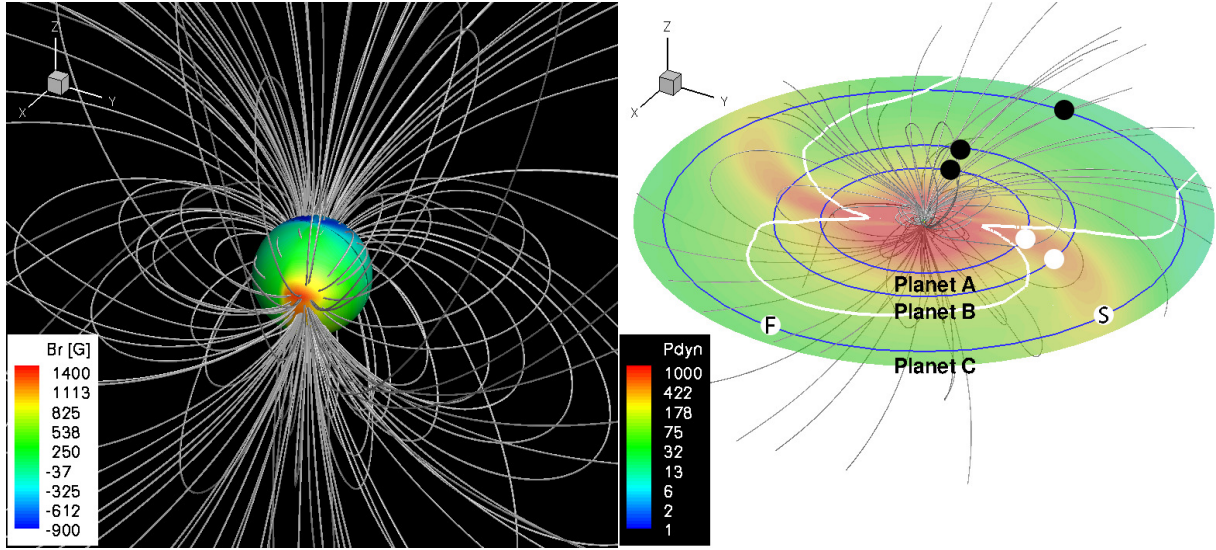


Figure 1.12: ZDI-driven 3D MHD simulation of the stellar wind around EV Lac. *Left:* Boundary condition of the simulation (at $R = 1 R_*$) coloured with the ZDI large-scale radial magnetic field from [Morin et al. \(2008\)](#). *Right:* Distribution on the equatorial plane of the dynamical pressure of the stellar wind, P_{dyn} , in ambient solar wind units. The circular orbits of the three exoplanets are presented. The white line denotes the crossing of the Alfvén surface with the equatorial plane. Coronal field lines are shown in gray in both panels. **Taken from:** [Cohen et al. \(2014\)](#).

are self-consistently calculated, following the Alfvén Wave Solar Model (AWSoM[†], [van der Holst et al. 2014](#)), implemented in the SWMF. The final steady-state stellar wind solution for EV Lac is presented in Fig. 1.12 (*right panel*).

The simulations of [Cohen et al. \(2014\)](#) indicate a total mass loss rate for EV Lac of $\dot{M}_* \sim 3 \times 10^{-14} M_{\odot} \text{ yr}^{-1}$; only 50% larger than the accepted value for the Sun (see Sect. 1.1.3). Taking into account the small surface area of this star ($A_* \simeq 0.123 A_{\odot}$), this value is roughly consistent with the astrospheric estimate from [Wood et al. \(2005a\)](#), via Lyman- α absorption (see Fig. 1.6).

Despite this relatively small mass loss rate, [Cohen et al. \(2014\)](#) predicts an extreme wind environment at the locations of the hypothetical planets around EV Lac and, in general, harsh conditions for planetary systems in the HZ of active M-dwarfs. This is a consequence of two connected fundamental points. The first one is related to the very close-in orbits required to be within the HZ of these systems (e.g., [Selsis et al. 2007](#)). As can be seen from Fig. 1.12 (*left*), the dynamical pressure of the stellar wind, P_{dyn} [‡], is up to three orders of magnitude larger than the ambient solar wind conditions at 1 AU. Variations on the same order are obtained for the magnetic field strength, B , and temperature, T , (associated with the stellar wind) at the different exoplanetary orbits. This would imply favourable

[†]A general description of the model can be found at the Community Coordinated Modeling Center (CCMC) page: <http://ccmc.gsfc.nasa.gov/models/modelinfo.php?model=SWMF/SC/IH>.

[‡]This quantity is defined as $P_{\text{dyn}} = \rho u_{\text{SW}}^2 / 2$, where ρ and u_{SW} are the local plasma density and stellar wind velocity, respectively.

conditions for the stripping of the planetary atmospheres due to the stellar wind (Lammer 2013; Lammer & Khodachenko 2015). Several studies have investigated the importance of magnetospheric shielding for the protection of the planetary atmosphere from stellar wind erosion (e.g., Grießmeier et al. 2004; Khodachenko et al. 2007; Vidotto et al. 2015), and even the possibility of detecting the developed bow-shock structure in near-UV transit light curves of hot-Jupiters (Vidotto et al. 2011; Llama et al. 2011, 2013).

However, by assuming Earth-like magnetospheres around planets A, B, and C (i.e., planetary dipolar field strengths of ~ 0.3 G), Cohen et al. (2014) showed that shielding and bow-shock structures may not be relevant for these particular systems. This brings back the second critical point, which is connected with the relatively enhanced magnetic properties in this type of stars (Sect. 1.1.1, Fig. 1.1). Due to the proximity to the host-star, some of the planetary orbits may cross (or may even be completely contained) within the so called *Alfvén surface* (AS) of the stellar wind (white line in Fig. 1.12, right). This surface is defined as the region where the stellar wind speed equals the local Alfvén speed of the plasma (given by $v_A = B / \sqrt{4\pi\rho}$, Mestel & Spruit 1987; Kawaler 1988; Mestel 1999), or equivalently, when the Alfvénic Mach number $M_A = u_{SW} / v_A = 1$. For reference, an $M_A \geq 8$ is obtained from typical solar wind conditions at Earth, which can be reduced down to 2 (or even below 1) during extreme CME events (Ridley 2007; Kivelson & Ridley 2008). Inside the AS ($M_A < 1$), whose size increases with the stellar magnetic field strength (Cohen & Drake 2014; Garraffo et al. 2015a), all the outflows are still magnetically-bound to the star. In this sub-Alfvénic flow regime, the stellar and planetary magnetic field lines reconnect directly without the development of a bow shock, significantly reducing the planetary atmosphere’s shielding from the stellar wind (Fig. 1.13, Cohen et al. 2014).

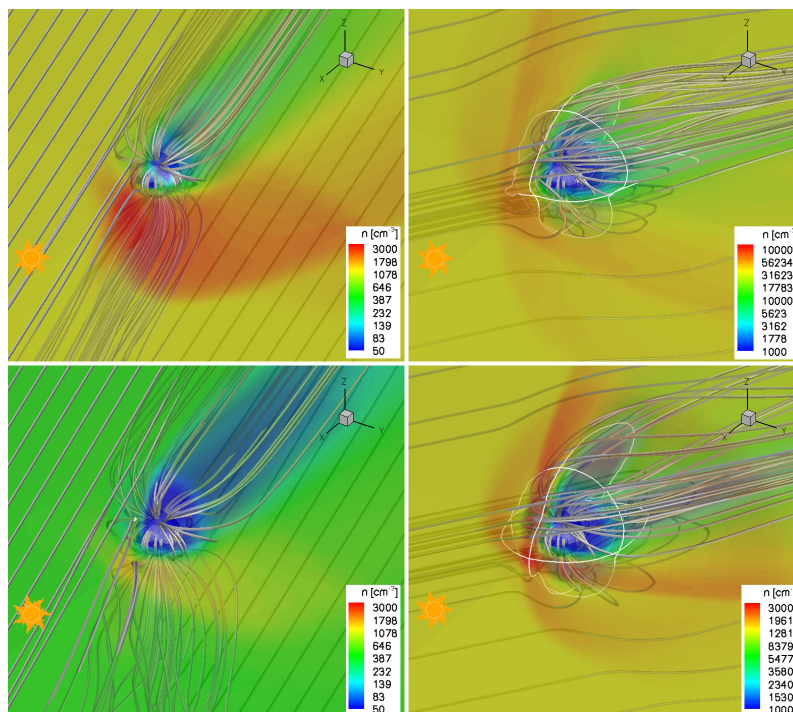


Figure 1.13: Simulated magnetospheric response for planets inside (*left*) and outside (*right*) the Alfvén surface of EV Lac. The *top* and *bottom* panels show the conditions for planets A and B, respectively (see Fig. 1.12). The colour scale represents the distribution of stellar wind particle density, n , expressed in cm^{-3} . Note the different scale between the *left* and *right* panels. Magnetospheric shielding against the stellar wind (indicated by the white line) is only obtained for super-Alfvénic conditions (*right*). Magnetic field lines are shown in gray. **Taken from:** Cohen et al. (2014).

1.2 Open issues

As presented in the last section, the information retrieved with ZDI and the numerical models derived from it have greatly contributed to our understanding of stellar magnetism and the environment of different types of stars. However, there are still open issues connected to these analyses which need to be addressed in order drive future progress in this research field. A summary of some of the most critical points is presented here.

ZDI: Criteria for comparisons

While a large number of papers have shown the robustness and limitations of the ZDI technique (e.g., [Donati & Brown 1997](#); [Hussain et al. 1998, 2000](#); [Piskunov & Kochukhov 2002](#); [Kochukhov & Piskunov 2002](#); [Kochukhov et al. 2012](#); [Rosén & Kochukhov 2012](#)), a standard procedure to determine the quality of the reconstructions is still missing. This significantly complicates the comparison and interpretation of studies which combine ZDI data (either observationally or numerically), given the relatively low control on possible systematics[†] introduced in the analysis.

Applicability of the models

Most of the ZDI-driven studies in the literature have been performed under the assumption that solar models, which describe the corona and wind, can be applied directly to other stars. While this assumption may hold for some systems, the range of applicability of these models has not been yet quantified. This point is extremely important, since all the stars mapped with ZDI are not only much more active than the Sun, but also display very different field topologies (see [Fig. 1.1](#)).

Lack of observational constraints

Connected to the last point, the predictions from the stellar numerical models remain largely untested. This is a direct consequence of extremely limited observational constraints for many systems. While legacy X-ray observations can provide some basic information for the different coronal models, the temporal incoherence of these data with observations from ZDI, makes the discrimination between different models very challenging. The situation is even more critical for the stellar wind models, as there are no observational constraints regarding the stellar wind structure, and mass loss rate estimates of Sun-like stars are only available for 5 single stars and 5 binary systems ([Fig. 1.6](#)).

[†][#SystematicsWillKillU](#)

1.3 About this Thesis

This dissertation has been carried out at the European Southern Observatory (ESO) under the supervision of Dr. Gaitee Hussain, within the programme of the International Max Planck Research School (IMPRS) on Astrophysics.

This work aims at studying the influence due to the multiple aspects of stellar magnetism on the physical conditions around Sun-like stars (G and K type). Special emphasis is given to the particular case of planet-hosts, where these environmental properties will strongly influence the exoplanets of a given system. To achieve this goal, some of the latest observational techniques applied in studies of stellar magnetism, in combination with sophisticated numerical models for space weather modelling in the solar system, are considered. The organisation of this thesis and the associated scientific publications are provided below.

Chapter 2

This chapter contains the spectropolarimetric analysis of the planet-hosting Sun-like star HD 1237, using observations acquired with the High Accuracy Radial velocity Planet Searcher (HARPS), attached at the ESO La Silla 3.6m telescope (ESO programme ID: 089.D-0138, PI: Hussain). This analysis includes the calibration and measurements of the chromospheric activity, refinement of the stellar rotation period, measurements of the average longitudinal magnetic field, and reconstruction of the large-scale field topology using ZDI. For the latter, a criterion for the selection of the optimal level of fit to the spectropolarimetric data is introduced.

Associated refereed publication: [A&A 582, A38 \(2015\)](#)

Activity and magnetic field structure of the Sun-like planet-hosting star HD 1237
Alvarado-Gómez, J. D.; Hussain, G. A. J.; Grunhut, J.; Fares, R.; Donati, J.-F.; Alecian, E.; Kochukhov, O.; Oksala, M.; Morin, J.; Redfield, S.; Cohen, O.; Drake, J. J.; Jardine, M.; Matt, S.; Petit, P.; Walter, F. M.

Specific contribution: *I generated all the plots/figures and carried out the data analysis and the discussion of the results. In particular, I developed the procedure for the optimal level of fit in the ZDI reconstruction. I have written the paper, taking into account the feedback from the co-authors. The HARPSpol data reduction was performed by a collaborator.*

Chapter 3

This chapter presents the analysis of HARPSpol observations of the Sun-like exoplanet-host HD 147513 (ESO programme ID: 089.D-0138, PI: Hussain). The results include: calibrated chromospheric activity measurements, estimates of basic properties of this star

(e.g., rotation period and inclination angle), night-to-night variability of the longitudinal magnetic field and radial velocity, and the ZDI large-scale magnetic field map.

Associated refereed publication: [A&A 585, A77 \(2016\)](#)

A spectropolarimetric study of the planet-hosting G-dwarf, HD 147513

Hussain, G. A. J.; **Alvarado-Gómez, J. D.**; Grunhut, J.; Fares, R.; Donati, J.-F.; Alecian, E.; Kochukhov, O.; Oksala, M.; Morin, J.; Redfield, S.; Cohen, O.; Drake, J. J.; Jardine, M.; Matt, S.; Petit, P.; Walter, F. M.

Specific contribution: *I measured the calibrated chromospheric activity of the star and carried out a preliminary ZDI analysis and interpretation of the data. This initial analysis served as basis for the final published results, which were obtained by a collaborator using an improved reduction pipeline. The paper was written by the first author and is included here for completeness.*

Chapter 4

This chapter contains the first set of ZDI-driven Magneto-Hydrodynamics (MHD) models, describing the simulated coronal structure of the systems studied in the previous chapters. Additional simulations are carried out for the planet-hosting K-dwarf star HD 22049 (ϵ Eridani), which are driven by ZDI maps generated from archival HARPSpol observations. The analysis considers a detailed qualitative and quantitative evaluation procedure, comparing the results of two solar simulations against satellite data. The connection between characteristics surface magnetic field driving the simulations and the obtained coronal structure, is explored in this chapter. This is done by comparing numerical simulations driven by two different implementations of the ZDI technique (ZDI and SH-ZDI). Some of the results include line-of-sight synthetic Extreme Ultra-Violet (EUV) and X-ray emission maps, and simulated emission measure (EM) distributions for each system. The latter are used to calculate synthetic EUV and X-ray luminosities, and compare them with previous observational studies in the literature.

The simulations were carried out in the facilities of the Computational Center for Particle and Astrophysics (C2PAP) at the Leibniz-Rechenzentrum (LRZ), as part of the project entitled “*Modelling the corona, winds and space weather conditions in moderately active Sun-like stars*” (Period 2015–2016, PI: Alvarado-Gómez).

Associated refereed publication: [A&A 588, A28 \(2016\)](#)

Simulating the environment around planet-hosting stars

I. Coronal structure

Alvarado-Gómez, J. D.; Hussain, G. A. J.; Cohen, O.; Drake, J. J.; Garraffo, C.; Grunhut, J.; Gombosi, T. I.

Specific contribution: *I performed all the simulations and carried out the post-processing work, analysis, and discussion of the numerical results. For the simulations of HD 22049,*

I reduced the HARPSpol raw data and generated the ZDI map used to drive the models. The SH-ZDI maps used in the simulations, and the computation of the synthetic EUV and X-ray luminosities, were provided by some of the listed co-authors. The paper was written by me and includes minor text contributions from one collaborator.

Chapter 5

The second set of ZDI-driven MHD models is presented here, which includes the simulated stellar winds and inner astrospheres of the systems of interest. As in the previous chapter, solar simulations are compared with spacecraft data and used to evaluate the reliability of the simulations. A fundamental result of this chapter is the characterisation of the structure of the stellar wind and its physical properties, in connection with the underlying distribution of the surface magnetic field. Moreover, a prediction for the mass loss and angular momentum loss rates of these systems is obtained. These results are compared and discussed in the context of previous observational and numerical works. Additional simulations are carried out for one of the systems (HD 1237), to investigate in more detail the conditions experienced by the exoplanet at various locations of its orbit. This is done by assuming a magnetosphere around the planet, which interacts self-consistently with the incident stellar wind. This analysis reveals a dominant role played by the stellar wind density (over the velocity), in the process of particle injection through the shield provided by the exoplanet magnetosphere. Following previous studies, the amount of magnetospheric radio emission from the planet in this system is refined, and the possibilities of its detection using current and future instrumentation are discussed. Finally, the stellar wind properties at the inner edges of the Habitable Zones (HZ) of these stars are calculated, which can be used in further studies of astrobiology and climate modelling of exoplanetary systems.

The simulations were carried out in the facilities of the Computational Center for Particle and Astrophysics (C2PAP) at the Leibniz-Rechenzentrum (LRZ), as part of the project entitled “*Modelling the corona, winds and space weather conditions in moderately active Sun-like stars*” (Period 2015–2016, PI: Alvarado-Gómez).

Associated refereed publication: [A&A 594, A95 \(2016\)](#)

Simulating the environment around planet-hosting stars

II. Stellar winds and inner astrospheres Alvarado-Gómez, J. D.; Hussain, G. A. J.; Cohen, O.; Drake, J. J.; Garraffo, C.; Grunhut, J.; Gombosi, T. I.

Specific contribution: *I carried out all the numerical simulations and performed the post-processing work, analysis, and discussion of the results. The paper was written by me, following minor style corrections from one collaborator.*

Chapter 2

Activity and magnetic field structure of the Sun-like planet-hosting star HD 1237

Abstract

We analyse the magnetic activity of the planet-hosting Sun-like star HD 1237, using HARPS spectropolarimetric time-series data. We find evidence of rotational modulation of the magnetic longitudinal field measurements that is consistent with our ZDI analysis with a period of 7 days. We investigate the effect of customising the Least-Squares Deconvolution (LSD) mask to the line depths of the observed spectrum, and find that it has a minimal effect on the shape of the extracted Stokes V profile but does result in a small increase in the Signal-to-Noise ratio ($\sim 7\%$). We find that using a Milne-Eddington solution to describe the local line profile provides a better fit to the LSD profiles in this slowly rotating star, which also affects the recovered ZDI field distribution. We also introduce a fit-stopping criterion based on the information content (entropy) of the ZDI map solution set. The recovered magnetic field maps show a strong (+ 90 G) ring-like azimuthal field distribution and a complex radial field dominating at mid latitudes (~ 45 degrees). Similar magnetic field maps are recovered from data acquired five months apart. Future work will investigate how this surface magnetic field distribution affects the coronal magnetic field and extended environment around this planet-hosting star.

2.1 Chapter organization

In this chapter we present the detailed study of the planet-hosting Sun-like star HD 1237, in which we investigate the large-scale magnetic field and chromospheric activity. This is the first step in characterising the impact the stellar magnetic field on the circumstellar environment around this system. In particular, the conditions and possible interactions via the magnetically driven stellar wind, with the Jupiter-size exoplanet that comes as close as 0.25 AU in its orbit (Naef et al. 2001). In section 2.2, we summarise the main properties of the star. Details of the observations and calibration procedures are given in section 2.3.

We present the activity diagnostics and variability in section 2.4. Section 2.5 contains a description of the implemented technique for extracting the magnetic field signatures from the spectropolarimetric data. The required steps for the imaging procedure and the resulting surface field maps are presented in section 2.6. In section 2.7, we discuss our findings in the context of previous and ongoing studies of solar-type stars. Our main conclusions are summarised in section 2.8.

2.2 HD 1237 stellar properties

HD 1237 (GJ 3021) is a bright ($V_{\text{mag}} = 6.58$), Sun-like star (G8V) located about 17.5 pc from the Sun in the southern constellation of Hydrus (Koen et al. 2010). This object is a relatively young (~ 0.88 Gyr), chromospherically active, and confirmed exoplanet host star. Naef et al. (2001) used the enhanced chromospheric activity to explain the large residuals arising from the best Keplerian orbital solution of the planet ($M_p \sin(i) = 3.37 \pm 0.14 M_{\oplus}$, $P_{\text{orb}} = 133.7 \pm 0.2$ d, $e = 0.51 \pm 0.02$, $a = 0.49$ AU).

Table 2.1: HD 1237 basic properties.

Parameter	Value	Reference
S. Type	G8V	Torres et al. (2006)
T_{eff} [K]	5572 ± 40	Ghezzi et al. (2010)
$\log(g)$	4.58 ± 0.2	Ghezzi et al. (2010)
R_* [R_{\odot}]	0.86 ± 0.07	Ghezzi et al. (2010)
M_* [M_{\odot}]	1.0 ± 0.1	Ghezzi et al. (2010)
$v \sin(i)$ [km s^{-1}] [†]	5.3 ± 1.0	This work
v_R [km s^{-1}]	-5.2 ± 0.2	This work
P_{rot} [d]	7.0 ± 0.7	This work
$\log(L_X)$	29.02 ± 0.06	Kashyap et al. (2008)
Age [Gyr] [‡]	~ 0.88	Saffe et al. (2005)

[†]: Other reports include 4.5 km s^{-1} (Schröder et al. 2009), $5.1 \pm 1.2 \text{ km s}^{-1}$ (Torres et al. 2006) and $5.5 \pm 1.0 \text{ km s}^{-1}$ (Naef et al. 2001).

[‡]: Age estimates range from 0.15 to 0.88 Gyr using various methods (see Naef et al. 2001 and Saffe et al. 2005). 0.88 Gyr corresponds to the age determined using isochrones.

Table 2.1 contains the basic stellar properties of HD 1237 taken from Ghezzi et al. (2010), Torres et al. (2006), and Saffe et al. (2005). Rotation period (P_{rot}) estimates are sparse, ranging from ~ 4.0 to 12.6 d, as summarised by Watson et al. (2010). As presented in section 2.6.1, we obtain $P_{\text{rot}} = 7.0 \pm 0.7$ d from our observations (Sect. 2.3). In addition, we estimated the radial velocity, v_R , and the rotational velocity, $v \sin(i)$, using an automatic spectral classification tool (MagIcS, Donati et al. 2012) and the fundamental properties of

the star (Table 2.1). Using several of our observed spectra, we found on average a $v \sin(i)$ of $5.3 \pm 1.0 \text{ km s}^{-1}$ and a v_R of $-5.2 \pm 0.2 \text{ km s}^{-1}$. Literature values for $v \sin(i)$ range between $\sim 4.5 \text{ km s}^{-1}$ and 5.5 km s^{-1} (Naef et al. 2001; Torres et al. 2006; Schröder et al. 2009). However, as indicated by Naef et al. (2001), the $v \sin(i)$ value can be over-estimated for metal-rich stars such as HD 1237. For the subsequent analysis, we adopted a $v \sin(i)$ of 5.3 km s^{-1} , which is consistent, within the errors, with the value reported by Naef et al. (2001) and Torres et al. (2006).

2.3 Observational data

We obtained observations using the polarimetric mode (Piskunov et al. 2011) of the HARPS echelle spectrograph (Mayor et al. 2003) at the ESO 3.6 m telescope at La Silla Observatory. The wavelength coverage of the observations range from 378 nm to 691 nm, with a 8 nm gap starting at 526 nm.

Data were reduced using the REDUCE package (Piskunov & Valenti 2002; Makaganiuk et al. 2011), which was modified for the HARPS instrument configuration. This package produces an optimal extraction of the bias-subtracted spectra after flat-fielding corrections and cosmic ray removal have been carried out. The continuum level is determined by masking out the strongest, broadest features (e.g., the Balmer lines) and then fitting a smooth slowly varying function to the envelope of the entire spectrum. Spectra are obtained with resolutions varying from 95 000 to 113 000, depending on the wavelength, with a median value of 106 000. Uncertainties are derived for each pixel assuming photon statistics. The star was observed at two epochs separated by 5 months (July and December) in 2012. A summary of the observations is presented in Table 2.2.

The exposure times listed correspond to one circularly polarised spectrum (Stokes V), which results from combining four individual sub-exposures using the ratio method. As explained in Donati et al. (1997), the polarisation signal is obtained by dividing spectra with perpendicular (orthogonal) polarisation states (for HARPSpol and Stokes V: 45° , 135° , 225° , and 315° , using the quarter waveplate). Additionally, a null-polarisation spectrum is constructed to check for possible spurious polarisation contributions in the observations. More details can be found in Bagnulo et al. (2009). Owing to bad weather conditions, two consecutive Stokes V spectra were added together for the night of 2012 July 23.

2.4 Magnetic activity and variability

To characterise the chromospheric activity level of the star during the observed epochs, we used the Ca II H (396.8492 nm) & K (393.3682 nm) lines and the classic Mount Wilson S-index, S_{MW} , defined as

$$S_{\text{MW}} = \frac{H + K}{R + V}. \quad (2.1)$$

Table 2.2: Journal of HARPSpol observations of HD 1237.

Date (2012)	HJD (2 400 000+)	UT (HH : MM : SS)	t_{exp} [s]	Stokes I Peak S/N	Phase (Φ)
<i>First epoch</i>					
Jul 15	56 123.359	08 : 04 : 36	3600.0	955	0.000
Jul 16	56 124.442	10 : 03 : 43	3600.0	1214	0.155
Jul 17	56 125.399	09 : 01 : 10	3600.0	841	0.291
Jul 18	56 126.361	08 : 06 : 35	3600.0	877	0.429
Jul 19	56 127.440	10 : 01 : 33	3600.0	753	0.583
Jul 20	56 128.356	08 : 00 : 16	3600.0	1098	0.714
Jul 21	56 129.374	08 : 25 : 27	3600.0	911	0.859
Jul 22	56 130.438	09 : 47 : 58	4800.0	1092	1.011
Jul 23 [†]	56131.397	08 : 32 : 33	6680.0	660	1.148
Jul 31	56 139.314	06 : 49 : 52	4800.0	926	2.280
Aug 02	56 141.303	06 : 32 : 21	5000.0	1040	2.564
<i>Second epoch [20.29+ rotation cycles since Jul 15 2012]</i>					
Dec 04	56 265.045	00 : 35 : 27	2800.0	1205	0.000
Dec 05	56 266.045	00 : 35 : 21	2800.0	964	0.142
Dec 06	56 267.044	00 : 34 : 40	2800.0	1018	0.285
Dec 07	56 268.044	00 : 33 : 59	2800.0	722	0.428

The columns contain the date, the corresponding Heliocentric Julian Date (HJD), the start time of the observations in UT, the exposure times, and the Stokes I peak signal-to-noise ratio (S/N). The rotational phase (Φ) listed in the last column is calculated using the rotation period derived in this work ($P_{\text{rot}} = 7.0$ d).

[†]: The listed values correspond to two spectropolarimetric exposures merged in a single observation due to bad weather conditions.

Here, H and K represent the fluxes measured in each of the Calcium line cores using 0.105 nm wide spectral windows, and R and V are the fluxes measured in the continuum over 2 nm windows centred at 390.1 nm and 400.1 nm, respectively, on both sides of the Ca II region.

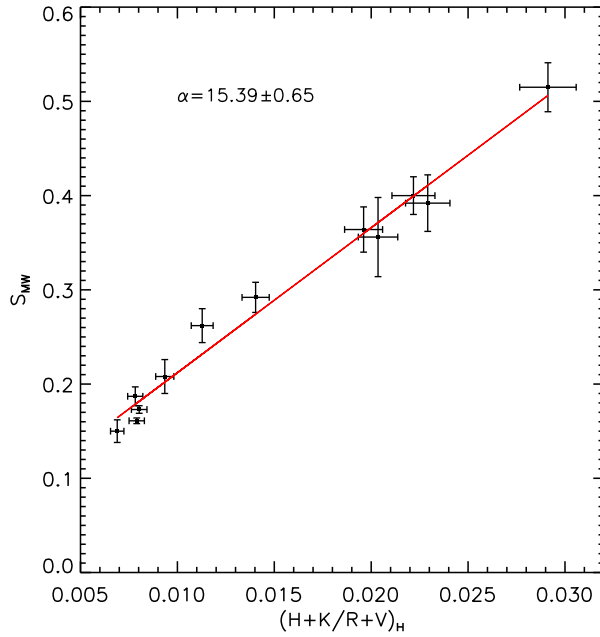
2.4.1 Index calibration

To compare the activity level of HD 1237 with other stars, we need to convert the measured HARPS S-index, S_{H} , to the Mount Wilson scale. For this, we require a calibration factor, α , which is an instrument-dependent quantity that linearly relates the values for the classic S_{MW} and the HARPS fluxes H , K , R , V :

$$S_{\text{MW}} = \alpha \underbrace{\left(\frac{H+K}{R+V} \right)}_{S_{\text{H}}}. \quad (2.2)$$

We estimated α by including a set of stars with previous measurements of chromospheric activity via S_{MW} (Santos et al. 2000) and within the HARPS observations database. The spectral type of the reference stars and their reported S_{MW} values are listed in Table 2.3. The linear relation between S_{MW} and the HARPS fluxes is plotted in Figure 2.1. The derived calibration factor, within the $1\text{-}\sigma$ uncertainty, is

$$\alpha = 15.39 \pm 0.65. \quad (2.3)$$



Name	S. type	S_{MW}	σ_{MW}
HD 1835	G3V	0.364	0.024
HD 10700	G8.5V	0.173	0.004
HD 22049	K2Vk	0.515	0.026
HD 23249	K1III-IV	0.150	0.012
HD 26965	G9III-IV	0.208	0.018
HD 30495	G1.5V	0.292	0.016
HD 61421	F5IV-V	0.187	0.010
HD 76151	G3V	0.262	0.018
HD 115617	G7V	0.161	0.003
HD 149661	K2V	0.356	0.042
HD 152391	G8.5Vk	0.392	0.030
HD 155885	K1V	0.400	0.020

Figure 2.1: Linear fit between Santos et al. (2000) S_{MW} values and the HARPS fluxes $\left(\frac{H+K}{R+V} \right)_H$. A 5% error is estimated in our HARPS flux measurements.

Table 2.3: Stars included in the α calibration.

All spectra were co-aligned using a high-S/N HARPS solar spectrum as reference. We estimate a 5% typical error size in our HARPS flux measurements based on the possible differences in the continuum normalisation, which was performed in the same way for all the stars in the calibration. Therefore, the errors in S_{H} are dominated by the conversion procedure. Using this calibration factor, we proceed with the estimation of the activity index S_{H} , with the corresponding indicators R_{HK} (Middelkoop 1982) and R'_{HK} (Noyes et al. 1984), which account for colour and photospheric correction, respectively.

2.4.2 Activity indicators

Figure 2.2 shows the cores of the Ca II H and K lines in the HARPS normalised spectra of HD 1237 for different observations, which are compared with the mean profile (*red*) derived from the entire data set. For the averaging procedure we take the slight differences in the wavelength range into account from each observation by an interpolation procedure to match the largest wavelength data points in the observed spectra. A high-S/N HARPS solar spectrum[†] is shown as reference.

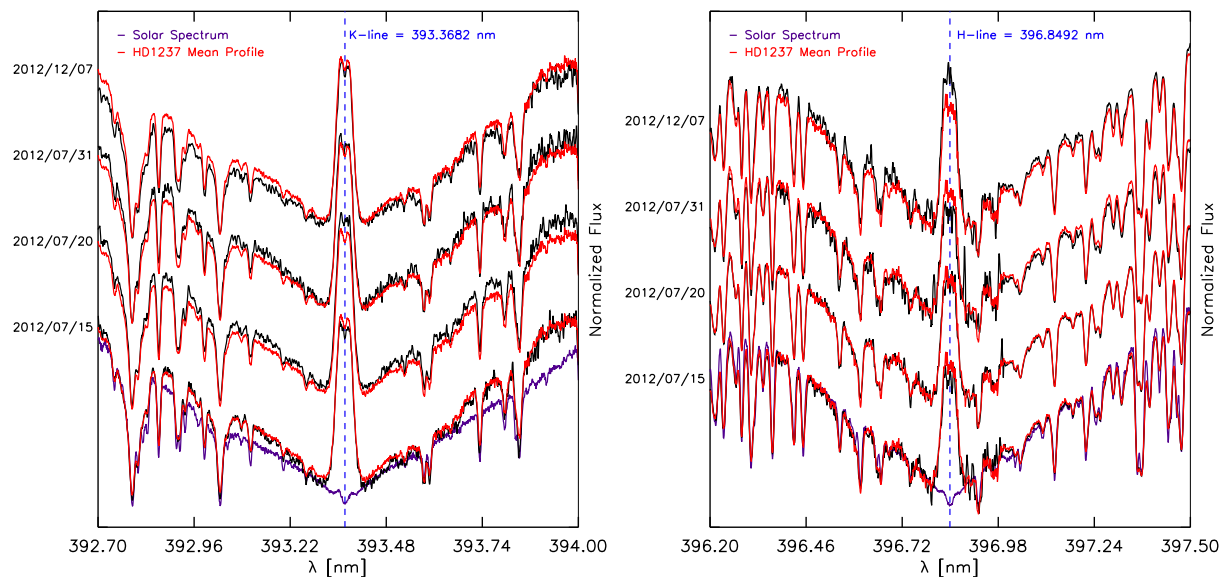


Figure 2.2: Core regions of the Ca II K (*left*) and H (*right*) lines of HD 1237. Four spectra from our sample are plotted with the corresponding dates on the left *y*-axis and vertically shifted (0.25 units) for visualisation purposes. The *black* spectrum at the top was taken at a much later epoch (2012 Dec. 07). The *red* line shows the mean profile for the entire dataset, while the *purple* line is a HARPS solar spectrum used as reference.

The upper plot shows one observation at a later epoch (2012 Dec. 7), where it is possible to observe a variation in the line profile. This is interpreted as a slight change in the chromospheric and photospheric activity of the star in comparison with the mean behaviour of the red line (which is dominated by profiles from the first epoch), especially in the H line (Fig. 2.2, *right panel*). The K-line region of the spectrum contained more noise. No change in the activity level of the star is visible in this particular line.

Figure 2.3 shows the measured HARPS fluxes, $(H + K)/(R + V)$, for each observation starting from 2012 Jul 15 (HJD = 2456 123.5). The *x*-axis units correspond to days after this initial date. The activity of the star showed a marginal variation, in a similar way as in the first epoch. This may be due to the rotation of active regions over the stellar surface.

[†]S/N: 347 @550 nm, Date: 2007 Apr. 12 – Low activity period.

The similarities between the activity levels between both epochs could be an indication of a stable large-scale magnetic field configuration.

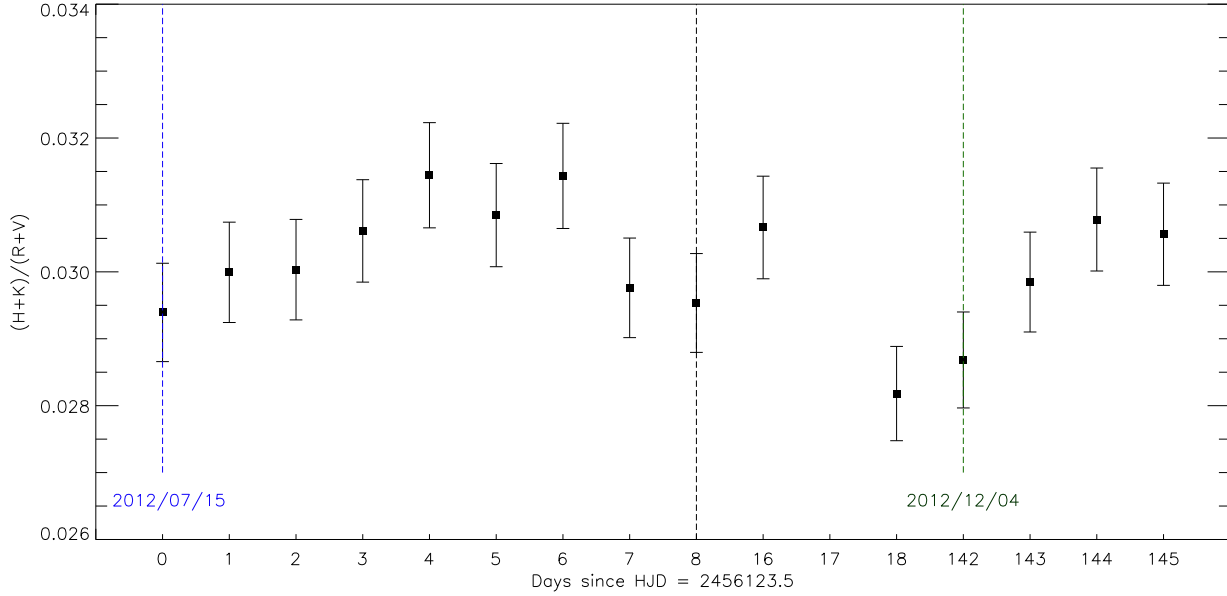


Figure 2.3: HARPS fluxes $(H+K)/(R+V)$ for the available observations of HD 1237. The *blue* and *green* vertical lines denote the beginning of each observed epoch. The x-axis contains the number of days since the Heliocentric Julian Date (HJD = 2 456 123.5) of the first observation (2012 Jul 15). The last two data points of the first epoch are unevenly distributed (after the vertical *black* line).

The chromospheric activity level of the star can be quantified by using Eq. (2.2) and the derived value for α in Eq. (2.3). We estimate an average value of $S_H \simeq 0.46 \pm 0.02$ for the available observations of HD 1237. Similar activity levels have been reported for the Sun-like star ξ boo A ($T_{\text{eff}} = 5600$ K, $P_{\text{rot}} = 6.4$ d, Age: ~ 0.2 Gyr, Mamajek & Hillenbrand 2008; Morgenthaler et al. 2012). As a reference value, the Solar S-index is $S_{\odot} \simeq 0.1783$ with a variation of ~ 0.02 from solar maximum to minimum (Lockwood et al. 2007).

Using the mean derived values of the S-index, we can now apply a transformation to obtain the parameter R_{HK} , which takes the colour of the star in the activity estimation into account (Middelkoop 1982), Here R_{HK} is defined as

$$R_{\text{HK}} = (C_{\text{CF}})(S_H)(1.34 \times 10^{-4}), \quad (2.4)$$

where C_{CF} is a colour-dependent function. For main sequence stars with $0.3 \leq (B - V) \leq 1.6$, C_{CF} is given by

$$\log(C_{\text{CF}}) = 0.25(B - V)^3 - 1.33(B - V)^2 + 0.43(B - V) + 0.24. \quad (2.5)$$

Noyes et al. (1984) derived an expression in order to include photospheric corrections to the Ca II core fluxes, R'_{HK} , which is written as

$$R'_{\text{HK}} = R_{\text{HK}} - R_{\text{phot}} , \quad (2.6)$$

with R_{phot} expressed also as a function of $(B - V)$:

$$\log(R_{\text{phot}}) = -4.898 + 1.918(B - V)^2 - 2.893(B - V)^3 , \quad (2.7)$$

and valid in the range of $0.44 < (B - V) \lesssim 1.0$. Table 2.4 summarises the activity indicators for the available observations of HD 1237. The errors quoted are the mean measurement errors for these quantities. The B and V magnitudes were taken from the Hipparcos catalogue ($B_{\text{mag}} = 7.335$, $V_{\text{mag}} = 6.578$, Koen et al. 2010). High activity levels are related to magnetic fields on the stellar surface. These magnetic signatures are encoded in the polarised spectra of the star and is discussed in the next section.

Table 2.4: Average activity indicators for HD 1237.

$\langle S_{\text{H}} \rangle$	$\log(R_{\text{HK}})$	$\log(R'_{\text{HK}})$
0.462 ± 0.019	-4.29 ± 0.04	-4.38 ± 0.05

2.5 Magnetic field signatures

The signal-to-noise ratio (S/N) in the observations is not high enough to detect magnetically induced spectropolarimetric signatures in single lines. However, by applying a multi-line technique, e.g., least squares deconvolution (LSD, Donati et al. 1997), it is possible to increase the S/N by a factor of ~ 50 – 100 , adding-up the signal from thousands of spectral lines over the entire spectral range (for HARPS: 378–691 nm), enhancing our sensitivity to magnetic signatures in the observations. A recent review of the LSD technique can be found in Kochukhov et al. (2010). This procedure requires a photospheric model (line list) matching the spectral type of our target star. This is done using an atomic line list database[†] (Kupka et al. 2000) and the stellar fundamental properties listed in Table 2.1. We assumed a micro-turbulence parameter of 1.3 km s^{-1} (Ghezzi et al. 2010) and solar abundance for the photospheric line list that included $\sim 15\,000$ lines within the HARPS spectral range.

From this initial photospheric line list, we generated two different masks used with the LSD calculation. In the first mask the strong lines (and lines blended with these lines) that form in the chromosphere or that break the basic assumptions of LSD (e.g., Ca II H & K, H α) are removed (cleaned mask). This reduced the number of lines included to $\sim 11\,000$. After the mask cleaning, a numerical routine based on the Levenberg-Marquardt, non-linear least-squares algorithm from the MPFIT library (Moré 1978; Markwardt 2009) is applied to fit the line mask to the observed Stokes I spectrum after adjusting the individual depths of the spectral lines (cleaned-tweaked mask). This is performed through the entire HARPS

[†]<http://vald.astro.uu.se/> – Vienna Atomic Line Database (VALD3)

wavelength coverage. This step is more commonly carried out when applying LSD to hot (OB-type) stars that have fewer lines (e.g., [Neiner et al. 2012](#)). Finally, LSD was applied to the spectropolarimetric data using the final masks, generating in this way a single, averaged line profile per observation (LSD Stokes I, V, and diagnostic N profiles). A velocity step $\Delta v = 1.4 \text{ km s}^{-1}$ was used to construct the LSD profiles. This velocity spacing considers two pixels per spectral element of the instrument (in the case of HARPSpol, $R = 2.5 \text{ km s}^{-1}$ and 3.4 px per resolution element).

As can be seen from Fig. 2.4, both procedures lead us to consistent results in the obtained LSD signatures of the star. While no clear change is observed in the null polarisation check, subtle qualitative differences appear in both Stokes profiles, in the sense that the cleaned-tweaked mask seems to get a broader unpolarised profile with a slightly weaker signature in the circular polarised profile, in comparison with the clean line mask. These minimal shape differences in the LSD line profiles can have a much greater effect in hot stars where fewer lines are generally available. On the other hand, the resulting S/N of the LSD profiles for each individual observation was systematically higher using the cleaned-tweaked mask than in the cleaned case, despite the same number of spectral lines in their masks (11 048). On average, a $\sim 7\%$ increase was obtained in the S/N of the LSD profiles with the cleaned-tweaked mask.

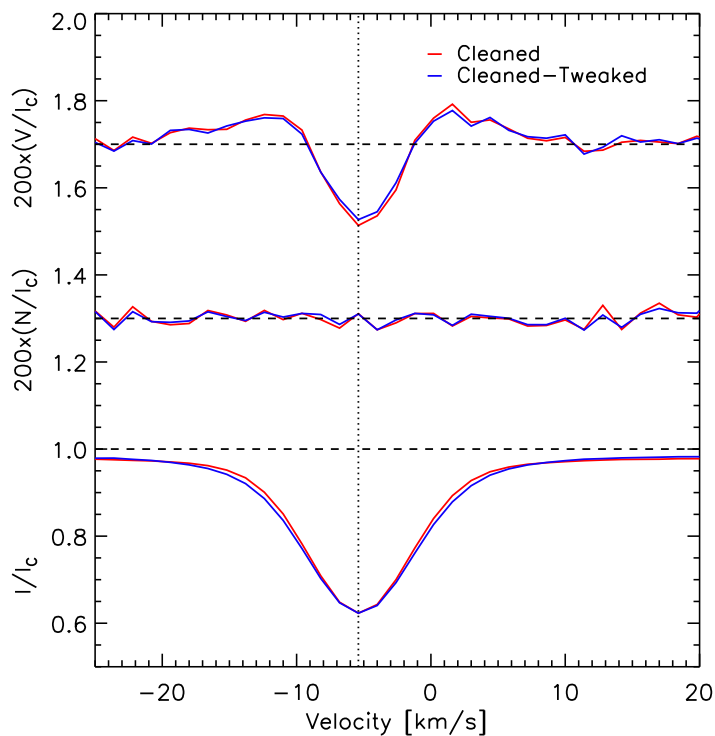


Figure 2.4: Derived LSD Profiles of HD 1237 from the observation on 2012 Jul 19. Stokes I (*bottom*), Stokes V (*top*), and the null (N) polarisation check (*middle*) are shown. The profiles obtained with a cleaned (*red*) and a cleaned-tweaked (*blue*) line masks are plotted for comparison.

2.5.1 Longitudinal magnetic field

Using the derived Stokes I and V LSD profiles, it is possible to obtain information about the surface averaged longitudinal magnetic field (B_ℓ). Following Donati & Landstreet (2009), an estimate of B_ℓ (in G) is given by

$$B_\ell = -714 \frac{\int vV(v)dv}{\lambda \bar{g} \int [1 - I(v)] dv} , \quad (2.8)$$

where the radial velocity shift v (in km s^{-1}) is measured with respect to the average line derived from LSD with central wavelength λ (in μm) and mean Landé factor \bar{g} . As this measurement is an integrated quantity over the visible surface, it cannot provide complete information for stars that host complex large-scale magnetic fields. From multiple measurements of B_ℓ taken over a stellar rotation period, it is possible to gain a first insight into inhomogeneities of the disk-integrated magnetic field. It is thus also possible to estimate the stellar rotation period, using the modulation in a time series of B_ℓ measurements, provided that they span more than one rotation period.

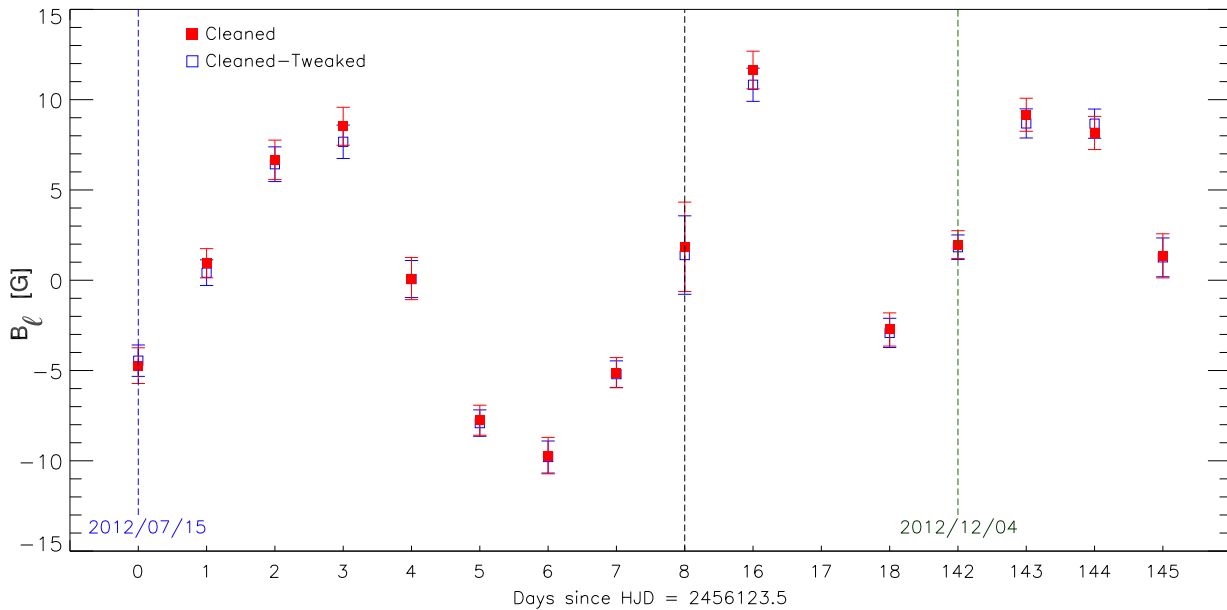


Figure 2.5: Calculated B_ℓ for the available observations of HD 1237. The *blue* and *green* vertical lines denote the beginning of each observed epoch. The x-axis contains the number of days since the Heliocentric Julian Date (HJD = 2456123.5) of the first observation (2012 Jul 15). The last two data points of the first epoch are unevenly distributed (after the *black* line). Colours indicate the line mask used for the LSD procedure.

Figure 2.5 shows the measurements of B_ℓ for the available observations of HD 1237. The integration was centred on the radial velocity of the star (-5.2 km s^{-1}) and covered the entire Stokes V signature ($\pm 12.5 \text{ km s}^{-1}$). The uncertainties were computed from standard error propagation from the spectra. The colours denote the line mask used in the LSD

procedure, showing that the slight differences in each of the measurements are consistent within the errors. This implies that either set of LSD profiles can be used to obtain robust longitudinal magnetic field measurements. As the two sets of profiles are so similar, there is only a difference in S/N without any noticeable impact on the maps structure.

Reflecting the additive nature of the chromospheric emission, B_ℓ shows a clearer rotational variation in comparison with S_H (Fig. 2.3), in contrast to the mixed polarity effects of the magnetic field. The behaviour of the longitudinal field is consistent throughout the observed epochs with an varying amplitude of roughly ~ 10 G. This value is somewhat higher than the solar value ($B_\ell < 4$ G, Daou et al. 2006; Kotov et al. 1998) and than the average value from snapshot observations of other Sun-like stars of the same and different spectral types (3.3, 3.2, and 5.7 G for F, G and K-dwarfs respectively, Marsden et al. 2014). However, caution is advised in these averaged comparisons, given the rotational variability of B_ℓ and the nature of a snapshot survey. Similar variations have been observed in the long-term monitoring of the active Sun-like star ξ Boo A (Morgenthaler et al. 2012).

2.6 Surface magnetic field mapping

2.6.1 Optimal line profile and stellar parameters

We reconstruct surface magnetic field maps by applying the tomographic inversion technique of Zeeman Doppler imaging (ZDI, Vogt et al. 1987; Semel 1989). As described by Hussain et al. (2000), ZDI has been used to recover magnetic field maps on the surfaces of stars ranging from T Tauri stars to binary systems (e.g., Barnes et al. 2004; Dunstone et al. 2008). The code recovers the magnetic flux distribution across the stellar disk, modulated by the stellar rotation, by using time series of photospheric absorption line profiles (LSD Stokes I) and circularly polarised profiles (LSD Stokes V).

To recover reliable magnetic field maps, it is necessary to properly model the LSD Stokes I and V profiles and their temporal variation. To do this, good constraints should be obtained on the local line profile description and the stellar parameters. Two different synthetic line shapes were tested: a Gaussian profile, which is commonly used in magnetic field studies in Sun-like stars (e.g., Boro Saikia et al. 2015), and a Milne–Eddington profile, fitted to a solar LSD profile derived from a high-S/N HARPS spectrum. This last approach was previously considered in ZDI of accreting T Tauri stars (Donati et al. 2008a) and M dwarfs (Morin et al. 2008). For both cases, we assumed a linear dependence of the continuum limb darkening with the cosine of the limb angle (slope $u \simeq 0.65$, Sing 2010).

In addition, we estimated the rotational period P_{rot} , and tried to retrieve the differential rotation profile (e.g., $\Omega(l) = \Omega_{\text{eq}} - d\Omega \sin^2(l)$, with l as the latitude angle on the surface, see Petit et al. 2002) and inclination angle i of the star. This is done by generating a grid of ZDI models that covers a range of values for the involved quantities and minimising the reduced χ^2 from synthetic line profile fitting (see Collier Cameron 1995; Hussain et al. 2009). Figure 2.6 (left) shows the results of the minimisation analysis over P_{rot} . As mentioned in Sect. 2.2, the rotation period of HD 1237 is not well known. Our analysis

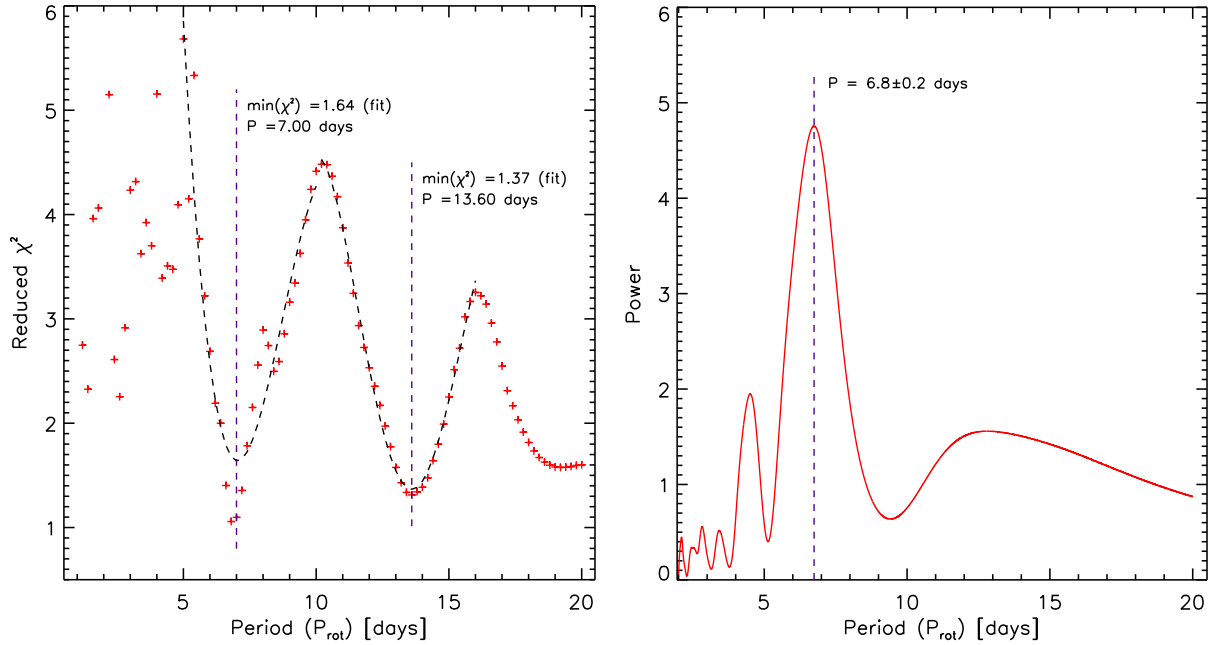


Figure 2.6: *Left:* Minimisation results for HD 1237 showing the reduced χ^2 as a function of P_{rot} . The *black* segmented lines corresponds to a fourth-order polynomial fit. *Right:* Power spectrum obtained from the Lomb-Scargle periodogram analysis on the temporal variation of B_ℓ (Fig. 2.5).

shows the harmonic behaviour of this parameter with a fundamental value of ~ 7.0 d. We estimate a 10% error for this period determination, given the width of the minima in the *left panel* of Fig. 2.5. This estimate is consistent with the high activity level measured in this star (Sect. 2.4). For completeness, we performed a Lomb-Scargle periodogram, using the first epoch dataset, on the temporal variations of B_ℓ (Fig. 2.5). Figure 2.6 (*right*) shows the obtained power spectrum, having a best-fit period of $P_{\text{rot}} = 6.8 \pm 0.2$ d with an associated P-value statistic of 5.18×10^{-5} (Zechmeister & Kürster 2009).

No good constraints were obtained by χ^2 minimisations for the differential rotation parameters and the inclination angle of the star. Therefore, no differential rotation profile was included in the mapping procedure. For the inclination angle, we considered the expected value from rigid body rotation, i.e., $\sin(i) = P_{\text{rot}} \cdot v \sin(i) / (2\pi R_*)$. Given the uncertainties of the involved quantities (see Table 2.1), the inclination angle should lie somewhere between 40 – 60° . We performed reconstructions for 40 , 50 , and 60° and find no substantial differences between these magnetic field reconstructions. We present here the maps obtained assuming a 50° inclination angle.

Finally, we compared the optimum stellar and line parameters associated with the LSD profiles produced using both masks (cleaned mask and clean-tweaked mask). No significant difference is found in the optimal parameters. In the subsequent analysis, therefore, we only consider the LSD profiles produced using the cleaned-tweaked mask.

2.6.2 Optimal fit quality: Entropy content in ZDI maps

The last of part of the analysis corresponds to the selection of the optimal fit quality (reduced χ^2), of the model with respect to the observations. In principle, the recovered field distribution and associated profiles should try to achieve the lowest possible value of χ^2 . Still, given the limitations of the observations and the ZDI technique (S/N, spatial resolution, phase-coverage, etc.), the goodness-of-fit level has to be determined carefully to avoid the appearance of numerical artefacts in the final maps. This is particularly important in the case of resolution-limited maps (i.e., slowly rotating stars). However, there are only a few published procedures for establishing a robust stopping criterion, i.e., the point at which noise starts to affect the reconstructed image.

Motivated by this, we propose a systematic method for estimating the optimal fit quality for a given set of ZDI magnetic field maps, using HD 1237 as a *test-case*. It is important to note here that since this procedure is defined *a posteriori* over the resulting maps themselves (2D images), it does not modify the regularisation functions imposed to ZDI. In this sense, its application to other stellar systems should be straightforward.

We begin with the definition of the entropy S , as an estimate of the information content in an image. A similar implementation of entropy is commonly used as a regularisation function in ZDI (see Piskunov & Kochukhov 2002). Following Sonka et al. 2007, let $P(k)$ be the probability that the difference between two adjacent pixels is equal to k . The image entropy can be estimated as

$$S = - \sum_k P_k \log_2(P_k), \quad (2.9)$$

where \log_2 is the base 2 logarithm. This implies that a larger or smaller amount of entropy in the image will depend on the contrast between adjacent pixels. An image that is perfectly constant will have an entropy of zero. For the methodology described below, we are not interested in the absolute values of the entropy, but rather its overall behaviour as a function of the reduced χ^2 .

For a given converged ZDI solution (i.e., a particular value of reduced χ^2), we can calculate the total entropy content (S_T) by applying the definition given by equation (2.9) to each one of the recovered maps:

$$S_T = S_R + S_M + S_A, \quad (2.10)$$

where S_R , S_M , and S_A represent the entropy contained in the radial, meridional, and azimuthal field components maps, respectively. Figure 2.7 shows in *red* the behaviour of S_T as a function of the reduced χ^2 for the ZDI solution set of HD 1237.

As expected, by decreasing the reduced χ^2 , the information content in the resulting ZDI solution increases (field strength and structure). The overall behaviour of the total entropy content and information growth is consistent for both cases. In the case of the Gaussian profile (Fig. 2.7, *left panel*), the entropy growth remains fairly constant (close

to zero) for high reduced χ^2 values, reaching a maximum[†] around $\chi^2 \simeq 1.2$. However, by that point the concavity of the curve has changed (negative second derivative), suggesting a different regime for the information growth in the ZDI solutions. This is interpreted as a noise signature, reflected as artefacts in the final maps leading to an additional increment in the information growth. For this reason we adopt as optimal fit level the reduced χ^2 value for which the rate of change in the information growth (second derivative) in the ZDI solution set is maximised. In this particular case, this occurs around $\chi^2 \simeq 1.4$, as indicated by the fourth-order polynomial fit (segmented line) in the left panel of Fig. 2.7. A similar criterion plot is constructed for the Milne-Eddington line profile (Fig. 2.7, right panel), where a lower optimal reduced $\chi^2 \simeq 1.1$ is achieved in this case[‡].

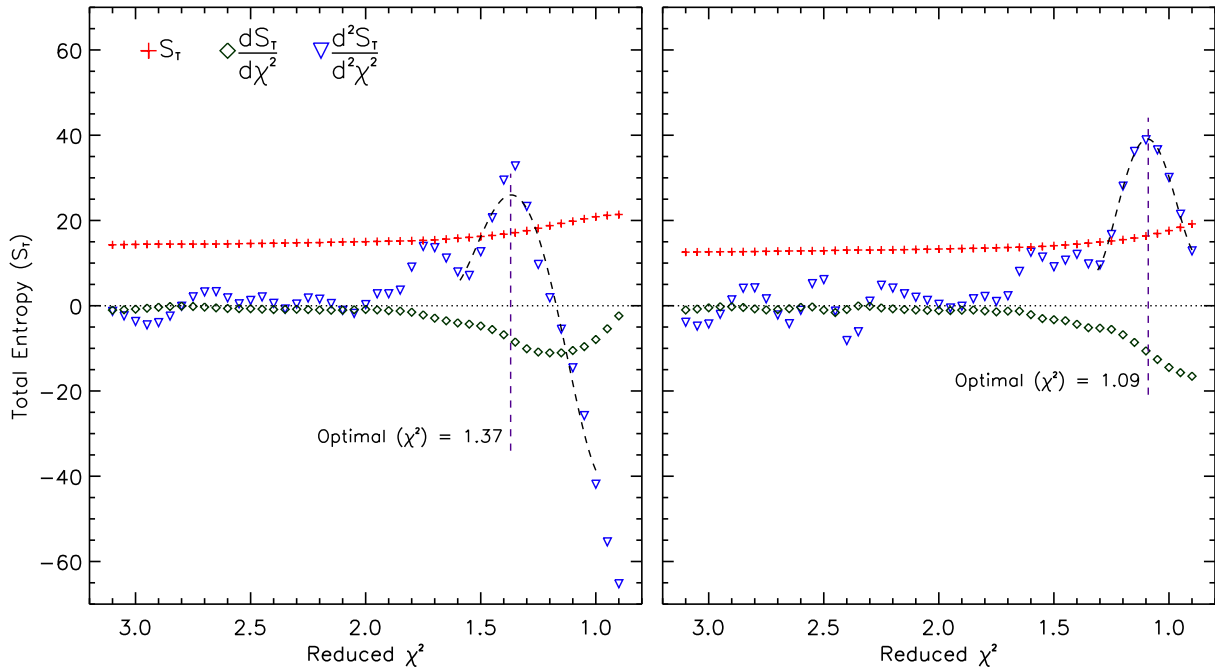


Figure 2.7: Optimal χ^2 selection criteria applied to the ZDI solution set of HD 1237. Each panel contains the results for the July dataset using the Gaussian (*left*) and Milne-Eddington (*right*) line profiles. The *red* symbols show the behaviour of the total entropy content S_T as a function of the reduced χ^2 . Each point corresponds to a converged ZDI solution. *Green* and *blue* symbols represent the first and second derivatives as indicated. The optimal fit level is defined as the value for which the rate of change in the information growth (second derivative) in the ZDI solution set is maximised, which is obtained with the aid of a fourth-order polynomial fit (segmented line).

[†]The apparent negative sign in $dS_T/d\chi^2$ is due to the reversed direction of the x-axis (reduced χ^2).

[‡]The same criterion was applied to generate the magnetic field maps in the December dataset (Appendix A). An optimal reduced $\chi^2 \simeq 0.6$ was obtained in this case, as expected for a dataset with fewer constraints.

2.6.3 ZDI maps and synthetic Stokes V profiles

We reconstructed the ZDI surface magnetic field maps and the synthetic circularly polarised profiles based on the time series of LSD Stokes V spectra. For this we used the cleaned-tweaked line mask (Sect. 2.5) and the stellar and line parameters derived in Sect. 2.6.1. The goodness-of-fit level in each case is selected under the criterion described in the last section.

Figure 2.8 shows the results of the ZDI procedure for the first-epoch observations (2012 July) of HD 1237. Four vertical panels are presented where the first three correspond to the Mercator-projected magnetic field maps in Gauss (G), decomposed into the radial (B_R , *top*), meridional (B_M , *middle*), and azimuthal (B_A , *bottom*) components. The spatial resolution of the maps is $\sim 18^\circ$ in longitude at the stellar equator (at the poles, the map has a considerably poorer resolution than the equator). However, the phase coverage also has a significant impact on the level of detail that can be recovered. In this case, the right-hand side would have a slightly better resolution than the left-hand side of the image. The horizontal dashed-line represents the visible stellar surface limit, which is determined by the estimated inclination angle of the star ($i = 50^\circ$, table 2.1). The fraction of the stellar surface lying below this line (i.e., from $-i$ to -90° in latitude) is not accessible from the observations. The last panel shows the fitted synthetic Stokes V profiles to the spectropolarimetric observations in each rotational phase (Φ).

The recovered maps show a relatively complex field distribution across the surface. The field is dominated by the azimuthal component, displaying a strong (~ 90 G) large-scale ring-like structure around 45° in latitude. In the radial component, two large and moderately strong (± 50 G) regions of opposite polarities are also located at higher latitudes, while weaker (± 25 G) small-scale features of mixed polarities appear close to the equator. These large magnetic features are somewhat preserved with reversed polarities in the meridional magnetic field maps. However, some cross-talk from the radial component may be present in the meridional map (see Donati & Brown 1997; Hussain et al. 1998, 2000).

Although the overall large-scale structure and field strength are consistent between both line profiles, several differences are clearly visible in the characteristics of the field components. First, the maps recovered using the Milne-Eddington line shape include additional small-scale features leading to a more complex field distribution in the surface. These are more prominent in the maps for the radial and meridional components. Second, the recovered magnetic field distribution, in the Milne-Eddington case, seems to be slightly shifted to lower latitudes. These differences can be understood from the fact that the Milne-Eddington line shape is a better representation of the derived LSD Stokes I profile. This is also true for the the shape of the circularly polarised profile, leading to a more detailed (additional small-scale structures) and a field distribution shifted to lower latitudes (as a consequence of the sensitivity in the wings of the profile). Both elements are translated into the lower optimal reduced χ^2 value that can be reliably achieved in this case (see Sect. 2.6.2), and therefore an improved fit (*bottom-right panel* in Fig. 2.8).

The reconstructed map for the second-epoch observations (2012 December) and the corresponding synthetic Stokes V profiles are presented in Appendix A.

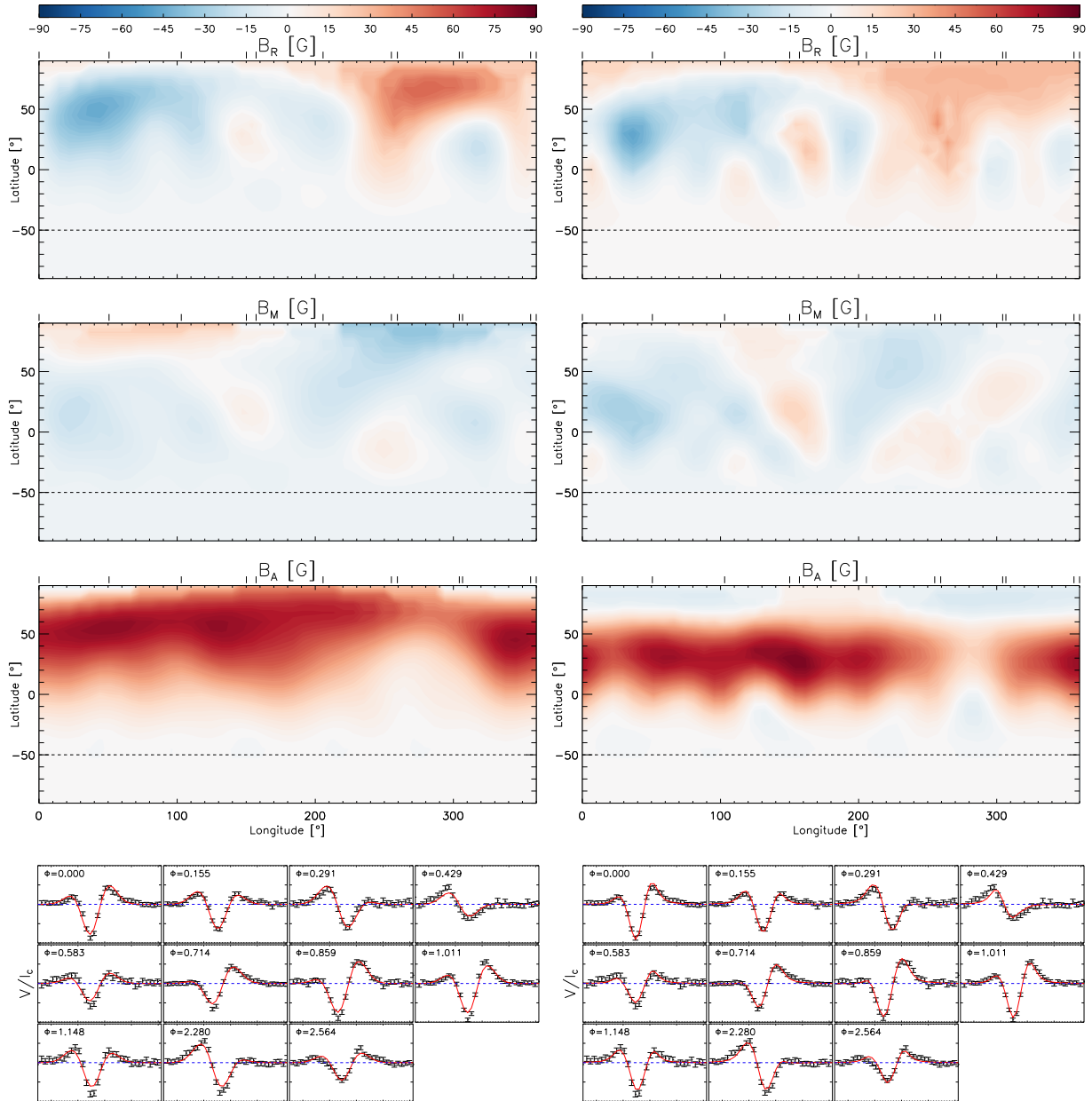


Figure 2.8: Results of the ZDI analysis for the first-epoch observations of HD 1237 using the Gaussian (*left*) and Milne-Eddington (*right*) line profiles. The first three panels show the surface magnetic field components B_R , B_M , and B_A . The colour scale denotes the polarity and the magnitude of each magnetic field component in Gauss (G), while the phase coverage is indicated by the *black* ticks in the upper y -axis. The segmented horizontal line indicates the surface visibility limit, imposed by the adopted inclination angle of the star ($i = 50^\circ$). The last panel shows the comparison between synthetic (*red*) and observed (*black*) Stokes V profiles obtained for this particular epoch in each observational phase Φ . The recovered maps fit the spectropolarimetric data to optimal reduced χ^2 values of 1.4 and 1.1 for the Gaussian and the Milne-Eddington profiles, respectively.

2.7 Summary and discussion

In this paper, we have presented a detailed study that covers two observational epochs of the activity and magnetic field structure of the Sun-like planet-hosting star HD 1237. The chromospheric activity level of HD 1237 estimated from the calibrated $S_H = 0.46 \pm 0.02$ and $\log(R'_{HK}) = -4.38 \pm 0.05$ values is similar to other active Sun-like stars (e.g., ξ Boo A, Morgenthaler et al. 2012) and considerably higher than the solar case (~ 3 times higher in terms of the average S index, Lockwood et al. 2007). A much larger difference has been reported for the X-ray activity level, with a $\log(L_X) = 29.02 \pm 0.06$ for HD 1237 (Kashyap et al. 2008), which is two orders of magnitude higher than the value estimated for the Sun during solar maximum (Peres et al. 2000). The chromospheric activity level remained fairly constant over the near five-month period between the two sets of observations. Our estimate falls between the previous measurements of $\log(R'_{HK}) = -4.27$ (Naef et al. 2001) and $\log(R'_{HK}) = -4.44$ (Saffe et al. 2005). Given the large uncertainties in the activity indicators, it is difficult to address whether these variations have some correspondence to a magnetic cycle in the star.

To extract magnetic field signatures from spectropolarimetric data, we applied the LSD multi-line technique to the observations. Two different line masks for the LSD profiles were compared and tested. The standard procedure involves employing a mask “cleaned” of chromospheric and strong NLTE line profiles (e.g., Marsden et al. 2014); we compared the results from this procedure with improving the line list further by “tweaking” line strengths, so that they are tailored to the line depths in the observed spectrum. Both approaches lead to similar results in the obtained LSD profiles, and therefore in the physical quantities inferred (e.g., the longitudinal magnetic field, B_ℓ). However, for the same number of spectral lines, the average S/N of the LSD profiles recovered with the aid of the cleaned-tweaked line mask was $\sim 7\%$ higher than in the cleaned case.

The longitudinal magnetic field (B_ℓ), estimated from the Stokes I and V LSD profiles, showed a clear rotational modulation with an amplitude of ~ 10 G. This behaviour was preserved in both observed epochs. Placing these measurements in the context of other stars, similar variations have been observed in the long-term monitoring of the active Sun-like star ξ Boo A ($B_\ell \sim 4\text{--}9$ G, Age: ~ 0.2 Gyr, Mamajek & Hillenbrand 2008; Morgenthaler et al. 2012), the K-dwarf exoplanet host ϵ Eri ($B_\ell \sim 10\text{--}12$ G, Age: $\sim 0.2\text{--}0.8$ Gyr, Janson et al. 2008; Jeffers et al. 2014b), and more recently for the young solar analogue HN Peg ($B_\ell \sim 14$ G, Age: ~ 0.2 Gyr, Eisenbeiss et al. 2013; Boro Saikia et al. 2015).

The chromospheric and X-ray activity levels of these stars are also very similar to HD 1237. The source ξ Boo A has an average S-index of $S_{HK} \simeq 0.45$ and $\log(L_X) \simeq 28.91$ (Gray et al. 1996; Wood & Linsky 2010), and ϵ Eri has strong magnetic activity with a mean $S_{HK} \simeq 0.50$ and $\log(L_X) \simeq 28.22$ (Jeffers et al. 2014b; Poppenhaeger et al. 2011). Similarly, previous reports for HN Peg show $S_{HK} \simeq 0.35$ and $\log(L_X) \simeq 29.19$ (Boro Saikia et al. 2015; Schmitt & Liefke 2004). Despite the various similarities among these systems, the complete relation between the magnetic field and its influence over different layers of the stellar atmosphere (activity) have not yet been fully understood. Similar to these other systems, the chromospheric activity of HD 1237 does not show a clear correlation with B_ℓ .

This is interpreted as the result of probing different spatial and temporal scales in each of these measured quantities.

We recovered the optimal stellar parameters of HD 1237 using a reduced χ^2 minimisation scheme, based on the tomographic inversion technique of ZDI. The analysis yielded a rotation period, $P_{\text{rot}} = 7.0 \pm 0.7$ d. Literature values of P_{rot} are uncertain, ranging between 4.1–12.6 d (see [Watson et al. 2010](#) and references therein). The 7.0-day value found in this work is consistent with the ZDI analysis and both the chromospheric and coronal activity levels of the star. Similar procedures were applied to estimate the inclination angle and the differential rotation of HD 1237. However, the available observations did not provide enough constraints for a robust determination of these parameters. Therefore, we considered an inclination angle derived using the stellar properties of the star and solid body rotation (i.e., $i \sim 50^\circ$). No differential rotation profile was included in the reconstruction of the magnetic field maps.

For the surface magnetic field mapping procedure, two different synthetic line shapes (Gaussian/Milne–Eddington) were tested in order to investigate their impact on the ZDI maps for slowly rotating solar-type stars. We showed that both profiles recover robust magnetic field maps. However, the Milne–Eddington line profile yields a better spectropolarimetric fit (lower optimal reduced χ^2 , leading to a more detailed structure recovered in the ZDI maps compared to the Gaussian case. In connection to this, a fit-stopping criterion based on the information content (entropy) of the ZDI maps solution set was introduced. This allows identification of the optimal reduced χ^2 value, avoiding to some extent the appearance of numerical artefacts in the ZDI maps. The optimal fit level is given by the reduced χ^2 value for which the rate of change of the entropy growth in the ZDI solution set is maximised.

The large-scale magnetic field of HD 1237 showed a complex distribution at the stellar surface. The strongest magnetic field features appear at middle latitudes ($\sim 45^\circ$) in the azimuthal and radial components. The field is dominated by the azimuthal component, displaying latitudinal belts or ring-like structures across the stellar surface. This has been observed in other studies of active Sun-like stars (e.g., [Folsom et al. 2014](#)) and in numerical simulations of a rapidly rotating Sun ([Brown et al. 2010](#)). As previously suggested, the appearance of significant or even dominant toroidal fields in the surface of these types of stars is connected with the rotation period, with ~ 12 d as the rotation threshold ([Petit et al. 2008](#)).

In comparison with other cool stars, HD 1237 ($P_{\text{rot}} = 7.0$ d, this work, $M_* = 1.0 \pm 0.1 M_\odot$, [Ghezzi et al. 2010](#)) could be located near ξ Boo A (G8V, Age: ~ 0.2 Gyr) and GJ 182 (M0V, Age: $0.50^{+1.0}_{-0.3}$ Gyr, [Liu et al. 2004](#)) in the mass-period, large-scale magnetic field diagram (Fig. 3 in [Donati & Landstreet 2009](#)) with a mostly toroidal field topology and a considerable contribution from the radial component. With the same spectral type as HD 1237, ξ Boo A displays a slightly weaker field in its surface (± 60 G) with an alternating dominance between the radial and the azimuthal components in the observed long-trend evolution (~ 4 yr, [Morgenthaler et al. 2012](#)). During the observed azimuthal-dominated epochs of this star, the field distribution is very similar to the one derived for HD 1237 in this work. A strong uni-directional azimuthal field appears at low latitudes with large mixed

polarity regions in the radial field and a minor contribution from the meridional component. However, the magnetic regions of ξ Boo A are much larger and less concentrated than the ones found for HD 1237. This could be related to the small difference in their rotation periods (6.43 d for ξ Boo A and 7.0 d for HD 1237) and/or with the differential rotation that may be occurring in the surface. A similar situation appears in the case of GJ 182 in terms of the recovered magnetic field topology. However, the field strength is much larger in this case (up to 400 G, [Donati et al. 2008b](#)), which is mostly connected with the rapid rotation, large latitudinal shear, and the nearly fully convective nature of this star.

Regardless of the low $v \sin(i)$ of HD 1237, it is clear that a more complex field distribution is required to fit the observed spectra. Some weaker small-scale regions are recovered closer to the stellar equator. Despite their relative low strength compared to the total surface field, the contribution from these small-scale features to magnetically-related phenomena may be significantly higher. In combination with strong mixed-polarity regions missed by ZDI, these features can influence the quiescent coronal emission ([Johnstone et al. 2010](#)), the X-ray modulation ([Arzoumanian et al. 2011](#)), and the wind structure around very active stars ([Lang et al. 2014](#)) and the Sun ([Garraffo et al. 2013](#)).

The large-scale field distribution appears similar at both of the observed epochs, confirming the observed chromospheric activity and longitudinal magnetic field behaviour. Using the final ZDI maps and the derived synthetic Stokes V profiles, we were able to reproduce the variations in B_ℓ consistently (for both observed epochs). As an example, the maximum value of B_ℓ in [Fig. 2.5](#) coincides when the large positive polarity region of the radial field is located close to the limb (Day 3). Similarly, the minimum value obtained for B_ℓ in [Fig. 2.5](#) results from the negative polarity region in the radial field map, this time located much closer to the disk centre. This corroborates the robustness of our ZDI magnetic maps for this system.

As mentioned in [Sect. 2.2](#), HD 1237 has a planetary companion with a mean separation of 0.49 AU and a projected mass of $M_p \sin(i) = 3.37 \pm 0.14 M_{\text{Jup}}$. This exoplanet is relatively far out in comparison with other similar systems where ZDI maps of the host star are available (see [Fares et al. 2013](#) and references therein). However, the enhanced activity levels of HD 1237 and the relatively strong and complex surface magnetic field (in connection with its stellar wind) could affect the conditions experienced by the exoplanet through its orbit significantly. Previous parametric studies of this system have predicted a relatively high mass loss rate ($\dot{M}_* \sim 85 \dot{M}_\odot$), which could even lead to magnetospheric radio emission from the exoplanet ([Stevens 2005](#)). This will be considered in a future study, incorporating the recovered ZDI magnetic field maps into a detailed 3D magnetohydrodynamics (MHD) code (SWMF/BATS-R-US, [Powell et al. 1999](#); [Tóth et al. 2012](#)), which was originally developed and validated for the solar wind and corona (e.g., [Sokolov et al. 2013](#); [van der Holst et al. 2014](#)) and recently applied in the stellar context (e.g., [Cohen & Drake 2014](#); [Cohen et al. 2014](#)).

2.8 Chapter conclusions

We reconstructed magnetic field maps of the young planet-hosting G-type star, HD 1237 using the technique of Zeeman Doppler imaging. As part of this detailed spectropolarimetric study, we have performed the following:

- We find that assuming a Milne-Eddington approximation for the local line profile produces a better fit to the shape of the observed LSD profiles. This influences the number of magnetic structures that can be recovered in the magnetic field maps.
- We propose a robust method for defining the stopping criterion in ZDI techniques. This allows one to choose the optimum degree of fit, beyond which the model ceases to provide a good fit to the observed dataset owing to the introduction of artefacts into the resulting image. We successfully applied this to two different datasets with vastly different degrees of phase sampling.
- As part of our optimisation routines, we recovered a rotation period of 7.0 d. This is consistent with the measured chromospheric and coronal activity levels of the star ($\log(R'_{HK}) = -4.38 \pm 0.05$, this paper; $\log(L_X) = 29.02 \pm 0.06$, [Kashyap et al. 2008](#)).
- The magnetic field reconstructions for HD 1237 are dominated by a band of strong uni-directional azimuthal field at high latitudes, accompanied by a complex multipolar radial field distribution. The largest magnetic regions show field strengths of ~ 90 and 50 G for the azimuthal and the radial field components, respectively.
- We note that the field topology recovered for HD 1237 is fully commensurate with studies of ξ Boo A and GJ 182, the two other stars that are closest to it in the mass-period diagram ([Donati & Landstreet 2009](#)). Larger sample sizes are needed to confirm these trends. If confirmed, it will be possible to predict the global magnetic field topologies and therefore the extended environments of planet-hosting stars at various stages in their evolution based on these fundamental parameters.

We will address the influence of the different magnetic scales on the coronal structure and wind properties of HD 1237 in a follow-up paper, using the ZDI maps presented here as boundary conditions (see [Cohen et al. 2010](#); [Cohen et al. 2011a](#)). Possible star-planet interactions occurring in the system via transient (e.g., CME events, [Cohen et al. 2011b](#)) or quiescent phenomena (e.g., planetary radio emission, [Stevens 2005](#); [Vidotto et al. 2012](#)) can also be considered in future work.

Chapter 3

A spectropolarimetric study of the planet-hosting G dwarf HD 147513

Abstract

The results from a spectropolarimetric study of the planet-hosting Sun-like star, HD 147513 (G5V), are presented here. Robust detections of Zeeman signatures at all observed epochs indicate a surface magnetic field, with longitudinal magnetic field strengths varying between 1.0–3.2 G. Radial velocity variations from night to night modulate on a similar timescale to the longitudinal magnetic field measurements. These variations are therefore likely due to the rotational modulation of stellar active regions rather than the much longer timescale of the planetary orbit ($P_{\text{orb}} = 528$ d). Both the longitudinal magnetic field measurements and radial velocity variations are consistent with a rotation period of 10 ± 2 d, which are also consistent with the measured chromospheric activity level of the star of $\log(R'_{\text{HK}}) = -4.64$. Together, these quantities indicate a low inclination angle, $i \sim 18^\circ$. We present preliminary magnetic field maps of the star based on the above period and find a simple poloidal large-scale field. Chemical analyses of the star have revealed that it is likely to have undergone a barium-enrichment phase in its evolution because of a higher mass companion. Despite this, our study reveals that the star has a fairly typical activity level for its rotation period and spectral type. Future studies will enable us to explore the long-term evolution of the field, as well as to measure the stellar rotation period, with greater accuracy.

3.1 Chapter organization

This chapter contains the analysis of high signal-to-noise (S/N) spectropolarimetric time series of the planet-hosting G-dwarf star, HD 147513. In a similar manner as in Chapter 2, we use these data to characterise the magnetic activity properties, and to map the surface large-scale topology in this system using ZDI. In Sect. 3.2 we give a more detailed description of the stellar system. Observations and the analysis of the chromospheric activity are

in Sects. 3.3 & 3.4, respectively. The photospheric line profiles are used to measure the longitudinal magnetic field and radial velocity, and to study the night-to-night variability in both these quantities (Sect. 3.5). The ZDI maps based on our best estimates of the stellar rotation period are presented in the Sect. 3.6. Our conclusions are summarised in Sect. 3.7.

3.2 HD 147513

HD 147513 (GJ 620.1 A, HR 6094) is a bright ($V_{\text{mag}} = 5.4$) G-dwarf at a distance of 12.9 pc (Valenti & Fischer 2005). Its main properties are listed in Table 3.1; these include both published values and those determined in the analysis presented here.

Table 3.1: HD 147513 basic properties.

Parameter	Value	Reference
Sp. Type	G5V	Soderblom & Mayor (1993)
$B - V$	0.62	Soderblom & Mayor (1993)
Age [Gyr]	~ 0.45	Rocha-Pinto & Maciel (1998)
T_{eff} [K]	5930 ± 44	Valenti & Fischer (2005)
$\log(g)$	4.612 ± 0.06	Valenti & Fischer 2005
M_* [M_{\odot}]	1.07 ± 0.01	Takeda et al. (2007)
R_* [R_{\odot}]	$0.98^{+0.03}_{-0.02}$	Takeda et al. (2007)
$v \sin(i)$ [km s^{-1}]	1.5 ± 0.4	Valenti & Fischer (2005)
i [$^{\circ}$]	18^{+12}_{-8}	This work
v_R [km s^{-1}]	13.232 ± 0.09	This work
P_{rot} [d]	10.0 ± 2.0	This work
$\log(R'_{\text{HK}})$	-4.64 ± 0.05	This work
$\log(L_X)$	28.92	Schmitt & Liefke (2004)

This star can be considered as moderately active, with an average X-ray luminosity of about 10^{29} erg s^{-1} in the 0.1–2.4 keV *ROSAT* PSPC band (Schmitt & Liefke 2004). For comparison, the average solar X-ray luminosity is approximately $10^{27.6}$ erg s^{-1} , varying by an order of magnitude over the course of the 11-year solar activity cycle (Judge et al. 2003). Chromospheric activity is indicated by significant emission in its Ca II H&K profiles with a range of R'_{HK} values reported in the literature ($-4.6 < \log(R'_{\text{HK}}) < -4.38$, Saffe et al. 2005). The rotation period of the star has been determined based on the above $\log(R'_{\text{HK}})$ values, and published estimates range between 4.7 d (Mayor et al. 2004) and 8.5 ± 2.2 d (Watson et al. 2010). Age estimates based on chromospheric activity place the star at 0.45 Gyr (Rocha-Pinto & Maciel 1998). The star may also be associated with the 0.5 Gyr Ursa Major moving group (King et al. 2003).

High precision radial velocity measurements spanning almost five years reveal the presence of a Jupiter-mass planet ($M \sin(i) = 1.21 M_{\text{J}}$, $P_{\text{orb}} = 528.4$ d). The semi-amplitude

is $K = 29.3 \pm 1.8 \text{ m s}^{-1}$ with a dispersion of 5.7 m s^{-1} . [Mayor et al. \(2004\)](#) report that the orbital properties of this planetary system are characteristic of intermediate-to-long orbital period radial velocity planets, with a semi-major axis, $a = 1.32 \text{ AU}$ and eccentricity, $e = 0.26$.

As also discussed by [Mayor et al. \(2004\)](#), the chemical analysis of HD 147513 points to a complex evolutionary history. Its high lithium abundance indicates its relative youth. However, the star is also found to be over-abundant in barium and s-process elements. [Porto de Mello & da Silva \(1997\)](#) suggest that this is due to mass transfer between HD 147513 and the AGB progenitor of the white dwarf, CD-38°10980, which is found to have a common proper motion. This well-studied white dwarf has an age of 30 Myr and is at a distance of 5360 AU from HD 147513 with an original mass of $2.6 M_{\odot}$. This more massive star may have driven sufficient mass transfer onto HD 147513 to explain its observed abundance of s-process elements. Indeed [Porto de Mello & da Silva \(1997\)](#) indicates that these stars may have been part of a multiple star system, bound with the binary, HR 2047; which is 24 pc away, a confirmed member of the UMa moving group, and which also shows evidence of barium enrichment (albeit to a lesser extent).

3.3 Spectropolarimetric observations

We secured high S/N circularly polarised spectra of HD 147513, with the aid of the polarimetric mode of the HARPS echelle spectrograph at the ESO 3.6-m telescope at the La Silla Observatory ([Piskunov et al. 2011](#); [Mayor et al. 2003](#)). The data were acquired in 2012 July under changeable weather conditions. Our observing log is presented in [Table 3.2](#).

All observations had the same exposure time of 3600 s for the full circularly polarised spectrum (Stokes V) sequence. This circularly polarised profile is obtained by combining four individual sub-exposures using the ratio method (see [Donati et al. 1997](#); [Bagunulo et al. 2009](#)), which also enables a null-polarisation spectrum to be constructed in order to check for possible spurious polarisation contributions ([Donati et al. 1997](#)).

Data were reduced using the ESPRIT package which has been adapted for the HARPS instrument ([Donati et al. 1997](#), [Hébrard et al. in prep.](#)). This package produces an optimal extraction of the bias-subtracted spectra

Table 3.2: Journal of HARPSpol observations of HD 147513.

Date (2012)	BJD (TT) (2 400 000+)	UT (HH:MM:SS)	Stokes I Peak S/N
Jul 15	51 623.53315	00 : 40 : 36	660
Jul 15	51 624.52049	24 : 22 : 28	810
Jul 17	51 625.54088	00 : 51 : 56	570
Jul 18	51 626.53188	00 : 39 : 03	720
Jul 18	51 627.50182	23 : 55 : 52	734
Jul 20	51 628.53529	00 : 44 : 09	923
Jul 22	51 630.59443	02 : 09 : 32	550
Jul 23	51 631.71964	05 : 09 : 56	340

The columns contain the date, the corresponding Barycentric Julian Date (BJD), the start time of the observations in UT, and the Stokes I peak Signal-to-Noise ratio (S/N). A fixed exposure time of 3600 s was considered for all observations.

after flat-fielding corrections. The slit shape is averaged over each order and used to compute the curvilinear coordinate system along which the spectra are extracted. The calibration frames required by the package are the bias frames, flat field frames and a good quality ThAr arc spectrum that were acquired each night. Spectra extracted using the REDUCE package (Piskunov & Valenti 2002; Makaganiuk et al. 2011) were almost identical compared to those reduced with the ESPRIT, with the latter showing slightly higher S/N levels. As barycentric corrections are also applied to the spectra reduced by ESPRIT, this is the dataset used in the analysis presented here. The extracted data have spectroscopic resolutions varying from 95 000 to 113 000, depending on the wavelength, with a median value of 106 000. Given the noise level of these data 1 m s^{-1} accuracy should be achievable in the radial velocity measurements.

3.4 Chromospheric activity

A sample spectrum from our dataset are shown in Fig. 3.1 (*red line*), clearly illustrating emission in the cores of both Ca II H&K profiles due to significant chromospheric heating and indicating a moderate magnetic activity level. To quantify the level of chromospheric activity in HD 147513, we apply the same conversion procedure of the HARPS Ca II fluxes to the Mount Wilson S-index scale (S_{MW} , see Sect. 2.4). An average S-index of 0.23 ± 0.01 is computed for our dataset. No significant variability is found in the Ca II H&K fluxes over eight days, indicating a constant contribution from the chromospheric active regions even as the star rotates[†].

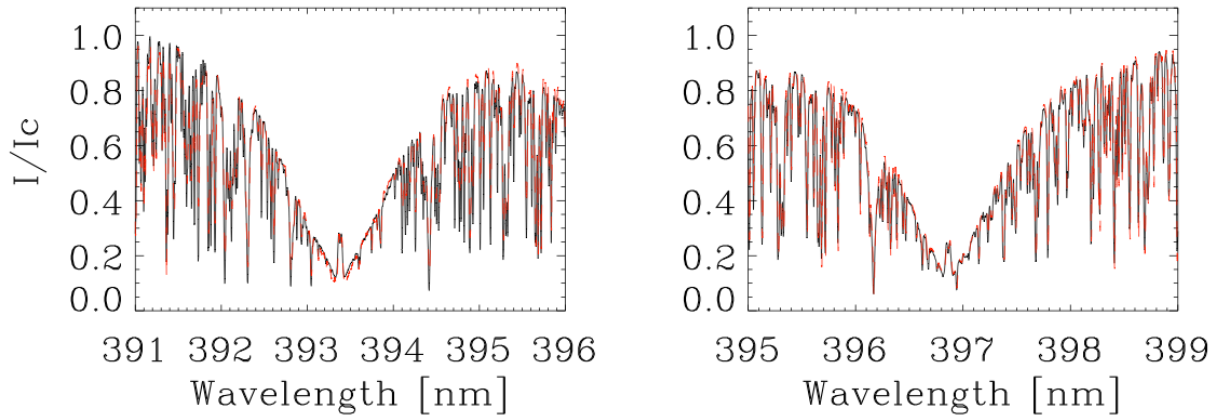


Figure 3.1: Comparison between Ca II H (*right*) and K (*left*) cores observed with HARPS in 2012 July 18 (red dotted line) and archive FEROS spectra from 2006 July 15 (black solid line). The HARPS spectra have been rebinned to enable a better comparison with the FEROS spectra, which have a lower spectroscopic resolution.

[†]The phase coverage of our spectropolarimetric time-series is sufficient to cover the range of estimated rotation periods in the literature (see Sect. 3.2).

As with the observations of HD 1237 (Sect. 2.4.2), the S-index is converted to the chromospheric activity indices, R_{HK} and R'_{HK} , applying the colour and photospheric corrections for main sequence cool stars with a $B - V$ of 0.62 (Middelkoop 1982; Noyes et al. 1984). This conversion results in average values of $\log(R'_{\text{HK}})$ of -4.64 ± 0.06 and $\log(R_{\text{HK}}) = -4.44 \pm 0.04$ for HD 147513.

As noted in Sect. 3.2 literature values of $\log(R'_{\text{HK}})$ range from -4.6 to -4.38 over a period spanning almost 20 years (from 1983 to 2004, Soderblom & Clements 1987; Saffe et al. 2005). In order to investigate whether long-term changes (e.g., due to magnetic activity cycles) might be at the root of these different measurements, we searched public archives for spectra of HD 147513 that cover the relevant wavelength range. Fig. 3.1 shows a comparison between spectra acquired in 2006 (archive FEROS spectra) with our 2012 HARPS spectra. It is clear that there is little variability over these two epochs and the corresponding R'_{HK} indices are therefore identical within the measurement errors. While this cannot exclude intrinsic variability over a wider range of timescales it is likely that the chromospheric activity level is more stable than suggested from the range of published measurements. We conclude that these variations are likely dominated by differences in conversions to the Mt. Wilson index from spectra acquired from a range of instruments.

It is possible to estimate the rotation period of the star within about 20% accuracy using its $\log(R'_{\text{HK}})$ index and the relations presented by Noyes et al. (1984). The Rossby number of the star is computed using its R'_{HK} index, while the convective turnover timescale, τ_c can be estimated from the star's $B - V$. We find a period of 12.4 d, for our value $\log(R'_{\text{HK}}) = -4.64$; this is somewhat larger but still compatible with the 8.5 d estimate of Watson et al. (2010), based on a $\log(R'_{\text{HK}})$ of -4.52 . However, it is completely incompatible with the 4.7 d value based on the highest $\log(R'_{\text{HK}}) = -4.38$ (Mayor et al. 2004). Combining these estimates for the stellar rotation period with its projected rotational velocity, $v \sin(i)$, and radius (Table 3.1), it is possible to compute the inclination angle of the star. For HD 147513 a relatively low inclination angle is expected; using the range of 4.7–12.4 d periods and radii, the inclination angle must be between 10–25°.

3.5 Photospheric line profiles & stellar magnetic field

As the large scale magnetic field in cool stars such as HD 147513 is expected to be relatively weak ($\ll 1$ kG), it is not possible to detect significant polarisation in individual photospheric line profiles. It is therefore necessary to employ a multi-line technique, e.g., Least Squares Deconvolution (LSD, Donati et al. 1997), to exploit the full wavelength coverage of the dataset (378–691 nm) and use the signal from thousands of photospheric spectral lines. It is typically possible to enhance the S/N by a factor of ~ 30 , compared to the original spectrum in this way.

The mask used in the LSD analysis is constructed from an atomic line list extracted for a star with the same basic parameters ($\log(g)$, T_{eff}) as HD 147513 from the VALD database[†]

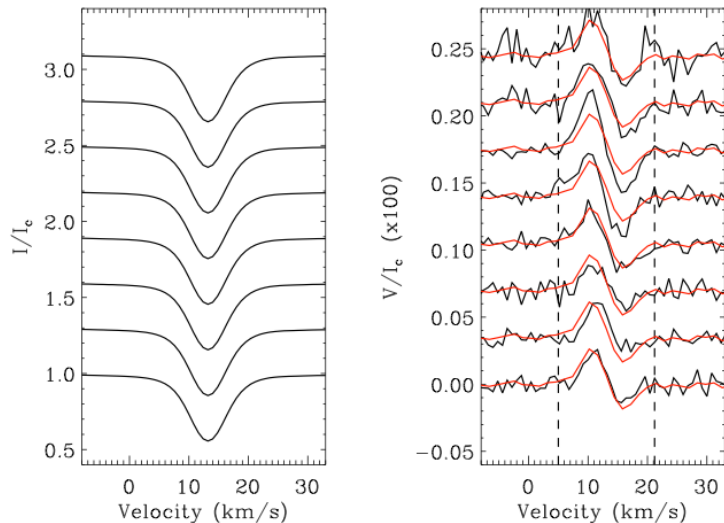
[†]<http://vald.astro.uu.se/> – Vienna Atomic Line Database (VALD3)

(Kupka et al. 2000). This initial line list is first “cleaned” of all strong lines, including any diagnostics that are likely to have significant contributions from the chromosphere (e.g., Ca II H&K, H α). The resulting line list is then further tailored to the star by adjusting the individual depths to fit those of the spectral lines of HD 147513. As discussed in Chapter 2 and Alvarado-Gómez et al. (2015), this “clean-tweaking” method is most commonly employed when applying LSD to hot (OB) stars (see Neiner et al. 2012). As cool stars have thousands of photospheric line profiles, this technique does not have as significant an impact on the LSD profiles but does increase them in S/N by between 5–10% compared to the original “clean” line mask. LSD is then applied to our spectropolarimetric dataset using these tailored clean-tweaked masks, cutting off at a depth of 0.1. This results in almost 4500 lines being used in the deconvolution. The velocity step used is 0.8 km s⁻¹, which corresponds to the average pixel size of the CCD.

3.5.1 LSD profiles

Fig. 3.2 shows the time series of the derived LSD profiles of HD 147513 over 8 days. The Stokes I (unpolarised) profile is shown in the left column, while on the right column the Stokes V (circularly polarised) profiles for each epoch (*black*) are compared to the mean profile of the entire dataset (*red*). The noise level in the Stokes I LSD profiles ($\sim 9.8 \times 10^{-4}$) remains fairly constant over the whole dataset. Definite positive magnetic field detections are found in each of the circularly polarised (Stokes V) profiles.

Figure 3.2: LSD Profiles of HD 147513. *Left:* Stokes I (unpolarised) and *right:* Stokes V (circularly polarised) profiles. The mean Stokes V profile (*red*) computed over this dataset has been over-plotted to investigate variability from night to night. The dashed vertical lines denote the velocity limits over which the B_ℓ measurements were calculated (Sect. 3.5.2).



From Fig. 3.2 it is clear that the shape of the Stokes V profiles is largely unchanged over the course of the observations, showing a classic antisymmetric shape with respect to the centre. There does however, appear to be a modulation in the amplitude of the Stokes V profiles which is indicative of a small level of inhomogeneity and non-axisymmetry in the large scale field of the star.

3.5.2 Longitudinal magnetic field

The derived LSD profiles can be used to compute the surface averaged longitudinal magnetic field (B_ℓ). This quantity is measured with respect to the intensity line profile, using the central wavelength λ ($0.519 \mu\text{m}$) and the mean Landé factor, \bar{g} (1.197) of the LSD profiles (see Eq. 2.8). The measurements of B_ℓ for HD 147513 are performed between 5.0 and 21.2 km s^{-1} from the line centre and show variability from night to night. The uncertainties on these values are determined via standard error propagation from the spectra.

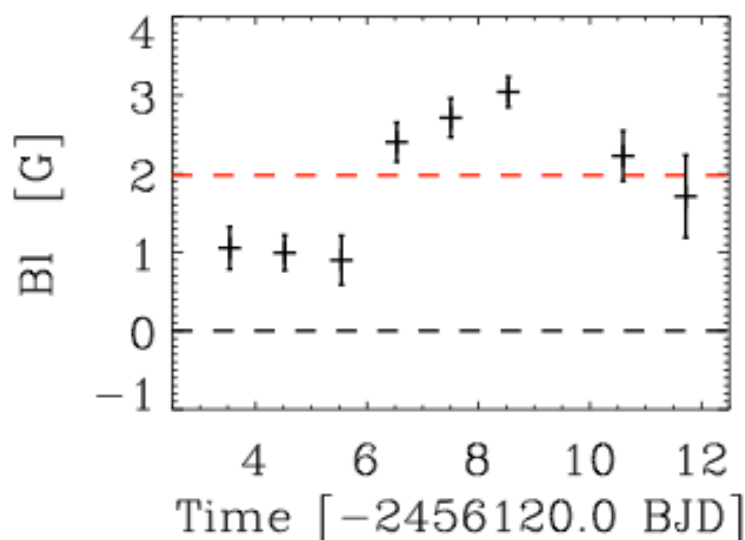


Figure 3.3: B_ℓ measurements of HD 147513 show significant variability over the 8-day span of the dataset. The x-axis shows the time in Barycentric Julian Date (see Table 3.2) and the red and black dashed lines denote the mean B_ℓ (2.0 G) and 0 G levels, respectively.

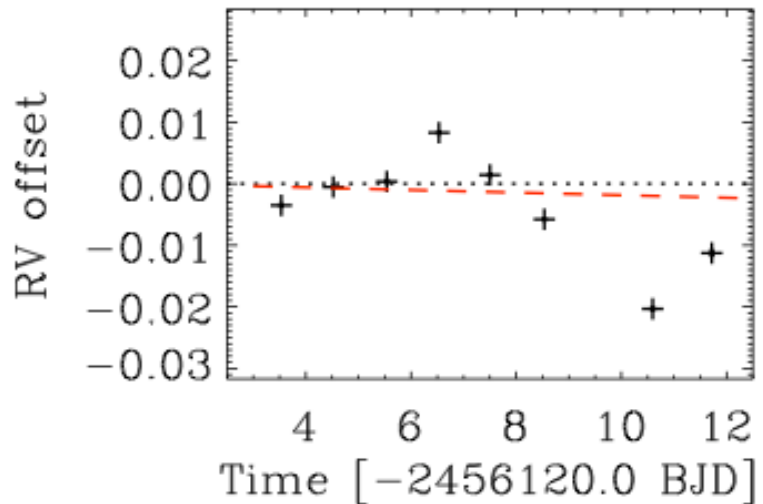
The range of values shown in Fig. 2.5 is higher than the range typically seen on the Sun, where $|B_\ell|$ is predominantly under 1 G; solar $|B_\ell|$ values can get as high as 3–4 G but only very rarely (Kotov et al. 1998). As noted in Sect. 3.2, the chromospheric and coronal magnetic activity levels of the Sun and HD 147513 are very different. It is therefore highly likely that these surface magnetic field measurements have a different origin; HD 147513 should have much larger, stronger active regions at the stellar surface compared to the Sun. The B_ℓ modulations observed in Fig. 2.5 are significant (over 3σ) and their timescale is consistent with that expected by rotational modulation of active regions. Fig. 2.5 strongly discounts the possibility of a period shorter than 8 d and hence excludes the previously published value of 4.7 d. Naturally this argument assumes that the variability is not driven by the emergence of new flux. Studies of active cool stars tracing star spot lifetimes typically show that the large-scale field should remain stable over a period of several weeks and so this appears to be a reasonable assertion (Barnes et al. 1998; Hussain 2002; Strassmeier 2009).

3.5.3 Radial velocity and activity

We measured the radial velocity (RV) at each observing epoch by least-squares fitting Gaussians to the Stokes I LSD profiles. The resulting measurements are shown in Fig. 3.4,

where the errors are smaller than the symbol sizes ($\pm 1 \text{ m s}^{-1}$). We find significant variations about a mean RV, $\bar{v} = 13.232 \pm 0.009 \text{ km s}^{-1}$ over 8-days. As the span of our observations is so much smaller than the orbital period of the planet, it is clear that these variations are stellar in origin. This is clearly demonstrated in the comparison of the measured RV variability with the expected RV contribution caused by HD 147513b in Fig. 3.4. This was computed using the ephemeris reported by [Mayor et al. \(2004\)](#). We note that the timescale of these variations is consistent with that shown by the B_ℓ measurements (Fig. 3.3). Unfortunately, as less than one full rotation period is sampled in these observations, it is not possible to establish whether this is definitively due to rotational modulation of active regions; although this appears to be the most likely explanation. In particular, as these spectra were obtained by integrating over 1 hour, shorter timescale phenomena (e.g., pulsations, granulation) are unlikely to contribute significantly to these RV measurements ([Dumusque et al. 2011](#)).

Figure 3.4: RV variability of HD 147513 in m s^{-1} over the 8-day span of the dataset about the mean ($\bar{v} = 13.232 \text{ km s}^{-1}$, dotted line). The red line shows the predicted RV contribution of the planet over the same time-frame. The latter has been calculated using the reported ephemeris ([Mayor et al. 2004](#)). As in Fig. 3.3, the x-axis shows the time of the observations in Barycentric Julian Date (BJD).



3.6 Large-scale magnetic field maps of HD 147513

We present here the maps of the large scale surface magnetic field of HD 147513, assuming the 10 d rotation period that provided the best fit to the temporal variability in both, B_ℓ and RV (Sects. 3.5.2 and 3.5.3). These maps have been reconstructed using the ZDI code presented in [Hussain et al. \(2002\)](#); this describes the field in terms of spherical harmonics and allows for both poloidal and toroidal field components. The local line profile has been modelled using a Milne-Eddington profile whose width and amplitude were adjusted to fit that of HD 147513 and the equivalent width of $67 \text{ m}\text{\AA}$, following the approach of [Donati et al. \(2008b\)](#) and [Alvarado-Gómez et al. \(2015\)](#). More specifically a Voigt profile was used in order to better fit the wings of the Stokes I LSD profiles in this low $v \sin(i)$ star. The width of the local profile was adjusted to find the best fit to the integrated Stokes I profile in agreement with the published $v \sin(i)$ value (Table 3.1). The model fits shown here all assume a linear limb darkening law, with a limb darkening coefficient of 0.65 ([Sing 2010](#)).

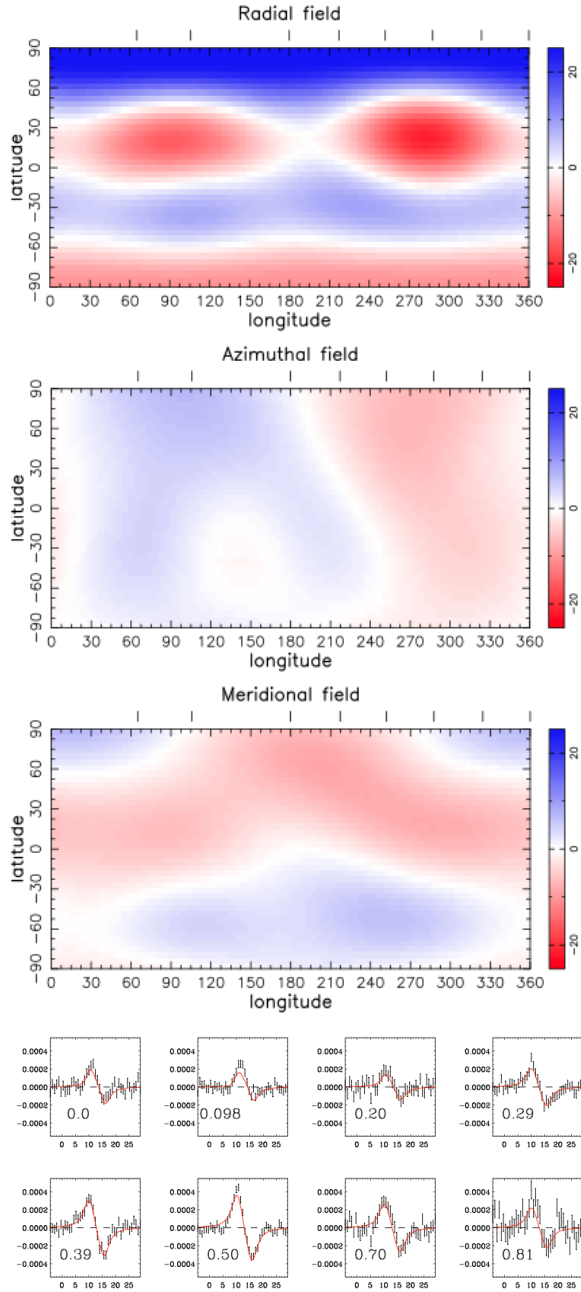


Figure 3.5: ZDI large-scale magnetic field maps of HD 147513 and fits to the Stokes V data. The first three panels show the radial, azimuthal and meridional field components respectively. *Red* and *blue* represent ± 25 G. The *bottom* panel shows the fits to the Stokes V profiles ($\chi_r^2 = 1$). The corresponding phases are listed in the *bottom-left* corner assuming a 10 d rotation period.

The resulting maps fit the observed data to a reduced χ^2 of 1 and are shown in Fig. 3.5. By restricting the solution to a dipolar solution ($l_{\max} = 1$) convergence cannot be found beyond χ_r^2 of 1.4. We adopt a maximum spherical harmonic degree of $l_{\max} = 3$ as we find no significant improvement by allowing higher-order modes in the optimal level of fit (calculated via the procedure presented in Sect. 2.6.2). These maps have been derived assuming an inclination angle of 18° . Magnetic field regions down to -18° latitude should contribute to the observed line profiles in stars with inclination angles of 18° . The region below the equator is mostly not visible due to the low inclination angle. Nevertheless field is reconstructed in the unobserved hemisphere due to the low order spherical harmonics used. Most of the energy (70%) is concentrated in the aligned dipolar, quadrupolar and octupolar components (25%, 24% and 21% respectively), with the rest predominantly divided between the $l = 1, m = 1$ and $l = 2, m = 2$ modes.

We note that no extra toroidal field component was required to fit the data. Toroidal fields have weaker contributions to circularly polarised profiles in low inclination angle stars, as Stokes V profiles are sensitive to the line-of-sight component of the magnetic field. Hence toroidal fields, particularly at high latitudes will have a weak contribution compared to radial field regions with similar strengths. Despite this it is still possible to exclude the presence of the type of dominant unidirectional azimuthal feature recovered in the maps of the more rapidly rotating G-type stars, HD 1237 (Alvarado-Gómez et al. 2015) and ξ Boo (Morgenthaler et al. 2012), as the signature would still be unambiguously detectable. ξ Boo is itself a relatively

low inclination star ($i = 28^\circ$), and shows a dominant toroidal field component at its highest activity states. Future observations of HD 147513 are necessary to reveal whether or not there is a similar change in the relative strength of the toroidal field component with its activity level.

We analysed how the uncertainty in the rotation period may affect the large scale field by reconstructing maps assuming periods of 8 and 12 days. The general structure remains very similar to that shown in Fig. 3.5 with the main features being either concentrated or smeared out with the shorter and longer period. The main difference is in the strength of the magnetic flux, which is 20–25% stronger and weaker in the maps derived for the 8-d and 12-d periods, respectively. This is expected as the phase coverage is more sparse in the 12-d map. Further observations spanning 16–20 days would be necessary to ascertain the period with greater accuracy.

3.7 Discussion and chapter conclusions

We have presented an analysis of spectropolarimetric data of the planet-hosting barium-rich G-dwarf, HD 147513. We measured an S-index of ~ 0.23 using the Ca II H & K lines and use this to compute a mean chromospheric activity index, $\log(R'_{\text{HK}})$, of -4.64 . We compared our HARPS spectra with archive FEROS Ca II H & K spectra acquired six years previously and find an identical level of chromospheric emission in the cores of the profiles, which indicates that the level of the activity remains more constant than the range of published $\log(R'_{\text{HK}})$ indices would suggest (Saffe et al. 2005).

We obtain robust magnetic field detections at all observed epochs and note that this star belongs to the group of low-moderate activity stars as classified in the “BCool” project. Marsden et al. (2014) find that stars with a similar S-index typically have a 60% chance of a definite magnetic field detection. In the same paper they conclude there is a smaller, 40% chance, of detecting a magnetic field in stars with similar $v \sin(i)$ values ($< 2 \text{ km s}^{-1}$). The chromospheric activity, $\log(R'_{\text{HK}}) = -4.64$, and longitudinal magnetic field measurements ($0.96 < B_\ell < 3.2 \text{ G}$) for HD 147513 reported here, indicate that it is fairly typical compared to the BCool star sample (Fig. 15 in Marsden et al. 2014). HD 147513 falls in the middle of the corresponding activity bin of the BCool sample, indicating that as with other cool stars its activity is determined predominantly by its age and rotation despite its unusual evolution and barium enrichment (see Sect. 3.2).

Stellar rotation periods can be estimated to about 20% accuracy based on their chromospheric $\log(R'_{\text{HK}})$ index. Our measurements indicate a period of 12.4 d. Least-squares fitting of sine-curves to the B_ℓ and RV measurements (Figs. 3.3 & 3.4) reveal rotation periods of 10.4 d and 9.3 d respectively, though longer periods cannot be excluded. Fitting both together we find a rotation period of 10 d, which is the period adopted for the ZDI reconstruction presented in Sect. 3.6. We can therefore definitively exclude the 4.7 d reported by Mayor et al. (2004). A 10 d period is consistent with an age of $\sim 0.5 \text{ Gyr}$ using different activity saturation-threshold braking laws (Krishnamurthi et al. 1997; Reiners & Mohanty 2012). However, as large spreads are found in rotation periods of stars with

similar masses at these ages, it is simply noted that the gyro-chronological age derived for HD 147513 is consistent with the age of the UMa group.

Significantly longer periods (> 20 d) are ruled out due to the relatively high values of the chromospheric and coronal activity indices. The low $v \sin(i)$ value of 1.5 km s^{-1} is therefore likely due to a low inclination angle. With a period of 10 d we compute an inclination angle of 18° , which is in good agreement with 15_{-6}^{+8} degrees, as determined by [Watson et al. \(2010\)](#). Based on the maximum and minimum likely values of the radius, rotation period estimates and $v \sin(i)$ measurements, we find that the inclination can vary between $10\text{--}30^\circ$.

Even though a good quality time series of HD 147513 was acquired, as the period covered appears to be less than the rotation period of the star, we cannot definitively measure the rotation period of the star using ZDI as done in previous studies (e.g., [Jeffers et al. 2014b](#); [Alvarado-Gómez et al. 2015](#)). The map of the large-scale surface magnetic field presented in Sect. 3.6 is produced using our best estimate of the period and the technique of ZDI. We investigate how the large scale structure is affected by the rotation period, varying the period between 8–12 days, and find that some aspects of the large scale field change (e.g., the magnetic field strength and energy). Regardless of the rotation period used no significant toroidal component is required and the Stokes V signatures can be adequately fit assuming a purely poloidal field. This is different to the ZDI analysis of the G8V star, HD 1237 ($P_{\text{rot}} = 7$ d); which shows a dominant toroidal field ([Alvarado-Gómez et al. 2015](#)). While a strong toroidal field of the type detected on HD 1237 can be definitively excluded in HD 147513, the reconstruction is not very sensitive to weaker toroidal field components. Furthermore, as shown in other stars with similar activity levels, e.g., ϵ Eri and ξ Boo, the toroidal field component may have a stronger contribution at other epochs ([Jeffers et al. 2014b](#); [Morgenthaler et al. 2012](#)).

We computed the expected RV signature of the planet and found this to be almost constant over the 8 d timescale probed by our observations. As noted, the measured RV variations show a similar modulation to that traced by B_ℓ and are consistent with the same period. It is therefore likely that the RV variability is stellar in origin and due to magnetic activity, e.g., due to a dark spot aligned with the dipolar field. Both surface spots/plage and broadening effects due to the small scale local field, are found to affect the shape of the line profiles albeit in different ways (e.g., [Dumusque et al. 2014](#); [Hebrard et al. 2014](#)).

We calculate a Root Mean Square (RMS) of 9 m s^{-1} in these RV measurements. This is 50% larger than the reported $\sigma(O - C)$ of $\pm 5.7 \text{ m s}^{-1}$ ([Mayor et al. 2004](#)). Those measurements were based on 30 observations acquired over 1690 d whereas ours have been collected on a timescale closer to the star's rotation period. The K -velocity amplitude due to the planetary orbit is $29.3 \pm 1.8 \text{ m s}^{-1}$. This is a higher level of activity jitter than previously reported and further observations would be necessary to confirm whether this level of jitter is typical for the star but would likely not significantly affect the planet detection.

We note that the RV RMS we measure is of the same order as that reported in the moderately active M2.5 dwarf, GJ 674, by [Bonfils et al. \(2007\)](#). Whereas the spot causing the RV variability in GJ 674 shows a clear correlation with chromospheric and photo-

spheric spectral indices, no such correlation is found for HD 147513. In HD 147513, the chromospheric activity index remains constant over the eight-day span of the observations. This different relationship between the RV signature of the active region and the chromospheric activity index may be due to the different spectral types of the stars, the lower chromospheric activity index of HD 147513, or differences in the geometric properties of the spot signatures in these two stars. Further studies combining spectropolarimetry with velocimetry are necessary to better understand the dependence of RV jitter on these parameters.

Chapter 4

Simulating the environment around planet-hosting stars – I. Coronal structure

Abstract

We present the results of a detailed numerical simulation of the circumstellar environment around three exoplanet-hosting stars. A modern global magnetohydrodynamic (MHD) model is considered that includes Alfvén wave dissipation as a self-consistent coronal heating mechanism. This chapter contains the description of the numerical set-up, evaluation procedure, and the simulated coronal structure of each system (HD 1237, HD 22049, and HD 147513). The simulations are driven by surface magnetic field maps, recovered with the observational technique of Zeeman-Doppler imaging. A detailed comparison of the simulations is performed, where two different implementations of this mapping routine are used to generate the surface field distributions. Quantitative and qualitative descriptions of the coronae of these systems are presented, including synthetic high-energy emission maps in the extreme ultra-violet (EUV) and soft X-ray (SXR) ranges. Using the simulation results, we are able to recover similar trends as in previous observational studies, including the relation between the magnetic flux and the coronal X-ray emission. Furthermore, for HD 1237 we estimate the rotational modulation of the high-energy emission that is due to the various coronal features developed in the simulation. We obtain variations during a single stellar rotation cycle of up to 15% for the EUV and SXR ranges. The results presented here will be used in the following chapter to self-consistently simulate the stellar winds and inner astrospheres of these systems.

4.1 Chapter organization

This chapter contains the results of a detailed numerical simulation of the circumstellar environment around three late-type exoplanet-hosts (HD 1237, HD 22049 and HD 147513), using a 3D MHD model. The simulations are driven by the radial component of the large-scale surface magnetic field in these stars, which have been recovered using two different

implementations of ZDI (Sect. 4.2). All three systems have similar coronal (X-ray) activity levels. While these are more active than the Sun, they would be classified as moderately active stars and well below the X-ray / activity saturation level (Pizzolato et al. 2003; Wright et al. 2011). A description of the numerical set-up is provided in Sect. 4.3, and the results are presented in Sect. 4.4. Section 4.5 contains a discussion in the context of other studies, and the conclusions of our work are summarized in Sect. 4.6.

4.2 Large-scale magnetic field maps

HD 1237, HD 147513, and HD 22049 are cool main-sequence stars (G8, G5, and K2, respectively) with relatively slow rotation rates ($P_{\text{rot}} \sim 7 - 12$ d). Each of these systems hosts a Jupiter-mass planet ($M_p \sin(i) > M_{\text{J}}^*$), with orbital separations similar to the solar system planets (Hatzes et al. 2000; Naef et al. 2001; Mayor et al. 2004; Benedict et al. 2006). Table 4.1 contains a summary of the relevant astrophysical parameters for each system, taken from various observational studies.

Table 4.1: Planet-hosting systems and their observational properties.

Star ID	S. Type	T_{eff} [K]	R_* [R_{\odot}]	M_* [M_{\odot}]	P_{rot} [d]	i [$^{\circ}$]	Age [Gyr]	Activity		$M_p \sin i$ [M_{J}^*]	a [AU]	$\langle \epsilon_{Br} \rangle$	
								$\log(R'_{\text{HK}})$	$\log(L_x)$			ZDI	SH-ZDI
HD 1237 ^a	G8V	5572	0.86	1.00	7.00	~ 50	~ 0.88	-4.38	29.02	3.37	0.49	4.65	30.77
HD 22049 ^b	K2V	5146	0.74	0.86	11.68	~ 45	~ 0.44	-4.47	28.22	1.55	3.39	2.32	30.66
HD 147513 ^c	G5V	5930	0.98	1.07	10.00	~ 20	~ 0.45	-4.64	28.92	1.21	1.32	- \ddagger	6.21

The values listed in Cols. 2–12 are taken from previous studies of each system and references therein: ^(a) Naef et al. (2001); Alvarado-Gómez et al. (2015) – ^(b) Drake & Smith (1993); Hatzes et al. (2000); Benedict et al. (2006); Jeffers et al. (2014b) – ^(c) Mayor et al. (2004); Hussain et al. (2016). The last two columns contain the (radial) magnetic energy density, $\epsilon_{Br} = B_r^2 / 8\pi$, averaged over the visible surface of the star, and estimated from the standard ZDI and the spherical harmonics implementation (SH-ZDI).

\ddagger : As a result of the low inclination and simple field geometry, the standard ZDI reconstruction was not possible in this case (see Brown et al. 1991).

Previous works have recovered the large-scale magnetic field on the surfaces of these stars by applying ZDI to time-series of circularly polarised spectra (Jeffers et al. 2014b; Alvarado-Gómez et al. 2015; Hussain et al. 2016). For the stars included in this work, this has been done with the spectropolarimeter NARVAL at the Telescope Bernard Lyot (Aurière 2003), and the polarimetric mode (Piskunov et al. 2011) of the HARPS echelle spectrograph (Mayor et al. 2003) on the ESO 3.6 m telescope at La Silla Observatory. For consistency, the ZDI maps included in the simulations have been reconstructed using data from the same instrument[†] (i.e., HARPSpol).

For the magnetic field mapping procedure, we considered two different approaches; the classic ZDI reconstruction, in which each component of the magnetic field vector is

[†]Therefore, for HD 22049 (ϵ Eridani) we only consider the January 2010 dataset (see Piskunov et al. 2011; Jeffers et al. 2014b).

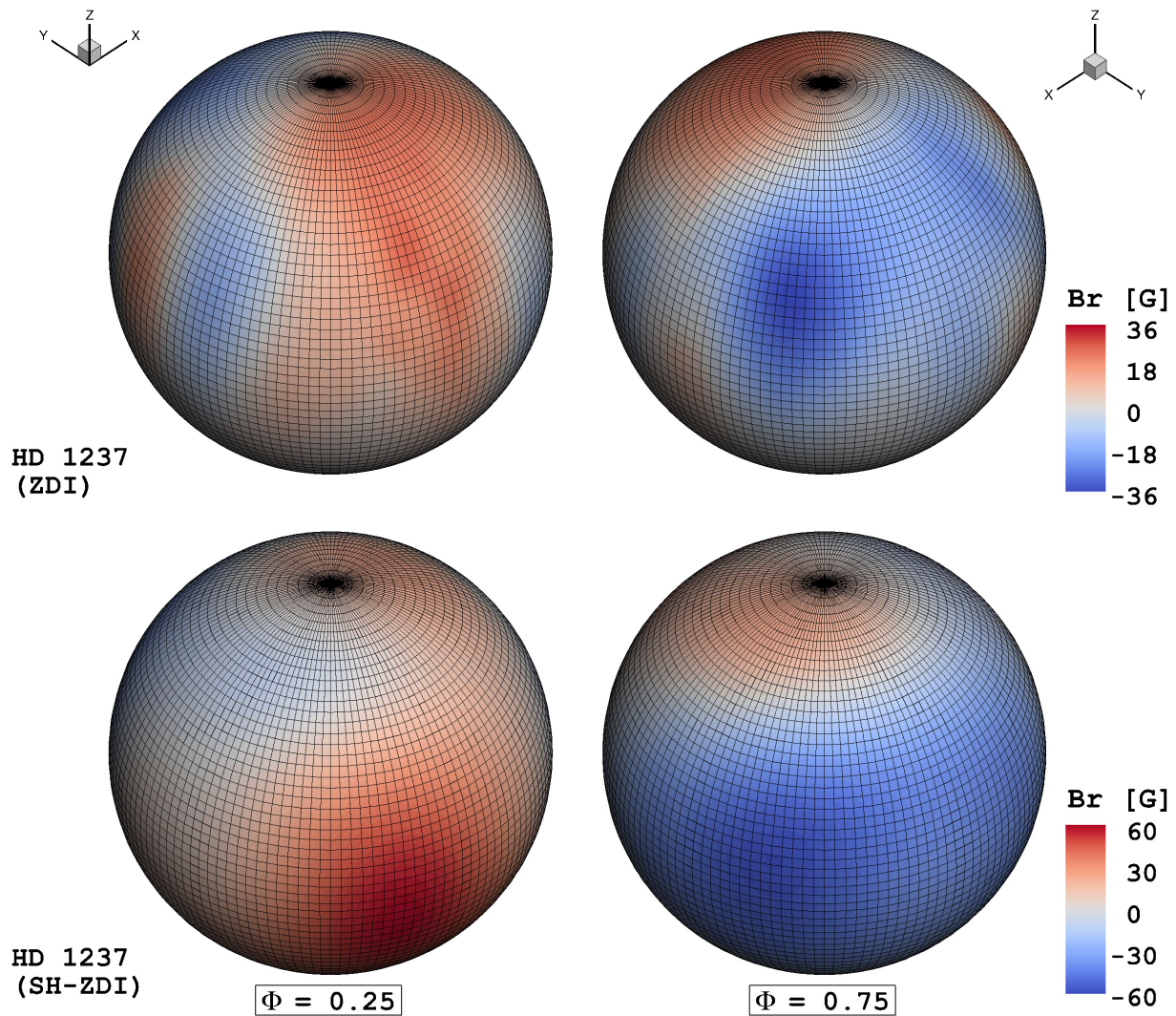


Figure 4.1: Surface radial magnetic field maps of HD 1237. A comparison between the standard ZDI (*top*) and the SH-ZDI (*bottom*) is presented. The colour scale indicates the polarity and the field strength in Gauss (G). Note the difference in the magnetic field range for each case. The stellar inclination angle ($i = 50^\circ$) is used for the visualisations.

decomposed into a series of independent magnetic-image pixels (Brown et al. 1991; Donati & Brown 1997), and the spherical harmonics decomposition (SH-ZDI), where the field is described by the sum of a potential and a toroidal component and each component is expanded in a spherical-harmonics basis (see Hussain et al. 2001; Donati et al. 2006). Both procedures are equivalent, leading to very similar field distributions and associated fits to the spectro-polarimetric data. However, as described by Brown et al. (1991), ZDI is not able to properly recover very simple field geometries (i.e., dipoles) and is more suitable for complex (spotted) magnetic distributions. This limitation is removed in the SH-ZDI implementation. Both procedures are restricted by the inclination angle of the star, and therefore a fraction of the surface field that cannot be observed is not recovered

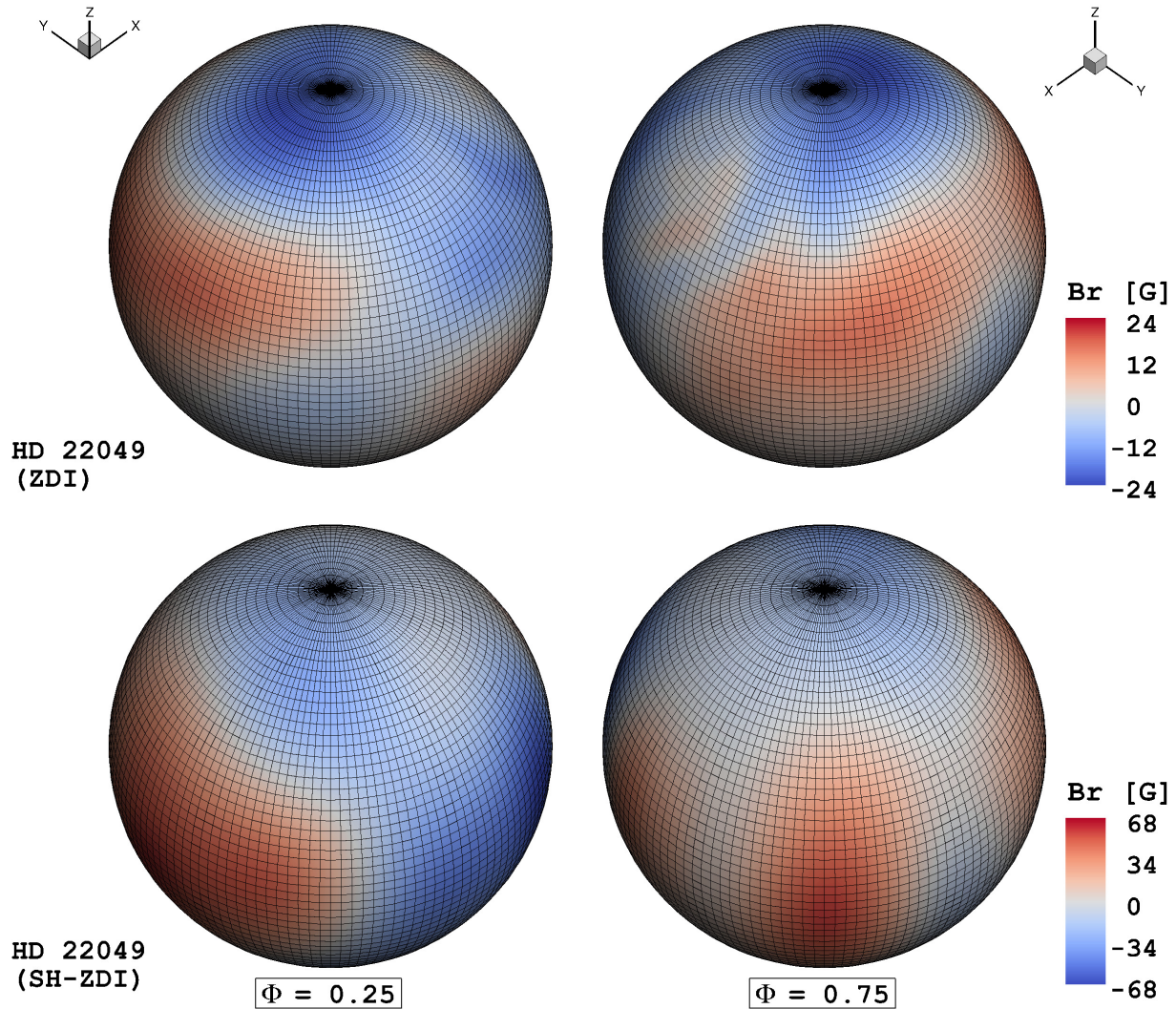


Figure 4.2: Surface radial magnetic field maps of HD 22049. A comparison between the standard ZDI (*top*) and the SH-ZDI (*bottom*) is presented. The colour scale indicates the polarity and the field strength in Gauss (G). Note the difference in the magnetic field range for each case. The stellar inclination angle ($i = 45^\circ$) is used for the visualisations.

in the maps. To correct for this effect, previous numerical studies have completed the field distribution by a reflection of the ZDI map across the equatorial plane (e.g., [Cohen et al. 2010](#)). More recently, [Vidotto et al. \(2012\)](#) have included complete symmetric and antisymmetric SH-ZDI maps to show that the map incompleteness has a minor effect on their simulation results. However, for the simulations performed here, which include the latest implementation of BATS-R-US, this may not be the case. A stronger effect may be expected on the overall coronal structure, as the mechanism for the coronal heating and the wind acceleration is directly related to the field strength and topology (e.g., Alfvén waves, see [van der Holst et al. 2014](#)).

Figures 4.1 and 4.2 show a comparison between the reconstruction procedures applied to HD 1237 and HD 22049, respectively. In general, the maps obtained using ZDI show a more complex and weaker field distribution than the SH-ZDI, where a smoother field topology is obtained. While there are similarities in the large-scale structure, discrepancies are obtained in terms of the amount of detail recovered in each case. These differences arise as a consequence of the constraints imposed for completing the SH-ZDI maps, which are all pushed to symmetric field distributions.

In general, the spatial resolution of the SH-ZDI maps depends on the maximum order of the spherical harmonics expansion (l_{\max}). For each case this is selected in such a way that the lowest possible l_{\max} value is used, while achieving a similar goodness-of-fit level (reduced χ^2) as the classic ZDI reconstruction (HD 1237: $l_{\max} = 5$, HD 22049: $l_{\max} = 6$, HD 147513: $l_{\max} = 4$). Higher values of l_{\max} would not alter the large-scale distribution, but would introduce additional small-scale field without significantly improving the goodness-of-fit. This step is fundamental for a consistent comparison because the final recovered field strengths depend on this. All these differences significantly affect the coronal and wind structure given their dependence with the field coverage and the amount of magnetic energy available in each case (Table 4.1).

The standard ZDI reconstruction was not possible for HD 147513 because of its low inclination angle ($i \sim 20^\circ$) and fairly simple large-scale topology. Therefore, we only considered the SH-ZDI map presented in Fig. 4.3 for this system previously published by Hussain et al. (2016).

To evaluate our numerical results, we performed two additional simulations taking the Sun as reference. The magnetic field distributions during solar minimum (Carrington rotation 1922, end of cycle 22), and solar maximum (Carrington rotation 1962, during cycle

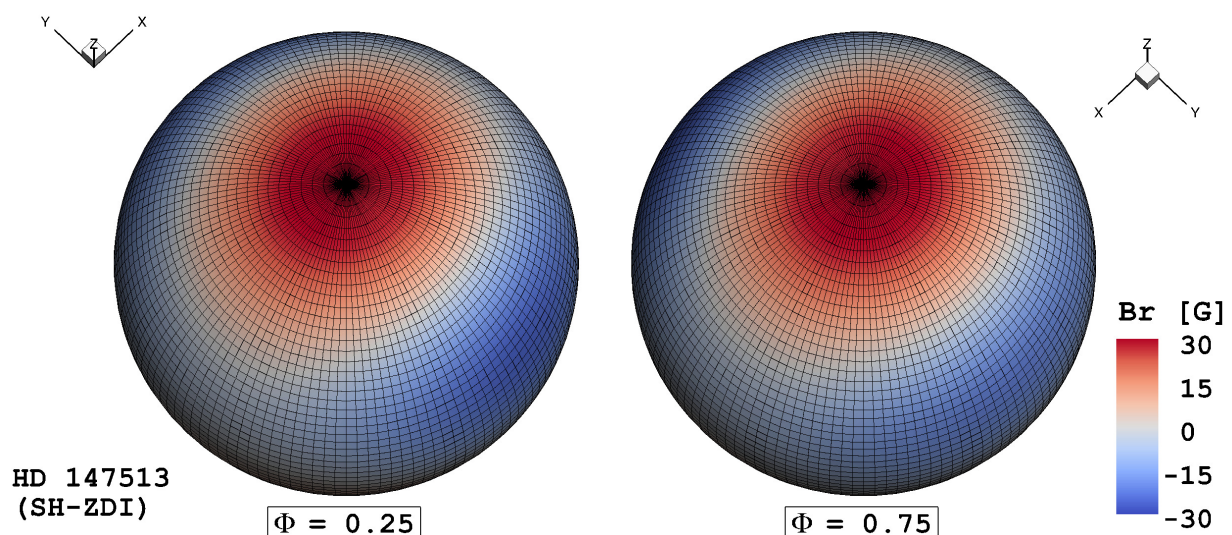


Figure 4.3: Surface radial magnetic field maps of HD 147513 using SH-ZDI. Two rotational phases (Φ) are presented. The stellar inclination angle ($i = 20^\circ$) is used for the visualisations.

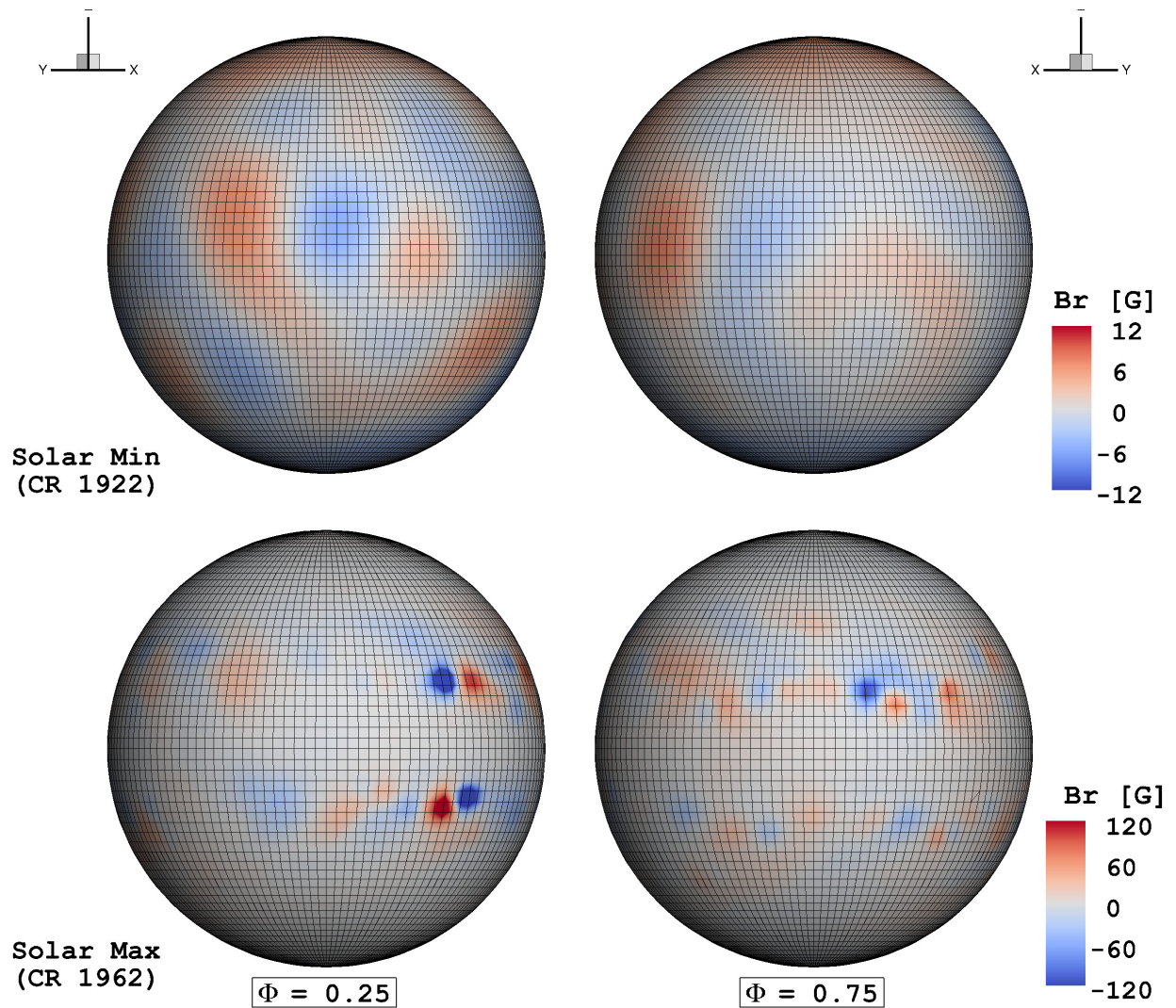


Figure 4.4: Surface radial magnetic field maps of the Sun during activity minimum (CR 1922, top) and maximum (CR 1962, bottom) taken by SOHO/MDI. Note the difference in the magnetic field range for each case. An inclination angle $i = 90^\circ$ is used for the visualisations.

23) were considered for this purpose. The large-scale magnetic field was taken from synoptic magnetograms, generated by the Michelson Doppler Imager instrument (MDI, Scherrer et al. 1995) on board the *Solar and Heliospheric Observatory* spacecraft (SOHO, Domingo et al. 1995). Figure 4.4 shows the comparison between the global magnetic field distribution for these activity epochs. During activity minimum, weak magnetic regions (a few Gauss) tend to be sparsely distributed across the entire solar surface (no preferential location for these regions is observed). Stronger small-scale magnetic fields, up to two orders of magnitude, can be found during activity maximum. In this case the dominant fields are highly concentrated in bipolar sectors (active regions) and are located mainly in two latitudinal belts at $\sim \pm 30^\circ$. Still, weaker magnetic fields can be found along the entire solar surface.

Finally, as is shown in Figs. 4.1 to 4.4, the numerical grid for all the input surface magnetic field distributions is the same. Therefore, the resolution of the solar coronal models was adapted to match the optimal resolution of the stellar simulations. In this way, a more consistent comparison of the results can be performed. The surface grid resolution ($\sim 10^{-2} R_*$) is sufficient to resolve the magnetic structures on the stellar ZDI / SH-ZDI maps entirely. However, in the solar case the internal structure of the active regions and the small-scale structures are not resolved. The effect of this limited resolution in magnetic field maps for solar simulations has been investigated previously by [Garraffo et al. \(2013\)](#). They found that the structure of the stellar wind is less sensitive to this factor than the coronal structure and associated emission (e.g., EUV and X-rays). This will be explored in more detail in the evaluation procedure, presented in Sect. 4.4.1.

4.3 3D MHD numerical simulation

The numerical simulations presented here were performed using the 3D MHD code BATS-R-US ([Powell et al. 1999](#)) as part of the Space Weather Modeling Framework (SWMF, [Tóth et al. 2012](#)). As discussed previously by [Cohen et al. \(2014\)](#), the SWMF encompasses a collection of physics-based models for different regimes in solar and space physics. These can be considered individually or can be coupled together to provide a more realistic description of the phenomenon or domain of interest. For the systems considered here, we included and coupled two overlapping domains to obtain a robust combined solution. The results we present here correspond to the stellar corona domain (SC module). In Chapter 5 we will describe the wind and the inner astrosphere (IH module). The solution for each domain was obtained using the most recent version of the SWMF modules[†].

The stellar corona domain extends from the base of the chromosphere ($\sim 1 R_*$) up to $30 R_*$. A 3D potential field extrapolation above the stellar surface was used as the initial condition. This initial extrapolation was performed based on the photospheric radial magnetic field of the star (e.g., ZDI maps, Sect. 4.2). In addition to the surface magnetic field distribution, this module requires information about the chromospheric base density, n_0 , and temperature, T_0 , as well as the stellar mass, M_* , radius, R_* and rotation period, P_{rot} . This differs from previous ZDI-driven numerical studies, where these thermodynamic boundary conditions were set to coronal values and were therefore not obtained self-consistently in the simulations ([Cohen et al. 2011b](#); [Vidotto et al. 2012](#); [Vidotto et al. 2015](#)).

For the stars considered here, we assumed solar values for the chromospheric base density ($n_0 = 2.0 \times 10^{16} \text{ m}^{-3}$), and temperature ($T_0 = 5.0 \times 10^4 \text{ K}$). This is justified because these systems, while more active than the Sun, are still within the X-ray un-saturated regime and the physical assumptions behind the coronal structure and the solar wind acceleration in the model are therefore more likely to hold. This assumption permits a consistent comparison with the solar case and between the systems considered. The remaining initial required parameters for each star are listed in Table 4.1. For the solar

[†]Code version 2.4

runs we used the sidereal rotation rate of 25.38 days (Carrington rotation).

We used a non-uniform spherical grid, dynamically refined at the locations of magnetic field inversion, which provides a maximum resolution of $\sim 10^{-3} R_*$. The numerical simulation evolves until a steady-state solution is achieved. Coronal heating and stellar wind acceleration, due to Alfvén wave turbulence dissipation, were calculated self-consistently. Electron heat conduction and radiative cooling effects are also taken into account. For more details we refer to Sokolov et al. (2013) and van der Holst et al. (2014). From this final solution, all the physical properties, such as number density, n , plasma temperature, T , velocity, \mathbf{u} and magnetic field, \mathbf{B} , can be extracted. We present the simulation results in the following section.

4.4 Results

We performed a detailed evaluation of the solution sets for the solar minimum and maximum cases in Sect. 4.4.1. Sections 4.4.2 to 4.4.4 contain the simulation results of the coronal structure for the stars considered. In each case we present the distribution of the thermodynamic conditions (n , T) and the magnetic energy density (ε_{Br}), which is associated with the radial field. A common colour scale is adopted for all stars to facilitate comparison[†].

In addition, synthetic coronal emission maps were generated at SXR and EUV wavelengths. This was done by integrating the square of the plasma density times the emissivity response function of a particular instrument along the line of sight towards the observer. In the SXR range we considered the specific response function of the AlMg filter of the *Soft X-Ray Telescope* (SXT), on board the *Yohkoh* spacecraft, to synthesise images in the 2 to 30 Å range (0.25–4.0 keV, *red* images). For the EUV range we used the sensitivity tables of the *Extreme ultraviolet Imaging Telescope* (EIT), on board the *Solar and Heliospheric Observatory* (SOHO), which led to narrow-band images centred at the Fe IX/X 171 Å (*blue*), Fe XII 195 Å (*green*), and Fe XV 284 Å (*yellow*) lines.

The coronal emission at these wavelengths has been extensively studied in the solar context and also served to calibrate the results from the SWMF in various works (see Garraffo et al. 2013; van der Holst et al. 2014). This procedure also allows the direct comparison of the synthetic images that are generated for different stars. For HD 1237 and HD 22049 we additionally compared the results driven by the different maps of the large-scale magnetic field (Sect. 4.2).

4.4.1 Evaluation of the solar case

The simulation results for the Sun are presented in Figs. 4.5 and 4.6. The synthetic images provide a fairly good match to EUV/SXR solar observations obtained during 1997 May 07

[†]Except in the magnetic energy density distribution for the solar minimum case (Fig. 4.5), where the range is decreased by a factor of 10.

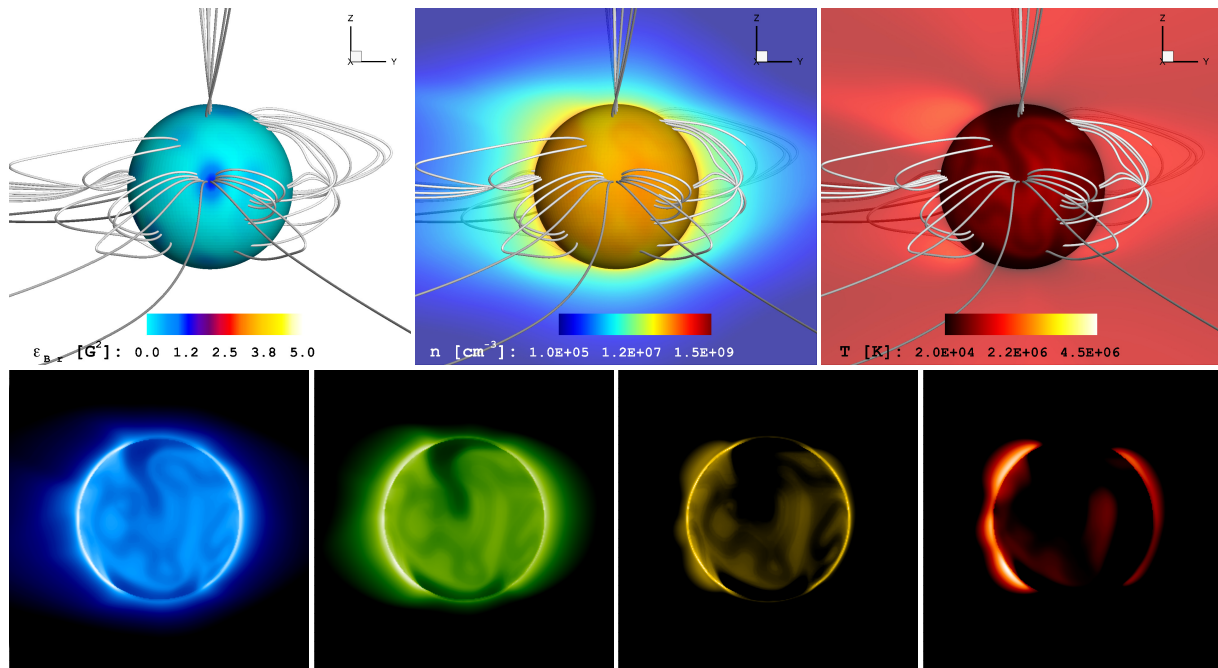


Figure 4.5: Simulation results for the coronal structure of the Sun during activity minimum (CR 1922). The *upper panels* contain the distribution of the magnetic energy density (ϵ_{Br} , left), the number density (n , middle) and temperature (T , right). For the last two quantities, the distribution over the plane $y = 0$ is presented. The sphere represents the stellar surface and selected 3D magnetic field lines are shown in white. Note the change of scale for ϵ_{Br} . The *lower images* correspond to synthetic coronal emission maps in EUV (blue: 171 Å, green: 195 Å, yellow: 284 Å) and SXR (red: 2–30 Å). The perspective is preserved in all panels with $i = 90^\circ$.

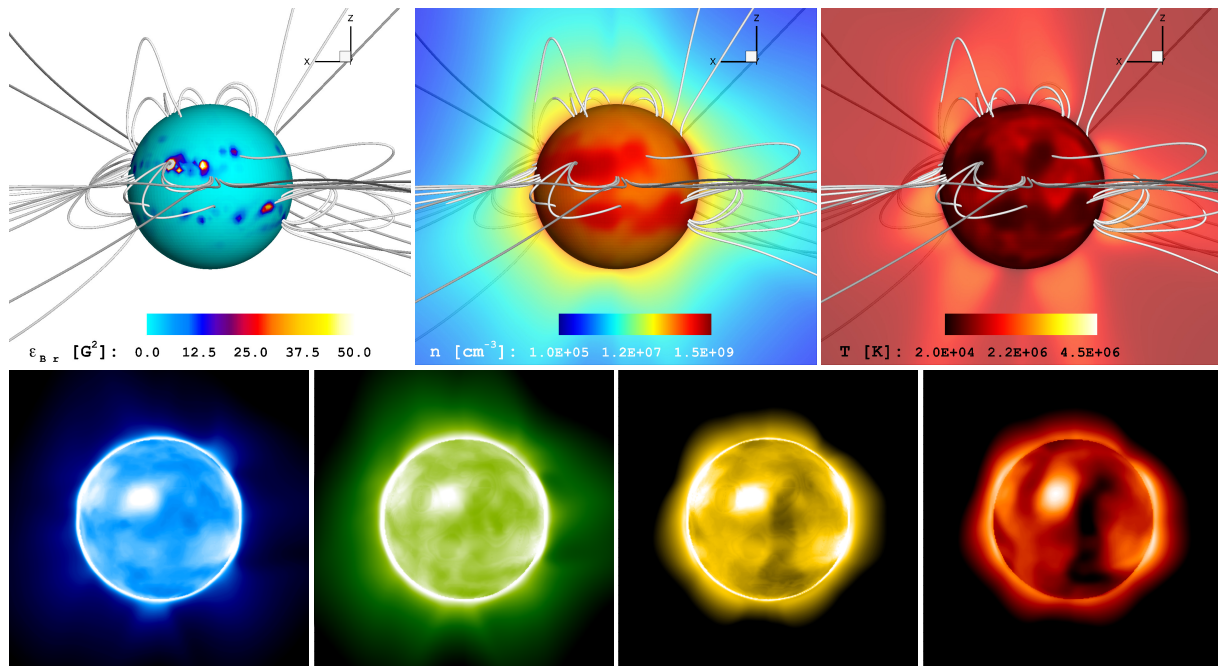


Figure 4.6: Simulation results for the coronal structure of the Sun during activity maximum (CR 1962). See caption of Fig. 4.5.

(activity minimum, Fig. 4.5) and 2000 May 10 (activity maximum, Fig. 4.6)[†]. The steady-state solution properly recovers the structural differences for both activity states. An open-field-dominated corona appears in the solar minimum case, displaying coronal holes near the polar regions of the Sun. In turn, the solar maximum case shows mainly close-field regions across the solar disk, with almost no open field-line locations. This will have implications for the associated solar wind structure, which will be discussed in Chapter 5.

In general, the differences in the magnetic activity or complexity are clearly visible in the steady-state solution. As expected, the thermodynamic structure of the corona and the associated high-energy emission show large variation in both activity states. To evaluate the simulation results, we need to quantitatively compare the numerical solutions for the Sun to the real observations (i.e., based on the SXR/EUV data). As was discussed in Sect. 4.2, this is particularly important as the solar simulations presented here were performed with limited spatial resolution (see also Garraffo et al. 2013). To do this, we compared the simulation results to archival *Yohkoh*/SXT and SOHO/EIT data[‡] that cover both activity epochs (Carrington rotations 1922 and 1962).

For the SXR range, we used the daily averages for the solar irradiance at 1 AU, described in Acton et al. (1999), and computed a mean value for each Carrington rotation. This leads to $1.02 \times 10^{-5} \text{ W m}^{-2}$ for solar minimum, and $1.21 \times 10^{-4} \text{ W m}^{-2}$ for solar maximum, in the 2–30 Å range. In terms of SXR luminosities, these values correspond to $2.86 \times 10^{25} \text{ ergs s}^{-1}$ and $3.42 \times 10^{26} \text{ ergs s}^{-1}$, respectively. However, more recent estimates, presented by Judge et al. (2003), lead to higher values in the SXR luminosities during the solar activity cycle (i.e., $10^{26.8} \text{ ergs s}^{-1}$ during activity minimum, and $10^{27.9} \text{ ergs s}^{-1}$ for activity maximum). From the steady-state solutions, we simulated the coronal emission in the SXR band with the aid of the emission measure distribution $EM(T)$ (Sect. 4.5.1) and following the procedure described in Sect. 4.5.2. This yields simulated values of $2.79 \times 10^{26} \text{ ergs s}^{-1}$ and $2.49 \times 10^{27} \text{ ergs s}^{-1}$ during activity minimum and maximum, respectively.

A similar procedure was applied for the EUV range. Images acquired by the EIT instrument during both activity periods were used for this purpose. We considered three full-disk images per day (one for each EUV channel, excluding the 304 Å bandpass) for a total of 87 images per rotation. After the image processing, we performed temperature and EM diagnostics, using the standard SolarSoftWare (SSW) routines for this specific instrument[†]. This led to a rough estimate of both parameters based on a pair (ratios) of EUV images. We used the temperature-sensitive line ratios of Fe XII (195 Å) / Fe IX/X (171 Å) and Fe XV (284 Å) / Fe XII (195 Å) for a combined sensitivity range of $0.9 \text{ MK} < T < 2.2 \text{ MK}$. We refer to Moses et al. (1997) for further information. As with the SXR range, we computed the mean observed values of these parameters for both rotations and compared them with simulated quantities derived from the synthetic EUV emission maps. The obtained values are presented in the Table 4.2.

[†]See <http://helioviewer.org/> for a quick-look comparison with observations from various instruments during these dates.

[‡]Available at the [Virtual Solar Observatory \(VSO\)](#)

[†]More information can be found in the [EIT user guide](#)

Table 4.2: Evaluation of the solar simulations in the EUV range.

Parameter	Min (Obs)		Min (Sim)		Max (Obs)		Max (Sim)	
	195/171	284/195	195/171	284/195	195/171	284/195	195/171	284/195
$\langle T \rangle [\times 10^6 \text{ K}]$	1.06	1.77	1.14	1.63	1.13	1.79	1.16	1.66
$\langle EM \rangle [\times 10^{26} \text{ cm}^{-5}]$	4.51	5.08	1.19	0.98	8.42	14.9	5.52	5.06

The listed values correspond to averages over an entire rotation, obtained from the observations (Obs) and the simulations (Sim). The two filter wavelength-ratios (in Å) used for the parameters estimation are indicated in each case.

We also compared the synthetic EUV emission to archival data from the *Geostationary Operational Environmental Satellite, GOES-13/EUVS* instrument[‡]. These measurements span different solar activity periods in comparison to the epochs considered in the simulations (CR 1922 and CR 1962). Therefore, we interpret these quantities as nominal values for the EUV variation during minimum and maximum of activity. We considered *GOES-13* data from channels A (50–150 Å) and B (250–340 Å), leading to average EUV luminosities for activity minimum and maximum of $\sim 2\text{--}5 \times 10^{27} \text{ erg s}^{-1}$ and $\sim 1 \times 10^{28} \text{ erg s}^{-1}$, respectively. The simulated coronal emission, synthesised in the same wavelength ranges, agrees very well with the observations, leading to $\sim 1.4 \times 10^{27} \text{ erg s}^{-1}$ during solar minimum, and $\sim 1.3 \times 10^{28} \text{ erg s}^{-1}$ at solar maximum.

The results from the evaluation procedure are consistent between the EUV and SXR ranges, showing a reasonable match between the simulations and the overall structure of the solar corona for both activity periods. Good agreement is obtained for the low-temperature region (195/171 ratio), with differences below +8% in the mean temperature for both epochs. The sign indicates the relative difference between the simulation (Sim) and the observations (Obs). A similar level of agreement (with reversed sign) is achieved for the hotter component of the corona (284/195 ratio). Furthermore, the simulated SXR emission properly recovers the nominal estimates for both activity periods, with resulting values lying between the observational estimates of [Acton et al. \(1999\)](#) and [Judge et al. \(2003\)](#). In a similar manner, the fiducial EUV luminosities during minimum and maximum of activity are well recovered. However, we note here that He II 304 Å line tends to dominate the *GOES-13* B bandpass. This line is overly strong compared with expectations based on collisional excitation (e.g., [Jordan 1975](#); [Pietarila & Judge 2004](#)), and therefore our model spectrum is expected to significantly under-predict the observed flux. That we obtain reasonably good agreement is likely a result of our emission measure distribution being too high at transition region temperatures (see Sec. 4.5.1, Fig. 4.13). In contrast, larger discrepancies are found for the *EM* distribution (over the sensitivity range of the EIT filters) for both coronal components. During activity minimum, differences of up to factors of -3.8 and -5.2 appear for the low- and high-temperature corona, respectively. Slightly smaller difference factors prevail during activity maximum for both components, reaching -1.5 and -3.0 , respectively.

[‡]See <http://www.ngdc.noaa.gov/stp/satellite/goes/>.

Some of these discrepancies can be attributed to assumptions of the model or its intrinsic limitations (see [van der Holst et al. 2014](#)). In this case, as discussed previously in Sect. 4.2, they arise mostly from the spatial resolution of the surface field distributions. The overall lower densities of the corona and the imbalance of emission at different coronal temperatures are directly related with the amount of confining loops and consequently with the missing (un-resolved) surface magnetic field and its complexity. In addition, as we show in the Sect. 4.5.2, the simulated stellar X-ray and EUV luminosities appear to be underestimated. This may indicate that some adjustments are required in the coronal heating mechanism when applying this particular model to resolution-limited surface field distributions (e.g., ZDI data). Further systematic work will be performed in this direction, analogous to the numerical grid presented in [Cohen & Drake \(2014\)](#), including also other coronal emission ranges covered by current solar instrumentation (e.g., *Solar Dynamics Observatory*, [Pesnell et al. 2012](#)).

4.4.2 HD 1237 (GJ 3021)

The coronal structure obtained for HD 1237 shows a relatively simple topology. Two main magnetic energy concentrations, associated with the field distributions shown in Fig. 4.1, dominate the physical properties and the spatial configuration in the final steady-state solution. The outer parts of these regions serve as foot-points for coronal loops of different length-scales. Close to the north pole an arcade is formed, which covers one of the main polarity inversion lines of the large-scale magnetic field.

As can be seen in Figs. 4.7 and 4.8, denser and colder material appears near these lines on the surface, resembling solar prominences or filaments. Larger loops extending higher in the corona connect the opposite ends of both magnetic regions. These loops confine coronal material through magnetic mirroring, which increases the local density and temperature of the plasma. Some of this heated plasma is visible in the synthetic emission images of the lower corona (*bottom* panels of Figs. 4.7 and 4.8).

Inside the two large magnetic energy regions, the coronal field lines are mainly open. This leads to the generation of coronal holes, where the material follows the field lines and leaves the star. In turn, this decreases the local plasma density and temperature in both regions, making them appear dark in the coronal emission maps. These coronal holes will have a strong influence on the structure of the stellar wind and the inner astrosphere. This will be discussed in detail in the next chapter.

In terms of the field distribution (i.e., ZDI/SH-ZDI, Sect. 4.2), the global structure of the corona of HD 1237 is similar in both cases. This was expected since the largest features in the surface field distributions are common in both procedures. However, as can be seen directly in Figs. 4.7 and 4.8, several qualitative and quantitative differences appear in various aspects of the resulting coronal structure. First, despite having the same thermodynamic base conditions, the SH-ZDI solution leads to a larger corona with an enhanced high-energy emission. This is a consequence of the available magnetic energy to heat the plasma, in combination with the size of the coronal loops (and therefore, the amount of material trapped by the field).

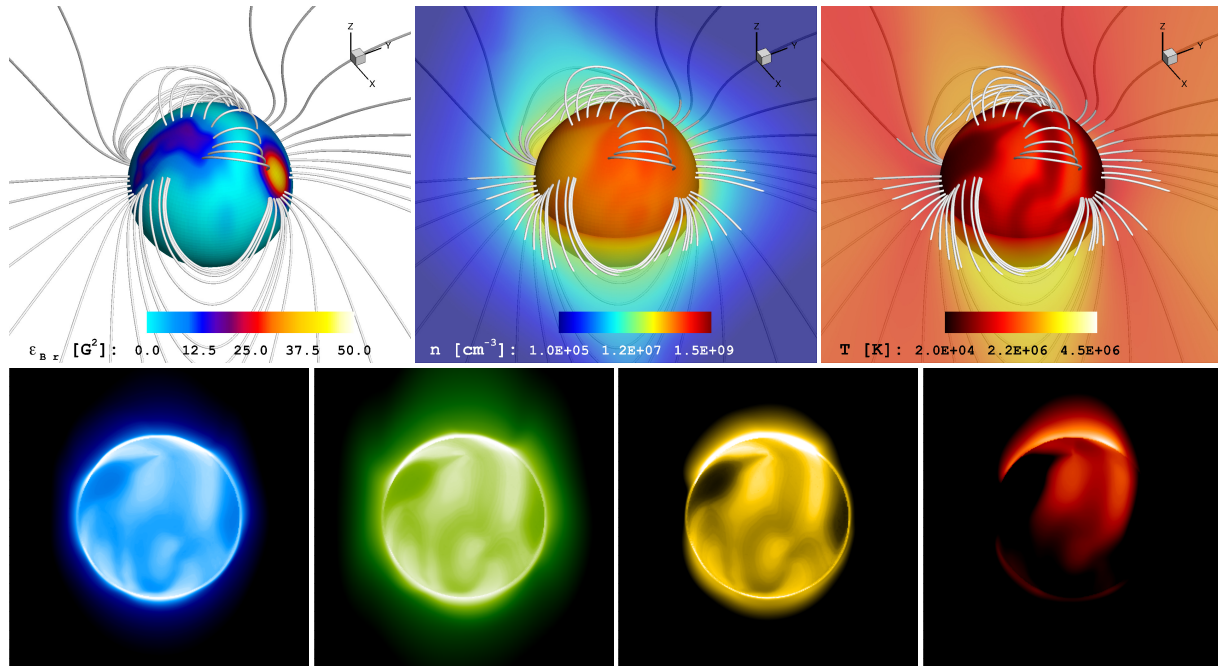


Figure 4.7: Simulation results for the coronal structure of HD 1237 driven by the ZDI large-scale magnetic field map. The *top* panels contain the distribution of the magnetic energy density ($\epsilon_{B,r}$, *left*), the number density (n , *middle*) and temperature (T , *right*). For the last two quantities, the distribution over the equatorial plane $z = 0$ is presented. The sphere represents the stellar surface and selected 3D magnetic field lines are shown in white. The *bottom* images correspond to synthetic coronal emission maps in EUV (*blue*: 171 Å, *green*: 195 Å, *yellow*: 284 Å) and SXR (*red*: 2–30 Å). The perspective is preserved in all panels with $i = 50^\circ$.

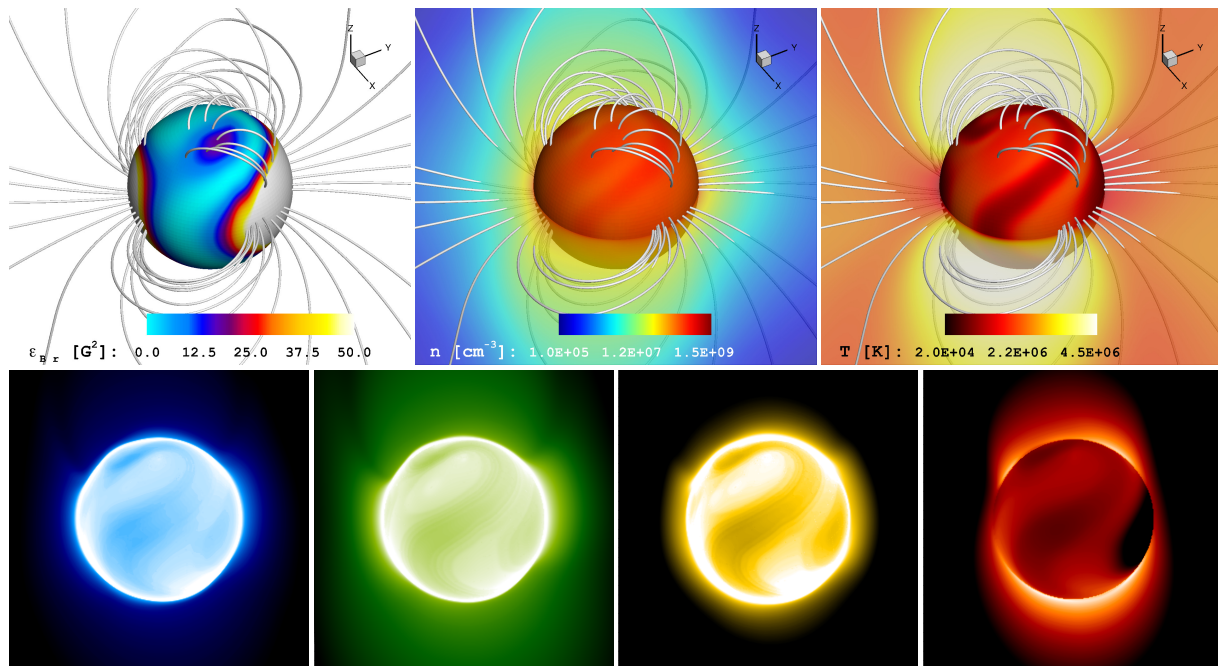


Figure 4.8: Simulation results for the coronal structure of HD 1237 driven by the SH-ZDI large-scale field map. See caption of Fig. 4.7. The 3D magnetic field lines are calculated in the same spatial locations as in the solution presented in Fig. 4.7.

Table 4.3: Average physical properties of the inner corona (IC) region (from 1.05 to 1.5 R_*).

Parameter	HD 1237		HD 22049		HD 147513	Sun	
	ZDI	SH-ZDI	ZDI	SH-ZDI	SH-ZDI	CR 1922 (Min)	CR 1962 (Max)
$\langle n \rangle_{\text{IC}} [\times 10^7 \text{ cm}^{-3}]$	3.66	7.74	3.38	8.30	4.80	1.80	4.78
$\langle T \rangle_{\text{IC}} [\times 10^6 \text{ K}]$	2.49	3.42	2.06	3.20	2.79	1.48	2.07
$\langle B \rangle_{\text{IC}} [\text{G}]$	4.58	16.43	3.34	14.39	5.37	0.94	2.31

To quantify these differences, we estimated the average density, temperature, and magnitude of the coronal magnetic field inside a spherical shell enclosing the region between 1.05 R_* and 1.50 R_* . This range captures the bulk of the inner corona, with the lower limit selected to avoid possible numerical errors in the average integration (due to the proximity with the boundary of the simulation domain). The integrated values obtained for each parameter and for the other stars are listed in the Table 4.3.

For HD 1237 we obtain differences by a factor of ~ 1.4 in temperature, ~ 2.1 in density and ~ 3.5 in magnetic field strength between the two cases. As the corona is hotter and denser in the SH-ZDI case, the resulting high-energy emission is almost featureless in the EUV channels ($T \sim 1\text{--}2$ MK). In addition, the effect of the surface field completeness is clear in the SXR image, where the coronal holes are shifted to lower latitudes and the emission comes from both hemispheres of the star (in contrast to the simulated emission in this range for the ZDI case).

As expected, HD 1237 shows enhanced coronal conditions compared to the Sun, especially for the SH-ZDI case (see Table 4.3). For the ZDI case the mean coronal density appears to be lower than the solar maximum value (by $\sim 25\%$). This may be connected with the incompleteness of the ZDI maps (Sect. 4.2), since a similar situation occurs for the ZDI solution of HD 22049 by roughly the same amount.

4.4.3 HD 22049 (ϵ Eridani)

The solutions for HD 22049 are presented in Figs. 4.9 and 4.10. The coronal structure in this case is highly complex, with several hot and dense loops connecting the different polarity regions of the surface field distribution. In some locations, the material is able to escape near the cusp of the loops, resembling helmet streamers in the Sun. For the SH-ZDI simulation, some of this escaping material is even visible in the EUV synthetic maps (in particular in the 195 Å channel – *Green* image in Fig. 4.10).

Similar to HD 1237, two large coronal holes are visible in the synthetic high-energy emission maps (especially in the ZDI simulation). However, in this case, the correlation with the stronger magnetic features in the surface is less clear than for HD 1237. A large filament crossing the entire disk is visible in both solutions, being more smooth in the SH-ZDI as expected from the underlying field distribution.

The comparison between the ZDI and SH-ZDI solution leads to similar results as for HD 1237. The variation in the average coronal density, temperature, and magnetic field strength reach factors of 2.5, 1.6, and 4.3, respectively (see Table 4.3).

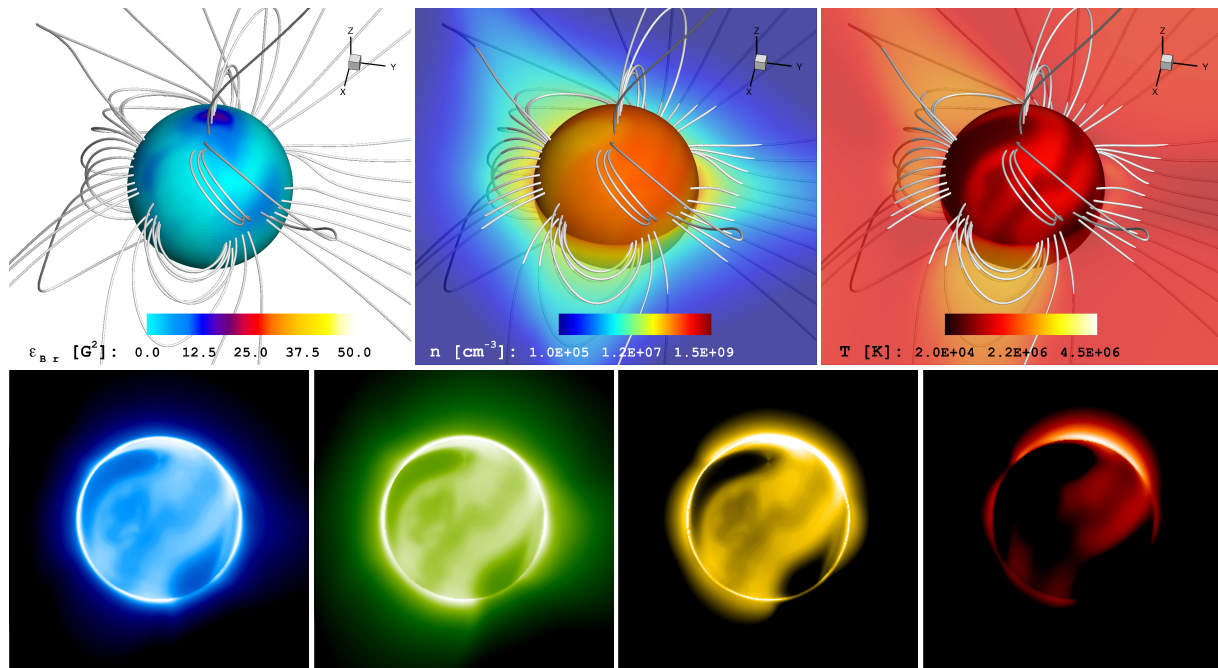


Figure 4.9: Simulation results for the coronal structure of HD 22049 driven by the ZDI large-scale magnetic field map. The *top* panels contain the distribution of the magnetic energy density ($\epsilon_{B,r}$, *left*), the number density (n , *middle*) and temperature (T , *right*). For the last two quantities, the distribution over the equatorial plane $z = 0$ is presented. The sphere represents the stellar surface and selected 3D magnetic field lines are shown in white. The *bottom* images correspond to synthetic coronal emission maps in EUV (*blue*: 171 Å, *green*: 195 Å, *yellow*: 284 Å) and SXR (*red*: 2–30 Å). The perspective is preserved in all panels with $i = 45^\circ$.

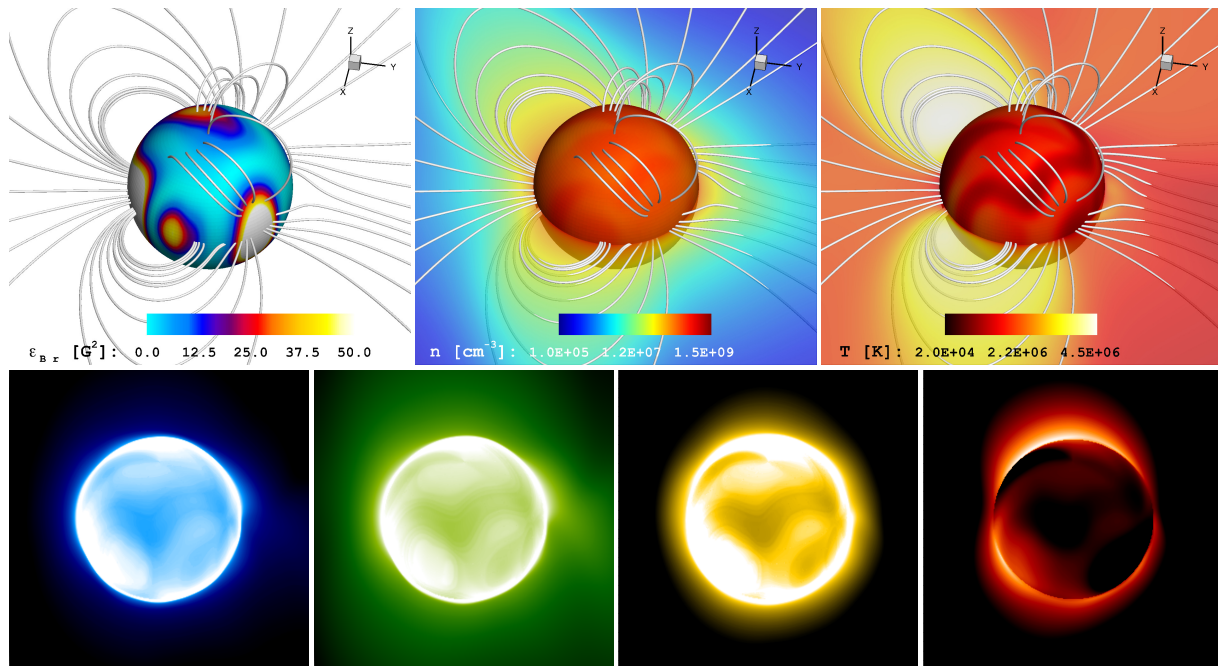


Figure 4.10: Simulation results for the coronal structure of HD 22049 driven by the SH-ZDI large-scale field map. See caption of Fig. 4.9. The 3D magnetic field lines are calculated in the same spatial locations as in the solution presented in Fig. 4.10.

The differences in the synthetic emission maps are also somewhat preserved with respect to the HD 1237 simulations; fewer coronal features are visible in EUV channels of the SH-ZDI solution, and the SXR emission is dominated by the closed field regions, which are distributed in this case in various locations of the 3D structure.

Finally, it is interesting to note here the similarities between the quantitative average properties of the ZDI solution of HD 22049 and the solar maximum case. The resulting mean temperatures and field strengths are commensurate among these simulations. However, large differences are evident in the qualitative aspects of the two solutions (see Figs. 4.9 and 4.6). No coronal holes are obtained for the solar maximum case, and the high-energy emission is highly concentrated from small portions of the corona (associated with active regions). This again can be understood in terms of the amount of magnetic structures resolved in the surface field distribution. Despite the degraded resolution for the solar case, the number of bipolar regions on the surface (sustaining dense coronal loops) is much larger than in the large-scale field maps recovered with ZDI. Instead, the ZDI coronal solution for HD 22049 is much more similar to the solar minimum case (Fig. 4.5). This clearly exemplifies the importance of combining quantitative descriptions, together with qualitative spatially resolved information for a robust comparison.

4.4.4 HD 147513 (HR 6094)

We present the steady-state coronal solution for HD 147513 in Fig. 4.11. As was mentioned earlier, we only considered the SH-ZDI field distribution in this case (see Sect. 4.2). The coronal structure is dominated by a rather simple configuration of poloidal loops, driven by the surface field distribution (mainly from the dipolar and quadrupolar components). This generates bands of trapped material, separated by the magnetic polarity inversion lines and distributed at different latitudes. Few open field regions are visible in the coronal structure, which are again located inside the largest magnetic energy concentrations.

One of these regions appears in the north pole of the star, which suffers a small distortion in the EUV images that is due to a numerical artefact of the spherical grid. The line-of-sight SXR emission displays a ring-like structure close to the limb, corresponding to the hottest material of the steady-state corona. Some faint emission can also be seen inside the stellar disk. As the estimated inclination angle for this star is small ($i \sim 20^\circ$), the coronal features are visible at almost all rotational phases.

The coronal properties listed in Table 4.3 show an average density similar to the solar case in activity maximum. However, as was presented in Sect. 4.4.1, the limited resolution of the surface field distribution can strongly affect this parameter. Given the relatively low resolution for the SH-ZDI map for this star, we expect larger discrepancies than were obtained for the solar case. In this sense, the average values obtained from the simulation correspond only to rough estimates of the actual conditions of the corona. This is considered in more detail in Sect. 4.5.1. Still, the geometrical configuration of this system provides an interesting view of the coronal features that cannot be easily obtained even for the solar case.

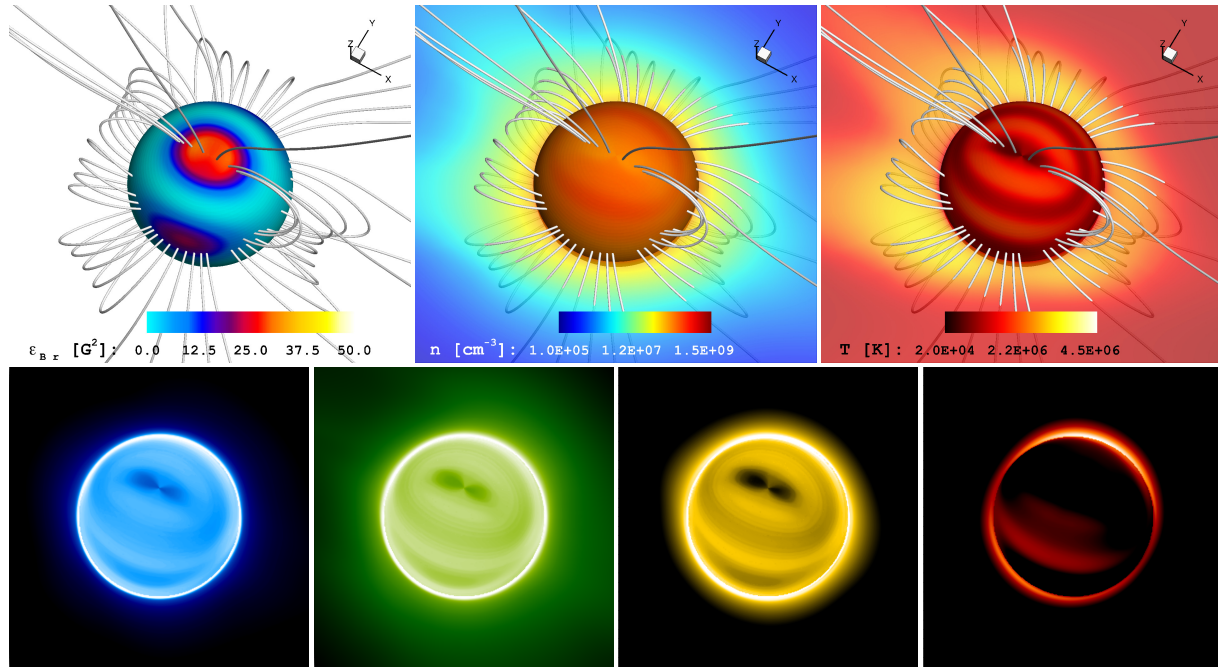


Figure 4.11: Simulation results for the coronal structure of HD 22049 driven by the ZDI large-scale magnetic field map. The *top* panels contain the distribution of the magnetic energy density (ϵ_{Br} , *left*), the number density (n , *middle*) and temperature (T , *right*). For the last two quantities, the distribution over the equatorial plane $z = 0$ is presented. The sphere represents the stellar surface and selected 3D magnetic field lines are shown in white. The *bottom* images correspond to synthetic coronal emission maps in EUV (*blue*: 171 Å, *green*: 195 Å, *yellow*: 284 Å) and SXR (*red*: 2–30 Å). The perspective is preserved in all panels with $i = 20^\circ$.

4.5 Analysis and discussion

Using the simulation results, we can relate the characteristics of the surface field distributions with the obtained coronal properties and the environment around these systems. We focus our discussion on three main aspects, including the thermodynamic structure, the coronal high-energy emission, and the stellar rotational modulation of the coronal emission.

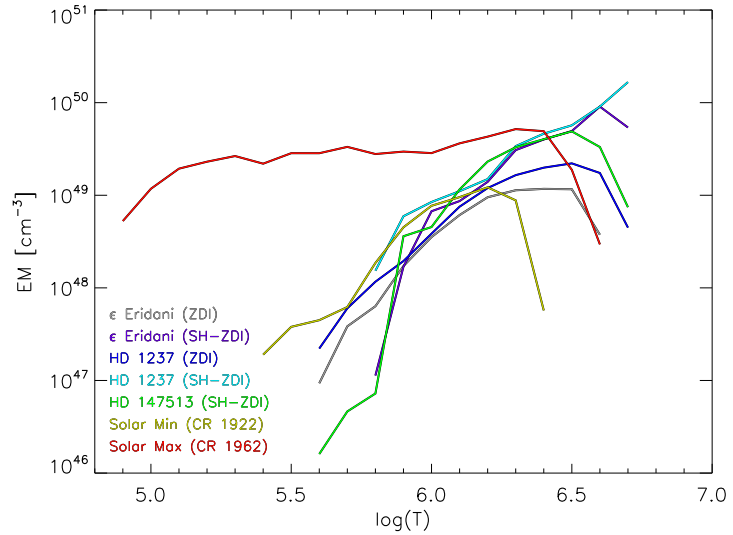
4.5.1 Thermodynamic coronal properties

From the simulated 3D structure in each star, we calculated the emission measure distribution, $EM(T)$, defined by

$$EM(T) = \int_{V(T)} n^2(T) dV(T), \quad (4.1)$$

where $n(T)$ is the plasma density at the temperature T , the integration only includes the volume of the grid cells at that particular temperature, and the volume covers all the closed field line regions in the steady-state solutions. We used temperature bins of 0.1 in $\log T$ starting from the base temperature (i.e., $\log T \simeq 4.9$) up to the highest temperature achieved in each simulation. Figure 4.12 contains the computed $EM(T)$ for all the considered cases. As expected, the peak values are located at $\log T > 6.0$, and move towards larger emission measures and higher temperatures with increasing average (radial) magnetic energy density $\langle \varepsilon_{Br} \rangle$ (see Table 4.1).

Figure 4.12: Emission measure distributions, $EM(T)$, calculated from the 3D steady-state solutions. Each colour corresponds to one of the simulations presented in Sect. 4.4, including the solar runs (Sect. 4.4.1).



In a similar manner to the solar case (Sect. 4.4.1), we compared the simulated quantities to observational values. The ZDI and SH-ZDI simulations of HD 22049 yield maximum EM values of $\log EM \simeq 49.1$ (at $\log T \simeq 6.4$) and $\log EM \simeq 50.0$ (at $\log T \simeq 6.6$), respectively. The peak temperature and emission measure of the ZDI model are significantly lower than those derived from both EUV and X-ray spectra ($\log EM \simeq 50.7$ at $\log T \simeq 6.6 \pm 0.05$, Drake et al. 2000; Sanz-Forcada et al. 2004; Ness & Jordan 2008). The SH-ZDI emission measure fares somewhat better, with good agreement in terms of the peak temperature. However, this model still predicts an emission measure significantly lower than observed, by roughly a factor of 5.

For HD 147513 available observations, from the broad-band filters of the *Extreme Ultraviolet Explorer* (EUVE) Deep Survey telescope, only provide rough estimates of the coronal conditions, suggesting a probable emission measure in the range $\log EM \sim 51\text{--}52$ (Vedder et al. 1993), but with no distinction on the temperature. In turn, the peak of the simulated distribution is located at $\log T \simeq 6.5$, with an associated value of $\log EM \simeq 49.7$. The discrepancy in emission measure might be related to the the relatively low spatial resolution of the SH-ZDI map driving the simulation (Sects. 4.2 and 4.4.4). The peak temperature is also slightly lower than what might be expected based on the emission measure distribution and the observed peak temperature of HD 22049.

There are no observational constraints in the literature for HD 1237 regarding the EM distribution. From the numerical simulations, we obtain peak values of $\log EM \simeq 49.3$ at $\log T \sim 6.5$ for the ZDI case, and $\log EM \simeq 50.2$ at $\log T \sim 6.7$ for the SH-ZDI case.

In all the stellar cases, the simulated EM distributions show maxima close to the expected values for stars within the considered levels of activity (see Table 4.1). However, the emission measures are systematically lower than indicated by observation.

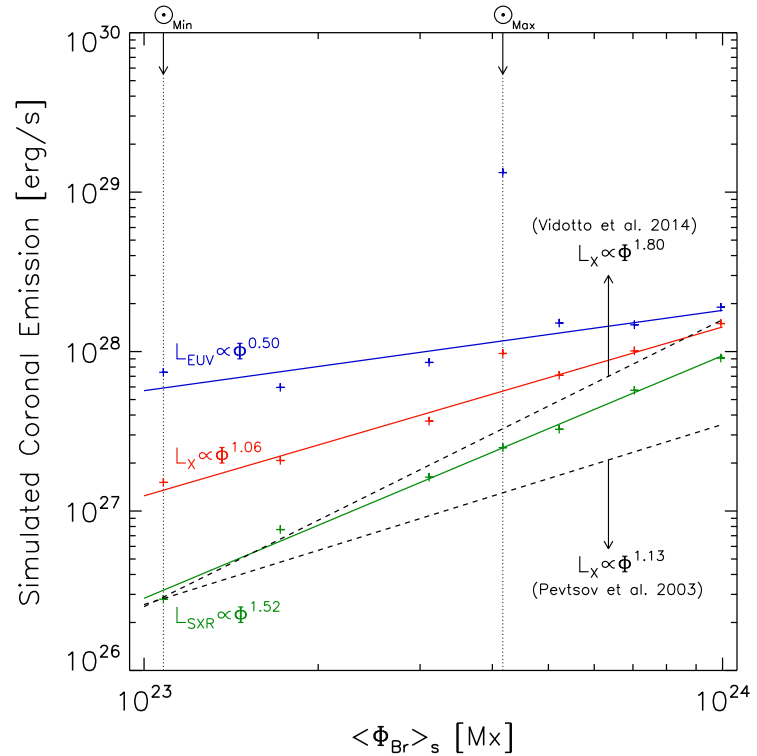
The behaviour of the simulated EM distribution for the solar maximum case (*red* line in Fig. 4.12) is particularly interesting compared with the remaining simulations. Both the peak emission measure and temperature agree well with assessments from full solar disk observations (e.g., Laming et al. 1995; Drake et al. 2000). However, the observations indicate a slope in the EM vs. temperature of the order of unity or greater, whereas the model prediction is much flatter. This results in a substantial over-prediction of the cooler emission measure at temperatures $\log T \leq 6$ compared with observations. The solar minimum EM distribution (*yellow* line in Fig. 4.12) is more similar to the stellar cases in this regard. These differences have a considerable impact on the predicted coronal emission, as discussed in the next section.

4.5.2 High-Energy emission and magnetic flux

An observational study performed by Pevtsov et al. (2003) showed a relation between the unsigned magnetic field flux, Φ_B , and the X-ray emission, L_X , covering several orders of magnitude in both quantities ($L_X \propto \Phi_B^{1.13 \pm 0.05}$). The analysis included various magnetic features of the Sun, together with Zeeman broadening (ZB) measurements of active dwarfs (spectral types F, G, and K), and pre-main sequence stars (see Saar 1996). More recently, Vidotto et al. (2014a) investigated the behaviour of various astrophysical quantities, including L_X , with respect to the large-scale magnetic field flux (recovered with ZDI). They also found a power-law relation for both parameters ($L_X \propto \Phi_B^{1.80 \pm 0.20}$). These observational results have been interpreted as an indication of a similar coronal heating mechanism among these types of stars.

In this context, we considered this relation from a numerical point of view by simulating the coronal high-energy emission (based on the $EM(T)$ distributions presented in the previous section) and comparing the predicted fluxes with the underlying surface magnetic field flux distributions ($\Phi_B = 4\pi |B_r| R_*^2$). In this analysis, we included the results from all the considered cases (e.g., solar and ZDI/SH-ZDI), treating the solutions independently. This allowed us to explore a broad range for both parameters while maintaining the considerations and limitations of the data-driven numerical approach. In principle, this can also be studied from a more generic numerical point of view (i.e., including different simulated field distributions). However, this would require implicit assumptions about the field strength and spatial configuration (mostly influenced by the solar case), which would introduce strong biases in the analysis. Considering the different recovered field maps (e.g., ZDI/SH-ZDI) as independent observations therefore represents a reasonable approximation.

Figure 4.13: Simulated high-energy coronal emission vs. unsigned radial magnetic flux $\langle\Phi_{Br}\rangle_s$. Each point corresponds to one of the simulations described in Sect. 4.4, including the solar cases as indicated. These values are calculated from synthetic spectra, based on the $EM(T)$ distributions (Sect. 4.5.1), and integrated in the SXR (2–30 Å, green), X-ray (5–100 Å, red) and EUV (100–920 Å, blue) bands. The solid lines correspond to fits to the simulated data points. The dashed lines are based on observational studies using X-ray, against magnetic field measurements using ZB (Pevtsov et al. 2003) and ZDI (Vidotto et al. 2014a).



Spectra were simulated for each of the emission measure distributions, $EM(T)$ over the X-ray and EUV wavelength regimes from 1 to 1100 Å on a 0.1 Å grid, covering all the bandpasses of interest to this work. Emissivities were computed using atomic data from the CHIANTI database version 7.1.4 (Dere et al. 1997; Landi et al. 2013) as implemented in the Package for INTeractive Analysis of Line Emission (PINTofALE)[†]. The radiative loss in the temperature range of interest for the stars in this study is dominated by metals (principally Si, Mg, and Fe), and the chemical abundance mixture has a concomitant influence on the predicted EUV and X-ray fluxes. HD 22049 and other intermediate-activity G and K dwarfs exhibit a solar-like “first ionization potential effect” in which elements with low first ionization potentials (≤ 13.6 eV) can be enhanced by factors of up to 4 in the corona relative to photospheric values (e.g., Laming et al. 1996; Wood & Linsky 2010). For the purposes of this study we did not try to match these abundances, but instead adopted the solar abundance mixture of Grevesse & Sauval (1998) as a standard reference set. Fluxes in the different bandpasses discussed below were obtained by integrating the synthetic spectra within the wavelength limits of interest.

Figure 4.13 shows the relation between the simulated high-energy coronal emission and the unsigned magnetic flux from the radial magnetic field maps. The latter, noted as $\langle\Phi_{Br}\rangle_s$, was averaged over the entire surface of the star. The colours correspond to the spectral ranges used for the integration, covering the SXR (2–30 Å, green), X-ray (5–100 Å, red), and EUV (100–920 Å, blue) bands. As indicated, a power-law fit was

[†]<http://hea-www.harvard.edu/~PINTofALE/>

applied to each channel (continuous lines), while the segmented lines correspond to the previous observational results from [Pevtsov et al. \(2003\)](#) and [Vidotto et al. \(2014a\)](#)[‡]. Two vertical arrows in the upper x-axis denote the results for the solar case (\odot_{Min} and \odot_{Max}).

Several aspects of [Fig. 4.13](#) are noteworthy. First, despite the reduced range in $\langle \Phi_{\text{Br}} \rangle_s$, we were able to retrieve a similar behaviour between radiative flux and magnetic flux as in previous observational studies with larger datasets. For the simulated X-ray range, the results are consistent with the relation obtained by [Pevtsov et al. \(2003\)](#), while in the SXR range the power-law dependence is more similar to the results obtained by [Vidotto et al. \(2014a\)](#). This reinforces the applicability of the model, at least to the levels of magnetic activity considered here. In addition, there appears to be a trend towards a steeper relation with increasing energy; from $\propto \Phi^{0.5}$ in the EUV, to $\propto \Phi^{1.06-1.52}$ in the X-ray and SXR ranges. In agreement with observations ([Mathioudakis et al. 1995](#)), [Fig. 4.13](#) shows that the X-ray emission will match and eventually dominate the EUV emission, at higher levels of magnetic activity (and associated magnetic flux). This is also qualitatively consistent with the spectral modelling values reported by [Chadney et al. \(2015\)](#) in terms of the surface fluxes, F_X , and F_{EUV} . According to their results, this should occur at activity levels slightly higher than those displayed by HD 22049. This behaviour may be connected with the appearance of strong azimuthal or toroidal fields in the large-scale field of these stars, as in the case of HD 1237 (see [Alvarado-Gómez et al. 2015](#) and references therein).

Comparing the synthetic flux results with observations and spectral modelling data (within the same energy ranges) published by [Sanz-Forcada et al. \(2011\)](#) reveals underestimated values in our models for L_X and L_{EUV} . At best, the discrepancy is lower than a factor of 2 in both energy bands, as in the case of the SH-ZDI solution of HD 22049. However, these differences can range up to $\sim 1-2$ orders of magnitude in some of our other stellar simulations. The largest discrepancies appear in the EUV band, reflecting the model emission measure deficiencies noted previously. Several observational and numerical factors could give rise to the relatively large mismatch of the results. These include instrumental and signal-to-noise ratio (S/N) effects in the EUV/X-ray observations (see [Sanz-Forcada et al. 2011](#)), the spatial resolution and missing flux in the ZDI reconstruction (see [Arzoumanian et al. 2011](#); [Lang et al. 2014](#)), temporal incoherence (connected with long-term variations associated with magnetic cycles), and the coronal heating model assumed, among others. Previous numerical studies have adjusted the thermodynamic base conditions to match the peak of the observed $EM(T)$ distribution ([Vidotto et al. 2012](#)), or the X-ray luminosity ([Llama et al. 2013](#)). However, as the dominant coronal emission changes with the magnetic activity of the star ([Mathioudakis et al. 1995](#); [Chadney et al. 2015](#)), this has to be performed in all high-energy bands for a consistent calibration. Despite the various problems and limitations, these comparisons serve as a benchmark to improve this data-driven approach and make it more reliable in stars different from the Sun.

[‡]We shifted the relation from [Vidotto et al. \(2014a\)](#) to match the [Pevtsov et al. \(2003\)](#) relation at the solar minimum value. This was performed for comparison purposes, as there are still discrepancies in the absolute values of the observational $L_X - \Phi_B$ relations, most likely connected with the method to estimate the surface magnetic flux (i.e., ZB in [Pevtsov et al. 2003](#) and ZDI in [Vidotto et al. 2014a](#)).

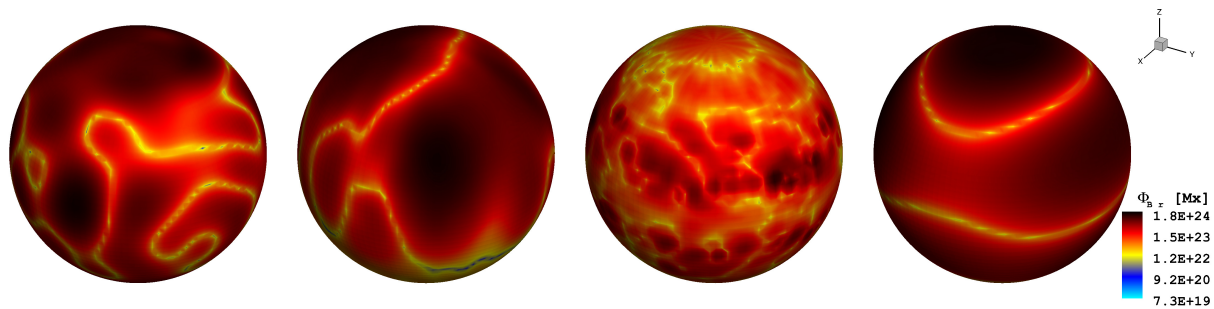


Figure 4.14: Spatial distribution of the surface radial magnetic flux, Φ_{Br} . The average surface magnetic flux increases from *left* to *right*, showing the Sun (Min), HD 1237 (ZDI), Sun (Max), and HD 147513 (SH-ZDI). The degree of complexity is clearly higher in the solar maximum case despite the degraded spatial resolution. The perspective is preserved in all cases with $i = 60^\circ$.

Finally, while both solar cases agree well with observed mean coronal temperatures and high-energy emission (see Sect. 4.4.1), the activity maximum solution appears far higher than the general trends in both the EUV and X-ray, as shown in Fig. 4.13. By removing these points from the power-law fits, the scatter is reduced considerably (by a factor of ~ 5 in the EUV and ~ 2.5 in the X-ray). This is directly connected with the resulting shape of the $EM(T)$ distribution, presented in Sect. 4.5.1, which is much flatter than observed. Consequently, the EUV flux is much higher by a commensurate margin than the solar minimum and the stellar counterparts. The “cool” plasma excess is related to the response of the coronal model heating law to the field topology and associated complexity (see Sect. 4.2). To show this in more detail, we compare the surface distribution of Φ_{Br} of four of the cases considered in ascending order of $\langle \Phi_{Br} \rangle_s$ (Fig. 4.14). Even with a degraded resolution, the solar maximum case contains a far more complex field distribution than in any of our ZDI models. This makes the comparison between the solar activity maximum case and ZDI-driven models extremely difficult. From this perspective, the solar minimum state provides a more suitable point of comparison for ZDI-based stellar studies. Indeed, the predicted fluxes for the solar minimum case are well-aligned with the power-law fits in Fig. 4.13.

4.5.3 Coronal features and rotational modulation

In this last section we calculate the rotational modulation of the high-energy emission that is due to the specific coronal features developed in the simulation. The stellar emission in the X-ray and EUV ranges plays a fundamental role in the thermal structure and dynamical evolution of planetary atmospheres (see Lammer et al. 2003; Lammer 2013). Processes such as heating of the exospheres or thermospheres, expansion, and atmospheric escape are highly sensitive to these parameters (Lammer et al. 2008; Guo 2011; Shaikhislamov et al. 2014). However, there are several observational difficulties, particularly in the EUV, in accessing these ranges of the electromagnetic spectrum, such as lack of instrumentation and strong absorption by the interstellar medium (Chadney et al. 2015). Various alternatives have been used to overcome these issues, including extrapolations based on average

solar EUV fluxes (Lecavelier Des Etangs 2007), coronal models from spectral synthesis (Sanz-Forcada et al. 2011), and predictions from rotational evolution models (Tu et al. 2015). Still, these procedures are not able to estimate the variability on time-scales comparable to the stellar rotation period, or from the geometrical configuration of the system (e.g., orbital inclination). Both elements can be considered in our data-driven numerical approach, provided that the entire 3D structure of the corona is generated. These factors can have important effects on exoplanetary conditions such as climate patterns and habitability (e.g., Forget & Leconte 2014) and on the detectability of transits either in X-ray (Poppenhaeger et al. 2013) or in the near-UV (Haswell et al. 2012; Llama et al. 2011).

For this purpose, we used the system analysed here that is the most extreme in terms of high-energy emission and proximity of the planet. This corresponds to HD 1237 using the SH-ZDI field distribution (Fig. 4.8, see also Table 4.1). From the steady-state coronal solution, we generated a set of synthetic high-energy emission maps covering an entire rotation of the star, with three different line-of-sight angles (30, 60, and 90°)[†]. Figure 4.15 contains the resulting rotational modulation of the coronal emission for each of the considered inclinations. These variations are induced by the different coronal features described in Sect. 4.4.2. Around 0.2 and 0.8 in rotational phase, the large coronal holes cross the stellar disk, while at $\Phi = 0.5$ and $\Phi = 1.0$, they are located near the limb (close to the perspective shown in Fig. 4.8).

As expected, the high-energy modulation is reduced for smaller inclination angles (e.g., closer to a pole-on view); it is lower than 5% of the mean value for both energy bands. For larger inclinations, the modulation increases, reaching up to $\sim 15\%$ in the 90° inclination case. These values are fully consistent with the X-ray modulation estimates in the HD 189733 (K2V) system obtained by Llama et al. (2013), which displays a comparable field strength at the stellar surface (± 30 G).

Depending on the magnetic field evolution, the modulation of the coronal emission could persist for time-scales longer than one rotation period of the star. This is the case for HD 1237, where the large-scale field seems stable on a time-scale of months (Alvarado-Gómez et al. 2015). A fraction of the coronal emission may show rotational modulation on time-scales comparable to the orbital period of the exoplanet ($P_{\text{orb}} = 133.7 \pm 0.2$ d, Naef et al. 2001). However, an additional component will be due to shorter term reconnection

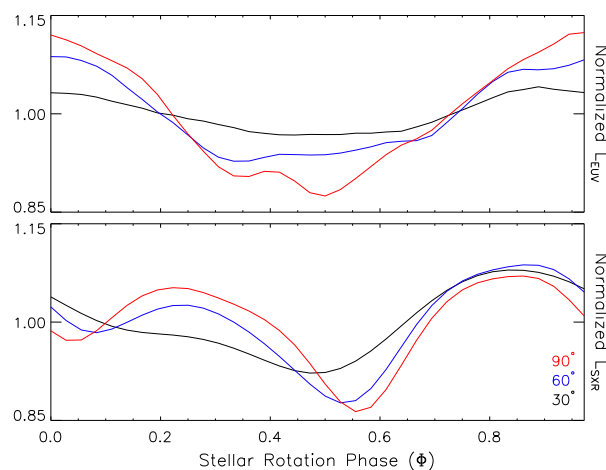


Figure 4.15: Rotational modulation of the high-energy coronal emission for HD 1237 (SH-ZDI), showing the EUV (*top*) and SXR (*bottom*) ranges. Colours indicate the inclination angle used for the calculation.

[†]This angle is measured between the stellar rotation axis and the position of the observer.

events (e.g., flares). Furthermore, as the planetary system has a high orbital eccentricity ($e \simeq 0.5$), any X-ray and EUV rotational modulation will most likely play a secondary role in terms of the irradiation environment. This will be considered in the next chapter, in combination with the influence of the magnetized stellar wind on the exoplanetary conditions.

A similar approach can be followed in other systems, provided ZDI reconstructions are available for the host star (see [Fares et al. 2013](#)). More complex scenarios are expected in hot-Jupiters, where the orbital period can be equal to or even shorter than the stellar rotation period. One example is the HD 179949 (F8V) system ([Fares et al. 2012](#)), where planet-induced coronal activity has been suggested ([Shkolnik et al. 2008](#)). Still, recent multi-wavelength observations of this system presented by [Scandariato et al. \(2013\)](#) appear to be consistent with rotational modulation alone. Nevertheless, this does not exclude the possibility of star-planet interactions in the system, which could be explored in more detail with the data-driven approach presented in this paper. Moreover, as has been shown by [Cohen et al. \(2011b\)](#), it is also possible to simulate in detail space weather phenomena, such as coronal mass ejections, in these extreme exoplanetary systems.

4.6 Summary and chapter conclusions

We have performed a detailed numerical simulation of the 3D coronal structure of three late-type planet-hosting stars (HD 1237, HD 22049, and HD 147513). A steady-state solution was calculated self-consistently, driven by the surface magnetic field distributions recovered with the technique of Zeeman-Doppler imaging. The main results of our study are summarised below.

- We compared the coronal solutions driven by two similar implementations of this mapping technique (ZDI and SH-ZDI). The global structure of the resulting corona is consistent in both cases. A quantitative analysis showed important differences in the thermodynamic conditions and in the coronal high-energy emission. We obtained differences of up to factors of 1.4 and 2.5 in the coronal temperature and density, respectively. This led to a larger variation in the predicted EUV and SXR emission, reaching up to one order of magnitude. These differences can be related to the amount of structure, field strength, and the map completeness in each case.
- The appearance of different coronal features in each star is highly dependent on the characteristics of the surface field distribution. Two large coronal holes appear as the most prominent elements in HD 1237. HD 22049 shows more complex details, displaying additional structures such as helmet streamers and filaments. For HD 147513, the simulation predicts a rather simple coronal topology, reflecting the low-complexity of its surface magnetic field.

- Comparable solar simulations in terms of spatial resolution and boundary conditions were considered (covering activity minimum and maximum). This included a detailed comparison with archival satellite data in the EUV and SXR ranges. For both activity states, good agreement was obtained in terms of the coronal temperature ($\sim 8\%$ difference) and in the high-energy coronal emission (SXR/EUV bands). On the other hand, the emission measure distribution showed larger discrepancies, with a considerable excess at the low-temperature end ($\log T < 6.0$) for the solar maximum case. In addition, within the temperature range of 1–2 MK, the EM appears underestimated by factors of ~ 3 and 5 for activity maximum and minimum, respectively. This is likely indicative of the need to recalibrate the coronal heating mechanism when applying this model to resolution-limited surface magnetic field distributions.
- Furthermore, while the comparison to the observations showed similar levels of agreement for both solar minimum and maximum cases (e.g., thermodynamic conditions and high-energy emission), the simpler structure of the large-scale magnetic field makes the former a better reference point for simulations based on ZDI maps (see Fig. 4.14).
- We considered the particular case of HD 1237 to estimate the rotational modulation in the high-energy emission that is due to the coronal features developed in our simulation. We obtained variabilities ranging from $\sim 5\text{--}15\%$ (depending on the line-of-sight angle) in the mean coronal EUV and SXR emission. Similar estimates have been reported for systems with similar surface field strengths (e.g., HD 189733, [Llama et al. 2013](#)).
- In addition, using the simulations, we were able to recover similar trends as in previous observational studies, including a relation between the magnetic flux (Φ_{Br}) and the coronal high-energy emission ([Pevtsov et al. 2003](#); [Vidotto et al. 2014a](#)). However, as this numerical model was specifically developed for the Sun, further adjustments will be required to better calibrate our results to the stellar data.
- Improvements in this approach can be performed by extending the range in Φ_{Br} . This could be done by isolating specific regions from high-resolution solar observations and by expanding the stellar sample to more active stars. For the latter case, it would be necessary to further adjust the coronal heating or the thermodynamic base conditions to match the observed coronal emission in all energy bands. Another possibility would involve a more sophisticated numerical treatment to be able to consider all the magnetic field components to drive the simulation (see [Fisher et al. 2015](#)).
- The results discussed in this work will be used in the next chapter to self-consistently simulate the stellar wind, inner astrosphere, and circumstellar environment of these systems. This includes the stellar mass loss rate, angular momentum loss rate, orbital conditions, and topology of the astrospheric current sheet.

Chapter 5

Simulating the environment around planet-hosting stars – II. Stellar winds and inner astrospheres

Abstract

We present the results of a comprehensive numerical simulation of the environment around three exoplanet-host stars (HD 1237, HD 22049, and HD 147513). Our simulations consider one of the latest models currently used for space weather studies in the Heliosphere, with turbulent Alfvén wave dissipation as the source of coronal heating and stellar wind acceleration. Large-scale magnetic field maps, recovered with two implementations of the tomographic technique of Zeeman-Doppler imaging, serve to drive steady-state solutions in each system. This chapter contains the description of the stellar wind and inner astrosphere, while the coronal structure was previously discussed in [Alvarado-Gómez et al. \(2016\)](#). The analysis includes the magneto-hydrodynamical properties of the stellar wind, the associated mass and angular momentum loss rates, as well as the topology of the astrospheric current sheet in each system. A systematic comparison among the considered cases is performed, including two reference solar simulations covering activity minimum and maximum. For HD 1237, we investigate the interactions between the structure of the developed stellar wind, and a possible magnetosphere around the Jupiter-mass planet in this system. We find that the process of particle injection into the planetary atmosphere is dominated by the density distribution rather than velocity profile of the stellar wind. In this context, we predict a maximum exoplanetary radio emission of 12 mJy at 40 MHz in this system, assuming the crossing of a high-density streamer during periastron passage. Furthermore, in combination with the analysis performed in [Alvarado-Gómez et al. \(2016\)](#), we obtain for the first time a fully simulated mass loss-activity relation, which is compared and discussed in the context of the relation based on astrospheric detections proposed by [Wood et al. \(2005a\)](#). Finally, we provide a characterisation of the global 3D properties of the stellar wind of these systems, at the inner edges of their habitable zones.

5.1 Chapter organization

This chapter provides continuity to the numerical work presented in Sect. 4, including now the stellar wind properties and inner astrospheric structure of three exoplanet hosts (HD 1237, HD 22049, and HD 147513). A description of the numerical set up, boundary conditions, and general characteristics in each simulation domain is provided in Sect. 5.2. Section 5.3 contains the results for each system, including the reference solar cases (i.e., activity minimum and maximum). We discuss our results in the context of previous observational and numerical studies in Sect. 5.4, and the main conclusions of our work are summarised in Sect. 5.5.

5.2 3D MHD simulation: Stellar winds and inner astrospheres

As in the previous chapter, the numerical simulations have been performed using the three-dimensional MHD code BATS-R-US (Powell et al. 1999) as part of the Space Weather Modeling Framework (SWMF, Tóth et al. 2005, 2012). We consider the Alfvén Wave Solar Model (AWSoM), which solves the two-temperature MHD equations with additional pressure and energy terms associated with the propagation, reflection, and transmission of low-frequency Alfvén waves. The complete description of the code and its numerical implementation can be found in van der Holst et al. (2014).

In this case we analyse the properties of the stellar wind, including the inner region of the stellar corona (SC module) and the resulting structure in the inner astrosphere (IH module). The solar/stellar cases, and the definition of the entire SC component, are identical as in Alvarado-Gómez et al. (2016). This includes base conditions typically assumed in high-resolution solar simulations, to match solar observations such as *in-situ* wind properties at 1 AU and line-of-sight EUV/X-ray images (Sokolov et al. 2013; Oran et al. 2013). As ZDI reconstructions necessarily have limited spatial resolution because they are insensitive to the small-scale surface field, we used solar magnetograms that have been spatially-filtered to a comparable resolution as the ZDI/SH-ZDI maps. This allows us to better quantify the effects of this limitation in our simulations consistently (see also Alvarado-Gómez et al. 2016). As previously discussed by Garraffo et al. (2013), we expect a much smaller effect in the wind structure than in the X-ray morphology.

The IH component covers the domain from $25 R_*$ up to $215 R_*$ (~ 1 AU in solar units). The physical conditions in this domain are calculated in the ideal MHD regime, and the simulations have been driven by coupling the steady-state stellar corona solutions described in the previous paper of this study, as the inner boundary conditions of the astrospheric component. A $5 R_*$ domain-overlap (from $25 R_*$ to $30 R_*$) is used in the coupling procedure between both domains[†]

[†]More details are available in <http://csem.engin.umich.edu/tools/swmf/documentation/HTML/SWMF/index.html>.

For the simulations of HD 1237, the inner astrospheric solution is additionally coupled as a boundary condition of the global magnetosphere (GM) module of the SWMF[†]. The spatial locations used for this coupling are described in Sect. 5.3.3. Inside the GM module, the boundary is set at $50 R_p$ (planet radii) towards the central star (day side). The spatial domain for this module extends up to $150 R_p$ in the night side and to $75 R_p$ in the perpendicular directions (orthogonal to the star-planet axis). Both simulation domains (IH and GM components), use a non-uniform cartesian grid which is automatically refined at the location of large gradients either of the magnetic field or plasma density. In this way the geometry of the astrospheric current sheet (in the IH module), and the bow shock structure (in the GM module) are properly resolved.

The inner boundary condition (located at $\sim 1 R_p$), is defined by the planetary parameters of mass, radius, and dipolar magnetic field strength. The mass is taken from the orbital solution determined by Naef et al. (2001). There are no observational constraints for the remaining two parameters. A Jupiter-size planet ($R_p = R_J$), with a fiducial dipolar field of $B_p = 1$ G, is assumed in this case. Previous observational and numerical studies focused on hot-Jupiter systems, have suggested stronger planetary magnetic fields (e.g., Shkolnik et al. 2005, 2008; Vidotto et al. 2010, 2012; Llama et al. 2011, 2013). However, the selection of a stronger (weaker) planetary magnetic field would mainly lead to a larger (smaller) size of the magnetosphere, following the relation $R_M \propto B_p^{1/3}$ (Eq. 5.2, Sect. 5.3.3). As we are interested in characterising the relative effects from the resulting stellar wind structure (and its connection with the magnetic field topology at the stellar surface), these are independent from the assumed field strength for the exoplanet.

5.3 Numerical results

The results for each simulation regime are presented in the following sections. From the solution in the SC module we computed the mass and angular momentum loss rates (Sect. 5.3.1). Inside the IH module, the steady-state solution led to the global structure of the wind and associated current sheet (Sect. 5.3.2). As in Alvarado-Gómez et al. (2016), we perform a consistent comparison between the solar and stellar cases. This includes the solar minimum and maximum activity states, as well as the ZDI / SH-ZDI driven simulations for the stellar cases. Finally, the results of HD 1237 are presented in Sect. 5.3.3, including the coupled solutions of the GM module, at two critical locations of the exoplanetary orbit.

5.3.1 Alfvén surface, mass and angular momentum loss rates

We initially describe the properties of the solar / stellar wind inside the SC module. Figures 5.1 to 5.3 show the equatorial distribution of the plasma density n , and radial wind speed u_r (*left* and *middle* panels, respectively), extracted from the corresponding steady-state solutions. The *right* panels contain the distribution of u_r over the current sheet

[†]See http://ccmc.gsfc.nasa.gov/cgi-bin/display/RT_t.cgi?page=mpause for real-time monitoring of the Earth's magnetosphere, using satellite data and the SWMF.

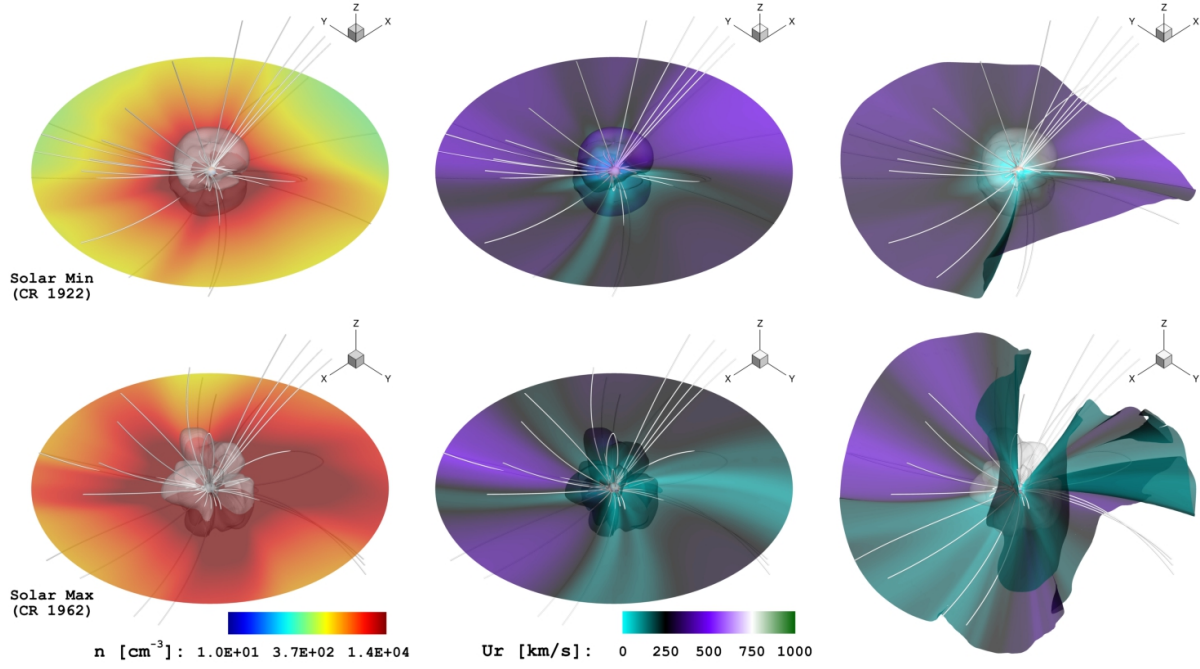


Figure 5.1: Simulation results in the solar corona (SC) domain for activity minimum (CR 1922, *top*) and maximum (CR 1962, *bottom*). The *left* and *middle* panels contain the projection onto the equatorial plane ($z = 0$) of the plasma density n , and the radial wind speed u_r , respectively. In the *right* panel the distribution of u_r on the developed current sheet structure ($B_r = 0$) is presented. The translucent shade denotes the Alfvén surface ($M_A = 1$) calculated from the steady-state solution. The corresponding colour scales for n and u_r are preserved among the different panels. Selected 3D magnetic field lines are shown in white.

structure, which is defined as the iso-surface with $B_r = 0$. We also compute the resulting Alfvén surface (AS) for each solution, displayed as a translucent shade in Figs. 5.1 to 5.3. This is performed by calculating the spatial locations at which the Alfvénic Mach number $M_A = u_{sw} / v_A = 1$. In this relation u_{sw} represents the local stellar wind speed, while v_A is the Alfvén speed of the plasma, determined by the ratio $B / \sqrt{4\pi\rho}$, with B and ρ as the local magnetic field strength and density, respectively.

Figure 5.1 shows the results of the solar simulations in this domain. For both activity states, the expected global thermodynamical properties of the solar wind are achieved; relatively fast and low density during solar minimum, and considerably slower and denser for activity maximum. Additionally, as evidenced by the developed current sheet (right panel in Fig. 5.1) and the geometry of the AS, the overall complexity of the driving magnetic field distribution is reflected in the wind solution. During activity minimum, the current sheet is mostly confined to the equatorial plane (with small deviations in particular sectors of the structure). The AS shows a two-lobe structure aligned with the rotation axis of the star (z -axis), which is usually obtained for simple (nearly dipolar) surface magnetic field distributions (e.g., Vidotto et al. 2014b; Cohen & Drake 2014). For activity maximum,

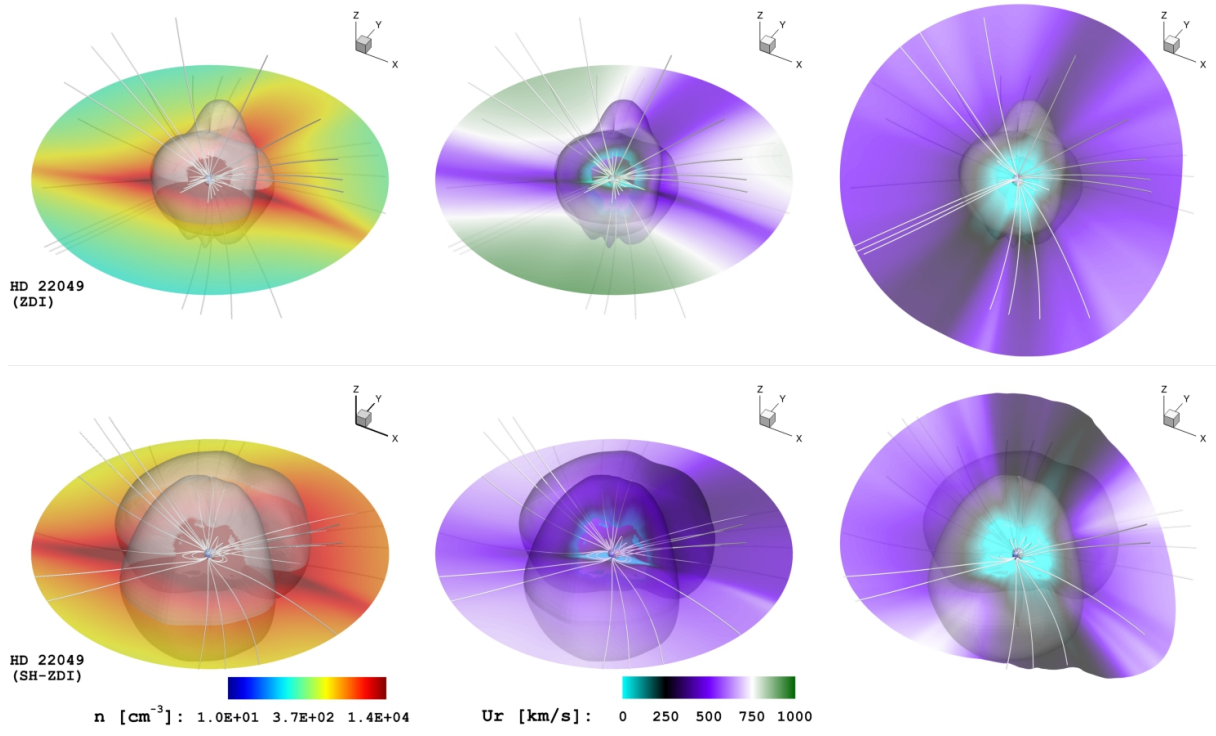


Figure 5.2: Simulation results in the SC domain for HD 22049 driven by the ZDI (*top*) and SH-ZDI (*bottom*) magnetic field maps. The *left* and *middle* panels contain the projection onto the equatorial plane ($z = 0$) of the plasma density n , and the radial wind speed u_r , respectively. In the *right* panel the distribution of u_r on the developed current sheet structure ($B_r = 0$) is presented. The translucent shade denotes the Alfvén surface ($M_A = 1$) calculated from the steady-state solution. The corresponding colour scales for n and u_r are preserved among the different panels. Selected 3D magnetic field lines are shown in white.

the structure of the current sheet shows warped sectors and greatly departs from the equatorial plane. Similarly the resulting AS in this case shows multiple lobes of irregular sizes, without any preferred orientation in the 3D domain. These fundamental differences are clearly seen in the resulting structure of the inner heliosphere, presented in Sect. 5.3.2.

The simulations of HD 22049 and HD 1237 led to similar wind structures in the SC domain (Figs. 5.2 and 5.3, respectively). Streamers can be observed on the equatorial plane (three for HD 22049 and two for HD 1237), with a mean density $n \simeq 10^3 \text{ cm}^{-3}$ and radial speeds of $u_r \sim 500 \text{ km s}^{-1}$ in the ZDI-driven cases. For the SH-ZDI simulation of HD 22049 two of these streamers are merged, creating a broader high-density sector on the equatorial plane. For both stars, the density drops by a factor of $\gtrsim 100$ between the streamers, while the velocity rises to $u_r \sim 1000 \text{ km s}^{-1}$ and 750 km s^{-1} for the ZDI and the SH-ZDI simulations, respectively. Similarly, a two-lobe AS structure is developed in all the simulations, which is consistently larger in the SH-ZDI cases (see Table 5.1). The alignment of the AS lobes deviates significantly from the rotation axis, leading to a current sheet structure nearly confined to a plane, highly inclined with respect to the projected

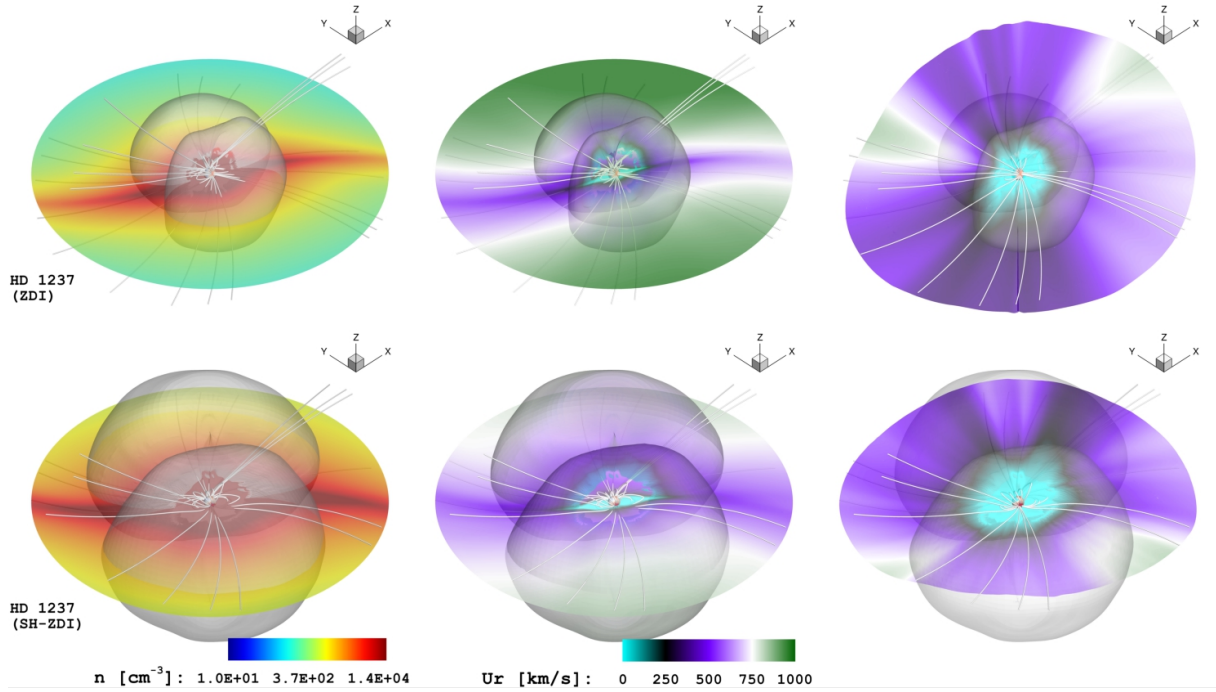


Figure 5.3: Simulation results in the SC domain for HD 1237 driven by the ZDI (*top*) and SH-ZDI (*bottom*) magnetic field maps. The *left* and *middle* panels contain the projection onto the equatorial plane ($z = 0$) of the plasma density n , and the radial wind speed u_r , respectively. In the *right* panel the distribution of u_r on the developed current sheet structure ($B_r = 0$) is presented. The translucent shade denotes the Alfvén surface ($M_A = 1$) calculated from the steady-state solution. The corresponding colour scales for n and u_r are preserved among the different panels. Selected 3D magnetic field lines are shown in white.

stellar equator (Figs. 5.2 and 5.3, *right panels*). The velocity of the wind along the current sheet is approximately 500 km s^{-1} in all cases, with variations up to $\pm 40\%$ in very small locations of the structure. These structures show a higher density ($n \simeq 10^4 \text{ cm}^{-3}$) in the SH-ZDI simulations, with roughly the same velocity as in the ZDI cases.

Compared to the previously described stellar cases, HD 147513 showed a rather different wind structure in this domain (Fig. 5.4). The high-density structures of the wind are much wider in this case, with associated radial speeds of $u_r \sim 250 \text{ km s}^{-1}$. The velocity of the wind remains below 750 km s^{-1} in the equatorial plane, and barely reaches this value in few locations of the 3D domain. Similar to the solar maximum case, the current sheet structure of HD 147513 shows warped sectors and clearly deviates from a planar structure (*right panel* of Fig. 5.4). This additional complexity can be also seen in the irregular lobes developed in the AS, which are also common with the solar simulation during activity maximum (Fig. 5.1, *bottom*).

These results clearly show the importance of the AS properties on the resulting wind structure. By definition, the AS corresponds to the boundary between magnetically-coupled outflows ($M_A < 1$) and the escaping stellar wind which no longer exerts torque

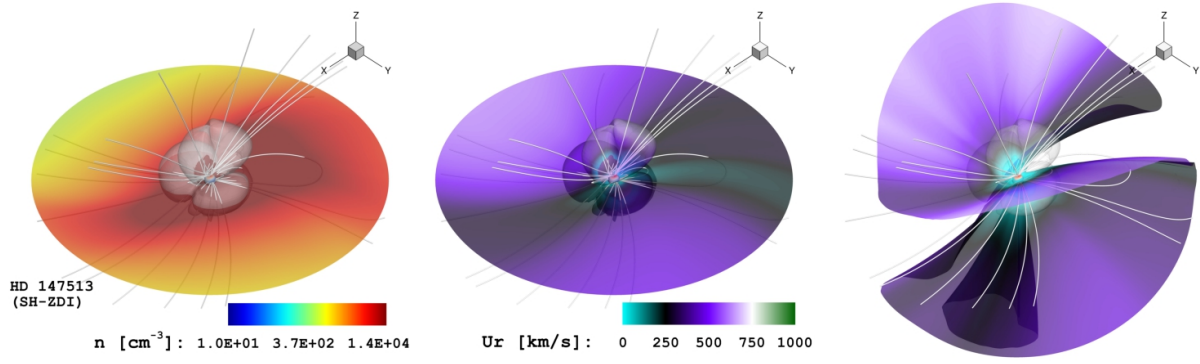


Figure 5.4: Simulation results in the SC domain of HD 147513 driven by the SH-ZDI magnetic field map. The *left* and *middle* panels contain the projection onto the equatorial plane ($z = 0$) of the plasma density n , and the radial wind speed u_r , respectively. In the *right* panel the distribution of u_r on the developed current sheet structure ($B_r = 0$) is presented. The translucent shade denotes the Alfvén surface ($M_A = 1$) calculated from the steady-state solution. Selected 3D magnetic field lines are shown in white.

on the star ($M_A > 1$). For this reason it is commonly used in modelling studies to calculate the mass loss rate, \dot{M} , and the angular momentum loss rate, \dot{J} , associated with the stellar wind (e.g., Cohen et al. 2010; Cohen & Drake 2014; Garraffo et al. 2015b). Furthermore, as illustrated in Figs. 5.1 to 5.3, the topology of the AS reflects to some extent the complexity of the magnetic field distribution driving the simulation (see also Vidotto et al. 2014b, 2015; Garraffo et al. 2015a), which in turn, in a self-consistent model, should be directly related to the resulting coronal structure (see Alvarado-Gómez et al. 2016). Finally, previous studies of planet-hosting stars with close-in exoplanets have also shown the importance of the exoplanet location with respect to the AS, which can lead to strong magnetic interactions and angular momentum transfer between the star and the planet (Cohen et al. 2014; Strugarek et al. 2014, 2015).

In addition, the AS provides a common framework to consistently compare our simulations in this domain, and to place our results in context with other studies in the literature. Table 5.1 contains a summary of the resulting stellar wind properties averaged over the AS, as well as the \dot{M} and \dot{J} values in each case. Several important results are obtained from this quantitative analysis. First of all, by taking an average of the activity minimum and maximum cases, we obtain a mean solar mass loss rate $\langle \dot{M}_\odot \rangle = 3.78 \times 10^{-14} M_\odot \text{ yr}^{-1}$, consistent with the nominal accepted value of $\dot{M}_\odot \simeq 2 \times 10^{-14} M_\odot \text{ yr}^{-1}$ (Wood 2004 and references therein), and the observed scatter during the course of the activity cycle (by a factor of ~ 2 , Cohen 2011).

If we analyse the solar simulations independently, the predicted mass loss rate during activity minimum agrees well with *Voyager II* data, averaged over the corresponding period of time at the spacecraft (i.e., ~ 9 months after[†] the CR 1922 of May 1997). However, a

[†]Approximate time required for the solar wind to reach *Voyager II* location, at the average speed predicted by the model in this epoch.

Table 5.1: Mass loss rates, \dot{M} and angular momentum loss rates, \dot{J} , calculated from the steady-state solutions. The additional stellar wind properties represent averages over the resulting Alfvén surface (AS), while $\langle R_{AS} \rangle$ corresponds to the mean AS radius in each case.

Parameter	HD 1237		HD 22049		HD 147513	Sun	
	ZDI	SH-ZDI	ZDI	SH-ZDI	SH-ZDI	CR 1922 (Min)	CR 1962 (Max)
$\dot{M} [\times 10^{-14} M_{\odot} \text{ yr}^{-1}]$	4.70	13.9	2.77	10.2	11.4	2.76	4.80
$\dot{J} [\times 10^{30} \text{ erg}]$	6.77	58.0	1.10	12.3	3.66	0.40	1.10
$\langle u_r \rangle_{AS} [\text{km s}^{-1}]$	679	654	562	493	363	364	171
$\langle n \rangle_{AS} [\times 10^4 \text{ cm}^{-3}]$	2.85	3.09	2.65	3.64	15.1	4.97	30.0
$\langle T \rangle_{AS} [\times 10^6 \text{ K}]$	2.33	1.52	1.81	1.34	1.54	1.26	0.84
$\langle B \rangle_{AS} [\times 10^{-2} \text{ G}]$	1.94	2.08	1.82	2.23	2.98	1.64	2.63
$\langle R_{AS} \rangle [R_{*}]$	12.0	19.6	10.2	15.6	7.1	6.4	6.8

similar comparison for the considered activity maximum epoch (i.e., ~ 14 months after the CR 1962 of Apr-May 2000), indicates that the solar mass loss rate in this case is overestimated by $\sim 40\%$ (Cohen 2011). This additional mass escaping the star can be interpreted as a deficit of confining loops in the lower corona (inside the AS), which results from the (spatial) resolution-limited magnetograms driving the simulation (see Alvarado-Gómez et al. 2016). While this condition was common among both solar simulations, the effect on the activity maximum case is larger, given the relative amount of complexity and magnetic flux lost in the process of spatially degrading the surface field distribution.

In a similar manner, the simulations yield an average solar angular momentum loss $\langle \dot{J}_{\odot} \rangle = 7.5 \times 10^{29} \text{ erg}$. Unlike the observational estimates of \dot{M}_{\odot} , values of \dot{J}_{\odot} are more uncertain (ranging between $\sim 10^{29} - 10^{31} \text{ erg}$), and usually determined via numerical models with different assumptions (e.g., Cohen et al. 2010; Matt et al. 2012; Cohen & Drake 2014; Garraffo et al. 2015b). The relatively small $\langle \dot{J}_{\odot} \rangle$ resulting from our simulations reflects the average size of the AS directly, which is known to increase with the field strength and decrease with the field complexity (see Réville et al. 2015a; Garraffo et al. 2015a). In the considered solar cases these dependencies are partially compensated, leading to a similar value of $\langle R_{AS} \rangle$ in both simulations (see Table 5.1).

Our result for $\langle R_{AS} \rangle$ in the solar minimum case, is very similar to the value obtained by the 2.5-dimensional simulations of Réville et al. (2015a) using the MHD PLUTO code (Mignone et al. 2007) and a similar activity epoch. Interestingly, for activity maximum we obtain a $\langle R_{AS} \rangle$ value which is roughly twice compared to their findings. This difference could be related (among with other possibilities), with the dimensional reduction of their approach, with specific properties of the driving magnetic field distribution (i.e., Carrington rotation and instrument used to map the magnetic field), and with the amount of small scale field included in each numerical implementation.

Unlike the average size of the AS, the fundamental properties of solar wind at this region show large variations between both activity states; differences by a factor of ~ 6 in the mean plasma density $\langle n \rangle_{AS}$, and by a factor of ~ 2 for the average radial wind speed $\langle u_r \rangle_{AS}$. Smaller differences are obtained for the remaining solar wind parameters.

For the considered stellar systems, important differences arise between the ZDI and SH-ZDI cases. For the mass and angular momentum loss rates, the resulting values of \dot{M} and \dot{J} of HD 1237 differ by a factors of ~ 3 and ~ 9 respectively, being larger in the SH-ZDI case. Similarly, the SH-ZDI simulation of HD 22049 yields \dot{M} and \dot{J} values which are several times larger than in the corresponding ZDI case (i.e., by factors of ~ 4 and ~ 11 , respectively). Smaller differences arise in the average size of the AS, $\langle R_{AS} \rangle$, being roughly 1.5 times larger in the SH-ZDI simulations of these two systems. The obtained differences in \dot{J} appear mainly as a result of its direct dependency with \dot{M} (see [Garraffo et al. 2015b](#)). On the other hand, the mass loss rate variations are connected to the relative differences in the surface field distributions driving the simulations (see [Alvarado-Gómez et al. 2016](#)), and the Alfvén wave energy transfer to the corona and wind implemented in the model. The latter is described via the Poynting flux of the emerging Alfvén waves, S_A , taken to be proportional to the field strength (and polarity) at the inner boundary of the simulation (i.e., $S_A \propto B_r$; see [van der Holst et al. 2014](#)). Previous studies based on the same MHD solver but with a different wind model (i.e., a thermally-driven polytropic stellar wind), do not display significant variations in \dot{M} when considering changes in the magnetic field geometry and / or the incompleteness of the ZDI maps (see [Vidotto et al. 2012](#), which is the basis for the models presented in [Vidotto et al. 2014b, 2015](#), [do Nascimento et al. 2016](#) and [Nicholson et al. 2016](#)). As the wind-driving mechanism in our simulations is based on Alfvén-wave turbulence dissipation, we find much stronger differences in these wind properties based on the large-scale magnetic field geometry. This is indicative of a radical difference between these other models and our simulations.

The remaining stellar wind properties (averaged over the AS), showed less variation between the ZDI and the SH-ZDI cases (see [Table 5.1](#)). Assuming the same initial base conditions, the SH-ZDI simulations led to denser (by $\sim 10\text{--}30\%$) and colder (by $\sim 25\text{--}35\%$) winds compared to the ZDI-driven cases. As with the solar simulations, the average stellar wind speed at the AS seems to be lower for higher surface field strengths. These differences are related to the radial behaviour of the thermodynamical quantities (i.e., $\langle R_{AS} \rangle$ is larger in the SH-ZDI case), and the underlying coronal structure, which in turn depends on additional factors such as the ZDI map resolution, completeness, and field complexity (see [Alvarado-Gómez et al. 2016](#)). This clearly shows the importance of numerical models which self-consistently simulate both, the corona and stellar wind domains. In the following section, we present the resulting solar and stellar wind properties inside the IH module.

5.3.2 Stellar winds and astrospheric current sheet

As mentioned in [Sect. 5.2](#), the simulations on the IH domain are driven by the steady-state solutions of the SC region, coupled at $25 R_*$ (white sphere in [Figs. 5.5 to 5.10](#) and [Fig. 5.12](#)). Similarly to the SC domain, we present the density structure of the wind, projected onto the equatorial plane, and the heliospheric / astrospheric current sheet. The associated colour scale for n is preserved between the SC and IH results, showing the consistency of the coupled MHD solution. Additionally, the 3D structure of the radial wind

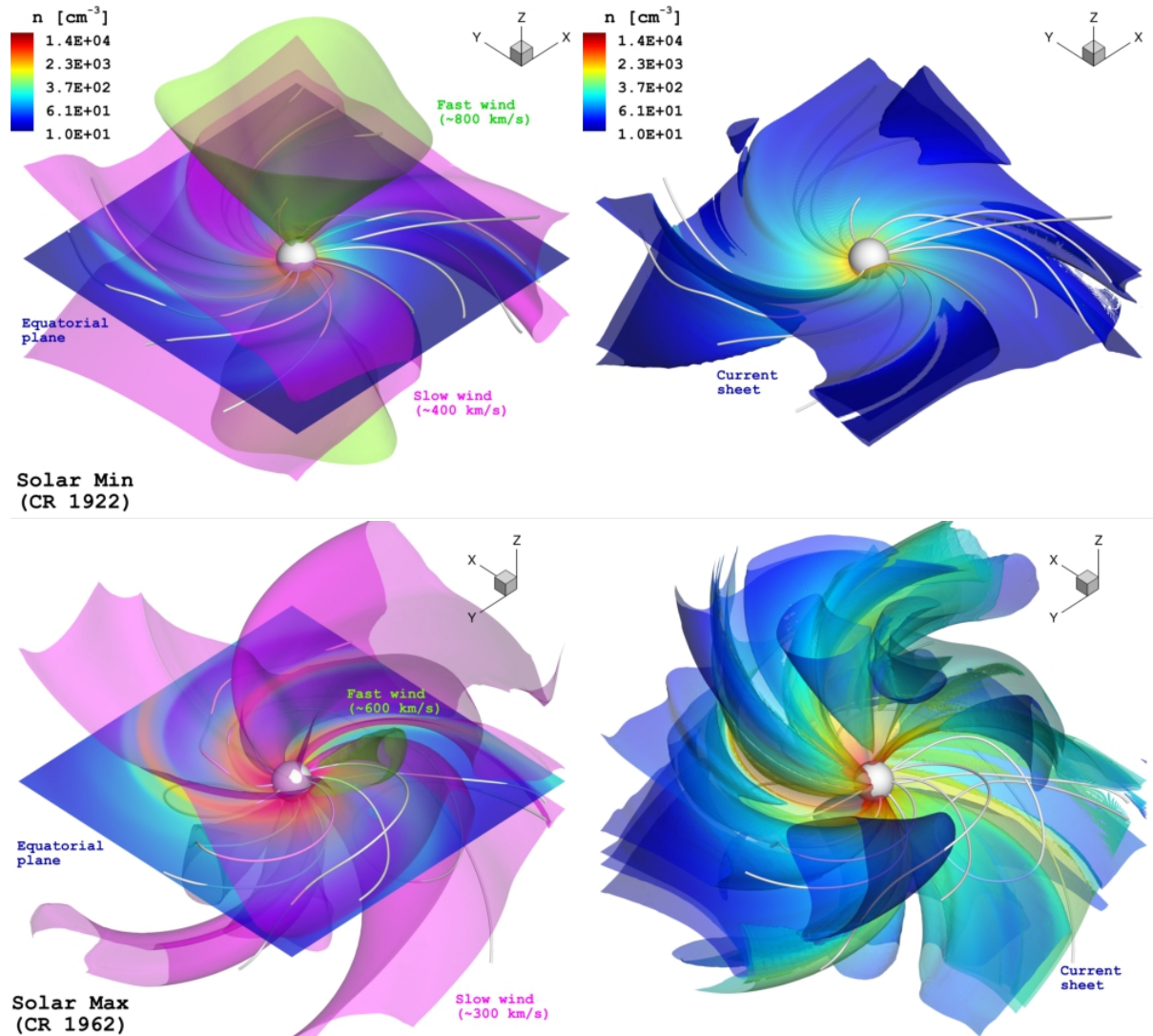


Figure 5.5: Simulation results in the inner heliosphere (IH) domain for activity minimum (CR 1922, *top*) and maximum (CR 1962, *bottom*). The central white sphere denotes the boundary with the solar corona (SC) domain at $25 R_{\odot}$ (Sect. 5.3.1). The density structure of the steady-state solution is displayed on the equatorial plane (*left*) and the heliospheric current sheet (*right*). In the left panel, the topology and associated magnitudes of the dominant radial velocity components (u_r) of the solar wind are also included (fast: *green* | slow: *magenta*). The density (n) colour scale is preserved among the different panels. Selected 3D magnetic field lines are shown in white.

velocity is visualised via two iso-velocity surfaces (translucent shades in Figs. 5.5 to 5.9, *left*), labeled as fast (*green*) and slow (*magenta*) wind components. The magnitude of the fast component is calculated using the peak wind velocity achieved in the simulation, and taking the *floor* with respect to a 100 km s^{-1} velocity bin width. The magnitude of the slow wind component is simply taken as half of the previously defined fast wind. As an

example, the solar minimum simulation showed a peak wind velocity of $u_r \sim 885 \text{ km s}^{-1}$, so the fast and slow wind iso-surfaces were taken at 800 km s^{-1} and 400 km s^{-1} , respectively (Fig. 5.5, *top*). The 600 km s^{-1} and 300 km s^{-1} solar wind components in the activity maximum case (Fig. 5.5, *bottom*), were defined in the same way, as a result of a peak wind speed of $u_r \sim 614 \text{ km s}^{-1}$ in the 3D domain.

As can be seen from Fig. 5.5, the expected global properties and topology of the solar wind (for both activity states), are properly recovered in the simulation. The activity minimum case shows the classical solar wind configuration, with the fast wind emerging from the poles, and the slow wind close to the equator, describing a “ballerina skirt” shape along the heliospheric current sheet (Fig. 5.5, *top-right*). In the activity maximum case, a more complex solution is obtained, with a 3D structure dominated by the slow component which is no longer restricted to lower latitudes. As the overall velocity of the wind is reduced (compared to the solar minimum case), the fast wind component is nearly inexistent in this solution (Fig. 5.5, *bottom left*). Additionally, a dramatic change in complexity can be observed in the heliospheric current sheet (Fig. 5.5, *bottom-right*), as was expected from the resulting topology of this structure inside the inner domain of the simulation (Sect. 5.3.1). The density structure of the solar wind is clearly enhanced during the activity maximum solution, as can be compared from the equatorial and current sheet projections in Fig. 5.5. This is quantified in more detail in Sect. 5.4.

Figure 5.6 contains the results for HD 22049, driven by the ZDI (*top*) and the SH-ZDI (*bottom*) magnetic field maps. As expected from the SC region (Sect. 5.3.1), differences in the geometry and the wind properties are developed in this domain. Only one broad fast wind region emerges in the ZDI-driven case, with an associated speed of $u_r \sim 1000 \text{ km s}^{-1}$ (Fig. 2.5, *top-left*). This wind component is roughly perpendicular to the astrospheric current sheet which, close to the star, displays a tilt of $\sim 45^\circ$ [†], and a rotational drag by the wind at farther distances (Fig. 5.6, *top-right*). In turn, four such fast wind regions are formed in the SH-ZDI simulation, displaying a $\sim 30\%$ reduction of the wind speed (Fig. 5.6, *bottom-left*). From this wind regime, the two broader structures are again nearly perpendicular to each side of the astrospheric current sheet, which in this case is almost orthogonal to the equatorial plane (Fig. 5.6, *bottom-right*). The remaining two fast wind regions appear as collimated jet-like structures, closely aligned with the local orientation of astrospheric current sheet. The latter, as with the solar minimum case (Fig. 5.1, *top*), shows a connection with the slow wind region in both simulations of HD 22029, where the denser material is carried away from the star.

The results for HD 147513 inside the IH simulation domain are presented in Fig. 5.7, where the maximum radial wind speed was $u_r \simeq 1040 \text{ km s}^{-1}$. Two cone-shaped regions, associated with the fast wind component, appear close the north pole of the star. No southern counterpart for these regions was obtained in the simulation. The topologies of the slow wind component and the astrospheric current sheet, clearly resemble the solar maximum solution in this domain (see Fig. 5.5, *bottom*). This is consistent with the results obtained inside the SC module (Sect. 5.3.1) and with the simulated global properties of

[†]With respect to the stellar rotation axis (i.e., z-axis).

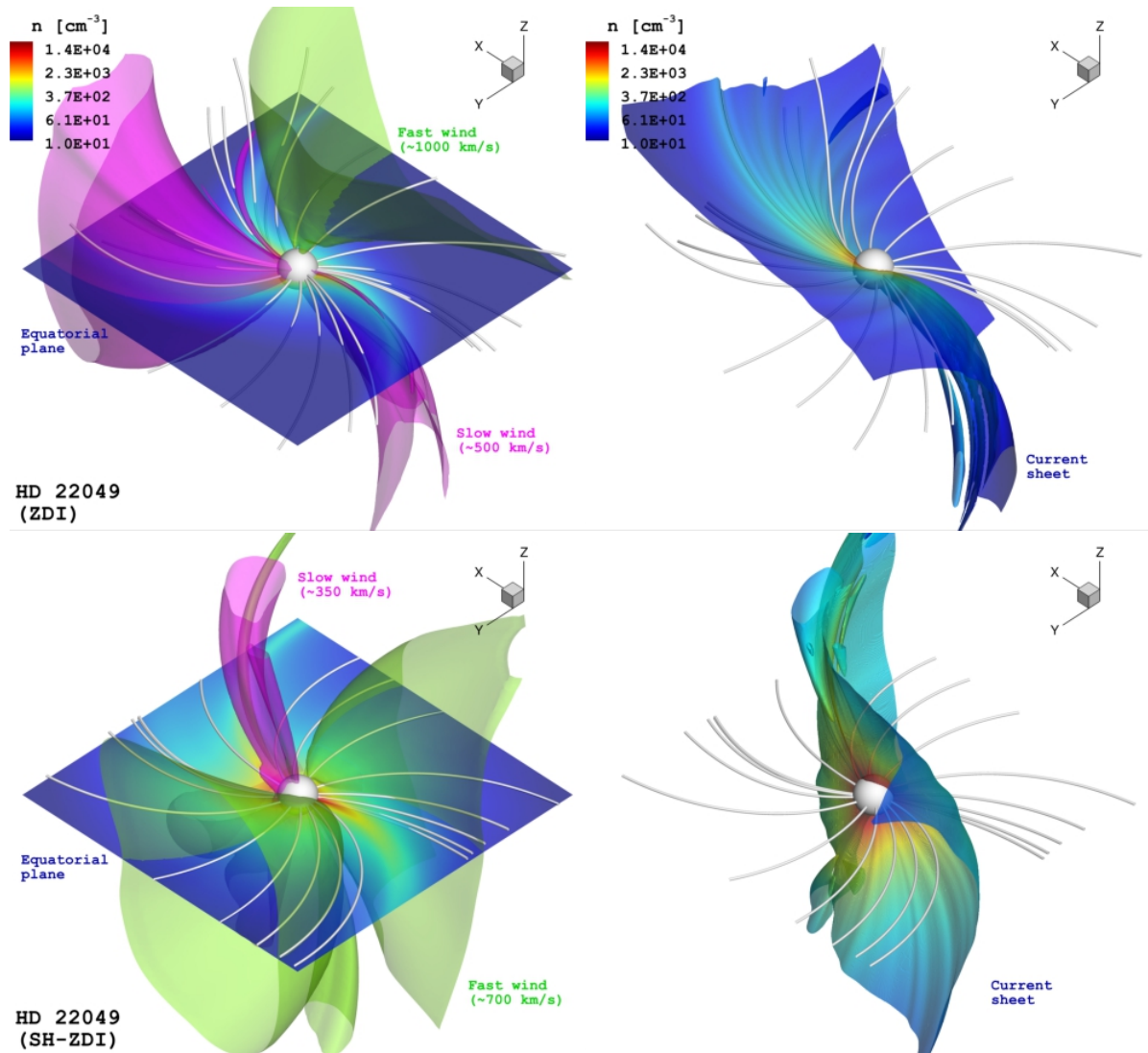


Figure 5.6: Simulation results in the IH domain for HD 22049 driven by the ZDI (*top*) and SH-ZDI (*bottom*) magnetic field maps. The central white sphere denotes the boundary with the SC domain at $25 R_*$ (Sect. 5.3.1). The density structure of the steady-state solution is displayed on the equatorial plane (*left*) and the astrospheric current sheet (*right*). In the left panel, the topology and associated magnitudes of the dominant radial velocity components (u_r) of the stellar wind are also included (fast: *green* | slow: *magenta*). The perspective and density colour scale are preserved among the different panels. Selected 3D magnetic field lines are shown in white.

the corona in both cases (Alvarado-Gómez et al. 2016). However, as discussed in the first paper of this study, these results could be affected by the relatively low spatial resolution of the SH-ZDI map of HD 147513 (see Hussain et al. 2016). Still, this solution indicates that the coronal structure and wind characteristics may be extremely complex, even for cases with a relatively simple surface field distribution. In this context, scaling relations

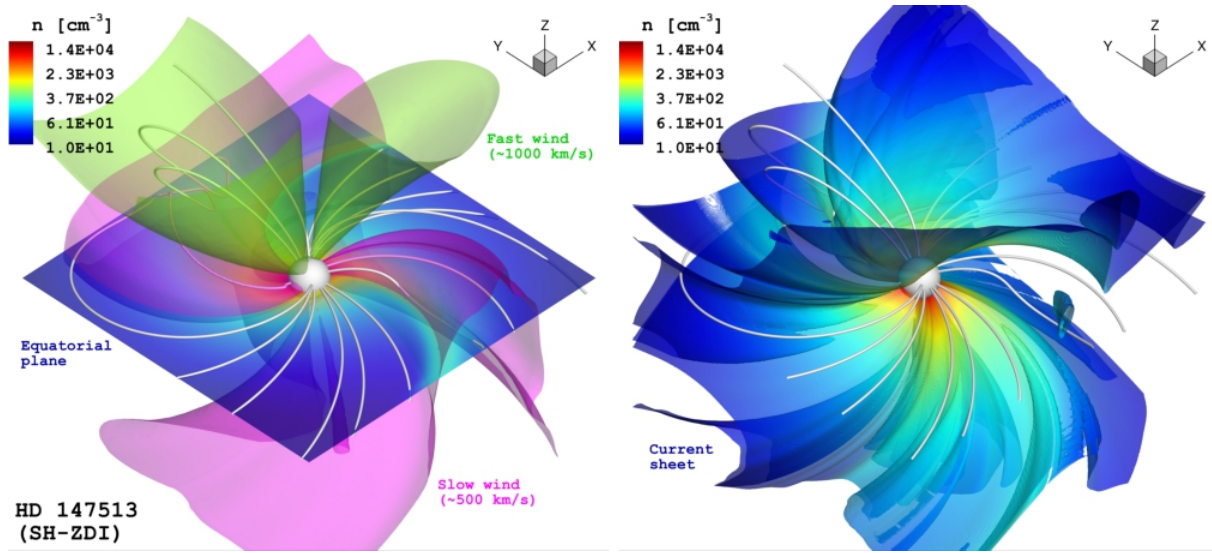


Figure 5.7: Simulation results in the IH domain for HD 147513 driven by the SH-ZDI magnetic field maps. The central white sphere denotes the boundary with the SC domain at $25 R_*$ (Sect. 5.3.1). The density structure of the steady-state solution is displayed on the equatorial plane (*left*) and the astrospheric current sheet (*right*). In the left panel, the topology and associated magnitudes of the dominant radial velocity components (u_r) of the stellar wind are also included (fast: *green* | slow: *magenta*). Selected 3D magnetic field lines are shown in white.

involving average stellar / magnetic properties and extrapolations, cannot provide complete descriptions of the coronal and wind conditions of a particular system. This is critical for characterising planet-hosting stars, where those specific environmental properties (e.g., coronal emission, stellar wind structure, mass loss, etc) will strongly affect the exoplanetary conditions of the system.

5.3.3 Environment of the HD 1237 system

The results of the simulations performed on the HD 1237 system, driven by the ZDI and SH-ZDI maps, are presented in Figs. 5.8 and 5.9, respectively. Two fast wind structures oriented in opposite directions, appear close to the equatorial region of the system. These structures are connected to the large, low-latitude coronal holes developed in this system (see Alvarado-Gómez et al. 2016). The wind speed reaches $\sim 1100 \text{ km s}^{-1}$ in the ZDI-driven case, dropping to $\sim 900 \text{ km s}^{-1}$ in the SH-ZDI simulation. As in some of the previously described cases, the fast wind regions appear roughly perpendicular to the astrospheric current sheet, along which the slow wind region develops. The global topology of the stellar wind is similar between both cases, yet an enhancement in the particle density is again obtained in the SH-ZDI case (see Sects. 5.3.1 and 5.3.2). A more quantitative comparison of all cases is presented in the following section.

As described in Sect. 5.2, the GM module of the SWMF was additionally coupled to the IH solution to investigate the exoplanetary conditions in relation to the developed stellar

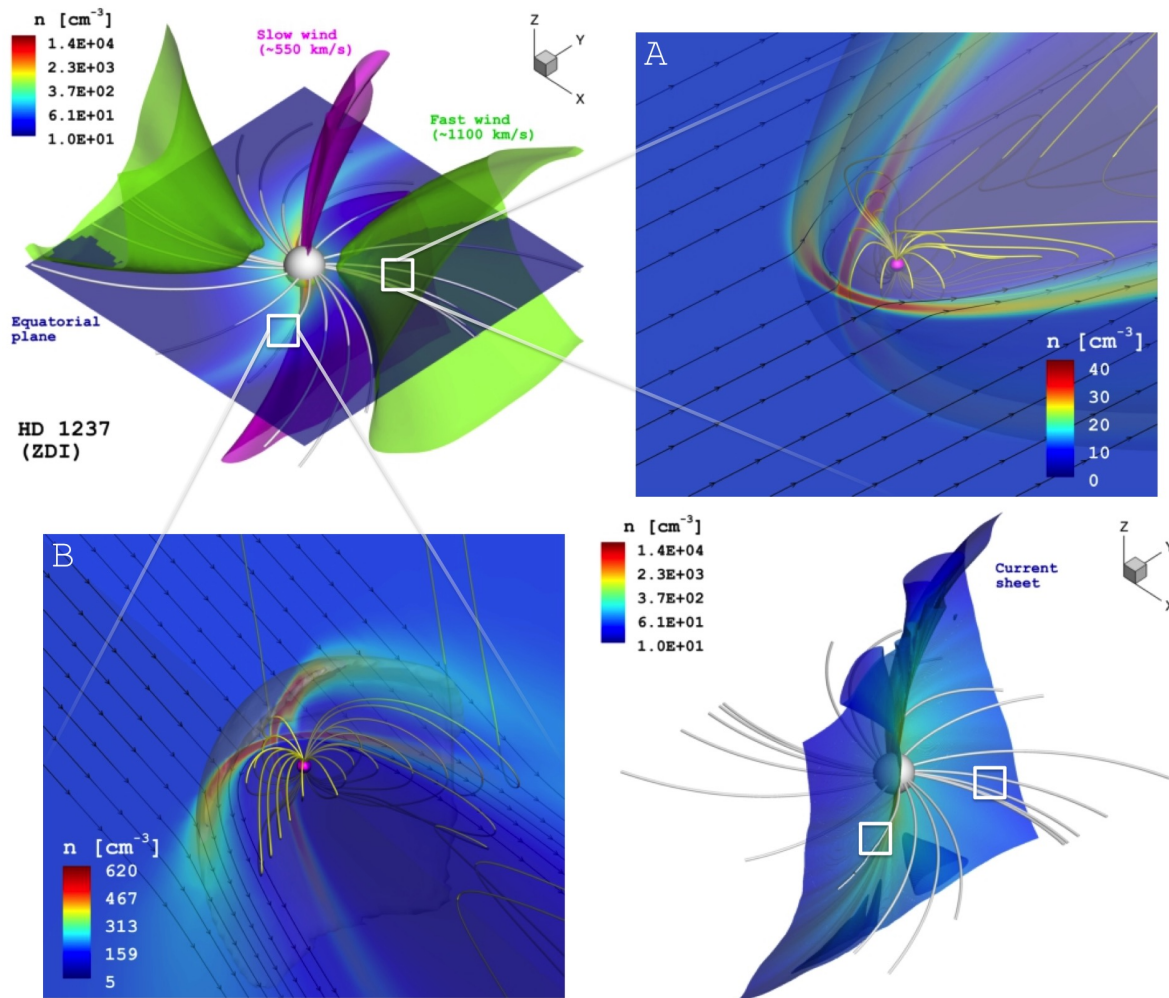


Figure 5.8: Simulated environment of the HD 1237 system driven by the ZDI magnetic field map. The structure of the stellar wind and astrospheric current sheet obtained from the IH module, are presented in the *top-left* and *bottom-right* panels, respectively. The density structure of the steady-state solution is displayed on the equatorial plane (*top-left*) and the astrospheric current sheet (*bottom-right*). In the *top-left* panel, the topology and associated magnitudes of the dominant radial velocity components (u_r) of the stellar wind are also included (fast: *green* | slow: *magenta*). The central white sphere denotes the boundary with the SC domain at $25 R_*$ (Sect. 5.3.1), and selected 3D stellar wind magnetic field lines are shown in white. The two remaining panels contain the simulation results of the GM module, obtained at the locations indicated on the IH domain by the white squares (not to scale). The distance to the star has been taken as the mean orbital separation of this system ($a = 0.49$ AU, Naef et al. 2001). The central purple sphere corresponds to the planetary surface ($1 R_p$) and selected 3D planetary magnetic field lines are displayed in yellow. The direction of the incident stellar wind is indicated by the black streamlines. The particle density distribution of the solution shows the development of a bow-shock structure in both cases (translucent white shade).

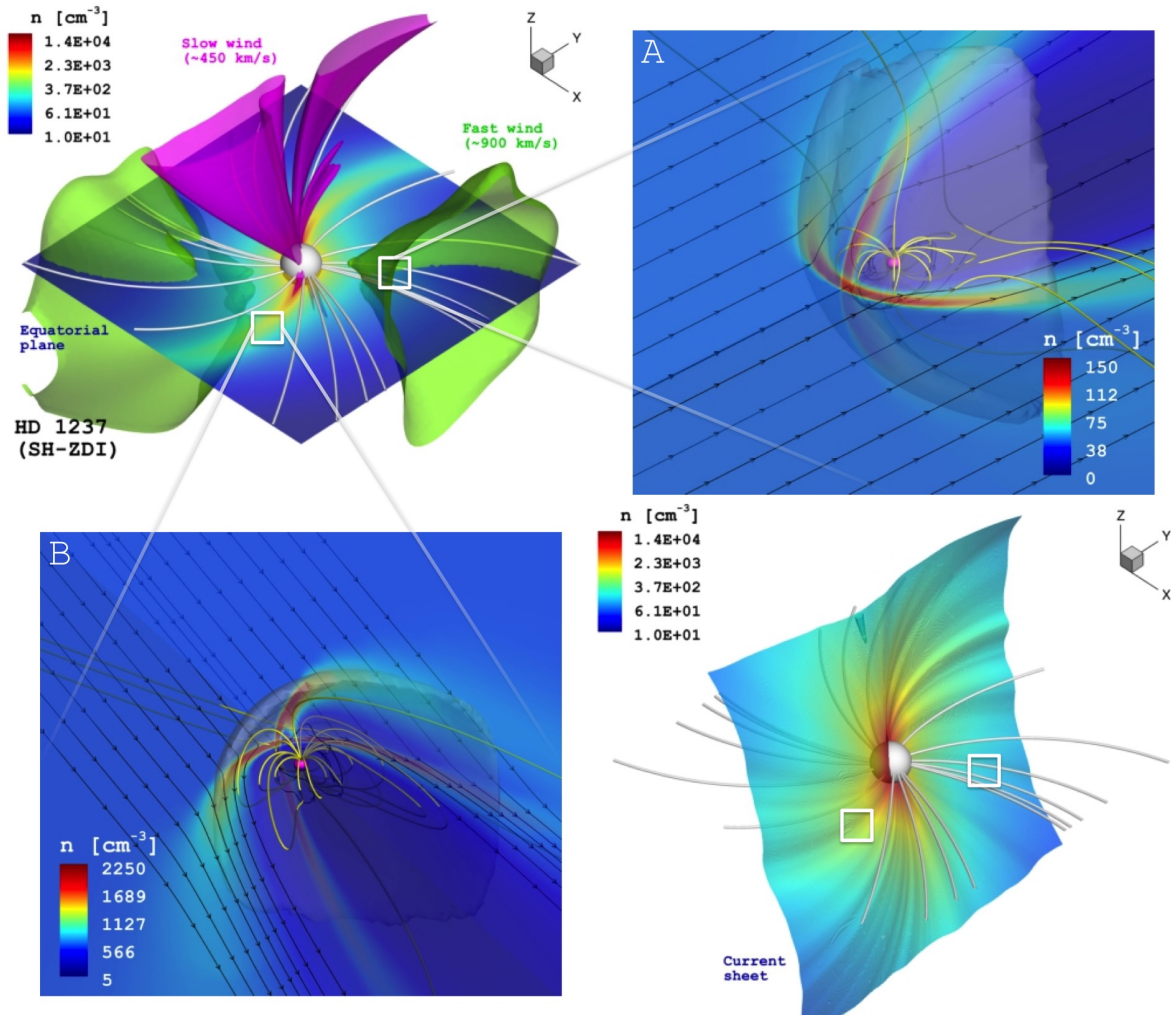


Figure 5.9: Simulated environment of the HD 1237 system driven by the SH-ZDI magnetic field map. The structure of the stellar wind and astrospheric current sheet obtained from the IH module, are presented in the *top-left* and *bottom-right* panels, respectively. The density structure of the steady-state solution is displayed on the equatorial plane (*top-left*) and the astrospheric current sheet (*bottom-right*). In the *top-left* panel, the topology and associated magnitudes of the dominant radial velocity components (u_r) of the stellar wind are also included (fast: *green* | slow: *magenta*). The central white sphere denotes the boundary with the SC domain at $25 R_*$ (Sect. 5.3.1), and selected 3D stellar wind magnetic field lines are shown in white. The two remaining panels contain the simulation results of the GM module, obtained at the locations indicated on the IH domain by the white squares (not to scale). The distance to the star has been taken as the mean orbital separation of this system ($a = 0.49$ AU, Naef et al. 2001). The central purple sphere corresponds to the planetary surface ($1 R_p$) and selected 3D planetary magnetic field lines are displayed in yellow. The direction of the incident stellar wind is indicated by the black streamlines. The particle density distribution of the solution shows the development of a bow-shock structure in both cases (translucent white shade).

Table 5.2: Parameters of the incident stellar wind and resulting properties inside the GM module for each location.

Location / Case	Incident stellar wind (IH module) [†]				Global Magnetosphere (GM module)		
	n [cm ⁻³]	T [$\times 10^5$ K]	\mathbf{u}_{sw} [km s ⁻¹]	\mathbf{B} [nT]	R_M [R_p] ^a	P_T^{max} [nPa] ^b	$\langle n \rangle$ [cm ⁻³] ^c
A / ZDI	10.9	5.37	(-829.5, 804.8, -5.4)	(-16.5, 10.5, 0.01)	7.7	51.5	1.13
A / SH-ZDI	45.5	3.40	(-641.3, 638.2, -0.2)	(-43.7, -28.7, 0.31)	6.5	101.7	3.05
B / ZDI	160.0	1.03	(-383.7, 466.4, -6.3)	(1.22, -3.31, -0.18)	6.4	165.2	9.13
B / SH-ZDI	596.7	1.12	(-222.5, 553.7, -5.8)	(1.15, -23.1, 0.60)	4.7	618.7	35.1

^a Magnetopause standoff distance (i.e., magnetopause day-side separation).

^b Maximum value of the total pressure ($P_T = P_{\text{gas}} + P_{\text{dyn}} + P_{\text{mag}}$) at the bow-shock location.

^c Average particle density at a spherical surface with $R = 2R_p$.

[†] Cartesian components of the vector quantities are provided.

wind properties in this system. Two different locations in the IH domain, represented by the white squares in Figs. 5.8 and 5.9, were used for this purpose. These locations correspond to a fast wind, low density region (sector A | Figs. 5.8 and 5.9, *top-right*), and a high-density streamer of the stellar wind, close to the astrospheric current sheet (sector B | Figs. 5.8 and 5.9, *bottom-left*). The distance to the central star was 0.49 AU in both cases, matching the mean orbital separation of this system (Naef et al. 2001). The interaction between the magnetised stellar wind and the planetary magnetosphere, led to the development of a bow-shock structure, which self-consistently reacts to the local conditions. A summary of the driving stellar wind properties, and the resulting magnetospheric conditions in both locations, is presented in Table 5.2.

A larger response from the magnetosphere was obtained in the SH-ZDI case as expected, given the incident stellar wind properties in the IH domain (see Table 5.2). In the fast wind region (location A in Figs. 5.8 and 5.9), the maximum total pressure at the bow-shock (P_T^{max}) appeared ~ 2 times larger in the SH-ZDI case compared to the ZDI simulation. This led to $\sim 15\%$ reduction in the magnetosphere size (in terms of the magnetopause standoff distance R_M) in the former case compared to the latter. A similar situation was obtained in the simulations at the high-density streamer sector (location B in Figs. 5.8 and 5.9). The SH-ZDI case yielded a ~ 3.7 times larger P_T^{max} value, and a $\sim 25\%$ reduction in R_M , in comparison with the ZDI-driven model. On the other hand, the resulting conditions were more extreme in the dense streamer sector (location B), than in the fast wind region (location A), regardless of the driving field distribution. This is evidenced by the ~ 10 times increase in the average particle density $\langle n \rangle$, between locations A and B (see Table 5.2), calculated at $1 R_p$ above the planetary surface (i.e., over a spherical surface with $R = 2 R_p$). As can be seen for Figs. 5.8 and 5.9, the developed wind structure shows a larger contrast in density than in velocity. This general property was common in the remaining systems considered here and in the solar cases (see Sect. 5.3.2). In this context, the results obtained for locations A and B indicate that, due to the structure of the stellar winds in these kind of stars, the process of particle injection into the planetary atmosphere would be more sensitive to the particle density rather than to the velocity profile of the stellar wind.

In connection with this last result, we can consider the simulated wind structure and the exoplanetary orbit to investigate the possible magnetospheric radio emission from the exoplanet of this system. The theoretical considerations for this kind of emission have been presented in various papers (e.g., Farrell et al. 1999; Zarka et al. 2001; Grießmeier et al. 2007; Jardine & Collier Cameron 2008; Nichols 2011; Nichols & Milan 2016), and extensive observational searches have been performed over the last decade (e.g., Lazio & Farrell 2007; Lazio et al. 2010a, 2010b; George & Stevens 2007; Lecavelier et al. 2009, 2011, 2013; Hallinan et al. 2013; Sirothia et al. 2014).

For the particular case of HD 1237, Stevens (2005) identified this system as a good candidate for detection, with a mean radio flux of 8 mJy at a peak frequency of ~ 40 MHz, reaching up to ~ 20 mJy during periastron passage. Lacking better information, Stevens (2005) used reasonable approximations regarding the stellar wind and planetary properties, such as a scaling relation from Wood et al. (2002) between the X-ray flux and the mass loss rate of the host star (see Sect. 5.4.1), spherical symmetry for the stellar wind, scaling of the planetary magnetic moment and radius, among others. While no better constraints are available for the planetary properties, our data-driven simulations provide a more realistic description of the wind of this star. For this reason, we retained the assumptions made by Stevens (2005) regarding the exoplanet properties of radius and magnetic moment \mathcal{M}_p (i.e., $R_p = R_{\text{J}} \simeq 7.2 \times 10^9$ cm; $\mathcal{M}_p = \mathcal{M}_{\text{J}} \simeq 1.6 \times 10^{30}$ G cm³). This implies that the 40 MHz peak frequency of the expected magnetospheric radio emission remains unaltered (see Stevens 2005). For this analysis we only consider the results from the SH-ZDI simulation, as it provides favourable conditions in terms of increased stellar wind density (See Figs. 5.8 and 5.9).

Following Zarka et al. (2001), the emitted radio power from the exoplanet, R^{pow} , will be proportional to the kinetic power $K_{\text{sw}}^{\text{pow}}$ associated with the wind-magnetosphere interaction (i.e., $R^{\text{pow}} = \alpha K_{\text{sw}}^{\text{pow}}$, with $\alpha = 7 \times 10^{-6\dagger}$). By combining the simulated stellar wind structure with the assumed exoplanetary properties, we can compute $K_{\text{sw}}^{\text{pow}}$, using the relation

$$K_{\text{sw}}^{\text{pow}} = nu_{\text{sw}}^3 \pi R_{\text{M}}^2, \quad (5.1)$$

where R_{M} denotes radius of the magnetosphere, which depends on the local conditions of the wind and the planetary magnetic field (e.g., Table 5.2). As discussed by Stevens (2005) and references therein, R_{M} can be expressed as

$$R_{\text{M}} \propto \left(\frac{\mathcal{M}_p^2}{16\pi nu_{\text{sw}}^2} \right)^{1/6}, \quad (5.2)$$

and therefore, can be calculated at each point of the simulation domain. However, as the exoplanet location is not arbitrary, only values of $K_{\text{sw}}^{\text{pow}}$ along the planetary orbit will be relevant for the predicted magnetospheric radio emission.

[†]This relation is known as the *Radiometric Bode Law*. See Zarka et al. (2001) and Lazio et al. (2004)

Figure 5.10: Pole-on view on the equatorial distribution of the kinetic power $K_{\text{sw}}^{\text{pow}}$ from wind-magnetospheric interaction (see text for details). The *green* (fast) and *magenta* (slow) velocity components of the stellar wind are identical as in Fig. 5.9 (*top-left*). The configuration of the exoplanet orbit (white ellipse), with respect to the structure of the stellar wind, maximises the radio power at P_1 (periastron), and yields a minimum in location P_2 .

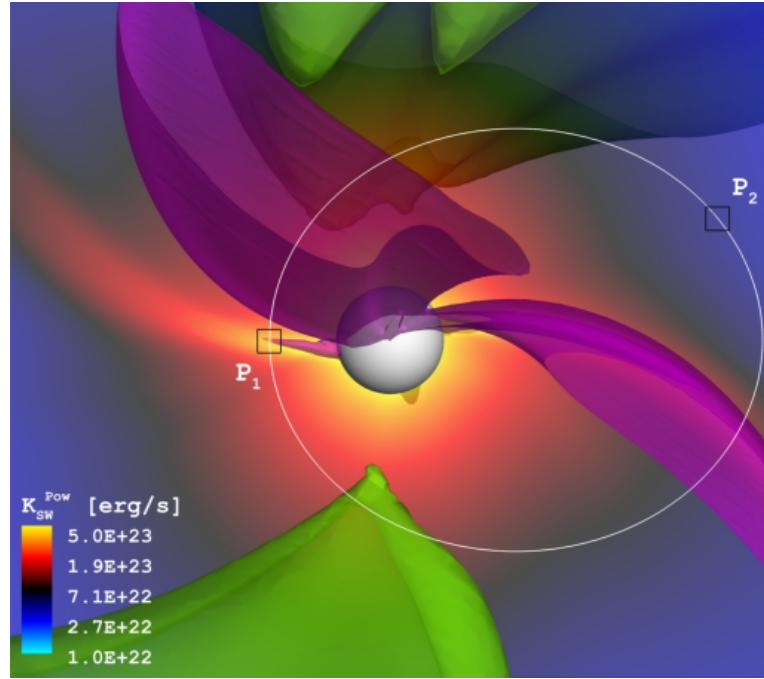


Figure 5.10 shows the equatorial distribution of $K_{\text{sw}}^{\text{pow}}$, alongside the dominant radial wind components of the SH-ZDI simulation of this system (pole-on view of Fig. 5.9, *top-left*). The exoplanet orbit, indicated by the white ellipse, has been constructed using the parameters listed by Naef et al. (2001). The wind-orbit layout presented in Fig. 5.10 corresponds to the optimal conditions for magnetospheric radio emission in this system (i.e., periastron passage through a dense wind streamer, location P_1 in Fig. 5.10). In this way, we obtain a maximum emitted radio power of $R^{\text{pow}} = \alpha K_{\text{sw}}^{\text{pow}} \simeq 3.5 \times 10^{18} \text{ erg s}^{-1}$, which yields a corresponding radio flux on Earth[†] of $F_{\oplus}^{\text{R}} \simeq 12 \text{ mJy}$. This value is reduced up to a factor of ~ 10 in the location marked as P_2 in Fig. 5.10, which does not coincide with apastron in this configuration.

Our maximum radio flux F_{\oplus}^{R} is roughly half of the previous estimate of 21.5 mJy of Stevens (2005). In turn, the predicted orbital variation in our simulation is more than twice as large as the ~ 4.5 factor obtained in this previous work. Given that this previous analysis was performed assuming a stellar wind velocity of 400 km s^{-1} (slower than the value predicted in our simulations at periastron by $\sim 25\%$), the higher radio power obtained by Stevens (2005) must be connected with the assumed stellar wind density (obtained via a spherically symmetric wind with $\dot{M} = 85.7 \dot{M}_{\odot}$). As will be discussed in the following section, this mass loss rate value is probably overestimated, supporting a lower value of the expected planetary radio flux. The difference in the orbital variation of F_{\oplus}^{R} appears as a consequence of a more realistic description of the 3D stellar wind structure provided by our data-driven simulation.

[†]We have used here the distance to HD 1237 of 17.5 pc (Koen et al. 2010).

Finally, the obtained values for the magnetospheric radio emission should be within the expected capabilities of the Square Kilometre Array (SKA), particularly in the low-frequency band (50 MHz up to 350 MHz, see [Zarka et al. 2015](#)). The on-sky location of this system [α (J2000): $00^{\text{h}} 16^{\text{m}} 16.68^{\text{s}}$, δ (J2000): $-79^{\circ} 51' 04.25''$], prevents observations with current instrumentation with low-frequency capabilities, such as the Low-Frequency Array (LOFAR) and the Ukrainian T-shaped Radio telescope (UTR-2).

5.4 Analysis and discussion

In a similar manner to [Alvarado-Gómez et al. \(2016\)](#), we use the simulation results to analyse several aspects of the environment of these systems. In this way, we consider the connection between the surface magnetic field properties, and the predicted mass and angular momentum loss rates associated with the wind (Sect. 5.4.1). In addition, a characterisation of the stellar wind properties at the inner edges of the habitable zones of these systems is presented in Sect. 5.4.2.

5.4.1 Magnetism and mass / angular momentum loss rates

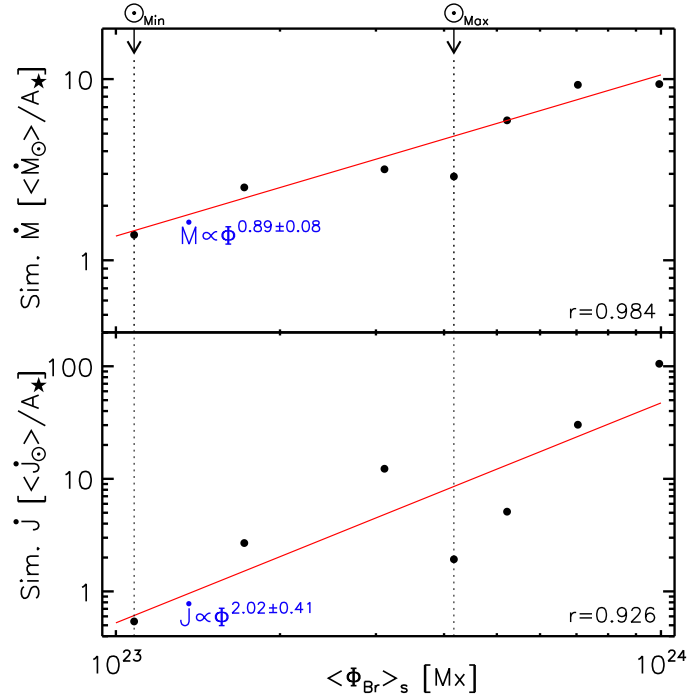
As with the first paper of this study, this analysis considers the results of our simulations independently (i.e., solar min/max and stellar ZDI/SH-ZDI cases). Figure 5.11 shows the dependence of the simulated mass and angular momentum loss rates (\dot{M} and \dot{J} , respectively), with respect to the unsigned radial magnetic flux Φ_{Br} , averaged over the stellar surface. An approximately linear dependence is obtained for \dot{M} ($\propto \Phi^{0.89 \pm 0.08}$)[†], while a quadratic relation (with increased scatter) is obtained for \dot{J} ($\propto \Phi^{2.02 \pm 0.41}$).

Given the direct dependence of \dot{J} with \dot{M} (see [Cohen et al. 2010](#); [Matt et al. 2012](#); [Cohen & Drake 2014](#); [Réville et al. 2015a](#); [Matt et al. 2015](#); [Garraffo et al. 2015b](#)), we will focus our discussion on the results obtained for the mass loss rate. A diagram similar to Fig 5.11, relating the simulated coronal radiation (e.g., EUV, X-rays) with $\langle \Phi_{\text{Br}} \rangle_{\text{s}}$ was presented in [Alvarado-Gómez et al. \(2016\)](#).

We can relate these observational studies with our simulations, by combining the \dot{M} – Φ relation shown in Fig. 5.11, with the $L_{\text{X}} \propto \Phi^{1.06}$ dependence obtained in [Alvarado-Gómez et al. \(2016\)](#). The latter becomes slightly more steep when expressed in terms of F_{X} (i.e., $F_{\text{X}} \propto \Phi^{1.13}$). By removing the dependence on Φ , we obtain a simulated mass loss-activity relation in the form of $\dot{M}_{(\text{sim})} \propto F_{\text{X}(\text{sim})}^{\gamma}$ with $\gamma = 0.79_{-0.15}^{+0.19}$, considerably flatter than the observed one. However, we stress that this is the first time that this relation is self-consistently constructed in a model, by computing the X-ray coronal emission and mass loss rate associated with the stellar wind, using the same data-driven numerical simulation. To understand the differences in these relations, we need to consider several aspects connected to our simulations and the observations. A comprehensive summary is listed below:

[†]For simplicity, in the following relations Φ represents $\langle \Phi_{\text{Br}} \rangle_{\text{s}}$.

Figure 5.11: Simulated mass loss rate (\dot{M} , *top*) and angular momentum loss rate (\dot{J} , *bottom*) as a function of the surface-averaged unsigned radial magnetic flux $\langle\Phi_{\text{Br}}\rangle_{\text{s}}$. Both quantities are expressed in units of average solar values (Sect. 5.3.1), normalised by the surface area of each star. Individual points denote the results of each simulation presented in Sect. 5.3, including the solar cases (indicated by the dashed vertical lines). The *red* solid lines show power-law fits to the simulated data with the corresponding correlation coefficient, r , in each case.



- As presented in Sect. 5.3, the results from the solar simulations are consistent with the observational data. This is not only the case for the mass loss rate (Sect. 5.3.1) but also for the topology and physical properties of the solar wind during activity minimum and maximum (Sect. 5.3.2, Fig. 5.5). Similar results were obtained for the simulated coronal structure for both activity states (Alvarado-Gómez et al. 2016).
- For the stellar systems considered here, an observational estimate of the mass loss rate is only available for HD 22040 (ϵ Eri, Wood et al. 2002). As can be seen from Table 5.1, the ZDI-driven simulation predicts an absolute mass loss rate $\dot{M}_{\text{ZDI}} \simeq \dot{M}_{\odot}$, while the SH-ZDI case leads to $\dot{M}_{\text{SH-ZDI}} \sim 5 \dot{M}_{\odot}^{\dagger}$. This last value differs by a factor of 6 from the estimation from astrospheric Lyman- α absorption ($\dot{M}_{\text{Ly-}\alpha} \simeq 30 \dot{M}_{\odot}$).

For the other two stars, HD 1237 and HD 147513, Stevens (2005) derived relatively high \dot{M} values ($\sim 86 \dot{M}_{\odot}$ and $105 \dot{M}_{\odot}$, respectively), by using an earlier version of the mass loss-activity relation proposed by Wood et al. 2002 (i.e., $\dot{M} \propto F_{\text{X}}^{1.15 \pm 0.20}$). As described before, the range of validity of this relation was revisited by Wood et al. (2005a) and Wood et al. (2014), indicating a break for $F_{\text{X}} > 10^6 \text{ erg cm}^2 \text{ s}^{-1}$, with evidence in support of much smaller \dot{M} values for stars in this activity regime. This evidence is not only given directly by the astrospheric detections of ξ Boo A and π^1 UMa (Wood et al. 2014), but also indirectly, by similar UV observations of a considerable number of active stars yielding non-detections (Wood et al. 2005b). Both stars, HD 1237 and HD 147513, have X-ray fluxes above this empirical F_{X} threshold (by factors of 2.1 and 1.9, respectively), thus the values listed in Stevens (2005) are probably overestimated.

[†]The reasons for this relative difference are discussed in Sect. 5.3.1.

- In the case of HD 22049, this discrepancy may be addressed by enhancing the base conditions in the simulation of this star. While this certainly would increase the mass loss rate (see [Cohen & Drake 2014](#)), this would also imply a different prediction for the coronal emission in all energy bands (e.g., EUV, SXR). As discussed in [Alvarado-Gómez et al. \(2016\)](#), the SH-ZDI simulation of this system provides reasonable agreement in both, EUV and X-rays, to the estimated coronal conditions via spectral synthesis diagnostics ([Sanz-Forcada et al. 2011](#)). Still, further adjustments will be explored for this system in a future systematic approach, in order to improve the balance in the coronal heating (i.e., to the Emission Measure distribution EM , see [Ness & Jordan 2008](#); [Alvarado-Gómez et al. 2016](#)), as well as to refine the predictions of the \dot{M} value. It might even be necessary to include reconnection events as an additional (or dominant) heating mechanism, which appear to drive the coronal conditions in very active stars such as HD 22049 (see [Drake et al. 2000](#)). As a drawback, this procedure introduces additional degrees of freedom for the model results, which then complicates the consistent comparison with the reference the solar cases (and with additional stellar simulations).
- Another possibility is related to a temporal dependence of the mass loss–activity relation. In the case of the Sun, it is well known that the coronal emission is enhanced by one order of magnitude over the course of the 11-year activity cycle ([Hathaway 2015](#)). In turn the solar mass loss rate shows little correspondence with the activity state, fluctuating within a factor of ~ 2 around a mean value of $\dot{M}_\odot \simeq 2 \times 10^{-14} M_\odot \text{ yr}^{-1}$ (Sect. 5.3.1, see also [Cohen 2011](#)). While there is at least one single star showing a similar cycle-induced[†] pattern as the Sun in X-rays (*ι* Horologii, see [Sanz-Forcada et al. 2013](#)), there is no evidence suggesting that stellar mass loss rates must be cycle-independent (or as near-to-independent as the Sun is). Therefore, variations of 1–2 orders of magnitude in \dot{M} , over the course of any possible activity cycle (or due to cycle-dominated transients such as Coronal Mass Ejections – CMEs, see [Drake et al. 2013](#)), cannot be excluded from the mass loss–activity relation. This would provide a natural explanation for the observed break in this relation, at the regime of high coronal activity.
- Given the magnetic nature of these two processes in Sun-like stars (coronal activity and mass loss), any time dependence of the mass loss–activity relation should be connected with the temporal evolution of the stellar magnetic field. Unfortunately, for the two stars considered in this work located above the break in this relation (HD 1237 and HD 147513), only single-epoch[‡] surface magnetic field reconstructions using ZDI are available ([Alvarado-Gómez et al. 2015](#); [Hussain et al. 2016](#)).

[†]The cycle length (~ 1.6 yr) is much shorter than the solar cycle, as expected from the relatively young age of the star (~ 500 – 740 Myr, see [Sanz-Forcada et al. 2013](#)).

[‡]Actually, two independent ZDI maps were recovered for HD 1237 separated by 5 months. However, the quality of the second map was far from optimal, due to a very limited phase coverage (Appendix A, see also [Alvarado-Gómez et al. 2015](#)). Still, this partial field reconstruction indicated very similar properties as with the robust ZDI maps of the first epoch, which have been used to drive the models presented here.

On the other hand, a long-term ZDI monitoring campaign of HD 22049 is currently being carried out by the BCoolest[†] collaboration. Six large-scale magnetic field maps have been recovered over a period of 7 years (2007–2013, see Jeffers et al. 2014b). As described in the previous Chapter, we have used the set of HARPSpol@ESO3.6m observations available for this star so far (acquired in 2010, Piskunov et al. 2011), to generate the ZDI maps driving the simulations. This was done to ensure a consistent comparison with ZDI-driven models of the other two stars (whose maps were recovered also using HARPSpol), by applying the same procedures and criteria in the reconstructions (see Alvarado-Gómez et al. 2015, 2016), minimising at the same time the effects introduced by driving the simulations using maps from different instruments. By relaxing these last requirements, we can make an order-of-magnitude estimate of the possible temporal variations in \dot{M} and F_X of HD 22049, due to the long-term evolution of its large-scale magnetic field. For this we use the ZDI information provided by Jeffers et al. (2014b), together with the F_X – Φ dependency derived from the results in Alvarado-Gómez et al. (2016), and the \dot{M} – Φ relation presented in Fig. 5.11.

Following this procedure, the recovered large-scale field distributions indicate an approximate change in $\langle \Phi_{Br} \rangle_s$ by a factor of ~ 2 in a time-scale of at least 5 years[‡]. This would imply variations in F_X and \dot{M} up to factors of ~ 2.4 and 2.1 , respectively. We stress here that this calculation corresponds to a first-order approximation, as we are neglecting several important elements such as the field topology, complexity, missing magnetic flux, map incompleteness, among others, which are known to influence the predictions of F_X and \dot{M} based on ZDI maps (e.g., Arzoumanian et al. 2011; Garraffo et al. 2013; Lang et al. 2014; Garraffo et al. 2015a; Garraffo et al. 2015b; Alvarado-Gómez et al. 2016). Nevertheless, archival X-ray observations of this star, available at the Nearby X-ray and Extreme UV Emitting Stars (NEXXUS 2) database[§] (Schmitt & Liefke 2004), indicate a variation in F_X within a time-scale of 10 years compatible with our previous estimate. Such change is sufficient to move HD 22049 above the previously mentioned threshold in the mass-loss activity relation ($F_X = 10^6 \text{ erg cm}^{-2} \text{ s}^{-1}$). Assuming a physical origin for this apparent break, the variation in F_X would imply a decrease in the mass loss-rate value of HD 22049, much larger than the one estimated above and reaching similar values as the ones predicted by our simulations.

- Last but not least, we must also consider the uncertainties associated with the observational estimates of mass loss rates. As explained by Wood et al. (2005a) and Wood et al. (2014), robust astrospheric detections require precise knowledge of the physical structure of the local ISM (e.g., the case of λ And, see Malamut

[†]<http://bcoolest.ast.obs-mip.fr>

[‡]This is obtained by considering the largest difference (including uncertainties) in either, the maximum (B_{max}) or the mean (B_{mean}) magnetic field values listed by Jeffers et al. (2014b). For the former, this occurred between the epochs of 2007 and 2012, while for the latter this was visible among the maps of 2008 and 2013.

[§]<http://www.hs.uni-hamburg.de/DE/For/Gal/Xgroup/nexxus/nexxus.html>

et al. 2014). This includes column densities, kinematics, and metal depletion rates (Redfield & Linsky 2004a; Redfield & Falcon 2008), together with local temperature and turbulent velocities (Redfield & Linsky 2004b), interpreted within a particular model of the morphology of the ISM (see Redfield & Linsky 2008, 2015; Gry & Jenkins 2014). While these studies have provided a detailed characterisation of the local ISM, intrinsic uncertainties and additional observational issues connected with the astrospheric detections, can certainly modify the estimated mass loss rates by large amounts (conservatively, by factors $\sim 2-3$; see Linsky & Wood 2014; Wood et al. 2002).

Some of the possibilities discussed before are currently being explored and will be presented in a future paper. This study will follow the same data-driven methodology presented here, applied to 70% of the stars with astrospheric detections (Wood et al. 2014) and with surface magnetic fields distributions recovered by ZDI[†] (see Vidotto et al. 2016 and references therein).

5.4.2 Stellar winds and habitable zones

Finally, we can use our 3D simulation results, to characterise the stellar wind conditions in the estimated boundaries of the Habitable Zones (HZ) of these systems. For the latter, we take advantage of the information provided in the Habitable Zone Gallery[‡] (HZG, Kane & Gelino 2012), regarding the *optimistic* and *conservative* calculations of the HZ (as defined in Kopparapu et al. 2013, 2014). We restrict our analysis to the inner edges of the HZs, given the enhancement of various stellar wind properties (e.g., density, magnetic field) closer to the star, which could influence the very definition of this boundary. Reference calculations at 1 AU are also performed for all the simulated cases. In the case of the Sun, the inner edges of the HZ are extremely close to 1 AU, thus we consider instead the semi-major axes of Mercury ($a_{\text{♁}} \simeq 0.39$ AU) and Venus ($a_{\text{♀}} \simeq 0.72$ AU).

As an example, Fig. 5.12 shows the optimistic (O_{I-HZ} , *red*) and conservative (C_{I-HZ} , *yellow*) inner edges of the HZ of HD 22049. These are displayed alongside the 1 AU boundary (*cyan*), and the stellar wind structure developed in the IH domain of the SH-ZDI simulation (Sect. 5.3.2, Fig. 5.6). As presented in the visualisation, we consider rings extending $\pm 5^\circ$ in inclination from the equatorial plane, to calculate different stellar wind properties and their variation (e.g., *min*, *mean*, *max*) at the distance of interest (see Table 5.3). In this manner the characterisation preserves the three-dimensional structure of the stellar wind, within the inclination range where the vast majority of exoplanets have been detected to date[§] (Han et al. 2014).

[†]Additional ZDI maps have been recovered using the NARVAL spectro-polarimeter (Aurière 2003), from observations acquired during 2015 (Program ID: L151N08 – PI: Morin).

[‡]<http://www.hzgallery.org/>

[§]<http://exoplanets.org/>

Table 5.3: Stellar wind characterisation at the inner edge of the HZs of the considered systems. The Optimistic (O_{I-HZ}) and Conservative (C_{I-HZ}) HZ limits have been taken from the HZG (Kane & Gelino 2012). Reference calculations at 1 AU are also included. The semi-major axes of Mercury ($a_{\text{♃}}$) and Venus ($a_{\text{♀}}$) are used in the solar cases. For each reference distance, the parentheses contain the (*min, mean, max*) values of a given parameter, calculated over a ring extending $\pm 5^\circ$ of inclination from the equatorial plane (see Fig. 5.12).

Parameters	HD 1237		HD 22049		HD 147513	Sun	
	ZDI	SH-ZDI	ZDI	SH-ZDI	SH-ZDI	CR 1922 (Min)	CR 1962 (Max)
<i>Ref. Distance:</i>	$D = 1.0$ AU		$D = 1.0$ AU		$D = 1.0$ AU	$D = 1.0$ AU (a_{\oplus})	
u_r [km s^{-1}]	(586, 983, 1191)	(601, 812, 925)	(522, 808, 1040)	(421, 642, 756)	(259, 433, 670)	(240, 355, 527)	(146, 265, 449)
n [cm^{-3}]	(3.25, 9.15, 62.9)	(13.7, 33.8, 182.4)	(3.22, 9.48, 48.3)	(15.2, 39.0, 212.0)	(11.5, 51.2, 380.7)	(5.44, 17.9, 125.8)	(15.0, 76.1, 910.0)
T [$\times 10^4$ K]	(3.43, 18.1, 29.1)	(4.05, 12.8, 19.8)	(3.05, 11.4, 20.1)	(3.76, 7.24, 11.1)	(0.72, 2.70, 10.5)	(0.79, 1.93, 7.98)	(0.29, 1.48, 13.0)
B [nT]	(1.3×10^{-2} , 6.34, 13.4)	(5.7×10^{-2} , 17.4, 29.3)	(1.8×10^{-2} , 4.43, 9.4)	(8.8×10^{-2} , 13.0, 21.0)	(6.6×10^{-2} , 4.07, 28.4)	(2.5×10^{-3} , 1.71, 10.8)	(1.6×10^{-2} , 4.87, 44.3)
P_T [nPa] ^a	(7.07, 11.2, 38.0)	(17.7, 30.3, 115.9)	(4.58, 8.29, 28.3)	(9.95, 24.4, 139.2)	(4.22, 11.8, 68.7)	(1.44, 3.41, 14.6)	(1.81, 8.56, 84.0)
<i>Ref. Distance: C_{I-HZ}</i>	$D = 0.76$ AU		$D = 0.58$ AU		$D = 0.84$ AU	$D = 0.72$ AU (a_{\oplus})	
u_r [km s^{-1}]	(582, 991, 1184)	(597, 818, 923)	(517, 799, 1032)	(415, 634, 750)	(256, 441, 669)	(229, 356, 531)	(133, 268, 460)
n [cm^{-3}]	(5.68, 14.3, 97.7)	(23.9, 52.9, 315.0)	(9.86, 28.3, 114.3)	(48.3, 119.4, 427.3)	(16.7, 69.5, 381.1)	(11.8, 34.1, 184.6)	(36.0, 144.2, 1770.0)
T [$\times 10^4$ K]	(5.19, 25.8, 39.9)	(5.97, 18.2, 27.0)	(7.12, 21.6, 38.0)	(8.07, 13.7, 20.7)	(0.92, 3.44, 10.9)	(1.29, 2.97, 8.86)	(0.54, 2.10, 12.0)
B [nT]	(1.7×10^{-2} , 10.6, 17.8)	(8.5×10^{-2} , 29.1, 42.9)	(0.10, 12.1, 17.5)	(7.5×10^{-2} , 35.4, 45.7)	(3.8×10^{-2} , 5.31, 25.9)	(7.2×10^{-3} , 2.75, 12.0)	(2.6×10^{-2} , 7.40, 57.9)
P_T [nPa]	(12.6, 18.4, 59.5)	(31.5, 49.1, 196.0)	(16.7, 24.5, 61.2)	(35.8, 73.5, 295.5)	(8.07, 16.5, 75.7)	(3.45, 6.50, 20.9)	(4.53, 15.7, 137.0)
<i>Ref. Distance: O_{I-HZ}</i>	$D = 0.60$ AU		$D = 0.46$ AU		$D = 0.67$ AU	$D = 0.39$ AU ($a_{\text{♃}}$)	
u_r [km s^{-1}]	(579, 960, 1180)	(595, 798, 918)	(512, 799, 1021)	(412, 634, 746)	(254, 425, 667)	(210, 353, 524)	(116, 269, 467)
n [cm^{-3}]	(9.37, 26.9, 153.6)	(38.7, 99.0, 504.2)	(15.9, 44.3, 177.4)	(78.9, 182.6, 693.5)	(26.9, 117.8, 464.9)	(42.5, 118.0, 353.4)	(122.0, 515.6, 2614.4)
T [$\times 10^4$ K]	(7.36, 32.0, 52.2)	(8.23, 22.8, 35.0)	(10.0, 28.7, 49.7)	(10.6, 18.3, 27.2)	(1.34, 4.23, 11.9)	(3.37, 6.53, 11.4)	(1.61, 4.62, 11.1)
B [nT]	(3.4×10^{-2} , 16.4, 24.9)	(7.1×10^{-2} , 45.6, 62.2)	(7.7×10^{-2} , 18.9, 25.4)	(0.18, 54.9, 68.4)	(0.15, 7.59, 24.9)	(2.65×10^{-2} , 7.49, 17.8)	(9.5×10^{-2} , 18.2, 61.3)
P_T [nPa]	(20.5, 31.8, 92.8)	(51.9, 86.0, 309.1)	(26.9, 38.2, 93.2)	(60.4, 112.4, 445.6)	(16.1, 26.0, 81.5)	(16.0, 22.2, 39.5)	(22.1, 53.5, 233.0)

^a Total pressure of the stellar wind ($P_T = P_{\text{gas}} + P_{\text{dyn}} + P_{\text{mag}}$).

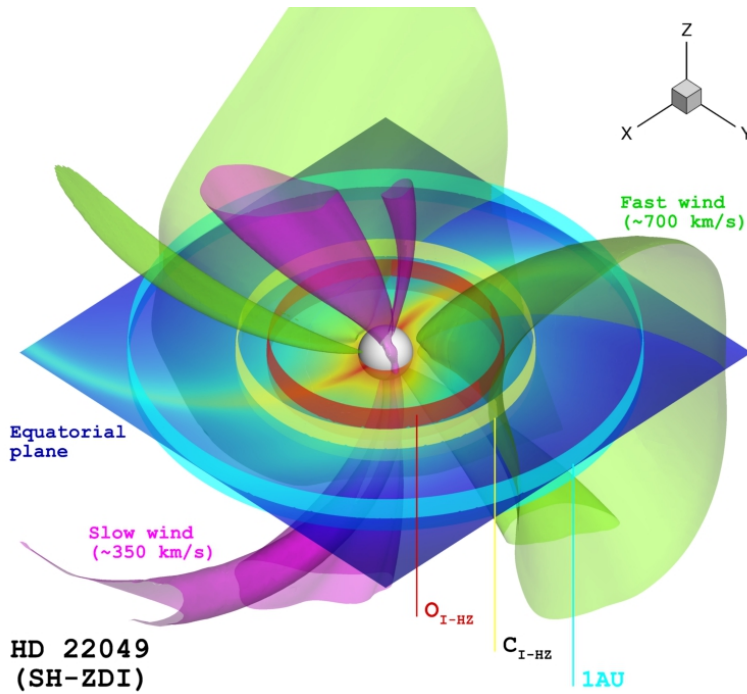


Figure 5.12: Stellar wind characterisation at the optimistic (O_{I-HZ} , red) and conservative (C_{I-HZ} , yellow) inner edges of the HZ of HD 22049. Similarly, the 1 AU boundary is used as reference (cyan). In all cases, we consider rings extending to $\pm 5^\circ$ of inclination from the equatorial plane (slightly exaggerated in the figure for visualisation purposes). The wind structure is the same as in Fig. 5.6 (bottom-left), rotated by 90° clockwise.

The simulated solar wind parameters at 1 AU are consistent with the nominal measurements performed by the *Advanced Composition Explorer* (ACE) spacecraft during different periods of activity. However, the wind particle density (n) is too high for the solar maximum simulation[†], which is connected to the overestimated mass loss rate for this epoch (see Sect. 5.3.1). Still, the simulated parameters are within feasible limits during periods of high activity (which would also involve transient events such as coronal mass ejections, see Webb & Howard 2012, Cohen et al. 2014).

The results listed in Table 5.3 allow a quick assessment of the circumstellar conditions among the different stellar cases and the Sun. For this, one can use the total pressure values associated to the stellar wind in each case (P_T). This quantity encompasses the thermal properties of the incident plasma ($P_{\text{gas}} = nk_B T$, with k_B as the Boltzmann constant), the dynamic pressure of the wind ($P_{\text{dyn}} = nu_{\text{sw}}^2 / 2$), and the contribution from the magnetic pressure ($P_{\text{mag}} = B^2 / 8\pi$). For instance, if the Earth were located at 1 AU from HD 1237, the total pressure acting over the magnetosphere would be on average one order of magnitude larger than the nominal conditions around the Sun. In particular sectors of the orbit (i.e., dense streamers in the SH-ZDI simulation), this value can reach more than 2 orders of magnitude of difference compared to the ambient solar wind. This would imply a reduction in the magnetosphere size by a factor $\sim 2.2^\ddagger$. While variations of this order have been observed in the actual magnetosphere of the Earth (see Pulkkinen 2007), this estimate does not include the effects from magnetic reconnection at the magnetopause (Frey et al.

[†]This is obtained by comparing the simulated average particle density with daily ACE measurements during the CR 1962. See <http://www.srl.caltech.edu/ACE/ASC/level2/new/intro.html>

[‡]This is estimated using Eq. (5.2), replacing the dynamical pressure of the wind (nu_{sw}^2) for the total pressure P_T

2003), or due to transient events such as CMEs (Khodachenko et al. 2007; Cohen et al. 2014, 2011b), which can disrupt the magnetospheric structure. This is extremely important in the case of highly active stars, as these transient events may even dominate completely the mass loss rate, wind, and energetic properties of the environment in these systems (see Drake et al. 2013).

Finally, this approach can be used to consider the stellar wind properties of the host-star to improve the different estimates of the HZs of these and other systems. One possibility might involve the inclusion into the HZ of a minimum planetary magnetic moment (consistent with the simulated stellar wind conditions), in order to sustain a magnetosphere up to a certain height (e.g., a few planetary radii). This new characteristic of the HZ boundary could even depend on the specific level of coronal activity of the planet-host (which can also be constructed using ZDI-driven models, see Alvarado-Gómez et al. 2016). This is important due to the fact that in the case of very active planet-hosts (specially M-dwarfs), the magnetic shielding has to compensate the atmospheric expansion induced by the enhanced high-energy emission of the star (e.g., EUV, X-rays, see Lammer et al. 2007), and stronger CMEs with an increased impact rate (see Kay et al. 2016). Such dynamic characterisation of the HZ is out of the scope of this investigation but will be explored in a future parametric study, including also additional systems for which ZDI maps are available.

5.5 Summary and chapter conclusions

We carried out elaborated simulations of the stellar wind and inner astrospheric structure of three planet-hosting stars (HD 22049, HD 1237, and HD 147513), using the Space Weather Modelling Framework (SWMF, Tóth et al. 2005, 2012). This Chapter complements the study presented in Alvarado-Gómez et al. (2016), which contains the results of the coronal structure modelling of these systems. Steady-state solutions were obtained for two coupled simulation domains, ranging from 1–30 R_* (SC domain) and from 25–215 R_* (IH domain). Large-scale magnetic field maps of these stars, recovered with Zeeman-Doppler imaging, serve to drive the solutions inside the SC domain, which are coupled self-consistently for a combined solution in the IH domain. A summary of our results and main conclusions is provided below:

- Following Alvarado-Gómez et al. (2016), simulations driven by two sets of similar large-scale magnetic field distributions (i.e., ZDI and SH-ZDI) were compared. It is worth noting that both sets of magnetic field maps provided equivalently good fits to the observations and showed substantial similarities in the overall structure of the stellar wind. However, several differences in the magneto-hydrodynamic properties of the solutions were found, including $\sim 10\text{--}30\%$ denser and $\sim 25\text{--}35\%$ colder stellar winds in the SH-ZDI solutions compared to the ZDI cases. In addition, the SH-ZDI simulations led to larger values in the average Alfvén surface size (by a factor of ~ 1.5), the mass loss rate \dot{M} (by a factors of $\sim 3\text{--}4$), and the angular momentum

loss rate \dot{J} (by roughly one order of magnitude). Therefore, the values listed in Table 5.1 should be actually interpreted as predicted ranges from this ZDI-driven model.

These variations arise as a consequence of the available magnetic energy to heat the corona and accelerate the wind, which in turn, relates to the different field strengths and map completeness provided by the ZDI and SH-ZDI reconstructions. This strongly differs from previous studies where older implementations of the numerical code used here are considered, and where the completeness in the driving magnetic field distributions yield no significant changes in the wind structure (e.g., Vidotto et al. 2012; see Sect. 5.3.1).

- The results from two different solar simulations, covering activity minimum (CR 1922) and maximum (CR 1962), were also considered. We showed that this numerical framework properly recovers the expected structure of the solar wind, including thermodynamical properties (e.g., density, temperature), mass loss and angular momentum loss rates (\dot{M}_\odot and \dot{J}_\odot , respectively; see Table 5.1), and global topology during each activity state (Figs. 5.1 and 5.5). However, the solar maximum simulation showed an over-enhanced plasma density at 1 AU (Sect. 5.4.2, Table 5.3), as a consequence of an overestimated mass loss rate (by $\sim 40\%$)[†]. This is interpreted as the result of a considerable fraction of missing mixed polarity regions in the driving magnetogram, which was artificially degraded for a more consistent comparison with the stellar cases (see Alvarado-Gómez et al. 2016).
- In general, the stellar wind solutions showed a clear relation with the driving magnetic field distribution, and the developed coronal structure in each case. For HD 22049 (Figs. 5.2 and 5.6) and HD 1237 (Figs. 5.3, 5.8 and 5.9) various fast-wind regions appeared self-consistently in the simulations, nearly perpendicular to the astrospheric current sheet structure (defined by $B_r = 0$), and with a spatial correspondence with the dominant features in their lower corona (e.g., coronal holes, see Alvarado-Gómez et al. 2016). The radial wind velocity in these regions reached up to $\sim 1100 \text{ km s}^{-1}$ in the ZDI simulations, dropping to $\sim 700 \text{ km s}^{-1}$ in the SH-ZDI cases (see Sect. 5.3.2).
- On the other hand, the simulation of HD 147513 yielded a much more complex wind solution (Figs. 5.4 and 5.7), compared to what could have been expected from the simple magnetic field distribution driving the simulation (Alvarado-Gómez et al. 2016). A highly warped astrospheric current sheet was obtained in this case, over which a dominant slow-wind component ($u_r \simeq 500 \text{ km s}^{-1}$) was developed. While these results could be affected by the comparatively low-resolution of the SH-ZDI map driving the simulation (see Hussain et al. 2016), this example indicates that numerical descriptions based on first order extrapolations of surface magnetic field

[†]This corresponds to a very rough estimate, as it relies on the single-point measurements and location of *Voyager II* as reference (<http://voyager.jpl.nasa.gov/mission/weekly-reports/index.htm>)

properties alone, cannot provide a complete picture of the wind complexity in a given system (e.g., [Matt et al. 2012](#)).

- For HD 1237 we investigated in detail the wind environment and the conditions experienced by the exoplanet of this system (Sect. 5.3.3). For this purpose we additionally coupled the Global Magnetosphere (GM) module of the SWMF, to the developed wind structure inside the IH domain. For each simulation (i.e., ZDI and SH-ZDI cases), two representative spatial locations were considered (Figs. 5.8 and 5.9). These included a low-density, fast wind stream, and a high-density, slow wind region. This analysis showed that the density structure of the stellar wind dominates, over the wind velocity, the process of particle injection into the planetary atmosphere (see Table 5.2). This is a consequence of the large density gradients obtained in the wind solutions (i.e., dense streamers with increments up to 4 orders of magnitude in n), compared to the relatively narrow range of resulting radial wind speeds (with variations only up to a factor of 2 in u_r for the entire 3D domain).
- Following [Stevens 2005](#), we additionally calculated the amount of exoplanetary radio emission from the wind-magnetospheric interaction in this system. We obtained a maximum radio flux on Earth of $F_{\oplus}^R \simeq 12$ mJy at 40 MHz, associated with a high-density streamer crossing during periastron passage (at 0.25 AU, [Naef et al. 2001](#)). This value is reduced by an order of magnitude during the orbital motion of the planet (approximately at 2/3 of a right-hand oriented orbit with respect to periastron, see Fig. 5.10). Our maximum emission prediction is lower by a factor of ~ 2 compared to the estimates of [Stevens \(2005\)](#), which were based on the mass loss-activity relation of [Wood et al. 2002](#), and the assumption of a spherically symmetric wind. Given the system's low declination, SKA is the only facility which could robustly detect and analyse this emission.
- From our simulations, and applying the methodology explained in [Cohen & Drake \(2014\)](#) and [Garraffo et al. \(2015b\)](#), we calculated the mass loss rate, \dot{M} , and angular momentum loss rate, \dot{J} , in these systems. We obtained absolute \dot{M} values, ranging from approximately $1 \dot{M}_{\odot}$ up to $\sim 7 \dot{M}_{\odot}$, and \dot{J} within a broader range of ~ 1 –60 times the solar prediction (Table 5.1). In combination with the results for the coronal structure ([Alvarado-Gómez et al. 2016](#)), we constructed, for the first time, a fully simulated mass loss-activity relation, expressed as $\dot{M}_{(\text{sim})} \propto F_{X(\text{sim})}^{\gamma}$ with $\gamma = 0.79^{+0.19}_{-0.15}$. A thoughtful discussion is presented in Sect. 5.4.1, comparing this result with the observational relation of [Wood et al. \(2005a\)](#) (e.g., $\dot{M} \propto F_X^{1.34 \pm 0.18}$), exploring various possibilities that could explain the discrepancy in these relations.
- Finally, by exploiting the 3D capabilities of our simulations we characterised the stellar wind structure at the inner edge of the Habitable Zone (HZ) of these systems (Sect. 5.4.2). The optimistic and conservative limits of this boundary, provided in the Habitable Zone Gallery (HZG, [Kane & Gelino 2012](#)), were considered. We included a 10° range in orbital inclination (e.g., Fig. 5.12), in order to provide more realistic

stellar wind parameters (allowing possible off-the-equator variations), and to capture the region where the majority of exoplanets have been found so far (Han et al. 2014). The results of this characterisation are presented in Table 5.3, and consider all the magneto-hydrodynamic properties of the stellar wind in these systems. Using the solar simulations, reference calculations at the locations of Mercury, Mars, and the Earth are also provided. These results will be used in a future study to perform a dynamical parametrisation of the inner edge of the HZ in these and other systems, accounting for the effects due to the stellar wind and the high-energy environment of the host star.

Outlook

The discovery of the first extrasolar planet around a main sequence star by [Mayor & Queloz \(1995\)](#), renovated the general interest in understanding the physical conditions around stars different from the Sun. One natural path to address this issue is to perform analogies with the solar system, and to evaluate their range of applicability for describing other stellar systems. In the case of the Sun, the characteristics and evolution of its magnetic field have been identified as the fundamental drivers of the physical conditions of its environment (e.g., coronal properties, high-energy emission, solar wind, heliospheric structure, etc.). Given that the Sun is a relatively inactive star, it is fundamental to understand these magnetism–environment connections for stars that show higher magnetic activity levels. In this context, this dissertation explored the stellar magnetic field and circumstellar environment of moderately-active Sun-like planet-hosting stars, following a combined observational–numerical methodology.

The observational component involved analysis of spectropolarimetric time-series and the technique of Zeeman Doppler Imaging (ZDI), generating a map of the surface large-scale magnetic field distribution (Chapters 2 and 3). Once the magnetic field topology was recovered, it was incorporated into a state-of-the-art numerical code which is currently used for space weather modelling and forecast in the solar system. In this way a consistent data-driven characterisation of the environment of each system was obtained (Chapters 4 and 5). In order to understand the capabilities and limitations of this modelling approach, solar and stellar simulations were systematically compared between each other and against observational data. This revealed that this procedure can properly recover the overall coronal and stellar wind conditions (reproducing successfully previous observational trends), at least up to the magnetic activity levels considered here (e.g., ~ 100 times more active than the Sun in X-rays).

A natural way forward in this investigation corresponds to the expansion of the characterised sample, in order to cover a broader range of stellar parameters, evolutionary stages and activity levels. International collaborations, such as Bcool[†], MaPP[‡], MaTYSSE[§], and TOUPIES^{*}, are currently increasing the database of spectropolarimetric observations and ZDI reconstructions.

[†]http://bcool.ast.obs-mip.fr/Bcool/Bcool___cool_magnetic_stars.html

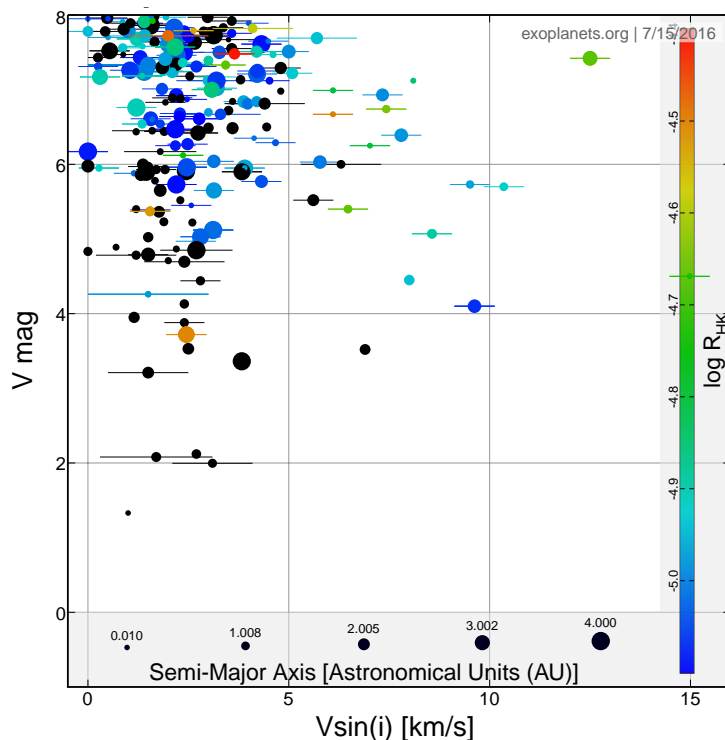
[‡]<http://lamwvs.oamp.fr/magics/mapp/FrontPage>

[§]<https://matysse.irap.omp.eu/doku.php?id=start>

^{*}http://ipag.osug.fr/Anr_Toupies/spip.php?rubrique2

Figure 5.13: Initial exploration for potential systems to be characterized with ZDI. Bright targets ($V_{\text{mag}} \leq 8.0$) with moderate activity ($\log R_{\text{HK}} \geq -4.9$; *cyan to red* symbols) are required for detecting the surface magnetic fields with current instrumentation. ZDI reconstructions should be also possible for a fraction of the planet-hosting stars with no chromospheric activity information (*black* symbols). The larger the $v \sin(i)$ of the star, the better the spatial resolution of the recovered ZDI map.

Adapted from: exoplanets.org.



In the case of planet-hosting stars, the number of systems with ZDI large-scale magnetic fields reconstructions is still relatively small (see [Fares et al. 2013](#); [Fares 2014](#)), but it has been slowly increasing in the last few years. This situation can be improved with additional ZDI observing campaigns of exoplanet hosts. Figure 5.13 shows an initial exploration in exoplanets.org for potential systems to be studied with ZDI, taking into account the limitations of the technique with current instrumentation. Relatively bright objects ($V_{\text{mag}} \leq 8.0$) with moderate magnetic activity levels ($\log R_{\text{HK}} \geq -4.9$), are required for robustly detect and map the surface large-scale magnetic field. While a significant number of planet-hosting systems lack chromospheric activity information (*black* symbols in Fig. 5.13), the statistics of the BCoolest snapshot survey presented by [Marsden et al. \(2014\)](#) indicate robust magnetic field detections in $\sim 25\text{--}50\%$ of the stars within this range of rotational velocities (i.e., $v \sin(i) \leq 6.0 \text{ km s}^{-1}$) using circular spectropolarimetry.

This simple exploration shows that with the aid of current facilities, the ZDI-driven methodology investigated in this dissertation could be applied to a considerable number of systems, including more than ~ 100 planet-hosting stars (Figure 5.13). Future instrumentation with similar capabilities, such as SPiRou[†], Neo-Narval[‡], and CRIRES+[§], will significantly increase this working sample, maximising the impact of this methodology on the research fields of stellar magnetism and exoplanet characterisation.

[†]<http://spirou.irap.omp.eu/>

[‡]<http://www.tbl.obs-mip.fr/INSTRUMENTATION2/neonarval>

[§]http://www.eso.org/sci/facilities/develop/instruments/crises_up.html#par_title

Appendix A

ZDI maps from the December 2012 dataset of HD 1237

We consider only the Milne–Eddington line profile for the 2012 Dec. dataset. Figure A.2 contains the recovered ZDI maps for this epoch with the corresponding synthetic Stokes V profiles. Despite having a lower phase coverage in this case, we were able to recover robust magnetic field maps, fitting the spectropolarimetric data up to an optimal reduced $\chi^2 = 0.6$ (Fig. A.1, see also Sect. 2.6.2). This low value of reduced χ^2 results as a consequence of the fewer constraints available for this dataset.

The field distribution clearly resembles the one obtained for the July dataset with a large contribution from the azimuthal and radial components to the total field. The main large-scale magnetic features are preserved between both observed epochs. This is consistent with the behaviour shown by the activity indicators (Sect. 2.4.2, Fig. 2.3) and the longitudinal magnetic field (Sect. 2.5.1, Fig. 2.5) in the entire dataset. Some of the smaller-scale structure is not recovered, and the ring of azimuthal field is not clear in this case. These changes are expected from the number of observations and phase coverage in this epoch (e.g., Donati & Brown 1997). The slight shift in longitude is due to the initial phase selection in this case, where $\Phi = 0.0$ is assigned to the observations acquired at HJD = 2 456 265.0 (Table 2.2).

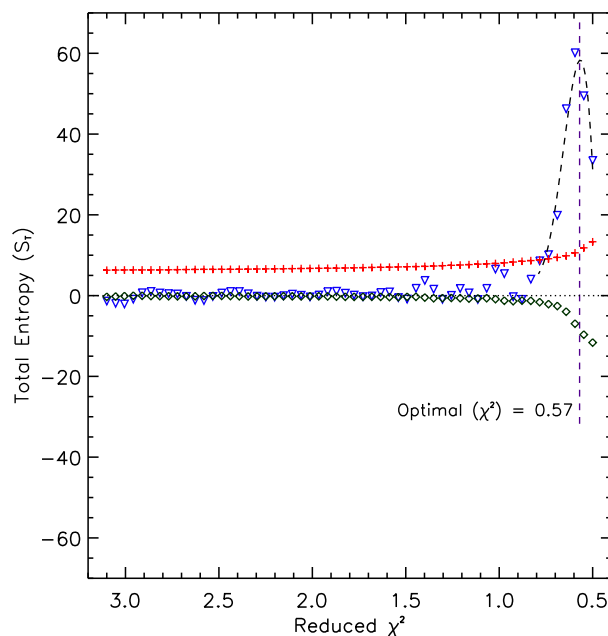
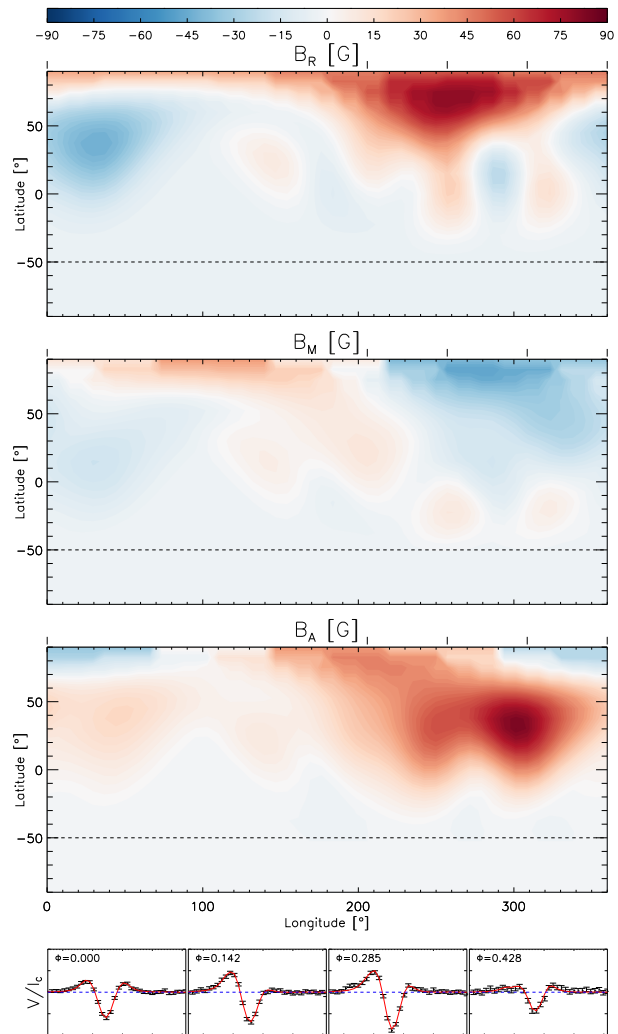


Figure A.1: Selection criteria for the optimal fit quality of the ZDI reconstructions of HD 1237 using the Dec. 2012 dataset.

Figure A.2: Results of the ZDI analysis for the second-epoch observations of HD 1237 using the Milne-Eddington line profile. The first three panels show the surface magnetic field components B_R , B_M , and B_A , respectively. The colour scale denotes the polarity and the magnitude of each magnetic field component in Gauss (G), while the phase coverage is indicated by the *black* ticks in the upper y -axis. The segmented horizontal line indicates the surface visibility limit, imposed by the adopted inclination angle of the star ($i = 50^\circ$). The last panel shows the comparison between synthetic (*red*) and observed (*black*) Stokes V profiles obtained for this particular epoch in each observational phase Φ . The recovered maps fit the spectropolarimetric data to optimal reduced $\chi^2 = 0.6$ (see Fig. A.1). For this epoch $\Phi = 0.0$ is assigned to the observations acquired at HJD = 2 456 265.0.



Bibliography

- Acton, L. W., Weston, D. C., & Bruner, M. E. 1999, *J. Geophys. Res.*, 104, 14827
- Alvarado-Gómez, J. D., Hussain, G. A. J., Cohen, O., et al. 2016, *A&A*, 588, A28
- Alvarado-Gómez, J. D., Hussain, G. A. J., Grunhut, J., et al. 2015, *A&A*, 582, A38
- Amard, L., Palacios, A., Charbonnel, C., Gallet, F., & Bouvier, J. 2016, *A&A*, 587, A105
- Arzoumanian, D., Jardine, M., Donati, J.-F., Morin, J., & Johnstone, C. 2011, *MNRAS*, 410, 2472
- Aurière, M. 2003, in *EAS Publications Series*, Vol. 9, *EAS Publications Series*, ed. J. Arnaud & N. Meunier, 105
- Bagnulo, S., Landolfi, M., Landstreet, J. D., et al. 2009, *PASP*, 121, 993
- Baliunas, S. L., Donahue, R. A., Soon, W. H., et al. 1995, *ApJ*, 438, 269
- Barnes, J. R., Collier Cameron, A., Unruh, Y. C., Donati, J. F., & Hussain, G. A. J. 1998, *MNRAS*, 299, 904
- Barnes, J. R., Lister, T. A., Hilditch, R. W., & Collier Cameron, A. 2004, *MNRAS*, 348, 1321
- Barnes, S. A. & Kim, Y.-C. 2010, *ApJ*, 721, 675
- Baruteau, C., Crida, A., Paardekooper, S.-J., et al. 2014, *Protostars and Planets VI*, 667
- Bastien, F. A., Stassun, K. G., Pepper, J., et al. 2014, *AJ*, 147, 29
- Benedict, G. F., McArthur, B. E., Gatewood, G., et al. 2006, *AJ*, 132, 2206
- Blackman, E. G. & Owen, J. E. 2016, *MNRAS*, 458, 1548
- Boisse, I., Bonfils, X., & Santos, N. C. 2012, *A&A*, 545, A109
- Bonfils, X., Forveille, T., Delfosse, X., et al. 2005, *A&A*, 443, L15
- Bonfils, X., Mayor, M., Delfosse, X., et al. 2007, *A&A*, 474, 293

- Boro Saikia, S., Jeffers, S. V., Morin, J., et al. 2016, ArXiv e-prints [1606.01032]
- Boro Saikia, S., Jeffers, S. V., Petit, P., et al. 2015, *A&A*, 573, A17
- Broggi, M., Snellen, I. A. G., de Kok, R. J., et al. 2012, *Nature*, 486, 502
- Brown, B. P., Browning, M. K., Brun, A. S., Miesch, M. S., & Toomre, J. 2010, *ApJ*, 711, 424
- Brown, S. F., Donati, J.-F., Rees, D. E., & Semel, M. 1991, *A&A*, 250, 463
- Butler, R. P., Marcy, G. W., Williams, E., Hauser, H., & Shirts, P. 1997, *ApJ*, 474, L115
- Catala, C., Donati, J.-F., Shkolnik, E., Bohlender, D., & Alecian, E. 2007, *MNRAS*, 374, L42
- Chadney, J. M., Galand, M., Unruh, Y. C., Koskinen, T. T., & Sanz-Forcada, J. 2015, *Icarus*, 250, 357
- Charbonneau, P. 2014, *ARA&A*, 52, 251
- Chen, P. F. 2011, *Living Reviews in Solar Physics*, 8
- Cohen, O. 2011, *MNRAS*, 417, 2592
- Cohen, O. & Drake, J. J. 2014, *ApJ*, 783, 55
- Cohen, O., Drake, J. J., Gloer, A., et al. 2014, *ApJ*, 790, 57
- Cohen, O., Drake, J. J., Kashyap, V. L., Hussain, G. A. J., & Gombosi, T. I. 2010, *ApJ*, 721, 80
- Cohen, O., Kashyap, V. L., Drake, J. J., et al. 2011a, *ApJ*, 733, 67
- Cohen, O., Kashyap, V. L., Drake, J. J., Sokolov, I. V., & Gombosi, T. I. 2011b, *ApJ*, 738, 166
- Cohen, O., Ma, Y., Drake, J. J., et al. 2015, *ApJ*, 806, 41
- Collier Cameron, A. 1995, *MNRAS*, 275, 534
- Cranmer, S. R. & Saar, S. H. 2011, *ApJ*, 741, 54
- Daou, A. G., Johns-Krull, C. M., & Valenti, J. A. 2006, *AJ*, 131, 520
- De Moortel, I. & Browning, P. 2015, *Philosophical Transactions of the Royal Society of London Series A*, 373, 20140269
- De Pontieu, B., McIntosh, S. W., Carlsson, M., et al. 2007, *Science*, 318, 1574
- Dere, K. P., Landi, E., Mason, H. E., Monsignori Fossi, B. C., & Young, P. R. 1997, *A&AS*, 125, 149
- DeRosa, M. L., Brun, A. S., & Hoeksema, J. T. 2012, *ApJ*, 757, 96

- do Nascimento, Jr., J.-D., Vidotto, A. A., Petit, P., et al. 2016, *ApJ*, 820, L15
- Domingo, V., Fleck, B., & Poland, A. I. 1995, *Sol. Phys.*, 162, 1
- Donati, J., Moutou, C., Malo, L., et al. 2016, ArXiv e-prints [[arXiv]1606.06236]
- Donati, J.-F. 2003, in *Astronomical Society of the Pacific Conference Series*, Vol. 307, *Solar Polarization*, ed. J. Trujillo-Bueno & J. Sanchez Almeida, 41
- Donati, J.-F. 2011, in *IAU Symposium*, Vol. 271, *Astrophysical Dynamics: From Stars to Galaxies*, ed. N. H. Brummell, A. S. Brun, M. S. Miesch, & Y. Ponty, 23–31
- Donati, J.-F. & Brown, S. F. 1997, *A&A*, 326, 1135
- Donati, J.-F., Gregory, S. G., Alencar, S. H. P., et al. 2012, *MNRAS*, 425, 2948
- Donati, J.-F., Hébrard, E., Hussain, G., et al. 2014, *MNRAS*, 444, 3220
- Donati, J.-F., Hébrard, E., Hussain, G. A. J., et al. 2015, *MNRAS*, 453, 3706
- Donati, J.-F., Howarth, I. D., Jardine, M. M., et al. 2006, *MNRAS*, 370, 629
- Donati, J.-F., Jardine, M. M., Gregory, S. G., et al. 2008a, *MNRAS*, 386, 1234
- Donati, J.-F. & Landstreet, J. D. 2009, *ARA&A*, 47, 333
- Donati, J.-F., Morin, J., Petit, P., et al. 2008b, *MNRAS*, 390, 545
- Donati, J.-F., Moutou, C., Farès, R., et al. 2008c, *MNRAS*, 385, 1179
- Donati, J.-F., Semel, M., Carter, B. D., Rees, D. E., & Collier Cameron, A. 1997, *MNRAS*, 291, 658
- Drake, J. F., Swisdak, M., & Opher, M. 2015, *ApJ*, 808, L44
- Drake, J. J., Cohen, O., Yashiro, S., & Gopalswamy, N. 2013, *ApJ*, 764, 170
- Drake, J. J., Peres, G., Orlando, S., Laming, J. M., & Maggio, A. 2000, *ApJ*, 545, 1074
- Drake, J. J. & Smith, G. 1993, *ApJ*, 412, 797
- Dressing, C. D. & Charbonneau, D. 2013, *ApJ*, 767, 95
- Dumusque, X., Boisse, I., & Santos, N. C. 2014, *ApJ*, 796, 132
- Dumusque, X., Glenday, A., Phillips, D. F., et al. 2015, *ApJ*, 814, L21
- Dumusque, X., Pepe, F., Lovis, C., et al. 2012, *Nature*, 491, 207
- Dumusque, X., Santos, N. C., Udry, S., Lovis, C., & Bonfils, X. 2011, *A&A*, 527, A82

- Dunstone, N. J., Hussain, G. A. J., Collier Cameron, A., et al. 2008, *MNRAS*, 387, 481
- Eisenbeiss, T., Ammler-von Eiff, M., Roell, T., et al. 2013, *A&A*, 556, A53
- Ekenbäck, A., Holmström, M., Wurz, P., et al. 2010, *ApJ*, 709, 670
- Fares, R. 2014, in *IAU Symposium*, Vol. 302, *IAU Symposium*, 180–189
- Fares, R., Donati, J.-F., Moutou, C., et al. 2009, *MNRAS*, 398, 1383
- Fares, R., Donati, J.-F., Moutou, C., et al. 2012, *MNRAS*, 423, 1006
- Fares, R., Moutou, C., Donati, J.-F., et al. 2013, *MNRAS*, 435, 1451
- Farrell, W. M., Desch, M. D., & Zarka, P. 1999, *J. Geophys. Res.*, 104, 14025
- Favata, F., Micela, G., Orlando, S., et al. 2008, *A&A*, 490, 1121
- Fisher, G. H., Abbett, W. P., Bercik, D. J., et al. 2015, *Space Weather*, 13, 369
- Fisk, L. A. & Gloeckler, G. 2014, *ApJ*, 789, 41
- Folsom, C. P., Petit, P., Bouvier, J., Donati, J.-F., & Morin, J. 2014, in *IAU Symposium*, Vol. 302, *Magnetic Fields throughout Stellar Evolution*, ed. P. Petit, M. Jardine, & H. C. Spruit, 110–111
- Folsom, C. P., Petit, P., Bouvier, J., et al. 2016, *MNRAS*, 457, 580
- Forget, F. & Leconte, J. 2014, *Philosophical Transactions of the Royal Society of London Series A*, 372, 30084
- Frey, H. U., Phan, T. D., Fuselier, S. A., & Mende, S. B. 2003, *Nature*, 426, 533
- Gallet, F. & Bouvier, J. 2013, *A&A*, 556, A36
- Garraffo, C., Cohen, O., Drake, J. J., & Downs, C. 2013, *ApJ*, 764, 32
- Garraffo, C., Drake, J. J., & Cohen, O. 2015a, *ApJ*, 807, L6
- Garraffo, C., Drake, J. J., & Cohen, O. 2015b, *ApJ*, 813, 40
- Gastine, T., Morin, J., Duarte, L., et al. 2013, *A&A*, 549, L5
- George, S. J. & Stevens, I. R. 2007, *MNRAS*, 382, 455
- Ghezzi, L., Cunha, K., Smith, V. V., et al. 2010, *ApJ*, 720, 1290
- Gloeckler, G. & Fisk, L. A. 2015, *ApJ*, 806, L27
- Gray, D. F., Baliunas, S. L., Lockwood, G. W., & Skiff, B. A. 1996, *ApJ*, 465, 945

- Grevesse, N. & Sauval, A. J. 1998, *Space Sci. Rev.*, 85, 161
- Grießmeier, J.-M., Stadelmann, A., Penz, T., et al. 2004, *A&A*, 425, 753
- Grießmeier, J.-M., Zarka, P., & Spreew, H. 2007, *A&A*, 475, 359
- Gry, C. & Jenkins, E. B. 2014, *A&A*, 567, A58
- Guo, J. H. 2011, *ApJ*, 733, 98
- Gurnett, D. A., Kurth, W. S., Burlaga, L. F., & Ness, N. F. 2013, *Science*, 341, 1489
- Hallinan, G., Sirothia, S. K., Antonova, A., et al. 2013, *ApJ*, 762, 34
- Han, E., Wang, S. X., Wright, J. T., et al. 2014, *PASP*, 126, 827
- Haswell, C. A., Fossati, L., Ayres, T., et al. 2012, *ApJ*, 760, 79
- Hathaway, D. H. 2010, *Living Reviews in Solar Physics*, 7, 1
- Hathaway, D. H. 2015, *Living Reviews in Solar Physics*, 12
- Hatzes, A. P. 2013a, *Astronomische Nachrichten*, 334, 616
- Hatzes, A. P. 2013b, *ApJ*, 770, 133
- Hatzes, A. P. 2014, *Nature*, 513, 353
- Hatzes, A. P. 2016, *A&A*, 585, A144
- Hatzes, A. P., Cochran, W. D., McArthur, B., et al. 2000, *ApJ*, 544, L145
- Haywood, R. D., Collier Cameron, A., Unruh, Y. C., et al. 2016, *MNRAS*, 457, 3637
- Hébrard, É. M., Donati, J.-F., Delfosse, X., et al. 2014, *MNRAS*, 443, 2599
- Hebrard, E. M., Donati, J.-F., Delfosse, X., et al. 2014, *MNRAS*, 443, 2599
- Hébrard, É. M., Donati, J.-F., Delfosse, X., et al. 2016, *ArXiv e-prints* [1606.01775]
- Hussain, G. A. J. 2002, *Astronomische Nachrichten*, 323, 349
- Hussain, G. A. J., Alvarado-Gómez, J. D., Grunhut, J., et al. 2016, *A&A*, 585, A77
- Hussain, G. A. J., Collier Cameron, A., & Donati, J.-F. 1998, in *Astronomical Society of the Pacific Conference Series*, Vol. 154, *Cool Stars, Stellar Systems, and the Sun*, ed. R. A. Donahue & J. A. Bookbinder, 1992
- Hussain, G. A. J., Collier Cameron, A., Jardine, M. M., et al. 2009, *MNRAS*, 398, 189
- Hussain, G. A. J., Donati, J.-F., Collier Cameron, A., & Barnes, J. R. 2000, *MNRAS*, 318, 961

- Hussain, G. A. J., Jardine, M., & Collier Cameron, A. 2001, MNRAS, 322, 681
- Hussain, G. A. J., van Ballegooijen, A. A., Jardine, M., & Collier Cameron, A. 2002, ApJ, 575, 1078
- Janson, M., Reffert, S., Brandner, W., et al. 2008, A&A, 488, 771
- Jardine, M. & Collier Cameron, A. 2008, A&A, 490, 843
- Jeffers, S. V., Barnes, J. R., Jones, H. R. A., et al. 2014a, MNRAS, 438, 2717
- Jeffers, S. V., Petit, P., Marsden, S. C., et al. 2014b, A&A, 569, A79
- Jensen, A. G., Redfield, S., Endl, M., et al. 2012, ApJ, 751, 86
- Johnstone, C., Jardine, M., & Mackay, D. H. 2010, MNRAS, 404, 101
- Johnstone, C. P., Güdel, M., Brott, I., & Lüftinger, T. 2015a, A&A, 577, A28
- Johnstone, C. P., Güdel, M., Lüftinger, T., Toth, G., & Brott, I. 2015b, A&A, 577, A27
- Jordan, C. 1975, MNRAS, 170, 429
- Judge, P. G., Solomon, S. C., & Ayres, T. R. 2003, ApJ, 593, 534
- Kane, S. R. & Gelino, D. M. 2012, PASP, 124, 323
- Kashyap, V. L., Drake, J. J., & Saar, S. H. 2008, ApJ, 687, 1339
- Kasting, J. F., Whitmire, D. P., & Reynolds, R. T. 1993, Icarus, 101, 108
- Kawaler, S. D. 1988, ApJ, 333, 236
- Kay, C., Opher, M., & Kornbleuth, M. 2016, ArXiv e-prints [[arXiv]1605.02683]
- Khodachenko, M. L., Ribas, I., Lammer, H., et al. 2007, Astrobiology, 7, 167
- King, J. R., Villarreal, A. R., Soderblom, D. R., Gulliver, A. F., & Adelman, S. J. 2003, AJ, 125, 1980
- Kivelson, M. G. & Ridley, A. J. 2008, Journal of Geophysical Research (Space Physics), 113, A05214
- Kochukhov, O., Makaganiuk, V., & Piskunov, N. 2010, A&A, 524, A5
- Kochukhov, O. & Piskunov, N. 2002, A&A, 388, 868
- Kochukhov, O. & Wade, G. A. 2010, A&A, 513, A13
- Kochukhov, O., Wade, G. A., & Shulyak, D. 2012, MNRAS, 421, 3004

- Koen, C., Kilkenny, D., van Wyk, F., & Marang, F. 2010, MNRAS, 403, 1949
- Kopparapu, R. K., Ramirez, R., Kasting, J. F., et al. 2013, ApJ, 765, 131
- Kopparapu, R. K., Ramirez, R. M., SchottelKotte, J., et al. 2014, ApJ, 787, L29
- Kotov, V. A., Scherrer, P. H., Howard, R. F., & Haneychuk, V. I. 1998, ApJS, 116, 103
- Koutroumpa, D., Lallement, R., Raymond, J. C., & Kharchenko, V. 2009, ApJ, 696, 1517
- Krishnamurthi, A., Pinsonneault, M. H., Barnes, S., & Sofia, S. 1997, ApJ, 480, 303
- Kupka, F. G., Ryabchikova, T. A., Piskunov, N. E., Stempels, H. C., & Weiss, W. W. 2000, Baltic Astronomy, 9, 590
- Laming, J. M., Drake, J. J., & Widing, K. G. 1995, ApJ, 443, 416
- Laming, J. M., Drake, J. J., & Widing, K. G. 1996, ApJ, 462, 948
- Lammer, H. 2013, Origin and Evolution of Planetary Atmospheres (Springer Berlin Heidelberg)
- Lammer, H., Kasting, J. F., Chassefière, E., et al. 2008, Space Sci. Rev., 139, 399
- Lammer, H. & Khodachenko, M., eds. 2015, Astrophysics and Space Science Library, Vol. 411, Characterizing Stellar and Exoplanetary Environments
- Lammer, H., Lichtenegger, H. I. M., Kulikov, Y. N., et al. 2007, Astrobiology, 7, 185
- Lammer, H., Selsis, F., Ribas, I., et al. 2003, ApJ, 598, L121
- Landi, E., Young, P. R., Dere, K. P., Del Zanna, G., & Mason, H. E. 2013, ApJ, 763, 86
- Lang, P., Jardine, M., Morin, J., et al. 2014, MNRAS, 439, 2122
- Lazio, W., T. J., Farrell, W. M., Dietrick, J., et al. 2004, ApJ, 612, 511
- Lazio, T. J. W., Carmichael, S., Clark, J., et al. 2010a, AJ, 139, 96
- Lazio, T. J. W. & Farrell, W. M. 2007, ApJ, 668, 1182
- Lazio, T. J. W., Shankland, P. D., Farrell, W. M., & Blank, D. L. 2010b, AJ, 140, 1929
- Lecavelier Des Etangs, A. 2007, A&A, 461, 1185
- Lecavelier Des Etangs, A., Sirothia, S. K., Gopal-Krishna, & Zarka, P. 2009, A&A, 500, L51
- Lecavelier Des Etangs, A., Sirothia, S. K., Gopal-Krishna, & Zarka, P. 2011, A&A, 533, A50
- Lecavelier des Etangs, A., Sirothia, S. K., Gopal-Krishna, & Zarka, P. 2013, A&A, 552, A65

- Linsky, J. L. & Wood, B. E. 2014, *ASTRA Proceedings*, 1, 43
- Linsky, J. L., Yang, H., France, K., et al. 2010, *ApJ*, 717, 1291
- Liu, M. C., Matthews, B. C., Williams, J. P., & Kalas, P. G. 2004, *ApJ*, 608, 526
- Llama, J., Vidotto, A. A., Jardine, M., et al. 2013, *MNRAS*, 436, 2179
- Llama, J., Wood, K., Jardine, M., et al. 2011, *MNRAS*, 416, L41
- Lockwood, G. W., Skiff, B. A., Henry, G. W., et al. 2007, *ApJS*, 171, 260
- Lundin, R., Lammer, H., & Ribas, I. 2007, *Space Sci. Rev.*, 129, 245
- Makaganiuk, V., Kochukhov, O., Piskunov, N., et al. 2011, *A&A*, 525, A97
- Malamut, C., Redfield, S., Linsky, J. L., Wood, B. E., & Ayres, T. R. 2014, *ApJ*, 787, 75
- Mamajek, E. E. & Hillenbrand, L. A. 2008, *ApJ*, 687, 1264
- Markwardt, C. B. 2009, in *Astronomical Society of the Pacific Conference Series*, Vol. 411, *Astronomical Data Analysis Software and Systems XVIII*, ed. D. A. Bohlender, D. Durand, & P. Dowler, 251
- Marsden, S. C., Petit, P., Jeffers, S. V., et al. 2014, *MNRAS*, 444, 3517
- Mathioudakis, M., Fruscione, A., Drake, J. J., et al. 1995, *A&A*, 300, 775
- Matt, S. & Pudritz, R. E. 2008, *ApJ*, 678, 1109
- Matt, S. P., Brun, A. S., Baraffe, I., Bouvier, J., & Chabrier, G. 2015, *ApJ*, 799, L23
- Matt, S. P., MacGregor, K. B., Pinsonneault, M. H., & Greene, T. P. 2012, *ApJ*, 754, L26
- Mayor, M., Bonfils, X., Forveille, T., et al. 2009, *A&A*, 507, 487
- Mayor, M., Pepe, F., Queloz, D., et al. 2003, *The Messenger*, 114, 20
- Mayor, M. & Queloz, D. 1995, *Nature*, 378, 355
- Mayor, M., Udry, S., Naef, D., et al. 2004, *A&A*, 415, 391
- McComas, D. J., Dayeh, M. A., Funsten, H. O., Livadiotis, G., & Schwadron, N. A. 2013, *ApJ*, 771, 77
- McIntosh, S. W., de Pontieu, B., Carlsson, M., et al. 2011, *Nature*, 475, 477
- Mengel, M. W., Fares, R., Marsden, S. C., et al. 2016, *MNRAS*, 459, 4325
- Mestel, L. 1999, *Stellar magnetism* (Oxford: Clarendon)

- Mestel, L. & Spruit, H. C. 1987, *MNRAS*, 226, 57
- Middelkoop, F. 1982, *A&A*, 107, 31
- Mignone, A., Bodo, G., Massaglia, S., et al. 2007, *ApJS*, 170, 228
- Moré, J. 1978, in *Lecture Notes in Mathematics*, Vol. 630, *Numerical Analysis*, ed. G. Watson (Springer Berlin Heidelberg), 105–116
- Morgenthaler, A., Petit, P., Morin, J., et al. 2011, *Astronomische Nachrichten*, 332, 866
- Morgenthaler, A., Petit, P., Saar, S., et al. 2012, *A&A*, 540, A138
- Morin, J., Donati, J.-F., Petit, P., et al. 2008, *MNRAS*, 390, 567
- Morin, J., Donati, J.-F., Petit, P., et al. 2010, *MNRAS*, 407, 2269
- Morin, J., Dormy, E., Schrunner, M., & Donati, J.-F. 2011, *MNRAS*, 418, L133
- Moses, D., Clette, F., Delaboudinière, J.-P., et al. 1997, *Sol. Phys.*, 175, 571
- Naef, D., Mayor, M., Pepe, F., et al. 2001, *A&A*, 375, 205
- Neiner, C., Grunhut, J. H., Petit, V., et al. 2012, *MNRAS*, 426, 2738
- Ness, J.-U. & Jordan, C. 2008, *MNRAS*, 385, 1691
- Nichols, J. D. 2011, *MNRAS*, 414, 2125
- Nichols, J. D. & Milan, S. E. 2016, ArXiv e-prints [[arXiv]1606.03997]
- Nicholson, B. A., Vidotto, A. A., Mengel, M., et al. 2016, *MNRAS*, 459, 1907
- Noyes, R. W., Hartmann, L. W., Baliunas, S. L., Duncan, D. K., & Vaughan, A. H. 1984, *ApJ*, 279, 763
- Opher, M., Drake, J. F., Zieger, B., & Gombosi, T. I. 2015, *ApJ*, 800, L28
- Oran, R., van der Holst, B., Landi, E., et al. 2013, *ApJ*, 778, 176
- Pepe, F., Ehrenreich, D., & Meyer, M. R. 2014, *Nature*, 513, 358
- Peres, G., Orlando, S., Reale, F., Rosner, R., & Hudson, H. 2000, *ApJ*, 528, 537
- Pesnell, W. D., Thompson, B. J., & Chamberlin, P. C. 2012, *Sol. Phys.*, 275, 3
- Petit, P., Dintrans, B., Morgenthaler, A., et al. 2009, *A&A*, 508, L9
- Petit, P., Dintrans, B., Solanki, S. K., et al. 2008, *MNRAS*, 388, 80
- Petit, P., Donati, J.-F., & Collier Cameron, A. 2002, *MNRAS*, 334, 374

- Petit, P., Donati, J.-F., Hébrard, E., et al. 2015, *A&A*, 584, A84
- Pevtsov, A. A., Fisher, G. H., Acton, L. W., et al. 2003, *ApJ*, 598, 1387
- Pietarila, A. & Judge, P. G. 2004, *ApJ*, 606, 1239
- Piskunov, N. & Kochukhov, O. 2002, *A&A*, 381, 736
- Piskunov, N., Snik, F., Dolgoplov, A., et al. 2011, *The Messenger*, 143, 7
- Piskunov, N. E. & Valenti, J. A. 2002, *A&A*, 385, 1095
- Pizzolato, N., Maggio, A., Micela, G., Sciortino, S., & Ventura, P. 2003, *A&A*, 397, 147
- Poppenhaeger, K., Robrade, J., & Schmitt, J. H. M. M. 2011, *A&A*, 529, C1
- Poppenhaeger, K., Schmitt, J. H. M. M., & Wolk, S. J. 2013, *ApJ*, 773, 62
- Porto de Mello, G. F. & da Silva, L. 1997, *ApJ*, 476, L89
- Powell, K. G., Roe, P. L., Linde, T. J., Gombosi, T. I., & De Zeeuw, D. L. 1999, *Journal of Computational Physics*, 154, 284
- Pulkkinen, T. 2007, *Living Reviews in Solar Physics*, 4
- Redfield, S. & Falcon, R. E. 2008, *ApJ*, 683, 207
- Redfield, S. & Linsky, J. L. 2004a, *ApJ*, 602, 776
- Redfield, S. & Linsky, J. L. 2004b, *ApJ*, 613, 1004
- Redfield, S. & Linsky, J. L. 2008, *ApJ*, 673, 283
- Redfield, S. & Linsky, J. L. 2015, *ApJ*, 812, 125
- Reiners, A., Bean, J. L., Huber, K. F., et al. 2010, *ApJ*, 710, 432
- Reiners, A. & Christensen, U. R. 2010, *A&A*, 522, A13
- Reiners, A. & Mohanty, S. 2012, *ApJ*, 746, 43
- Réville, V., Brun, A. S., Matt, S. P., Strugarek, A., & Pinto, R. F. 2015a, *ApJ*, 798, 116
- Réville, V., Brun, A. S., Strugarek, A., et al. 2015b, *ApJ*, 814, 99
- Ridley, A. J. 2007, *Annales Geophysicae*, 25, 533
- Robrade, J., Schmitt, J. H. M. M., & Favata, F. 2012, *A&A*, 543, A84
- Rocha-Pinto, H. J. & Maciel, W. J. 1998, *MNRAS*, 298, 332

- Rodler, F., Lopez-Morales, M., & Ribas, I. 2012, *ApJ*, 753, L25
- Rosén, L. & Kochukhov, O. 2012, *A&A*, 548, A8
- Saar, S. H. 1996, in *IAU Symposium*, Vol. 176, *Stellar Surface Structure*, ed. K. G. Strassmeier & J. L. Linsky, 237
- Saffe, C., Gómez, M., & Chavero, C. 2005, *A&A*, 443, 609
- Santos, N. C., Mayor, M., Naef, D., et al. 2000, *A&A*, 361, 265
- Sanz-Forcada, J., Favata, F., & Micela, G. 2004, *A&A*, 416, 281
- Sanz-Forcada, J., Micela, G., Ribas, I., et al. 2011, *A&A*, 532, A6
- Sanz-Forcada, J., Stelzer, B., & Metcalfe, T. S. 2013, *A&A*, 553, L6
- Scandariato, G., Maggio, A., Lanza, A. F., et al. 2013, *A&A*, 552, A7
- Scherrer, P. H., Bogart, R. S., Bush, R. I., et al. 1995, *Sol. Phys.*, 162, 129
- Schmitt, J. H. M. M. & Liefke, C. 2004, *A&A*, 417, 651
- Schröder, C., Reiners, A., & Schmitt, J. H. M. M. 2009, *A&A*, 493, 1099
- Selsis, F., Kasting, J. F., Levrard, B., et al. 2007, *A&A*, 476, 1373
- Semel, M. 1989, *A&A*, 225, 456
- Shaikhislamov, I. F., Khodachenko, M. L., Sasunov, Y. L., et al. 2014, *ApJ*, 795, 132
- Shaviv, N. J. 2003, *Journal of Geophysical Research (Space Physics)*, 108, 1437
- Shibata, K. & Magara, T. 2011, *Living Reviews in Solar Physics*, 8, 6
- Shkolnik, E., Bohlender, D. A., Walker, G. A. H., & Collier Cameron, A. 2008, *ApJ*, 676, 628
- Shkolnik, E., Walker, G. A. H., Bohlender, D. A., Gu, P.-G., & Kürster, M. 2005, *ApJ*, 622, 1075
- Sing, D. K. 2010, *A&A*, 510, A21
- Sirothia, S. K., Lecavelier des Etangs, A., Gopal-Krishna, Kantharia, N. G., & Ishwar-Chandra, C. H. 2014, *A&A*, 562, A108
- Soderblom, D. R. & Clements, S. D. 1987, *AJ*, 93, 920
- Soderblom, D. R. & Mayor, M. 1993, *ApJ*, 402, L5
- Sokolov, I. V., van der Holst, B., Oran, R., et al. 2013, *ApJ*, 764, 23

- Sonka, M., Hlavac, V., & Boyle, R. 2007, *Image Processing, Analysis, and Machine Vision* (Thomson-Engineering)
- Stevens, I. R. 2005, *MNRAS*, 356, 1053
- Strassmeier, K. G. 2009, *A&A Rev.*, 17, 251
- Strugarek, A., Brun, A. S., Matt, S. P., & Réville, V. 2014, *ApJ*, 795, 86
- Strugarek, A., Brun, A. S., Matt, S. P., & Réville, V. 2015, *ApJ*, 815, 111
- Suzuki, T. K., Imada, S., Kataoka, R., et al. 2013, *PASJ*, 65 [[arXiv]1212.6713]
- Takeda, G., Ford, E. B., Sills, A., et al. 2007, *ApJS*, 168, 297
- Terada, N., Kulikov, Y. N., Lammer, H., et al. 2009, *Astrobiology*, 9, 55
- Testa, P., Saar, S. H., & Drake, J. J. 2015, *Philosophical Transactions of the Royal Society of London Series A*, 373, 20140259
- Torres, C. A. O., Quast, G. R., da Silva, L., et al. 2006, *A&A*, 460, 695
- Tóth, G., Sokolov, I. V., Gombosi, T. I., et al. 2005, *Journal of Geophysical Research (Space Physics)*, 110, A12226
- Tóth, G., van der Holst, B., & Huang, Z. 2011, *ApJ*, 732, 102
- Tóth, G., van der Holst, B., Sokolov, I. V., et al. 2012, *Journal of Computational Physics*, 231, 870
- Tu, L., Johnstone, C. P., Güdel, M., & Lammer, H. 2015, *A&A*, 577, L3
- Udry, S., Bonfils, X., Delfosse, X., et al. 2007, *A&A*, 469, L43
- Valenti, J. A. & Fischer, D. A. 2005, *ApJS*, 159, 141
- van der Holst, B., Sokolov, I. V., Meng, X., et al. 2014, *ApJ*, 782, 81
- Vedder, P. W., Patterer, R. J., Jelinsky, P., Brown, A., & Bowyer, S. 1993, *ApJ*, 414, L61
- Vidal-Madjar, A., Lecavelier des Etangs, A., Désert, J.-M., et al. 2003, *Nature*, 422, 143
- Vidotto, A. A., Donati, J.-F., Jardine, M., et al. 2016, *MNRAS*, 455, L52
- Vidotto, A. A., Fares, R., Jardine, M., et al. 2012, *MNRAS*, 423, 3285
- Vidotto, A. A., Fares, R., Jardine, M., Moutou, C., & Donati, J.-F. 2015, *MNRAS*, 449, 4117
- Vidotto, A. A., Gregory, S. G., Jardine, M., et al. 2014a, *MNRAS*, 441, 2361

- Vidotto, A. A., Jardine, M., & Helling, C. 2010, *ApJ*, 722, L168
- Vidotto, A. A., Jardine, M., & Helling, C. 2011, *MNRAS*, 414, 1573
- Vidotto, A. A., Jardine, M., Morin, J., et al. 2013, *A&A*, 557, A67
- Vidotto, A. A., Jardine, M., Morin, J., et al. 2014b, *MNRAS*, 438, 1162
- Vogt, S. S., Butler, R. P., Rivera, E. J., et al. 2010, *ApJ*, 723, 954
- Vogt, S. S., Penrod, G. D., & Hatzes, A. P. 1987, *ApJ*, 321, 496
- Watson, C. A., Littlefair, S. P., Collier Cameron, A., Dhillon, V. S., & Simpson, E. K. 2010, *MNRAS*, 408, 1606
- Webb, D. F. & Howard, T. A. 2012, *Living Reviews in Solar Physics*, 9
- Wood, B. E. 2004, *Living Reviews in Solar Physics*, 1, 2
- Wood, B. E. & Linsky, J. L. 2010, *ApJ*, 717, 1279
- Wood, B. E., Linsky, J. L., & Güdel, M. 2015, in *Astrophysics and Space Science Library*, Vol. 411, *Characterizing Stellar and Exoplanetary Environments*, ed. H. Lammer & M. Khodachenko, 19
- Wood, B. E., Müller, H.-R., Redfield, S., & Edelman, E. 2014, *ApJ*, 781, L33
- Wood, B. E., Müller, H.-R., Zank, G. P., & Linsky, J. L. 2002, *ApJ*, 574, 412
- Wood, B. E., Müller, H.-R., Zank, G. P., Linsky, J. L., & Redfield, S. 2005a, *ApJ*, 628, L143
- Wood, B. E., Redfield, S., Linsky, J. L., Müller, H.-R., & Zank, G. P. 2005b, *ApJS*, 159, 118
- Wright, N. J., Drake, J. J., Mamajek, E. E., & Henry, G. W. 2011, *ApJ*, 743, 48
- Zarka, P., Lazio, J., & Hallinan, G. 2015, *Advancing Astrophysics with the Square Kilometre Array (AASKA14)*, 120
- Zarka, P., Treumann, R. A., Ryabov, B. P., & Ryabov, V. B. 2001, *Ap&SS*, 277, 293
- Zechmeister, M. & Kürster, M. 2009, *A&A*, 496, 577

Acknowledgements

I would like to express my sincere thanks to my supervisor, Gaitee Hussain, for being such an amazing mentor during these years. Thanks a lot for all your time, guidance, patience, and for teaching me so many valuable lessons which have greatly enriched my career, although I must confess here that would require several PhD's to reach your level of diplomacy. I am looking forward to keep working with you in the future!

I also want to thank my fellow mentor, Jason Grunhut, for the assistance and availability since day zero of this job. Thanks for being the "outsider" to the field, bringing up great (and long!) discussions and interesting ideas.

I would like to acknowledge my collaborators, Cecilia Garraffo and Ofer Cohen, for their support and help during this process. Special thanks to Jeremy J. Drake for all the assistance, motivation, and for all the confidence he has put on me. Additional thanks to the reviewers of this dissertation: Thomas Preibisch, Artie Hatzes, Andreas Glindemann, Bernhard Mayer, Joseph Egger, and Klaus Dolag.

Special thanks to my colleagues in Colombia of the Group of Solar Astrophysics and the Observatorio Astronómico Nacional, particularly, to Prof. Benjamín Calvo Mozo, for all the support and encouragement in preparation for this major step of my career.

I want to thank the IMPRS program and ESO for giving me the opportunity of participating in a world-class PhD programme. I will be always very proud of this accomplishment. Thanks to the awesome group of ESO Students, Fellows and Staff members, for sustaining the great atmosphere in every coffee, seminar, and meeting. Special thanks to Dietrich Baade, who I greatly admire, for all the advise and motivation during my time here.

Many thanks to Laura, Florian, Claudia, Matteo, Jethro, Phil, Chris, Carolina and Matias (I was not going to forget about you weon!), for being such great friends, even in times when I was a crappy one. Special thanks to my friend and best officemate ever, Karina. Thanks for all the laughs we had in the office and for helping me (us) in so many occasions. I will certainly miss you my Germanizer friend, but I am pretty sure that we will meet again! I am not forgetting my other office mates, Carlo and Aleksandar, to whom I am also grateful for passing and keeping alive the spirit of the 524!

Last but not least, I would like to give many thanks to my family at home: Eliana, for being my force and motivation everyday; to my family in Germany: Yaneth, Michael, Lilibet, Luna and Ada, for all the great nights in which you make me (us) feel welcome in your place; to my family in Colombia: my Mom, Fabiola, and my brothers, Jorge and Daniel, for always believing in me; finally to my lifelong friends, Camo, Toby, Ed, Camilo, Guila and Chiqui, for being always there, no matter the time or the distance.

...And the warriors who live forever, fight on until the end.